Ingénierie de condensats artificiels pour l'étude du rôle de l'ARN et des moteurs moléculaires sur le contrôle de leur formation

Audrey Cochard

Sorbonne Université

École doctorale 388

Chimie Physique et Chimie Analytique de Paris Centre

Département de Chimie – École Normale Supérieure

Et

Laboratoire de Biologie du Développement – Sorbonne Université

Engineering artificial condensates in cells to study the role of RNA and molecular motors in controlling their formation

Par Audrey COCHARD

Thèse de doctorat de Chimie Physique

Dirigée par Zoher GUEROUI et Dominique WEIL

Présentée et soutenue publiquement le 21 septembre 2022 devant un jury composé de :

Mme BESSE Florence	Directrice de recherche	Rapportrice
M. COPPEY Mathieu	Directeur de recherche	Président du jury
M. ERDEL Fabian	Chargé de recherche	Rapporteur
M. GUEROUI Zoher	Directeur de recherche	Directeur de thèse
Mme LEDUC Cécile	Directrice de recherche	Examinatrice
Mme WEIL Dominique	Directrice de recherche	Directrice de thèse

ACKNOWLEDGEMENTS

Ces quatre années de thèse n'auraient pas été les mêmes sans les gens qui m'ont entourée. Sûrement la partie la plus importante de ce manuscrit, ces remerciements vont être longs au vu du nombre de personnes que j'aimerais citer. Si vous préférez sauter cette section, allez à la page 5, qui n'est pas deux pages après cette page pourtant numérotée 3, car je n'ai pas anticipé la longueur de cette section.

I would like first to thank my thesis reviewers, Florence Besse and Fabian Erdel, for accepting to evaluate my work despite having to read my manuscript during summer, and for coming all the way to Paris for my Ph.D. defense. I would like to thank also the examinators, Cécile Leduc and Mathieu Coppey for accepting to attend my defense despite the busy schedule implied by September.

Un grand merci à mes directeurs de thèse Zoher et Dominique.
Zoher, merci de m'avoir accueillie dans ton laboratoire dès le stage de master 2, pour les nombreuses discussions, pour ton enthousiasme qui m'a permis de garder ma motivation tout au long de ces quatre années, et pour m'avoir accordée ta confiance pour l'encadrement des stages de Leonard et Pauline, des expériences très formatrices et que j'ai beaucoup appréciées. Je voudrais également te remercier très sincèrement pour les conseils et le temps que tu consacres à me guider dans mes choix de carrière.
Dominique, merci pour l'accueil au sein de ton équipe et pour le point de vue de biologiste que tu as apporté à ma thèse. Merci également pour ton implication dans la relecture de mon manuscrit jusqu'au tout dernier jour. Enfin, merci de me montrer à quel point il me faut encore progresser au Scrabble, je vais continuer à mobiliser ma famille pour m'entraîner !

A tous les membres de l'équipe de Zoher, passés et présents, merci pour les bons moments, les goûters, les discussions (scientifiques ou non), les rires…
Un immense merci à Marina pour le temps et la patience dont tu as fait preuve en me formant à mon arrivée au laboratoire (« à mon arrivée » ou plutôt pendant 9 mois, jusqu'à ton départ). J'espère que tu n'as pas trop regretté de m'avoir dit de ne pas hésiter à poser des questions.
Marie-Aude, un merci ne suffirait pas à décrire le pilier que tu es pour le laboratoire. Mais en l'absence de mots plus appropriés, merci pour ton aide au quotidien et merci de répondre à mes nombreuses questions (certes, souvent en râlant). Nous sommes devenues bien plus que de simples collègues (c'est la souffrance au body tonic ça, ça rapproche), et j'espère que tu ne penses pas te débarrasser de moi avec mon départ, d'ailleurs c'est raté, je reste trois mois de plus.
Mary, merci pour ta présence pendant toute la première moitié de ma thèse, qui n'aurait pas été la même sans la possibilité de pencher ma tête juste un peu à gauche pour te parler, et sans nos sorties courses à pied le soir (bon en vrai on ne l'a pas fait tant de fois que ça mais faisons genre).

Leonard, merci pour ta bonne humeur et ton gâteau aux pommes. Ce fut très chouette d'apprendre à encadrer avec toi, même si ce fut un encadrement particulier pour cause de pandémie mondiale. Pauline, ton stage s'est lui déroulé sans accrocs, merci d'avoir lancé le projet moteur ! Laura, merci de rendre la mezzanine un peu plus agréable grâce à toutes tes petites plantes qui survivent tant bien que mal à l'absence de lumière. Chems, merci pour ta bonne humeur à toute épreuve, et bonne chance pour ta belle thèse à venir. Merci également à Wei-An et Shunichi pour l'accueil à mon arrivée au labo.

A tous les membres de l'équipe de Dominique, merci pour votre accueil, vos conseils et vos enseignements. Merci aux participants des soirées Scrabble et pour les autres, j'espère que l'escape game sera davantage fédérateur !
Adham et Marie-Noëlle, merci d'avoir accepté de prendre part au projet moteur. Michel, un grand merci pour les semaines de clonage à 4 mains et pour m'avoir transmis tes astuces de cloneur expérimenté. Merci Marianne de m'avoir formée au smFISH aux côtés de Marina et de m'avoir si souvent prêté ta paillasse. Merci à Michèle pour la formation au western blot. Merci Maïté pour ton regard aiguisé de biologiste à l'affût des barres d'échelle manquantes.

J'aimerais aussi remercier sincèrement Arthur (et Mary d'avoir provoqué notre rencontre !) : merci pour ton script qui a changé le cours de ma thèse, et pour ton aide, ton temps et ta patience pour que je le prenne en main.

I would like to thank Saito-sensei for welcoming me in his lab. Thank you very much for the great scientific experience, as well as for teaching me about Japanese food and sake! Yoshii-sensei, thank you for mentoring me during my stay and for guiding me around the lab. Thank you also to Sora and Tomo, whom I had the pleasure to first work with in France. Sora, thank you for your warm welcome in Germany! And Tomo, thank you so much for your help in trying to get me inside my building on my last evening in Kyoto when I forgot my key card inside!

Je voudrais aussi remercier tous les membres du pôle CPBMV : Isabelle, Emmanuelle, Thomas, Alison, Annamaria, Bea, Damien, Emilie, Kätlin, Marc, Raja, Tiphaine, Aliénor, Damien, Emilie, Fayrouz, Julien, Marc, Raja, Tiphaine, Yoan, Yuriy, Hélène, Clément, Emma, Ian (et j'en oublie sûrement). Merci à tous pour la bonne ambiance, les goûters, les fat Fridays… Mention spéciale pour Aliénor, merci pour tes conseils et bon courage pour la fin de ta thèse !

Je tiens également à remercier très chaleureusement le personnel administratif, Pauline, Elza, Delphine et Delphine, Nathalie, Anne : merci pour votre aide au quotidien, votre disponibilité, et surtout le sopalin. J'attends avec impatience l'épisode 2 de The Office version ENS !

J’aimerais adresser toute une page de remerciements au « groupe des petits chats » (pas sûre que tout le monde valide le nom), à jamais soudés par 18km de zig-zags en barque, un vol en avion avec Didier le pilote qui pilote sans les mains, les chocolats chauds de Lille (parce que bon Lille c’est beau mais en novembre, c’est surtout froid), la grêle de Saint-Malo en mai… Mais comme les numérotations de pages ne collent déjà pas, je vais essayer de me restreindre. Mary, même si je t’ai déjà remerciée plus haut, tu mérites bien une seconde mention pour ta bonne humeur et ton enthousiasme. Lulu, merci d’être là, tu as rendu ma thèse bien plus drôle, on s’est bien marrés quand même, et on continue de le faire, c’est chouette que tu ne sois pas parti trop loin pour le début de ton post-doc. J’espère que tu ne m’oublieras pas quand tu seras à la Nouvelle York des Etats-Unis avec Vivi qui s’est arrangé pour soutenir le même jour que moi, non mais quand même c’est pas croyable ça (ok c’est moi qui ai eu la date en deuxième mais bon quand même il aurait pu décaler). Les « filles de Jussieu », comment décrire le déchirement émotionnel de votre déménagement ? Heureusement que vous n’êtes parties qu’à 15 minutes de l’ENS. Fanny, ma presque coloc à 900 mètres près, merci pour toutes ses soirées en tête à tête chez toi, pour nos confidences, et merci d’avoir été un soutien tout au long de ma thèse (et pour ta fameuse tarte courgette feta). Et un énoooorme merci d’avoir fait le déplacement depuis Lausanne pour ma soutenance, quel plaisir pour moi de t’avoir à mes côtés ! Et compte sur moi pour revenir te voir à Lausanne ! Hela, merci pour ta bonne humeur et ton sourire à tout épreuve. Je compte bien organiser un petit voyage de groupe au Canada pour qu’on vienne tous te rendre visite ! Et enfin Louise, la petite dernière de la bande (au niveau de la thèse, je t’entends déjà râler), bon courage pour la rédaction et la fin de ta thèse qui je suis sûre va se passer comme sur des roulettes. Je t’offrirai des gommettes à ta soutenance.

Enfin, un gigantesque merci à ma famille, à qui je pourrais également dédier toute une page, pour leur soutien et leur amour au quotidien qui ont rendu supportables les moments difficiles et encore plus beaux les moments de joie. J’espère que la soutenance vous aura permis de comprendre un peu ce que j’ai fait avec mes petites cellules dans leurs petites boîtes pendant 4 ans. Merci maman, papa, de continuer à répondre à mes appels presque quotidiens sans être exaspérés (ou au moins merci de bien dissimuler votre exaspération). Merci Guigui de m’appeler quand tu t’ennuies sur ton vélo ou quand tu marches sur un chemin un peu trop plat à ton goût, c’est toujours ça de pris ; merci aussi d’avoir passé le premier confinement avec moi, même si tu n’as pas eu le choix, et d’en avoir fait presque un bon souvenir grâce à ta présence (et à tes dahls de lentilles). Merci Christopher d’être venu à ma soutenance même si tu ne portes pas particulièrement Paris dans ton cœur. J’ai hâte de venir te rendre visite à la montagne.

Enfin (cette fois pour de vrai), mes derniers remerciements sont pour Michaël. Merci d'avoir été présent pour la fin de ma thèse, de m'avoir nourrie pendant ma rédaction et de me faire relativiser quand c'est nécessaire. Merci aussi pour Bob (kibob), qui est d’une grande aide, même si les tours de Pise vont sûrement perdurer encore un peu car les habitudes sont parfois difficiles à perdre.

LIST OF ABBREVIATIONS

ALS: amyotrophic lateral sclerosis

ATP: adenosine triphosphate

BICD2: bicaudal D2

C. elegans: *Caenorhabditis elegans*

CID: chemically-induced dimerization

CLIP: crosslinking immunoprecipitation

Corelet: core scaffolds to promote droplets

C_{sat}: saturation concentration

dCas9: dead Cas9

DFC: dense fibrillar component (of the nucleolus)

EGFP: enhanced green fluorescent protein

emGFP: emerald green fluorescent protein

ER: endoplasmic reticulum

FAPS: fluorescence-activated particle sorting

FC: fibrillar center (of the nucleolus)

FKBP: FK506-binding protein

FLuc: firefly luciferase

Fluoppi: fluorescent protein-protein-interaction-visualization

Fm: F36M-FKBP (point mutant of FKBP)

FRAP: fluorescence recovery after photobleaching

FRB: FKBP-rapamycin binding protein

Ft: ferritin

FTH1: ferritin heavy chain 1

GC: granular component (of the nucleolus)

HEK293: Human embryonic kidney

HeLa: Epithelial cells named after Henrietta Lacks from whom they were harvested

IDP: intrinsically disordered protein

IDR: intrinsically disordered region

iLID: improved light inducible dimer

iPOLYMER: intracellular production of ligand-yielded multivalent enhancers

iPOLYMER-LI: intracellular production of light-yielded multivalent enhancers with light inducibility

K_d: dissociation constant

LARIAT: light-activated reversible inhibition by assembled trap

LLPS: liquid-liquid phase separation

lncRNA: long non-coding RNA

m^6A: N^6-methyladenosine

mCh: mCherry

MCP: MS2 coat protein

mRNA: messenger RNA

NPC: nuclear pore complex

NPM1: nucleophosmin 1

OptoDroplet: optogenetic droplet

PABP: poly(A)-binding protein

PB: P-body

PC: partition coefficient

PHR: photolyase homology region

PiXELL: Pix Evaporates from Liquid-like droplets in Light

PML NBs: promyelocytic leukemia nuclear bodies

PPI: protein-protein interactions

PPPS: polymer-polymer phase separation

PRM: proline rich motifs

PTM: post-translational modification

PUF: pumilio and FBF homology domain

PULR: PUF-assisted localization of RNA

PUM.HD: pumilio homology domain

RBD: RNA-binding domain

RBP: RNA-binding protein

rDNA: ribosomal DNA

RNA-MS2: RNA with 4 MS2 stem loops in its 3'UTR

RNP: ribonucleoprotein

RRM: RNA recognition motifs

rRNA: ribosomal RNA

scFv: single-chain variable fragment

sfGFP: super-folder green fluorescent protein

SG: stress granule

sgRNA: single guide RNA

SIM: SUMO interacting motif

Sm(i)FISH: single molecule (inexpensive) Fluorescence *In Situ* Hybridization

snRNPs: small nuclear ribonucleoproteins

SPD-5: spindle-defective protein 5

SPREC-In: synthetic protein-recruiting condensates

SPREC-Out: synthetic protein-releasing condensates

ST: SunTag

TR: transcriptional regulator

CONTENTS

CHAPTER I: General introduction: Biomolecular condensates as a way to organize subcellular space

Contents

I.1. Generalities about biomolecular condensates

Cellular biochemistry is complex and requires spatial and temporal control. One way for spatiotemporal regulation is subcellular organization through functionally distinct compartments. Such compartments are ubiquitous across living organisms and can both facilitate or inhibit reactions by either concentrating or segregating biomolecules. Eukaryotic cells display numerous membrane-bound organelles, such as the nucleus, mitochondria and endosomes, that participate in the spatial restriction of biochemical reactions and other cellular functions. Their lipid bilayer membranes play an essential role in keeping the interior of the organelles spatially distinct from the cellular environment, with membrane transport machineries providing the necessary exchanges to regulate organelles composition. However, another class of organelles, membraneless organelles, seem equally prominent in organizing the cellular space despite the lack of a defined separation between their interior and the bulk (Fig. I.1). These micron-scale compartments, found throughout both the cytoplasm and the nucleoplasm, are also called biomolecular condensates to refer to their ability to concentrate biomolecules, proteins and nucleic acids, regardless on their precise compositions, physical properties and morphologies[1]. This name also echoes liquid-liquid phase separation (LLPS), a concept borrowed from soft-matter physics which recently appeared as a common framework underlying the formation of condensates. The phase boundaries of phase-separated condensates would enable spatial and temporal restriction of biomolecules but also diffusion and exchange with the environment, which are required for cellular biochemistry. These properties would enable the condensates to take part in various cell processes, from RNA metabolism to DNA repair. Though condensates are principally described in eukaryotic cells, they have also recently emerged as an organization principle of bacterial cells[2,3]. We will however here focus on eukaryotic cell condensates and address several questions: can we define a unifying framework to describe the mechanisms underlying condensates in cells? What molecular determinants decide which molecules interact to form condensates? We will first list and describe condensates in eukaryotic cells (I.1.2), before looking deeper into LLPS as a common model underlying the formation and growth of condensates (I.1.3). Finally, we will look at the relationship between structure, dynamics and functions of biomolecular condensates, that recent lines of research try to address to explain how material properties of condensates can define their cellular functions (I.1.4).

I.1.1. Biomolecular condensates in eukaryotic cells

The first observation of a condensate, the nucleolus, dates back to the first half of the 19th century[4]. Biomolecular condensates are now known to be ubiquitous in eukaryotic cells where they take part in the organization of both the nucleoplasm and the cytoplasm (Fig. I.1). In the nucleus, we can find notably the nucleolus, where the transcription of ribosomal RNA (rRNA) and ribosome assembly occur[4], Cajal bodies, involved in the assembly and maturation of small nuclear ribonucleoproteins (snRNPs)[5], promyelocytic leukemia nuclear bodies (PML NBs), implicated in various cellular processes like senescence and antiviral defense[6], nuclear speckles, that stock splicing factors[7], and nuclear pore complexes (NPC), that enable both nuclear import and export[8]. In the cytoplasm, we can mention P-bodies (PBs), that store translationally repressed messenger RNAs (mRNAs)[9], stress granules (SGs), that store mRNAs in stress response pathways[10], RNA transport granules that convey RNAs along the axons of neurons to notably localize their translation[11], and germ granules that segregate specific components to the germ line[12].

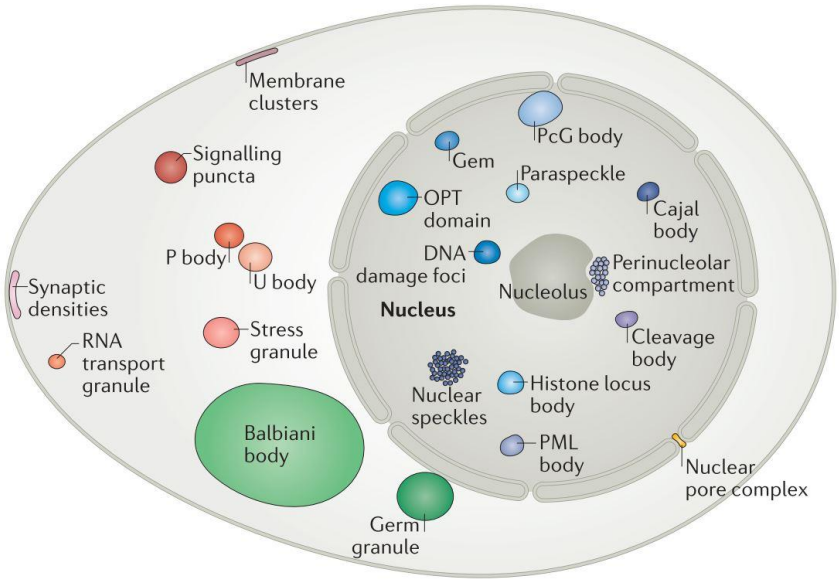

Figure I.1: Biomolecular condensates in eukaryotic cells. Adapted from[1]. Representation of the diversity of condensates found in eukaryotic cells, including for completeness some that are cell type-specific (like germ granules in germ cells) or context-specific (like SGs in stress conditions).

Condensates are very diverse in composition, localization, and functions. They can be conserved between different eukaryotic cells, like the nucleolus in the nucleus, or PBs and SGs in the cytoplasm that are found both in animal and plant cells. Some are also cell-specific, like germ granules in germ cells and RNA transport granules in neurons, or may require specific environmental stimuli to form, like SGs that appear in response to various stresses.

Condensates usually concentrate 10 to hundreds of different proteins, as well as RNAs, though some of them, like PML NBs do not accumulate RNAs[13]. In addition to immunofluorescence and tagging of proteins with fluorescent proteins that allowed for the identification of proteins concentrated in condensates, recent advances in proteomics and transcriptomics analyses have revealed insightful information on the content of biomolecular condensates. The nucleolus for example contains over 4500 different proteins[14]. The purification of SGs by differential centrifugation showed that they are enriched in more than 1500 mRNAS[15,16]. A fluorescence-activated particle sorting (FAPS) method enabled the purification of endogenous PBs and unraveled an enrichment of more than 100 unique proteins and 6000 RNAs[17]. Condensates components can be unique to a specific condensate or shared, as illustrated by mRNAs able to transition bidirectionally between PBs and SGs, whose protein composition contain also shared components[10,18]. Moreover, condensate composition can be context-dependent, like the content of mRNAs in SGs that can vary under different stress conditions, which could be a consequence of differences in the specificity of translation repression[16].

Interestingly, despite the enrichment of over 150 proteins in PML NBs[19], only the PML protein is required for the formation of these condensates[20]. This highlights the difference between two categories of condensate components which are scaffolds and clients[21]. The first are essential for the formation of the condensates, and their depletion leads to a decrease in the number and/or the size of the structures, or even to the absence of condensates. PML knocked-out cells are indeed devoid of PML NBs[20]. Another example comes from spindle-defective protein 5 (SPD-5) that was shown to be necessary for centrosomes in C. elegans[22]. Scaffold components are not necessarily proteins, as illustrated by architectural RNAs like the long non-coding RNA (lncRNA) NEAT-1, which is necessary and sufficient for paraspeckle assembly in the nucleus, or mRNA that is required for PB and SG formation in the cytoplasm[23,24]. The second category of condensate components, clients, consists in biomolecules that are not required for the assembly of the condensates but partition into them, often through direct interactions with scaffold components. Abolishing PML NBs-associated proteins BML helicase and Sp100 for example did not result in the absence of PML NBs, showing that these proteins are not essential for their formation [20]. In reality, the separation between scaffolds and clients is not easy, and condensates also count many components with intermediate behaviors, that are not required for condensate assembly but still modify their propensity to assemble.

Despite this variability in assembly, composition, localization, and functions, a unifying model underlying the formation of biomolecular condensates has recently emerged as a consequence of observations of their liquid-like behavior. This model, liquid-liquid phase separation (LLPS), is well described in soft matter physics, and brings light on how these structures are able to condense biomolecules while allowing fast exchange with the cellular environment.

I.1.2. Liquid-liquid phase separation as a common model of formation

I.1.2.a. Evidence of liquid-like properties of biomolecular condensates

Pioneer experiments on P granules in *Caenorhabditis elegans (C elegans)* in 2009 highlighted for the first time liquid-like properties of a membrane-less organelle: spherical, the P granules could fuse with each other and relax into a spherical shape, and fluorescence recovery after photobleaching experiments (FRAP) showed a high protein mobility on a short time scale, with a rapid diffusion both toward the surrounding cytoplasm and within the granule (Fig. I.2)[12]. These three properties, that are the round shape due to surface tension, the ability to fuse and relax into a spherical droplet, and the fast rearrangement of components, recapitulate liquid-like behavior and are shared by numerous other membrane-less organelles. Fusion events and subsequent relaxation into spheres were thus observed for instance for Cajal bodies and PML NBs, as well as for the bigger nucleoli[25–27]. Condensate components show moreover a high mobility over second to minute time scales, like proteins in nuclear speckles and nucleoli[28], Cajal bodies[29], and PML NBs[30]. FUS assemblies, either on sites of DNA repair in the nucleus or SGs in the cytoplasm, also showed fusion events and relaxation, and fast diffusion[31]. These shared liquid-like properties suggest a common mechanism of formation by liquid-liquid phase separation (LLPS)[32].

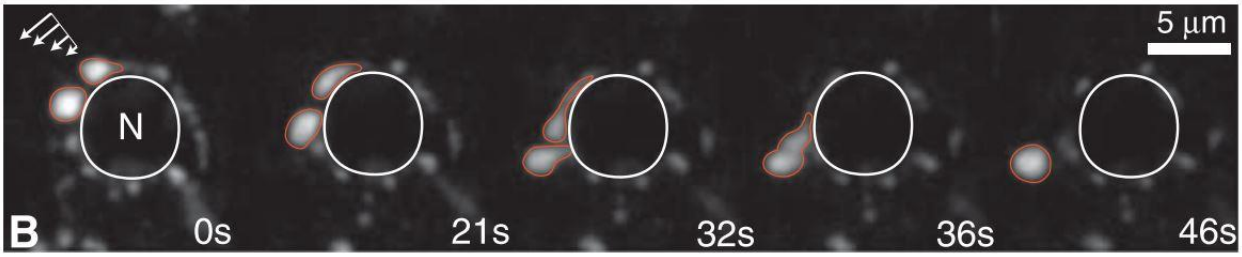

Figure I.2: P granules of a *C. elegans* embryo behave like liquids. Adapted from[12]. Dripping and coalescence of P granules under shear stress.

I.1.2.b. The principle of liquid-liquid phase separation

In a one-component system (one solute in a solvent), LLPS is a process whereby the solute initially homogeneously distributed in a solution demixes into a two-phase stable system. One phase is solute-rich (the dense phase) while the other is solute-poor (the dilute phase). In this simple view, LLPS occurs when the homotypic solute-solute interactions are stronger than heterotypical solvent-solute interactions, making it more energetically favorable to have two phases, despite the unfavorable decrease in entropy. The conditions for LLPS occurrence are determined by a set of parameters (concentration, temperature, pression, pH…). If we consider a system with fixed parameters except for an increasing solute concentration, LLPS will occur over a saturation concentration C_{sat}. As the concentration keeps increasing, new solute will join the dense phase and increase its volume without modifying its concentration, while the concentration of the dilute phase will remain equal to C_{sat}. This framework can be recapitulated in a phase diagram, with the binodal or coexistence curve defining the phase boundaries: under conditions outside of the binodal, the solution remains monodisperse, while conditions below the binodal lead to two-phase systems (Fig. I.3 left).

In the case of biomolecular condensates, in this simplified picture, the solute is often a protein or a nucleic acid, and the solution is the cellular environment, either the cytoplasm or the nucleoplasm. The entropy of mixing is dominated by the attractions between the phase-separated molecules. Reconstitution of single component droplets, either in cells or *in vitro*, followed the trend anticipated by such phase diagrams. For example, light-induced OptoDroplets (see I.2.2.b.) only form when the overall concentration is superior to C_{sat}[33]. Likewise, FUS family proteins phase separate *in vitro* over different C_{sat} that are dictated by interactions between tyrosine and arginine residues[34].

However, biomolecular condensates are in reality multicomponent systems, with many proteins and RNAs, which could impact their behavior. Indeed, though OptoDroplets based on homotypic interactions give rise to a constant dilute concentration equals at C_{sat} during droplet formation, introduction of heterotypic interactions with cellular components leading to multicomponent condensates results in absence of C_{sat} and instead in an increased dilute concentration[35]. This suggests the need of higher-dimensional phase diagrams to describe the behavior of biomolecular condensates (Fig. I.3 right)[35].

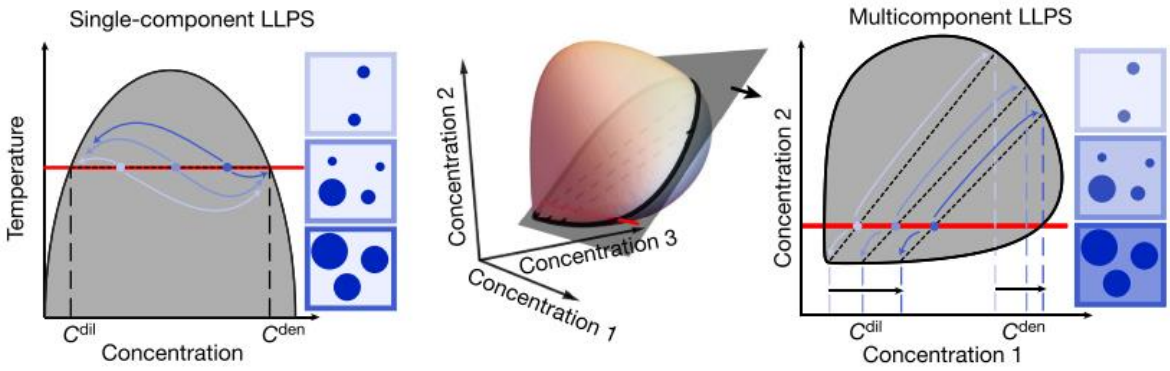

Figure I.3: Phase diagram for a single-component system (left) and for a multicomponent system (right). Adapted from[35]**.** For a multicomponent system, two-dimensional phase diagrams are slices of a higher-dimensional phase diagram. Phase separation occurs in the grey regions delimited by the binodal. In the grey regions, for a component concentration increasing along the red line, the concentrations of the dilute and dense phases are defined by the dashed tie lines: they remain fixed for a single-component system, while they increase for a multicomponent system.

In a multivalent system, points outside the binodal do not lead to phase separation, either because the global concentration of components is too low relatively to their interaction affinity or because of an imbalance in the component stoichiometry, as shown by the expression of a two-component system able to phase separate in yeast[36]. As pointed out by this study, reconstitution systems with minimal composition, though far much simpler than endogenous biomolecular condensates, can bring insightful information on the requirements to achieve phase separation. They have also enabled to bring to light the impact that post-translational modifications (PTMs), mutations, or changes in the environment (temperature…) can have on C_{sat} by modifying the affinity of protein-protein interactions (PPI). For example, the control of the phosphorylation degree of the transmembrane protein nephrin by kinases, by modifying the valence of the interaction with the nephrin partner NCK, itself interacting with N-WASP, could shift C_{sat} from the micromolar to the nanomolar regime[37]. Mutations modulating the dissociation constant between interacting domains of phase-separating components, and thus the affinity of the proteins, were also showed to induce a shift in the phase diagram[36].

Altogether, LLPS is a useful framework to study the mechanisms underlying the formation of biomolecular condensates in cells.

I.1.2.c. Molecular determinants driving LLPS in cells

In vitro, almost all proteins can phase separate. However, many proteins lose that ability under physiological conditions. This raises an important question: what defines the ability of a protein or a nucleic acid to promote phase separation in cell?

Multivalence, i.e., the presence of multiple binding sites on the same biomolecule, has been pointed out as a key molecular feature required for phase separation. Multivalent domains can be separated in two categories: folded domains and intrinsically disordered regions (IDRs). Folded domains form stable secondary and tertiary structures, while IDRs are typically low complexity sequences that do not form a defined three-dimensional structure but rather adopt a dynamic continuum of structures (Fig. I.4).

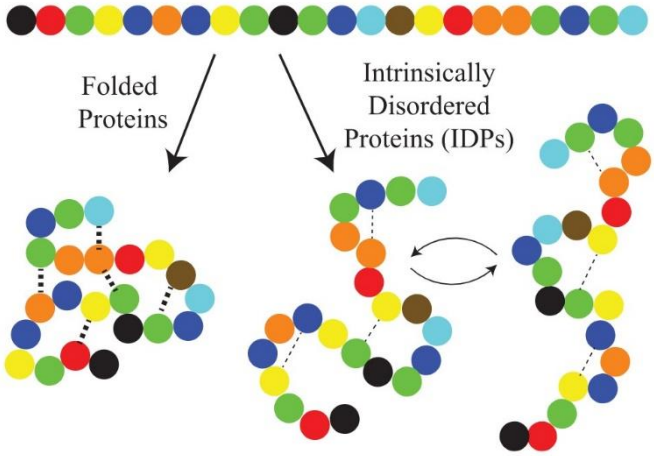

Figure I.4. Difference in tertiary structure between a folded protein and an intrinsically disordered protein. From[38]. Strong intramolecular interactions lead to a folded protein with a highly stable tertiary structure, while weaker intramolecular interactions lead to multiple possible tertiary structures separated by low energy barriers and thus to proteins with conformational heterogeneity (IDRs).

The hypothesis that modular proteins, i.e., proteins with multiple folded domains, could be scaffolding biomolecular condensates, first emerged from the observation of their enrichment in condensates, and was corroborated by pioneer experiments from the Rosen lab. They showed that SH3 domain repeats bind to proline rich motifs (PRM) and form droplets *in vitro* above a C_{sat}, that is reduced for higher valency repeats, thus highlighting the importance of valency in the formation of condensates (Fig. I.5)[37]. Expression in cells of these constructs led to liquid-like droplets similar to endogenous condensates. The SH3/PRM system is at the core of the formation of membrane clusters containing the transmembrane protein Nephrin and its interacting partners Nck and N-WASP, involved in an actin regulatory signaling pathway[37,39]. Other multivalent interacting scaffolds were shown to phase separate

in vitro, like SUMO3 repeats and repeats of SUMO interacting motif (SIM), or the PTB protein, that contains four RNA recognition motifs (RRMs), and an RNA with five repeats of the RRM recognition sequence[21]. Phase separation driven by multivalent motifs of modular proteins that can bind to complementary domains on either proteins or RNAs thus appears as a fundamental mechanism of biomolecular condensates formation.

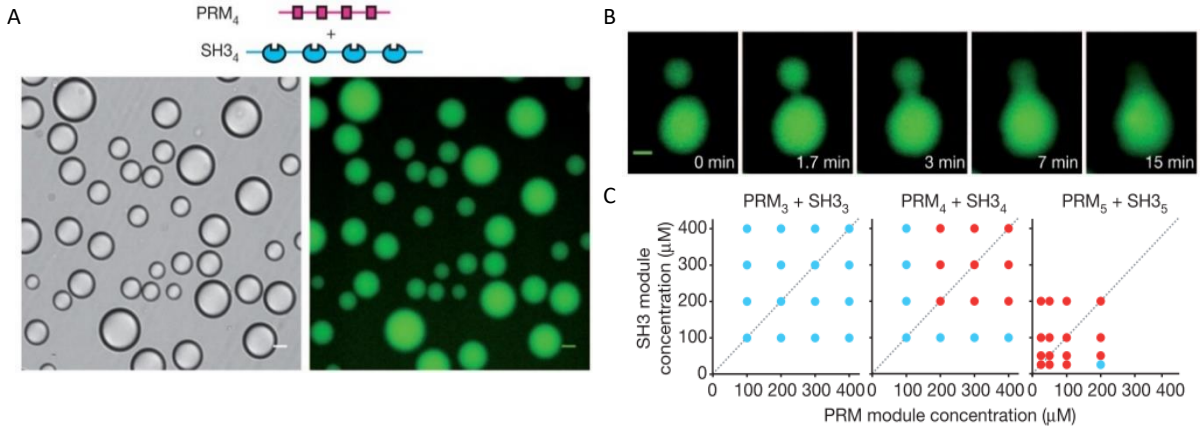

Figure I.5. Repeats of SH3 and PRM form liquid-like condensates *in vitro*. Adapted from[37]. A. Multivalent purified proteins of four repeats of SH3 and PRM (300 µM of each fusion protein) phase-separate into droplets as seen here by differential contrast microscopy (left) and wide-field fluorescence microscopy (right). Scale, 20 µm. **B.** Droplets have a liquid-like behavior as illustrated in this time-lapse imaging by their ability to coalesce and relax in a spherical shape. Scale, 10 µm. **C.** The phase boundary is highly dependent on the valency of the interacting proteins: a higher valency leads to droplet formation at lower concentrations (blue points: no phase separation, red points: phase separation).

In addition to modular proteins, many other proteins found in biomolecular condensates are intrinsically disordered proteins (IDPs) or contain IDRs[40]. IDRs are low complexity sequences, i.e., they display a poor sequence diversity and are enriched in a limited number of amino acids, primarily polar amino acids (serine, threonine, glycine, glutamine, and asparagine) and aromatic residues (tyrosine and phenylalanine). Some of them also contain amino acids with electrically charged side chains (positive lysine and arginine and negative aspartate and glutamate)[40].

The observation of the abundance of IDRs in biomolecular condensates, along with *in vitro* experiments that have highlighted the ability of IDRs to form droplets, have pointed out IDRs as driving forces for intracellular phase separation through a rich set of weak interactions promoted by their particular amino acid composition. Nott et al. thus showed that the RNA helicase DDX4, found in P granules in worms, form phase-separated condensates both *in vitro* and in cells through weak intramolecular and intermolecular electrostatic cation-pi interactions between positively charged arginine residues and aromatic residues, and probably pi-stacking interactions between aromatic residues[41]. These electrostatic interactions are highly dependent on salt, temperature and concentration[41]. In accordance with electrostatic interactions-based phase separation, salt was also shown to destabilize droplet assembly promoted by the N-terminal arginine/glycine-rich IDR of LAF-1, a DDX3 RNA helicase also found in P granules, that is necessary and sufficient to form condensates *in vitro* and in cells[42]. A similar domain of the nucleolus DFC marker F1B1 was shown to be sufficient to form droplets *in vitro*[43]. LLPS of hnRNPA1, an RNA-binding protein (RBP) found in SGs, is also mediated by a low complexity domain[44]. A lower salt concentration favors the phase separation of hnRNPA1 while disrupting interactions of phenylalanine residues impedes LLPS, highlighting the contribution of electrostatic interactions and aromatic residues in the LLPS behavior of hnRNPA1[44]. Similarly, the amyotrophic lateral sclerosis (ALS)-associated protein FUS form droplets *in vitro* and in cells through weak and transient interactions mediated by the prion-like low complexity domain of FUS[31].

Importantly, a given protein can have both folded domains and IDRs, and both can participate in the formation of condensates. An example is nucleophosmin 1 (NPM1), abundantly present in the granular component of the nucleolus. The oligomerization domain of NPM1, leading to a pentamer assembly with a radial array of NPM1 IDRs, along with acidic tracks both in the folded domain and the IDR of NPM1, which are able to bind proteins displaying multiple arginine residues, create the multivalency needed for phase separation[45]. G3BP1-mediated formation of SGs also requires both the dimerization domain of the protein and intermolecular interactions between IDR domains of G3BP1 proteins[46]. Interestingly, at low RNA concentrations, intramolecular interactions between two G3BP1 IDRs create a closed conformation of the protein and prevent the formation of SGs. After for example a stress-induced translation arrest and release of mRNAs from polysomes, the binding of RNA to one of the two IDRs makes the other one available to interact with another G3BP1 protein (Fig. I.6).

Multivalent weakly adhesive intermolecular interactions between folded domains of modular proteins or short linear motifs within IDRs are thus driving forces of phase separation[1]. Importantly, RNA molecules, that can also contain structured and unstructured regions, can also participate in multivalent interactions and thus play an important role in the biogenesis of condensates.

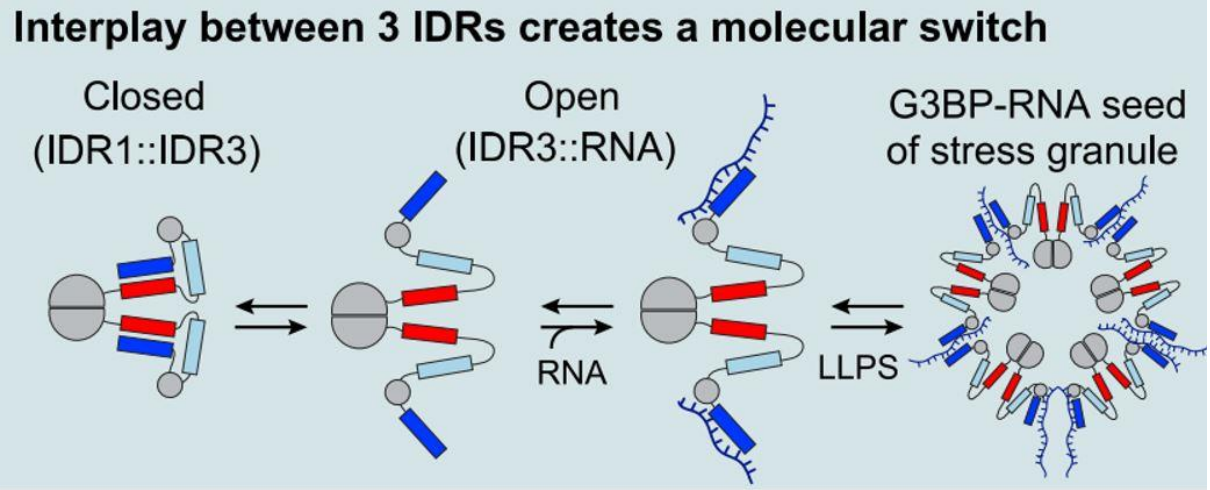

Figure I.6. Molecular switch underlying the formation of SGs. Adapted from[46]. Interactions between RNAs and one IDR of G3BP1 stabilizes the open conformation of G3BP1 and enables intermolecular interactions underlying SG assembly.

I.1.2.d. Limits of the LLPS model

The model of LLPS has brought a unifying framework to study biomolecular condensates in cells. However, as every model, it can be completed or even refuted in certain cases[47].

Three properties, described in part I.1.3.a., were first used as the basic criteria to define LLPS in cells following the observations of the liquid-like properties of the P granules in C. elegans and the nucleolus in *Xenopus laevis* oocytes[12,27]. These three properties are (1) the spherical shape due to surface tension, (2) the ability to coalesce after touching and (3) the fast internal rearrangement and external exchange[32]. However, some biomolecular condensates do not follow all three criteria. This is for example the case of paraspeckles, which assemble around NEAT1 lncRNA[23]. Indeed, though individual paraspeckles are spherical, increasing the concentration of NEAT1 does not lead to a homogeneous growth of the condensates in all directions with a maintained spherical shape, but to an elongation along a single axis[48]. The resulting structures were shown to be chains of paraspeckles, indicating the inability of the condensates to fuse and relax into spherical shapes. Besides contradicting two of the three initial criteria defining LLPS (the spherical shape and the ability to fuse), paraspeckles fail to recapitulate other behaviors expected for condensates falling within the LLPS framework. First, paraspeckles cannot exist independently of NEAT1, which contradicts the LLPS model whereby condensates can exist independently of a specific polymer[49]. rRNA for example promotes nucleoli formation and accelerates coarsening but droplets can nevertheless form in the absence of rRNA[50]. Secondly, instead of being set by the concentration of scaffold components, as would be expected for

LLPS, the size of paraspeckles depends on the length and abundance of NEAT1, with truncated versions of NEAT1 leading to smaller paraspeckles[23]. These discrepancies highlight the fact that the LLPS model, though very attractive, is maybe not a global answer.

Recently, a micellization model was proposed to explain the behavior of paraspeckles[51]. Paraspeckles adopt a core-shell structure, with the 5' and 3' terminal regions of NEAT1 in the shell, and the middle domain, interacting with the oligomerizing RBP NONO, in the core. This structure and the cylindrical shape that paraspeckles can display are reminiscent of micelle structure of block copolymers (polymers composed of several chemically distinct polymer blocks). Therefore, in the micellization model, NEAT1 and interacting RBPs are treated as an amphipathic triblock copolymer, with the 5' and 3' regions being hydrophilic domains exposed to the nucleoplasm, and the middle domain, bridged by NONO, being a hydrophobic core (Fig. I.7). Repulsive interactions between the 3' or the 5' regions of distinct NEAT1 molecules explain the inability to fuse and the cylindrical shape of paraspeckles. The model also accounts for the dependency of the size of the condensates on the transcription level of NEAT1.

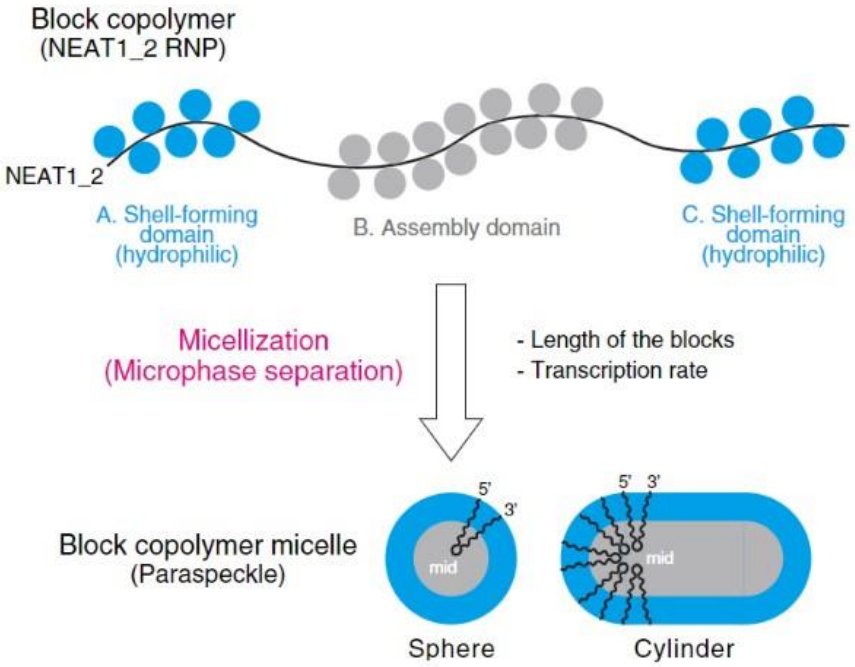

Figure I.7: Micellization model of paraspeckles. Adapted from[51]. NEAT1_2 (longer isoform of NEAT1) and interacting RBPs (blue and grey circles) are considered as a triblock copolymer, with two shell-forming hydrophilic domains, and proteins involved in paraspeckles assembly (e.g., NONO, grey circles) binding to the middle domain. The length of the three blocks and the transcription rate of NEAT1 impact the size and shape of paraspeckles.

Heterochromatin compartments are another example of condensation that may rely on different mechanisms than LLPS. They may indeed be described by simple cooperative binding of proteins to chromatin structure, or by phase separation via two different mechanisms: LLPS or polymer-polymer phase separation (PPPS)[52]. While LLPS is based on multivalent interactions between condensates components (in the case of heterochromatin compartments, multivalent interactions between chromatin-associated proteins, Fig. I.8C), PPPS relies on intramolecular crosslinking of a polymer, leading to a collapsed instead of an extended structure (here, chromatin-associated proteins would crosslink chromatin segments, or bridging could be mediated by internucleosomal interactions, Fig. I.8B). A first important difference between LLPS and PPPS is that the latter strongly rely on the polymer scaffold. Therefore, condensates formed by PPPS disassemble when the polymer scaffold is removed, on the contrary to condensates formed by LLPS (Fig. I.8D)[52]. Another difference lies in the size of the condensates that depends on the length of the underlying polymer in PPPS and not on the concentration of soluble components, on the contrary to LLPS.

LLPS and PPPS are two very useful and convenient models that can take part in the explanation of condensate behaviors, but distinguishing between different mechanisms can be tricky. Indeed, a component in a condensate can display some characteristics consistent with the LLPS model while another one does not, as it is the case for Rad52 and Rfa1, two components of DNA repair foci[53]. Moreover, experimental observations like rapid recovery after photobleaching (measured by FRAP experiments) are not sufficient to conclude that a LLPS mechanism is at stake, and refuting it on the basis of the absence of a constant C_{sat} in the dilute phase is also a too fast shortcut in the case of multicomponent systems, as we saw in part I.1.3.b.

The unknown nature of the interactions leading to the formation of a condensate can be another obstacle for proclaiming that it is formed by LLPS. This is for instance the case for centrosomes, whose key scaffolding proteins do not display classic motifs associated with LLPS and described in the previous part (multivalent folded domains or IDRs). The centrosome moreover does not exhibit the liquid-like behavior expected for condensates formed by LLPS, which raises the question of whether weak interactions, as would be expected for LLPS, could be underlying its biogenesis[54].

Altogether, we should keep in mind that alternate mechanisms for condensate formation may exist besides LLPS and should be integrated in the global framework to help interpreting experimental observations. Furthermore, LLPS is a thermodynamic equilibrium process. Yet, cells are out-of-equilibrium systems, as highlighted by the coexistence of small condensates without coarsening into one single droplet, on the contrary to LLPS theory predictions (see part I.3.2). Cells must thus employ nonequilibrium processes to stay out-of-equilibrium, like PTMs to tune the interactions underlying phase separation, as evoked in part I.1.3.b. The impact of nonequilibrium processes over phase separation processes are still poorly understood and are actively investigated[55].

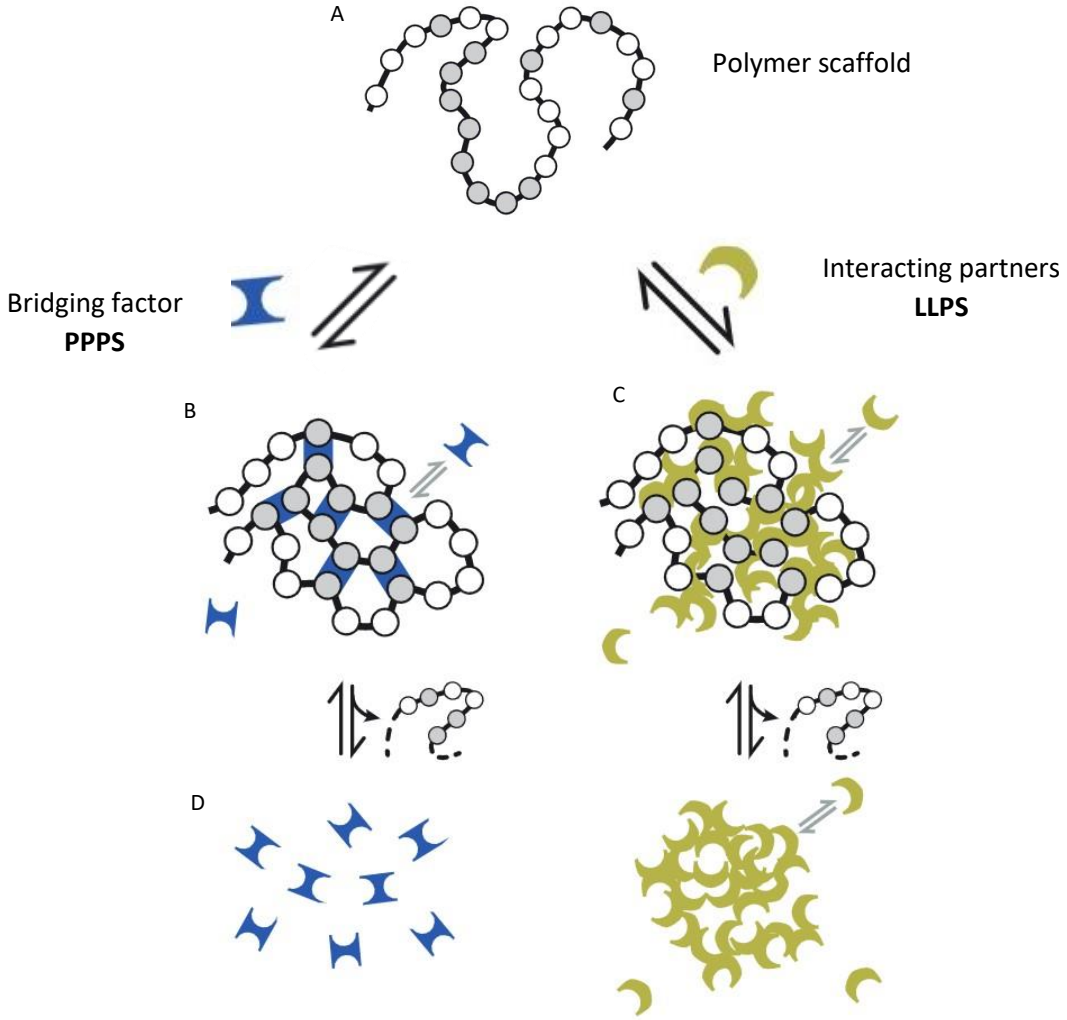

Figure I.8: Polymer-polymer phase separation vs liquid-liquid phase separation in heterochromatin compartments assembly. Adapted from[52]. A. A polymer scaffold (chromatin for chromatin subcompartments), with specific binding sites in grey, can form condensates with different mechanisms. **B.** In PPPS, proteins (blue) bridge the binding sites, without necessarily interacting with each other. **C.** In LLPS, proteins (light green) interact with the polymer scaffold, as well as with each other, forming a liquid-like droplet. **D.** Removal of the polymer scaffold leads to the dissolution of the condensate in PPPS, while the liquid-like droplet in LLPS should persist.

I.1.3. Linking structure, dynamics and functions of biomolecular condensates

Biomolecular condensates can adopt a broad range of material properties, which highlights a potential link between their material properties and their functions (Fig. I.9). Indeed, the material properties of the condensates differ from the properties of their cellular environment (higher viscosity and internal structure), and raise the question of whether the dense phase, and its emergent biophysical properties, are required for the cellular functions.

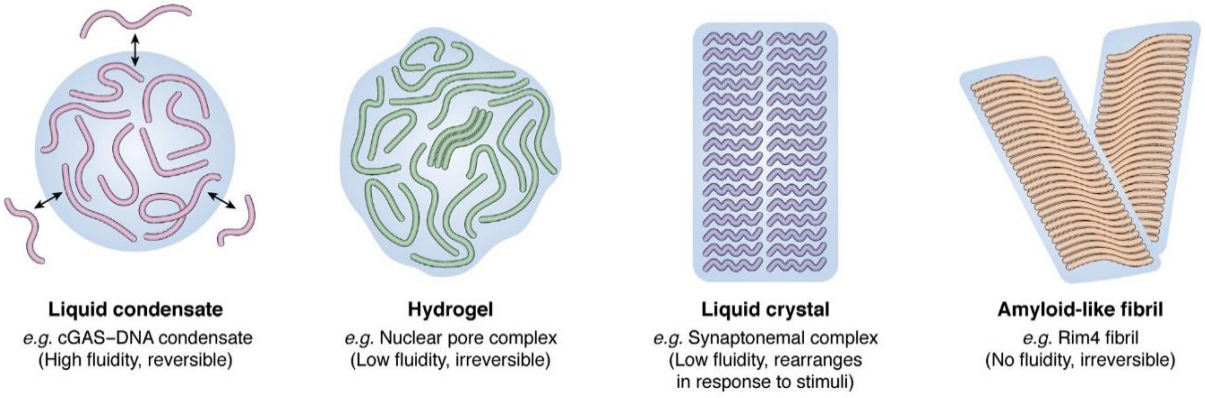

Figure I.9: Biomolecular condensates can exhibit different material properties. Adapted from[56]. Liquid condensates are highly dynamic (high fluidity and fast exchange) and reversible. Hydrogels are less dynamic (low fluidity and limited exchange with the environment) and generally irreversible. Liquid crystal structures are ordered arrangements with limited mobility. Solid-like condensates, such as amyloid-like fibrils, exhibit no fluidity and are completely irreversible.

As seen previously, most condensates exhibit liquid-like properties, yet some behave more like a solid or a hydrogel, as the NPC whose gel-like structure is thought to act like a selective molecular sieve regulating the active transport between the nucleus and the cytoplasm[8]. Besides global material properties that vary between different types of condensates, some of them also display a heterogeneous internal structure. SGs for example have a core-shell structure, i.e., they contain highly concentrated stable cores surrounded by a dynamic and less concentrated shell[15]. Subcompartmentalization is also well-known in the case of the nucleolus, which is divided into three structures, the fibrillar center (FC), the dense fibrillar component (DFC) and the granular component (GC) that engulfs the first two compartments (Fig. I.10). The compartments were shown to have different material properties and surface tension, determining the core-shell architecture[43]. Ribosomal DNA (rDNA) is transcribed between the FC and the DFC, and then processed while migrating into the GC where it assembles with ribosomal proteins. The viscoelastic properties of the DFC, that displays slower fusion dynamics than the GC, has been proposed to decrease the flux of pre-ribosomal particles to enable enzymatic processes crucial to rRNA stability, while the more fluid GC may allow accessibility of the ribosomal proteins to the pre-ribosomal particles coming from the DFC[43]. Supporting this idea, gelation of the nucleolus, via

expression of proteins found in the three subcompartments and fused with a module that can self-oligomerize under light induction, thus tuning the mobility of the proteins, has been shown to affect its function in ribosome biogenesis by modifying the flux of rRNA[57]. The material properties of condensates may thus directly impact their cellular function.

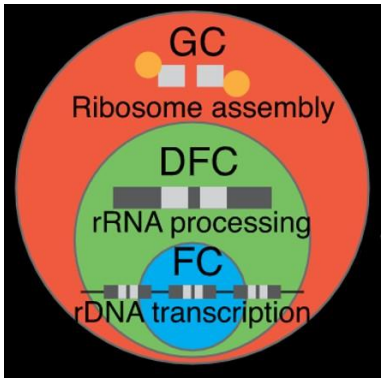

Figure I.10: Multilayered organization of the nucleolus and ribosome biogenesis. Adapted from[43]. The three structural entities of the nucleolus, which are the fibrillar center (FC), the dense fibrillar component (DFC) and the granular component (GC), each play a different role in ribosome biogenesis. In the FC, the polymerase I machinery transcribes the rDNA, rRNA is processed in the DFC, and ribosomes are assembled in the GC before being exported in the cytoplasm.

Besides exhibiting different material properties than their surrounding environment, condensates locally enhance the concentration of specific biomolecules. The dense phase may thus increase both reaction rates by concentrating biomolecules, and specificity by keeping other molecules promoting side reactions out of the condensates (Fig. I.11). The enhancement of the reaction efficiency may also pass through an exclusion of an inhibitor of the reaction from the dense phase (Fig. I.11). On the contrary, condensates may also decrease reaction rates by sequestering biomolecules and depleting them from the cytoplasm or nucleoplasm, thus preventing them from reacting with other substrates (Fig. I.11). Several examples of enhancement or reduction of reaction kinetics were reviewed by Lyon et al[58]. Such pathways for tuning of reaction rates were moreover used to engineer metabolic pathway through programmable assembly and disassembly of condensates containing the substrates of interest[59,60].

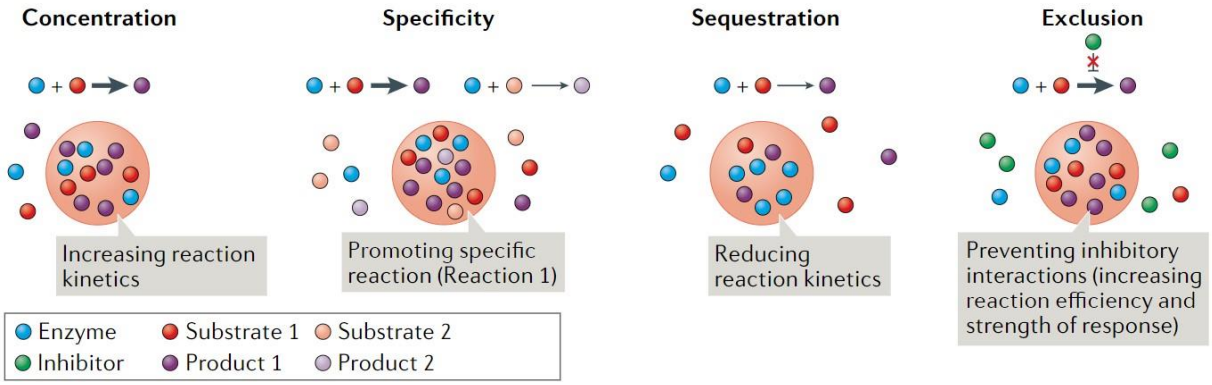

Figure I.11: Condensates may have different effects on biochemical reaction rates. Adapted from[58]. Enrichment of both enzyme and substrate in condensates will increase the reaction kinetics, while enrichment of only one of the two, for example the enzyme, will reduce the reaction kinetics. Exclusion of an inhibitor from condensates will promote product production.

Interestingly, the interplay between structure and function can be bidirectional, as illustrated by transcriptional condensates in mitochondria, that on the one hand reduce the rate of transcription, and whose structure on the other hand is modified by the newly synthetized RNA. Biophysical mechanisms removing the RNA are thus here essential to maintain the steady-state structure of the condensates[61].

However, the functional contribution of LLPS is not always straightforward. For example, LLPS is commonly thought to enhance transcription rate. Supporting this hypothesis, light-induced condensates of the transcriptional regulator TAF15, recruiting endogenous PolII, showed enhanced transcription compared with cells kept in the dark and unable to form droplets[62]. Yet, a recent paper saw no difference in transcription efficiency between transcription factors engaging in multivalent interactions under and over the critical concentration for droplet formation (Fig. I.12)[63]. It seems therefore crucial to separate the effect of intrinsic multivalent interactions between biomolecules and LLPS. The hypothesis of transcription factories concentrating RNA polymerases may even come from the limited resolution of light microscopy which hinders the spatial resolution of gene visualization. A very recent paper bypassed this limitation by imaging the nascent RNAs of long and highly expressed genes, and revealed the organization of transcription loci in transcription loops, i.e., genes covered by elongating polymerases and carrying nascent RNAs[64].

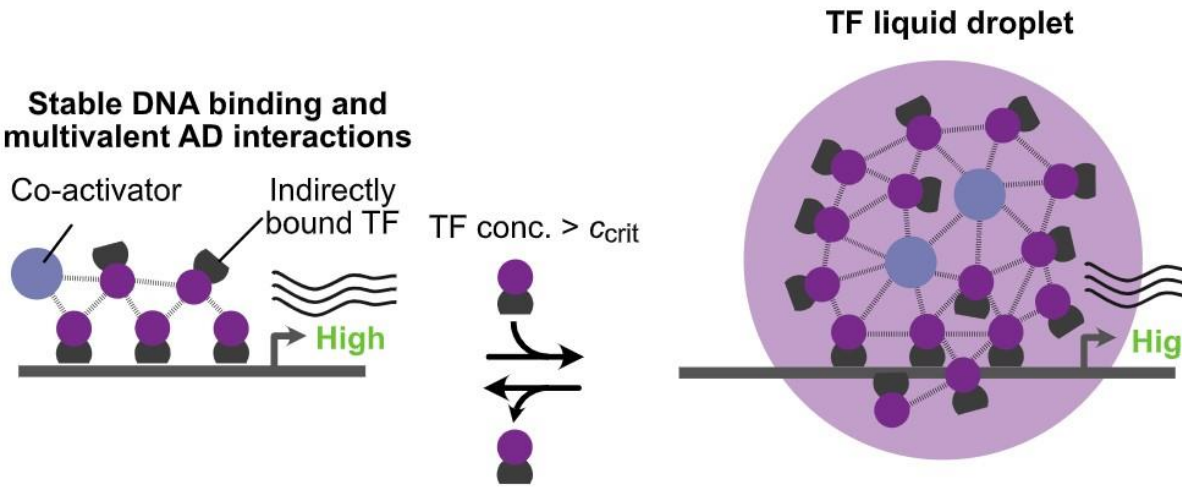

Figure I.12: Transcription activation by transcription factors (TF) depends on multivalent interactions between TF activation domains (AD). Adapted from[63]. Multivalent interactions increase the transcription activation capacity of TF by stabilizing the TF-DNA binding (left). LLPS of transcription factors reflects their capacity to engage in multivalent interactions but do not further enhance transcription compared to multivalent interactions under the critical concentration required for phase separation.

I.2. Reconstitution of biomolecular condensates in test tubes and in cells

I.2.1. The benefit of artificial approaches

Endogenous biomolecular condensates have a complex composition which complicates their manipulation in cells. Their assembly process is moreover redundant, in the sense that preventing the expression of one protein generally does not abolish the formation or dissolve the condensates. Deciphering the underlying processes driving intracellular phase separation as well as the relationship between structure, dynamics and functions thus requires reconstitution studies. *In vitro* experiments with purified proteins have proved essential to circumvent the lack of tools to work in a cellular context and have helped uncover the molecular features responsible for phase separation through precise compositional control. Such approaches using multivalent or intrinsically disordered proteins known to belong to endogenous condensates have enabled to investigate the driving forces of phase separation. For instance, repeats of SH3 and PRM were shown to form liquid droplets *in vitro* with phase diagrams highly dependent on valency[37] (Fig. I.5). Experiments with purified repeats of human SUMO3 and SIM has enabled the development of a model whereby scaffolds associate and phase-separate into condensates through heterotypic interactions, then recruit clients with an efficiency depending on the scaffold stoichiometry (the scaffold in excess displays free sites and can interact with its cognate client), and increasing with the valency of the client (Fig. I.13)[21]. Though these *in vitro* experiments are based

on engineered systems with a much simpler composition than endogenous biomolecular condensates, they allow for a framework that can explain the behavior of natural condensates. For example, the first paper cited here[37] has led to a better understanding of the formation process of membrane clusters of signaling molecules, while observations of PML NBs and PBs in cells followed the scaffold-client model depicted by SUMO/SIM experiments in the second paper[21]. Complex coacervates, based on the assembly and phase separation of molecules of opposite charge, used as model systems for charge-driven liquid droplets have moreover brought insights into the requirements for coexistence of multiple phases in a single condensate, as it is the case for SGs and nucleoli for example[65].

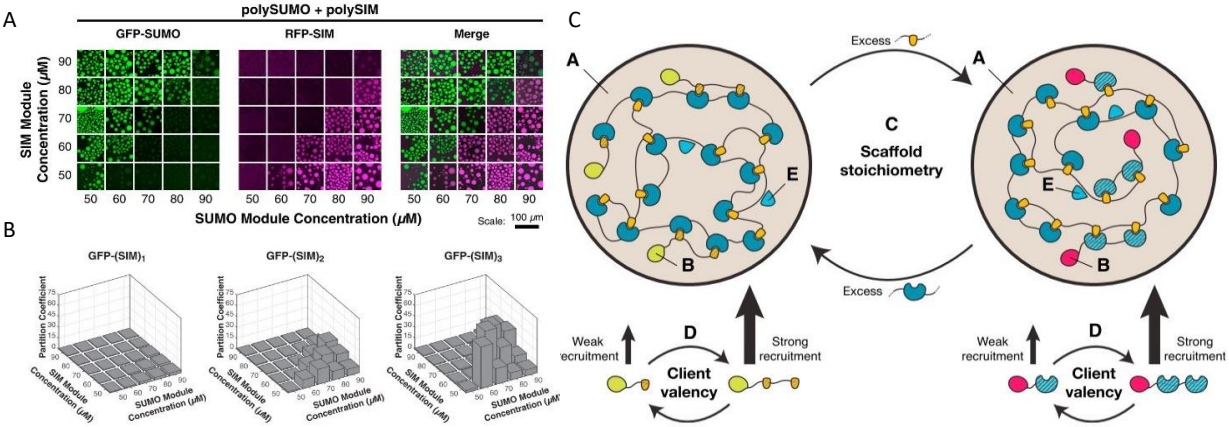

Figure I.13: Client recruitment in condensates depends on scaffold stoichiometry and client valency. Adapted from[21]. **A.** Monovalent client (GFP-SUMO or RFP-SIM) are enriched when the cognate scaffold (polySIM or polySUMO respectively) is in excess. PolySUMO and polySIM are made of 10 repeats of SUMO and SIM respectively. 100 nM of each client was added to a mix of the indicated concentrations of scaffold proteins. **B.** The partition coefficient (PC) of a client (ratio of concentrations in the droplet to the bulk phase) increases with client valency as illustrated here with the PCs of GFP-$(SIM)_n$, with n = 1, 2, or 3. 100 nM of client was added to a mix of the indicated concentrations of scaffold proteins. **C.** Model for the composition of biomolecular condensates: multivalent scaffolds phase separate into liquid-like droplets (A) that enrich clients (B), distinguishable from their hatched patterns, with an efficiency depending on the scaffold stoichiometry (C) and the valency of the client (D). (E) shows clients recruited through interactions with other interactions of the scaffold proteins whose enrichment is not dependent on the scaffold stoichiometry.

In addition to the elaboration of general model to describe the driving forces of phase separation, *in vitro* experiments have also enabled to investigate the role of specific components in the phase separation of natural condensates. A subset of proteins localizing to PBs were thus shown to build a network of multivalent interactions sufficient to reconstitute phase-separated condensates *in vitro*[66]. A similar strategy with purified DDX3 RNA helicase protein LAF-1, found in Caenorhabditis elegans P granules, showed that an IDR of the protein is necessary and sufficient for phase-separation *in vitro*[42]. Fusing several of this LAF-1 IDR and thus increasing the multivalence of the scaffold enhances its propensity to phase-separate[67]. The molecular determinants of IDP-based phase separation were actively studied through mutations and deletions experiments of natural IDP, which highlighted which factors can be important for phase separation, like the overall amino acid composition, post-translational modifications, and interactions between specific residues[34,41,68–71]. Such studies have improved our capacity to predict the phase-separation behavior of specific IDPs.

Besides bringing important insights into the mechanisms underlying phase-separation, *in vitro* reconstitution of condensates can also enable proof-of-concepts experiments for the design of engineered bio-inspired condensates with novel functionality. For example, engineered condensates from purified multimeric LAF-1 IDRs fused with cargo motifs and with protease cut sites enabled a controlled release of cargos[67]. Fusion of LAF-1 IDR to a solubility tag like the maltose binding protein, both separated by either a protease cleavage site or a protein cleaved in response to illumination at a certain wavelength allowed to engineer light-inducible IDR-driven coarcervation[67,72]. Another example is the engineering of *de novo* artificial IDPs inspired by native IDPs that have enabled to build phase-separated system with controlled C_{sat}, paving the way for future design of functional intracellular phase-separated droplets with tailor-made properties[60].

The precise control in composition and parameters of *in vitro* experiments have thus allowed great advances in our understanding of biomolecular condensates. However, they are unable to recapitulate the cellular environment (cellular crowding, promiscuity, physiological concentrations of condensate scaffold components…). Therefore, reconstitution experiments in cell are required to further elucidate the mechanisms at stake. Some of the *in vitro* studies introduced previously tested their constructs in cells to ensure that the hypotheses formulated from *in vitro* experiments were recapitulated in the intracellular environment[21,34,37,41,42,60,67–69,72]. In addition to overexpression experiments based on expression of recombinant proteins involved in endogenous condensates, which have enabled to further elucidate the molecular determinants of specific proteins for phase separation[73], recent lines of research have also focused on the development of versatile tools to trigger the formation of artificial condensates in cells, with a high control over their composition and stability. These tools rely on the use of either IDRs or dimerizing peptides, which both have been shown to take part in the formation of biomolecular condensates, as developed in part I.I.3. Dimerizing peptides have the advantage to enable a better control of the multivalency that can be easily tuned. Synthetic condensates can adopt different physical

states (liquid droplet, hydrogels, or insoluble aggregates), and thus can be valuable tools for the study of the mechanisms underlying the formation of endogenous condensates, physiological and pathological, as well as of the link between their physical state and their functions. It is therefore interesting to classify the numerous synthetic approaches depending on which type of molecule they rely on (IDRs or dimerizing peptides) or on the physical state of the synthetic condensates, as has been done previously[74]. In the next section, I have adopted another classification purely based on the implementation method of the strategies, and I divided the tools in constitutive and inducible formation approaches. In constitutive formation approaches, the ability of scaffold components to interact with each other with a sufficient multivalency is intrinsic and the formation of condensates is spontaneous when the C_{sat} is reached (Fig. I.14). Inducible formation approaches rely on the use of either a chemical or a light stimulus to achieve the level of multivalency required for the formation of condensates (Fig. I.14). Therefore, constitutive formation approaches allow for condensates stable in time, while inducible formation approaches can bring spatiotemporal control over the formation and dissolution. Both categories are thus complementary and useful to study a broad range of aspects of biomolecular condensates.

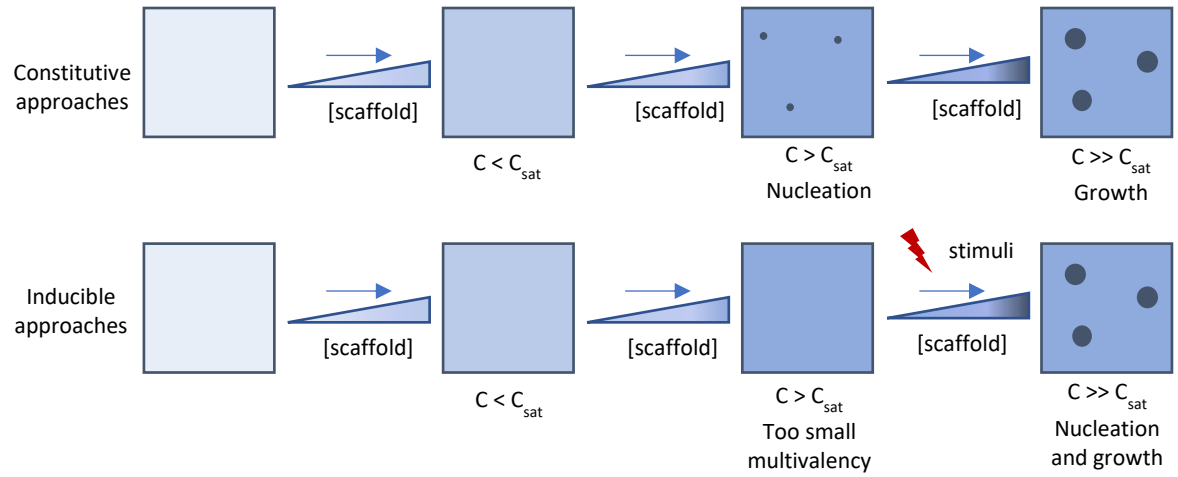

Figure I.14: Constitutive and inducible formation approaches. In constitutive approaches, scaffold proteins phase separate over C_{sat}, while in inducible approaches, a stimulus is required to induce the necessary multivalency level.

I.2.2. Reconstitution studies of biomolecule condensates in cells

I.2.2.a. Constitutive formation of biomolecular condensates in cells

Constitutive approaches for reconstitution studies of condensates are based on the expression in cells of recombinant proteins able to phase separate through their IDR or multivalent domains. The strategies can be based on proteins that are known to phase separate in living systems, like the PopZ protein from the bacterium *Caulobacter crescentus*[73]. In contrast with many IDRs that were shown to be required for phase separation, a recent preprint highlighted another function for the IDR of PopZ. Indeed, the phase separation of PopZ is promoted by a helical domain, while the IDR fluidizes the condensates through electrostatic repulsion, a property that can be tuned by modifying the length and the distribution of acidic residues[72]. Other strategies rely on the use of proteins known to multimerize. Among these strategies, Zoher Gueroui's lab developed prior to my arrival the ArtiGranule system, which relies on the spontaneous formation of nanocages of 24 monomers of the light chain of ferritin: the expression in cells of monomers of ferritin fused in N-ter to F36M-FKBP (Fm), a homodimerizing mutant of the FK506-binding protein (FKBP), led to nanocages functionalized with up to 24 Fm proteins able to interact with each other and thus driving phase separation (Fig. I.15)[75]. The incorporation in the scaffold of the Pumilio homology domain (PUM.HD), which is the RNA-binding domain of Pumilio 1, a translational repressor enriched in P-bodies, led to the specific recruitment of Pumilio 1 endogenous RNA targets and their associated RBPs[75].

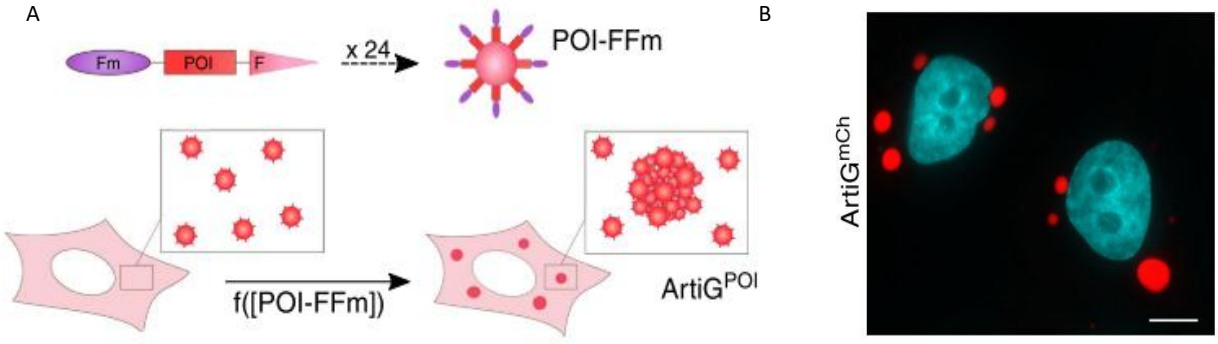

Figure I.15: Formation of ArtiGranules in cells. Adapted from[75]**. A.** Nanocages of 24 monomers of ferritin, each fused to a Fm protein, phase separate through Fm-Fm homodimerization after reaching C_{sat}. **B.** Confocal image of ArtiGranules (POI in A = mCherry) in HeLa cells, 24 h after transfection. Scale, 10 µm.

One of the advantages of reconstitution studies through expression of recombinant proteins is the possibility to tune the properties of the proteins (concentration, valency, force of interaction….). Investigating different concentrations of PUM.HD in ArtiGranules thus showed that the higher the concentration was, the smaller the condensates were[75]. This may come from surface steric hindrance due to the recruited Pumilio partners, more numerous for higher concentrations of PUM.HD, which would impede growth of the condensates, as will be further developed in part I.3.2. Another example illustrating the possibility to tune scaffold proteins properties comes from a recent paper that developed a synthetic system relying on two fusion proteins (Fig. I.16) whose interaction with each other is tunable by point mutation, and used a yeast display system to visualize the modification in the phase diagram, showing the role of the affinity in enhancing the phase separation[36].

As stated before, in addition to bringing information on the formation and regulation of condensates, reconstitution studies can exploit liquid-liquid phase separation for other applications. Along these lines, Fluoppi (fluorescent protein-protein-interaction-visualization) was recently developed as a tool to investigate the interaction between two proteins in cells: the first protein was fused to p62 PB1 domain, which homodimerizes, and the second protein was fused to Azami-Green, a tetramerizing coral-derived green fluorescent protein, leading to green puncta if the two proteins interacted with each other (Fig. I.17)[76]. The same scaffold proteins were used to engineer SPREC-In and -Out (synthetic protein-recruiting/-releasing condensates), synthetic protein condensates systems that allow for the controlled recruitment or release of a protein of interest by chemically induced dimerization or optogenetics[77].

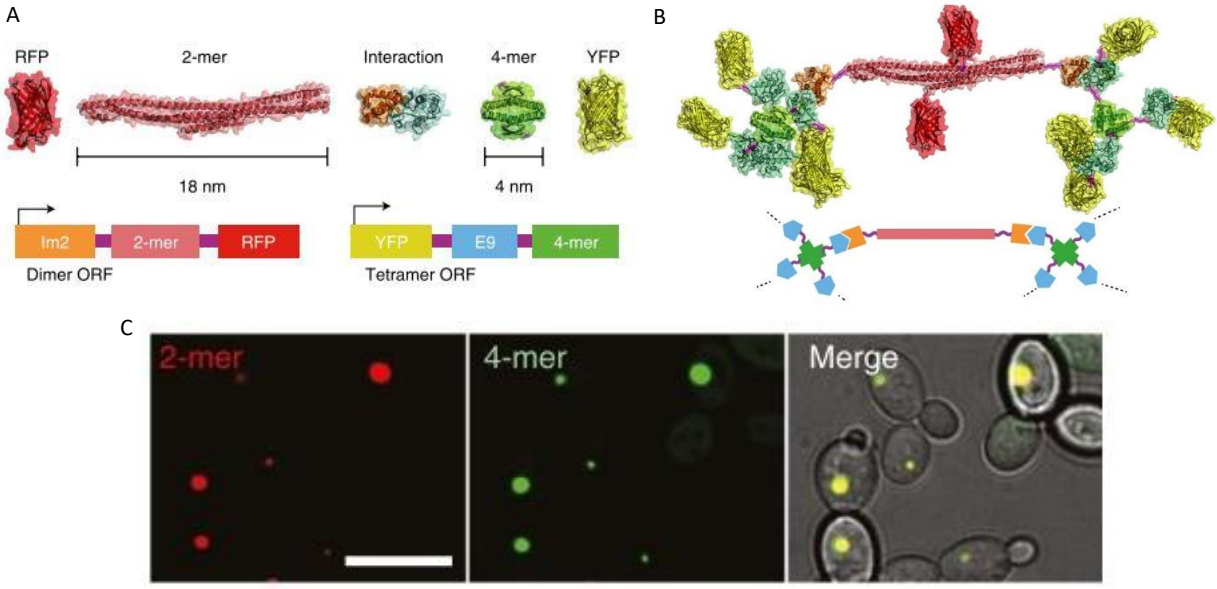

Figure I.16: Synthetic system for phase separation in living cells with tunable phase diagram. Adapted from[36]**. A.** Schematic of the two constructs, each constituted of an interaction domain (2-mer or 4-mer), an oligomerization domain (the colicin E9 or immunity Im2 proteins, which interact with each other with an affinity that can be tuned by mutation), and a fluorescent protein (RFP or YFP). **B.** Structure (top) and schematic (down) of the interaction between the two constructs. **C.** Expression in yeast cells of the two constructs leads to self-assembly and formation of bright puncta. Scale, 10 µm.

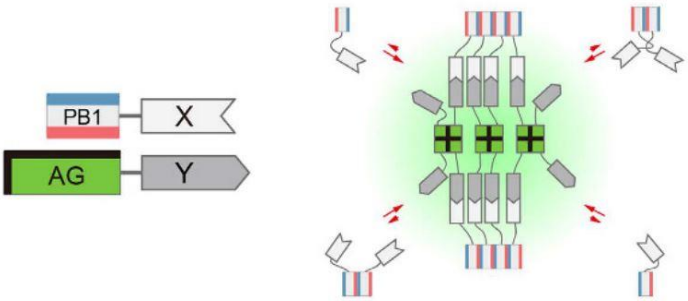

Figure I.17: Fluoppi: a tool to investigate protein-protein interactions (PPI) in cells. Adapted from[76]**.** Schematic of the PPI-dependent formation of fluorescent puncta in cells.

I.2.2.b. Inducible formation of biomolecular condensates in cells

Unlike constitutive approaches, inducible strategies are based on the use of an inducer of phase separation that can be either light, triggering the association between protein domains, often plant-derived, or a small chemical drug enabling chemically-induced dimerization (CID).

Fusing the IDRs of various condensate proteins, like FUS and DDX4, to the photolyase homology region (PHR) of the plant *Arabidopsis thaliana* Cry2, which homodimerizes upon blue-light illumination, allowed Brangwynne's lab to investigate the ability of these domains to trigger phase separation into either liquid droplets or more solid-like gels depending on the location in the phase diagram (Fig. I.18)[33]. This optogenetic system, named OptoDroplets, was also used to explore the link between the C_{sat} and the interaction strength, and to highlight a possible mechanism to explain localized phase separation of transcription condensates and subsequent bursts in transcription[62].

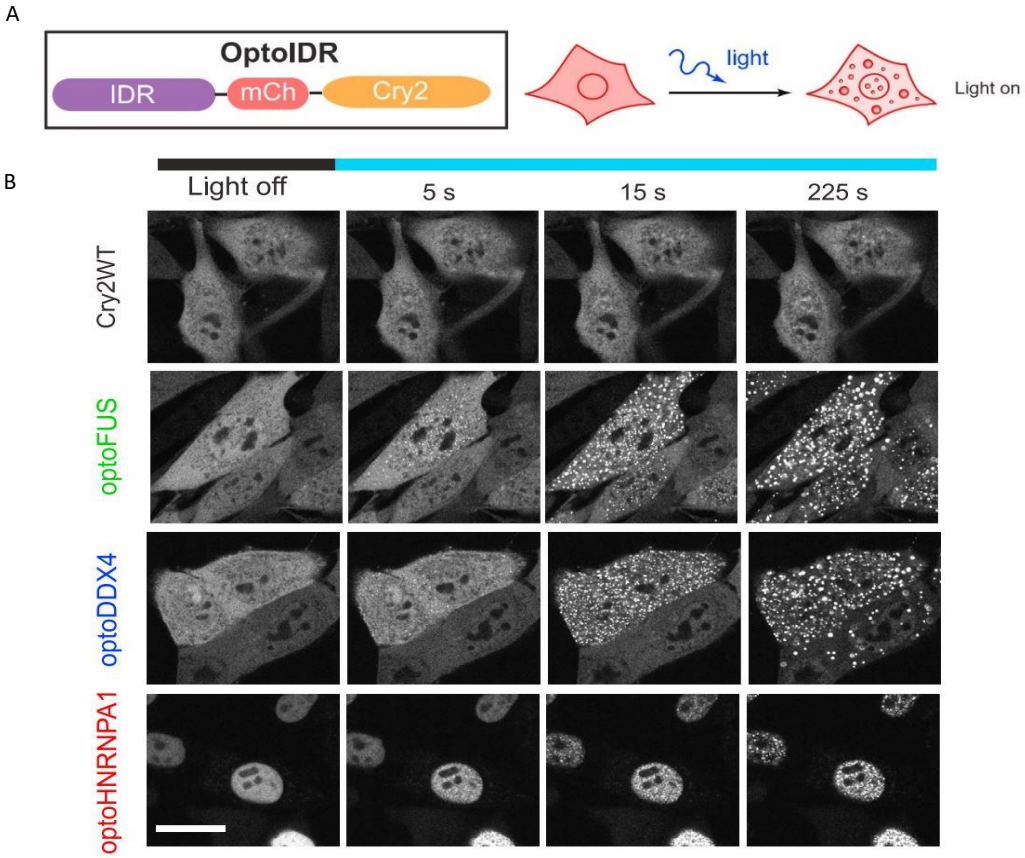

Figure I.18: OptoDroplets. Adapted from[33]. A. The dimerizing Cry2 is fused to the IDR of a protein enriched in a biomolecular condensate and the fusion protein should undergo phase separation under blue light illumination. **B.** Fusing the IDR of FUS (optoFUS), DDX4 (optoDDX4) or HNRNPA1 (optoHNRPA1) to Cry2 leads to fast cluster assembly under blue light illumination in NIH 3T3 cells.

To circumvent the deactivation time of Cry2 of several minutes that limited the temporal control of formation and dissolution cycles, the same lab developed the Corelet system[78]. In that system, ferritin heavy chain (FTH1) nanocages are functionalized with the engineered protein improved light inducible dimer (iLID). The strong heterodimerization of iLID and its partner SspB upon blue light illumination triggers the recruitment of various IDRs to the nanocages which thus become multivalent scaffolds for IDR oligomerization (Fig. I.19)[78]. This system was used to examine the impact on phase diagrams of PTMs, that can occur through the cell cycle or during stress exposure for example. It also enabled the development a facilitated phase separation model by diffusive IDR capture that would locally enhance the saturation and make phase separation possible even with a globally too dilute concentration (Fig. I.19C)[78]. More recently, Corelets allowed for a model depicting the role of seeds, i.e., biomolecular facilitating the nucleation of condensates, for specific nucleation[79].

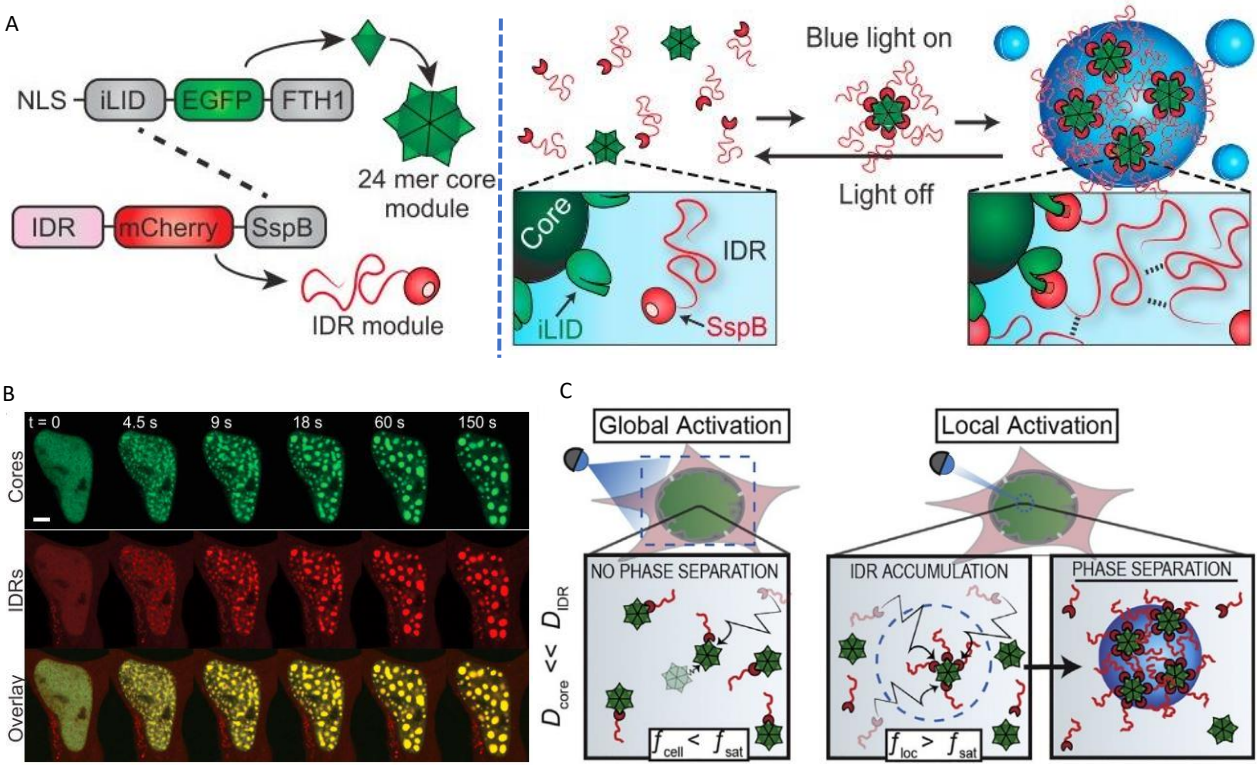

Figure I.19: Corelets. Adapted from[78]. A. Schematic of the two Corelet constructs: the first enables the localization in the nucleus of EGFP-labelled 24-mer cores of ferritin through the nuclear localization signal (NLS). These cores are functionalized with iLID domains, that upon blue light illumination interact with the mCherry-labelled SspB domain of the second construct, conjugated to an IDR domain that promotes phase separation. **B.** Corelets enable light-induced intracellular phase separation, as illustrated by this time-lapse confocal imaging (IDR = N-terminal of FUS IDR) in HEK293 cells. Scale, 5 µm. **C.** Facilitated phase separation model: local activation (dashed blue line) of iLID-SspB dimerization drives a diffusive flux of IDRs towards the slowly diffusing ferritin cores, leading to high local valency that exceeds the required threshold for phase separation.

Another optogenetics tools, CasDrop, combined iLID-SspB dimerization-based formation of condensates enzymatically dead Cas9 (dCas9) (Fig. I.20)[80]. This method enables to target the formation of condensates to specific gene loci, and helped investigate the relationship between formation of nuclear condensates and chromatin structure[80]. It was thus revealed that liquid-like condensates preferentially formed in low-density chromatin regions, and can restructure the genome by pulling together targeted genomic loci to which they are bound while pushing out non-targeted regions of chromatin[80].

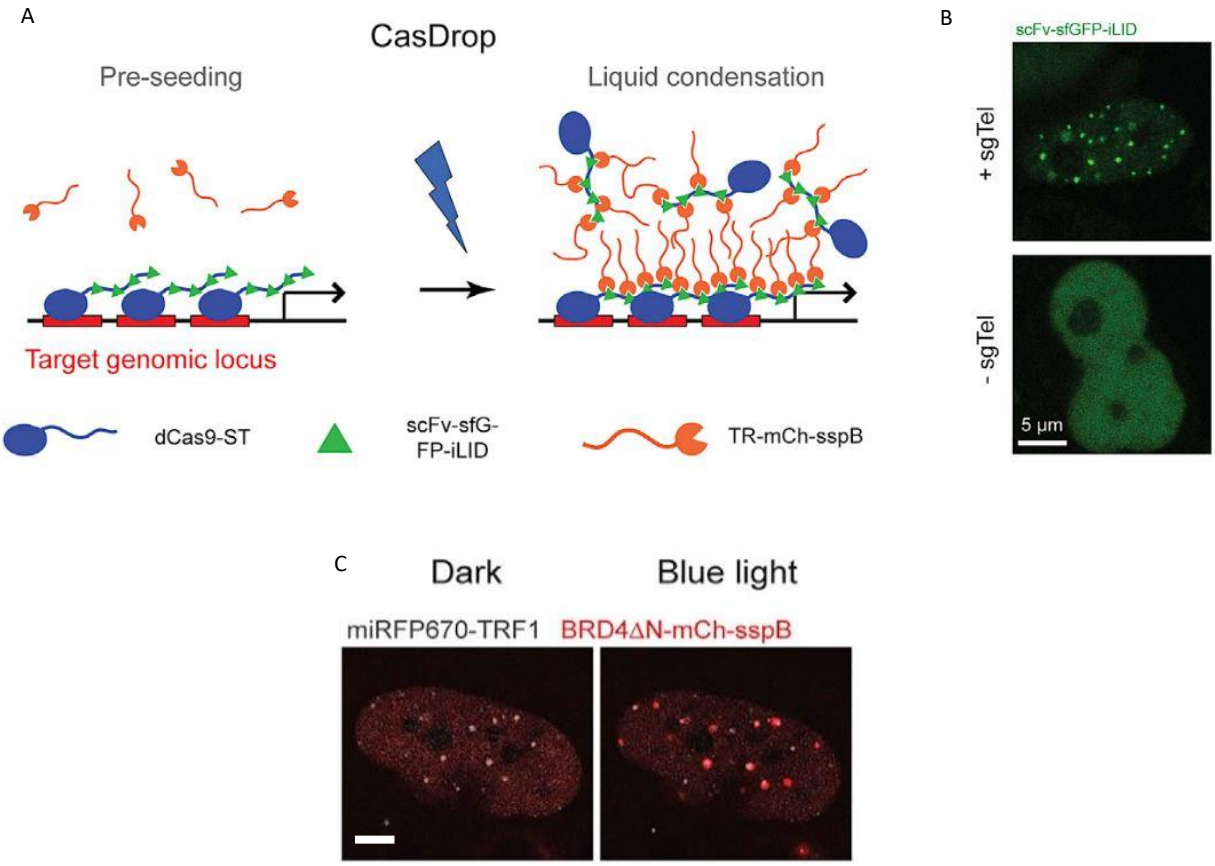

Figure I.20: CasDrop, a tool to target the light-induced formation of condensates at specific gene loci. Adapted from[80]. A. Schematic of the CasDrop system modules: in the presence of a single guide RNA (sgRNA) targeting a specific target genomic locus, dCas9 can localize on that genomic locus. dCas9 fused to SunTag (ST) can interact with super-folder GFP (sfGFP)-labelled single-chain variable fragment (scFv) antibody, cognate for the ST and fused to an iLID domain. Upon blue-light illumination, the multiple iLID domains interact with sspB labelled with mCherry (mCh) and fused to a transcriptional regulator (TR), an IDR protein, which drives phase separation. **B.** In the presence of sgRNA for telomeres (sgTel), dCas9-ST and scFc-sfGFP-iLID pre-seed puncta at telomers (top). Without sgRNA, no pre-seeding is observed (bottom). **C.** Light-induced formation of condensates at telomeres in a NIH 3T3 cell expressing the three CasDrop modules described in (A), miRFP670-TRF1 for the labelling of telomeres, and sgRNA for telomeres. Scale, 5 µm.

An interesting inverse system for optogenetic control of the dissociation of the condensates instead of their formation was developed by fusion of IDR domains to PixD and PixE, two proteins from the cyanobacterium *Synechocystis* that associate in the dark into a large complex, which dissociates upon blue light illumination (Fig. I.21)[81]. This strategy, names PiXELL (Pix Evaporates from Liquid-like droplets in Light), was used to corroborate a computational model that predicted long-term spatial patterns following a locally applied stimulus[81]. The OptoDroplet and PiXELL systems were used to engineer condensates in yeast strains able to enhance a metabolic flux, increasing drastically both the level of the desired product and the selectivity, which shows the possibility to use synthetic condensates for metabolic engineering[59].

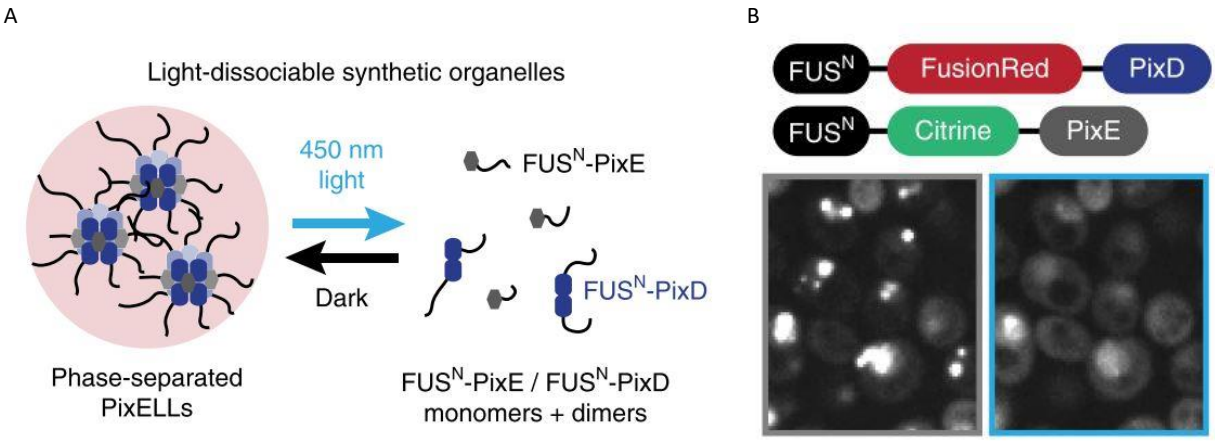

Figure I.21: PiXELL: light-dissociable synthetic condensates. Adapted from[59]. A. Schematic of droplets promoted by the interactions between the N-terminal of FUS IDR and the multivalence brought by PixD/PixE complexes in the dark that undergo dissociation under blue-light illumination. **B.** FusionRed fluorescence in yeast cells of the PiXELL system in the dark (left, presence of condensates), and under blue light illumination (right, condensates are dissolved). Scale, 5 µm.

Besides homodimerizing, Cry2 interact with the protein C1B1 under blue-light illumination, a property that was used to build the LARIAT (light-activated reversible inhibition by assembled trap) and mRNA-LARIAT (mRNA-light-activated reversible inactivation by assembled trap) optogenetic methods (Fig. I.22)[82,83]. In the LARIAT system, C1B1 was fused to the Ca2+/calmodulin-dependent protein kinase IIα, which self-assembles into a 12-mer, while in mRNA-LARIAT it was fused to a ferritin monomer. In both cases, cores bearing up to 12 or 24 C1B1 were able to interact with high multivalence with dimers of Cry2 under blue-light illumination, leading to reversible clusters of the multivalent proteins in cells (Fig. I.22). The LARIAT and mRNA-LARIAT systems were designed to sequester proteins or mRNAs of interest, respectively. In LARIAT, sequestering proteins in the clusters inhibited their functions in cells, while in mRNA-LARIAT trapping mRNAs reduced their translation

efficiency by preventing their access to ribosomes, a property that was used to probe the role of newly synthesized β-actin protein in cell migration. These two methods showed another possible application for phase-separated condensates for investigating the physiological functions of specific proteins or RNAs in cells as well as the importance of their localization in cell.

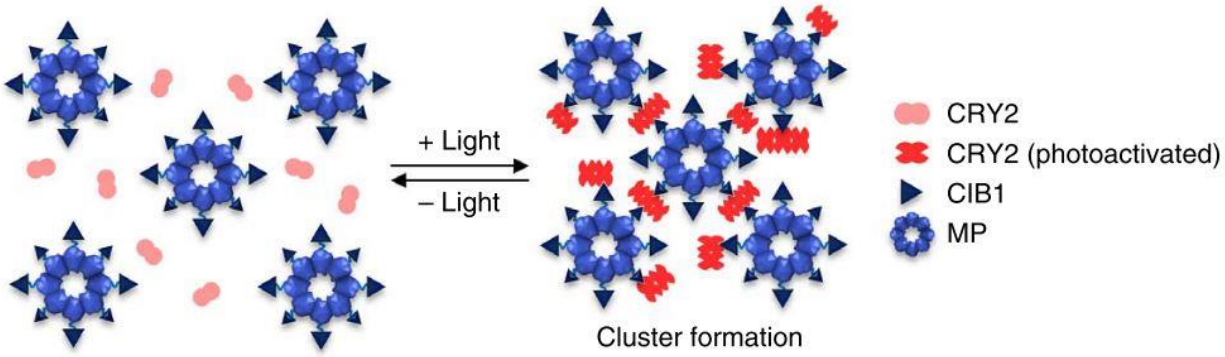

Figure I.22: LARIAT methodology. Adapted from[82]. Schematic of the blue light-induction of clusters formation in the LARIAT and mRNA-LARIAT systems.

One of the most prominent systems of CID is the fast and strong rapamycin-induced dimerization of FK506 binding protein (FKBP) and FKBP-rapamycin binding protein (FRB). Multivalent constructs of FKBP and FRB formed hydrogel network in cell and *in vitro*, with an efficiently tightly linked to the number of repeats, highlighting the importance of multivalence for phase separation (Fig. I.23)[84]. This iPOLYMER system (intracellular production of ligand-yielded multivalent enhancers) and its light-inducible counterpart iPOLYMER-LI (intracellular production of light-yielded multivalent enhancers with light inducibility), which has the advantage to be reversible, were successfully turned into SG analogs co-localizing with endogenous SGs components by incorporating into the scaffold the RNA-recognition motif of the SG protein TIA1[84].

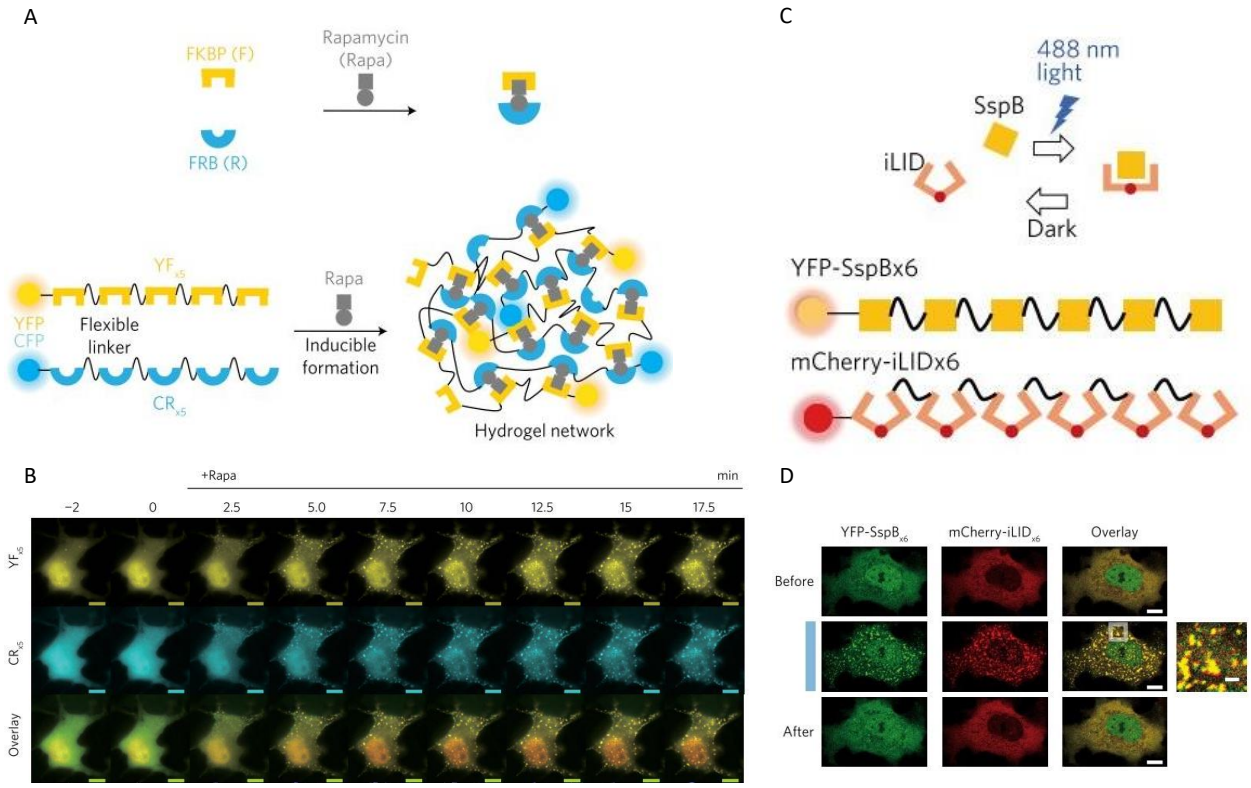

Figure I.23: iPOLYMER and iPOLYMER-LI. Adapted from[84]. A. Schematic of a hydrogel network formation through rapamycin-induced multivalent interactions between repeats of FKBP and FRB proteins. **B.** Time-lapse imaging of fluorescent puncta formation in a COS-7 cell after addition of rapamycin. Scale, 10 µm. **C.** Design of iPOLYMER-LI, which relies on the light-induced interaction of repeats of iLID and SspB. **D.** Reversible puncta formation of a COS-7 cell expressing the two iPOLYMER-LI modules. Scale, 10 µm (2 µm for the zoom in image).

Altogether, numerous systems for reconstitution of phase-separated condensates in cells with modular properties were developed in recent years. This broad array of tools can be applied in various ways: first and foremost, to address unanswered questions about the mechanisms underlying the formation and the control of the material properties of endogenous condensates, but also to develop bio-inspired materials with tunable novel functions, and to investigate the physiological importance of specific proteins and RNAs in cells.

I.3. Physical-Chemistry considerations for condensate formation

I.3.1. RNA as a polymer involved in biomolecular condensate formation

Many condensates contain both proteins and RNAs. The latter are often considered simply as carrier of the genetic code information and intermediates between the transcription of DNA and the translation into proteins (mRNAs). However, RNAs have several attributes that can contribute to the formation of condensates or to the tuning of their composition or material properties (Fig. I.24).

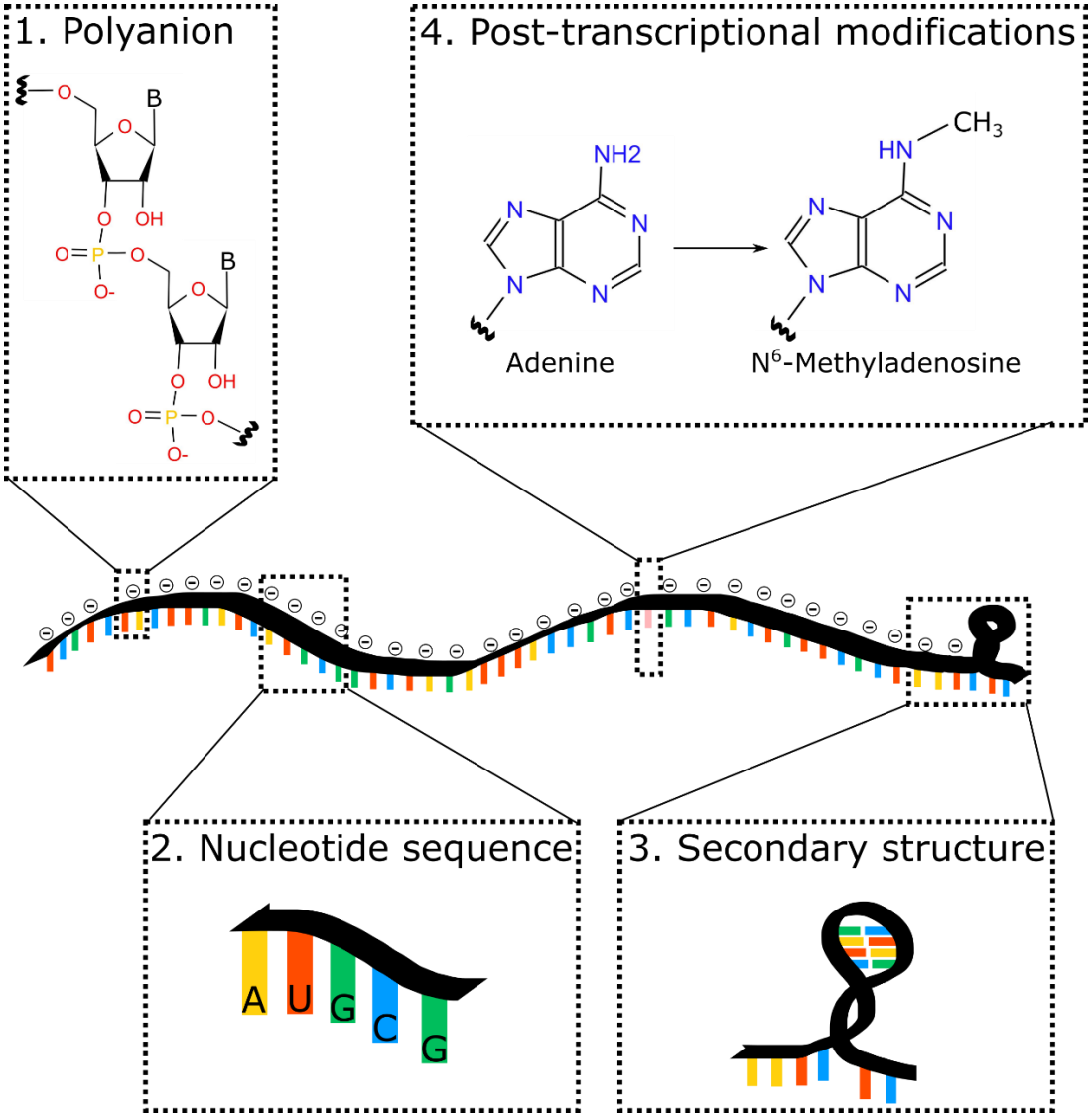

Figure I.24: RNA molecules have several attributes than can all play a role in phase separation. RNAs are notably polyanions that have specific nucleotides sequences, adopt secondary structures and can undergo post-transcriptional modifications.

First, RNAs are negatively charged polyelectrolytes due to the phosphate groups found in every nucleotide. They can thus take part in non-specific interactions with positively charged proteins and contribute to the formation of condensates through complex coacervation.

Secondly, an RNA molecule has a definite sequence of nucleotides that can exhibit RBP-binding sites and allow specific RNA-RBP interactions. Specific RNA-RNA interactions and non-specific random associations between RNAs through for example non-canonical base-pairing and base stacking can also contribute to condensate assembly[85]. The nucleotide composition can moreover contribute to condensates properties, as was highlighted by the use of homopolymers of RNA (poly(A), poly(C) and poly(U)) that gave rise to condensates with different material properties[86].

Electrostatic or sequence-specific interactions involving RNAs and resulting from the first two attributes discussed here are all the more important for condensate regulation given that RNAs are usually longer than proteins. A single RNA can thus recruit multiple RBPs and introduce multivalency, which is at the core of phase separation as developed previously. The length of NEAT1 thus regulates phase separation of paraspeckles (see part I.1.3.d)[23]. The ability to interact with multiple RBPs, beside taking part in the formation process, may also tune the material properties of condensates by modulating the interactions between protein IDRs, as illustrated by RNA that decreases the viscosity and enhances dynamics of droplets[42]. Interactions between RNAs and TDP-43 moreover prevent aberrant phase separation of TDP-43 involved in amyotrophic lateral sclerosis and frontotemporal dementia[87].

Thirdly, in addition to the primary structure defined by the nucleotides sequence, RNAs adopt secondary structures (e.g., hairpins) that can define structure-based interactions. By displaying or masking hybridization sequences and thus altering the ability of different RNAs to engage in intermolecular interactions, secondary structures were shown to regulate the sorting of mRNAs in the same or different droplets[88]. This compositional specificity can be further enhanced by protein binding that can lead to structural rearrangements[88]. Another example illustrating how RNA secondary structure can play a role in the formation of condensates comes from RNA G-quadruplex, composed of several planal layers of four guanine residues, that seems to favor phase separation through multivalent interactions with RNAs and RBPs[89].

Finally, RNAs can undergo post-transcriptional modifications that could influence phase separation through modifications of RNA-protein and RNA-RNA interactions or of RNA secondary structure[90]. For example, the methylation of adenosine to give N^6-methyladenosine (m^6A), which is the most abundant mRNA modification in eukaryotes, may promote the phase separation of m^6A-mRNA and m^6A-binding proteins, which subsequently partition in either PBs in unstressed cells, or SGs during stress[91]. Echoing the second point developed here, the partitioning would be enhanced for polymethylated mRNAs that could bind to multiple RBPs and thus favored interactions between their

IDRs[91]. These results were however contested by a recent preprint that pointed out that m^6A-mRNA partition similarly intro SGs in wild-type cells and m^6A-deficient cells[92].

Altogether, RNA has been shown to contribute to the formation, material properties and composition of condensates. The features of an RNA molecule, such as its length, structure, nucleotides composition and expression level, could potentially tune its contribution. Further studies will undoubtedly uncover other inputs of RNA in phase separation.

I.3.2. Parameters controlling the size of biomolecular condensates and surface effects

In the thermodynamic equilibrium framework, condensates formed by LLPS should evolve towards a single large droplet through coarsening to minimize the surface to area ratio. Three mechanisms are at play in condensates growth: addition of components from the surrounding environment, coalescence, and Ostwald ripening, whereby smaller droplets dissolve for the benefit of bigger ones. These three growth pathways could be observed in several *in vitro* reconstitution experiments[42,93].

However, the observations differ in cells where many condensates do not grow over a certain size and multiple droplets can coexist, as illustrated by the several submicrometric PBs in the cytoplasm and PML NBs in the nucleus. The principles underlying condensate size and the formation of multiple coexisting droplets are progressively uncovered. The size of condensates could first be cell size-dependent in the case of a maintained concentration of components, for example for embryonic cells (Fig. I.25A)[94]. Indeed, this hypothesis of a limited pool of components was proposed to explain the direct relation of the centrosome size to the cell size in *C. Elegans* embryo[95]. However, this regulatory process cannot account for cells that grow without producing new phase separating components. One other possible mechanism is the presence of active ATP-based processes driving condensates away from the equilibrium[96–99]. Chemical reactions could indeed regulate the ability of proteins to phase separate and suppress Ostwald ripening. Such a model was notably developed to account for some properties of the centrosome, like its exclusive nucleation at the centrioles and the existence of two co-existing centrosomes[100]. Besides active processes, a simulation-based study have highlighted that the ratio between the characteristic times of component diffusion and bond formation/rupture between interacting multivalent components could also be at play in the regulation of condensate size, as well as the number of available binding sites, with saturated interactions that could limit growth over a certain size (Fig. I.25B)[101,102]. Other mechanisms that could take part in the regulation of condensate size include the cytoskeleton, which for example mechanically stabilizes large nuclei against

gravitational forces and thus prevents their fusion, and interplay with membranes, which slows down diffusion and coalescence[103,104].

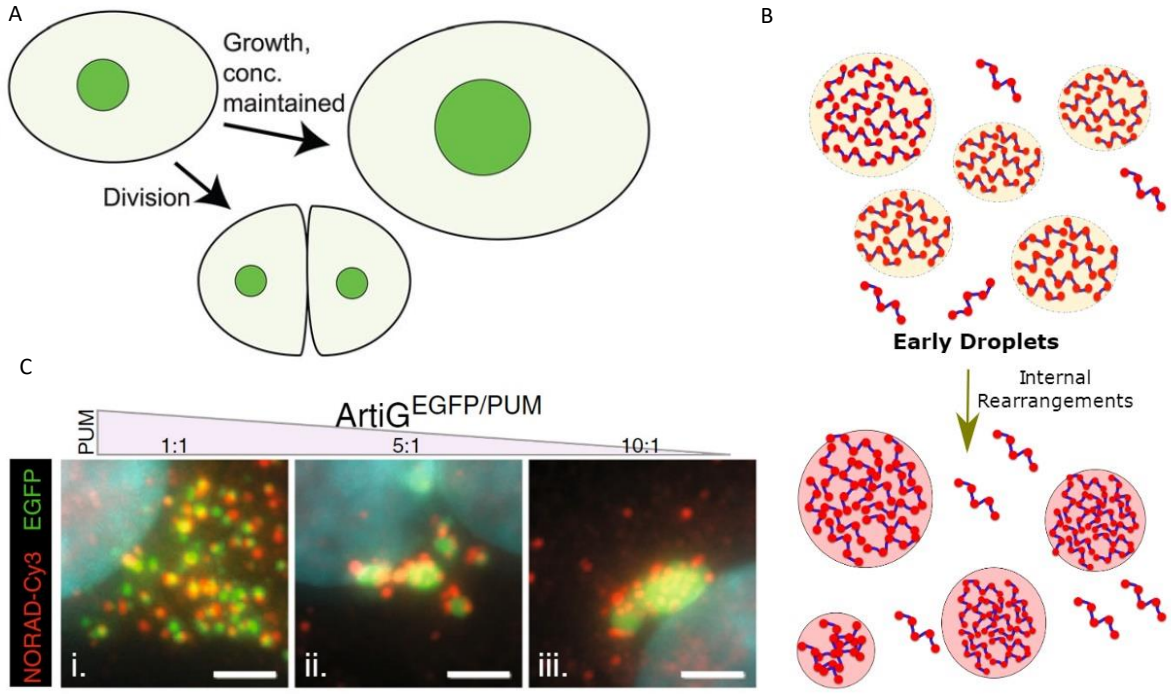

Figure I.25: Various mechanisms can play a role in the regulation of condensates size. A. In a system with a constant concentration of total components, the size of a phase-separated droplet will scale with the cell size. Adapted from[94]. **B.** Aging into highly cross-linked structures with saturated interactions can prevent further growth of condensates. Adapted from[101]. **C.** The size of condensates can depend on the concentration of clients recruited at the surface and acting like surfactants or Pickering agents. Here, the more ArtiGranules are enriched with the RBP Pumilio and thus can recruit endogenous components at the surface, the smaller they are. Adapted from[75].

Another meaningful factor to consider in the regulation of condensate size is surface effects. Indeed, the surface of condensates is an environment distinct from the core of condensates and the dilute phase. Yet, surface effects on condensates are still understudied and have only begun to be investigated. Besides its distinct composition, the condensate surface can have a specific structure. A very recent preprint indeed recently highlighted the inhomogeneous network structures of IDR-based condensate[105]. Proteins at the interface showed a most extended structure and an orientation perpendicular to the interface. Predominant intermolecular interactions in the interior of the condensates lead to a more folded structure, and intramolecular interactions in the dilute phase result in an even more folded structure[105]. This extended conformation could promote β-sheet formation of hnRNP1A proteins by bringing their aggregation-prone regions closer to each other, explaining why amyloid formation was observed to occur specifically at the interface of hnRNP1A condensates[106].

Owing to the distinct characteristics of the condensate surface, surface effects have emerged as crucial for the stabilization of condensates against coarsening. Condensates can be stabilized by a high surface charge density, leading to repulsive forces between condensates prohibiting their coalescence[107]. In a similar fashion as the protein Ki-67 that prevents individual chromosome from coalescing by forming a repulsive molecular brush layer, biomolecules on the surface of condensates can act as surfactants and reduce the surface tension of condensates[108]. Surfactant proteins should consist in a domain prone to phase separate and another that does not phase separate. This composition should thus promote adsorption of surfactant proteins at the surface of phase-separated droplets. Recently, such proteins were demonstrated to control condensate size in a concentration-dependent manner in an *in vitro* study[109]. A simulation study further elucidated the impact of the scaffold/surfactant ratio on the stability of multidroplet systems[110]. Adsorption of amphiphilic molecules, in addition to regulate condensate size, could also stabilize multiphase droplets[65]. Surface proteins may also stabilize condensates and prevent coarsening by acting like Pickering agents, that unlike surfactants are not amphiphilic molecules but nanoscale solid particles. The intrinsically disordered protein MEG-3 was for example shown to behave as a Pickering agent by forming clusters at the surface of P granules of *C. Elegans*, which lower the surface tension of condensates and limit their coarsening[111]. Biomolecules acting as either surfactants or Pickering agents thus appear to be important regulator of condensate size by reducing surface tension and / or resulting in steric hindrance preventing coarsening. This is further illustrated by the effect of incorporating PUM.HD to the artificial condensates ArtiGranules, which as explained before provides the ability to recruit endogenous RNAs and RBPs of the PB interactome at the surface of the condensates. This resulted in a size dependence of the condensates on the quantity of Pumilio within the ArtiGranules: a higher quantity led to many sub-micrometric coexisting condensates that did not coalesce, while a lower quantity led to a reduced number of larger ArtiGranules (Fig. I.25C)[75]. The endogenous recruited biomolecules were here proposed to hinder growth by both sub-unit addition and coalescence[75]. Another example comes from the yeast enzyme Bre1, involved in H2B ubiquitination, that was shown to form a shell around condensates of the Large1 protein and to prevent their growth by prohibiting fusion events[112].

The diverse mechanisms that have been put forward to explain the deviation of native condensates from the equilibrium are not exclusive, and cells arguably leverage all of them to regulate condensates size and number. The interplay between the various mechanisms and how much they are at stake for different condensates or in different cell types remains unclear.

I.3.3. Interplay between biomolecular condensates and the cytoskeleton

The cytoskeleton is a dense and complex network of interlinking protein filaments (microtubules, actin filaments, and intermediate filaments) present in the cytoplasm of all eukaryotic cells, and playing a critical role in many cellular processes[113]. Among other roles, the cytoskeleton determines cell shape by contributing on the one hand to the cell mechanical resistance to deformation, and by reorganizing in response to external mechanical forces on the other hand, through polymerization and depolymerization. During cell division, the microtubules network rearranges into the mitotic spindle, which segregates the chromosomes. Importantly, the cytoskeleton contributes to the cellular organization by facilitating intracellular transport of supramolecular structures, including membrane-bound organelles and biomolecular condensates. This ability comes from the polarized nature of microtubules and actin filaments, which are constituted of asymmetrical subunits at the molecular level (α/β tubulin dimers for microtubules, and monomeric actin for actin filaments). These polymers can thus be used as tracks for molecular motors to move, preferentially in one direction, and take along various cargos. Different motors are involved depending on the cargoes and the direction of transport: kinesins that move toward the microtubule plus-ends (i.e., anterograde motors, except for the members of the kinesins-14 family); dynein and members of the kinesin-14 family that are microtubule minus-end directed (i.e., retrograde motors); and finally, myosin motors that are actin-based[114].

Interactions between the cytoskeleton and membrane-bound organelles have been observed for many years[115]. Over the past few years, a rich mutual interplay between the cytoskeleton and biomolecular condensates has also progressively been brought to light[115,116]. On the one hand, condensation can participate in the organization of the cytoskeleton network by concentrating cytoskeletal monomers and triggering the nucleation of cytoskeletal filaments (Fig. I.26A). For example, in addition to the centrosome that is the main microtubule organizing center, other condensates can participate in the organization of the microtubule network, as was for example shown by the *in vitro* phase separation of the microtubule-associated protein tau, which concentrates tubulin, and thus exceeds the nucleation threshold and induces the polymerization of microtubule bundles[117,118]. On the other hand, the viscoelastic cytoskeletal network can physically restrain the growth of condensates. They can indeed prevent their coalescence by spatially separating individual droplets (Fig. I.26B) or precluding gravitational effects that can affect the largest condensates, as it is the case with the nuclear actin scaffold that was shown to keep the nucleoli in *Xenopus laevis* eggs from coalescing due to gravity[103]. Growth by sub-unit addition or Ostwald ripening can also be limited because of the mechanical resistance of the cytoskeletal network, in a similar fashion to nuclear condensates that preferentially grow in regions of low chromatin density[80].

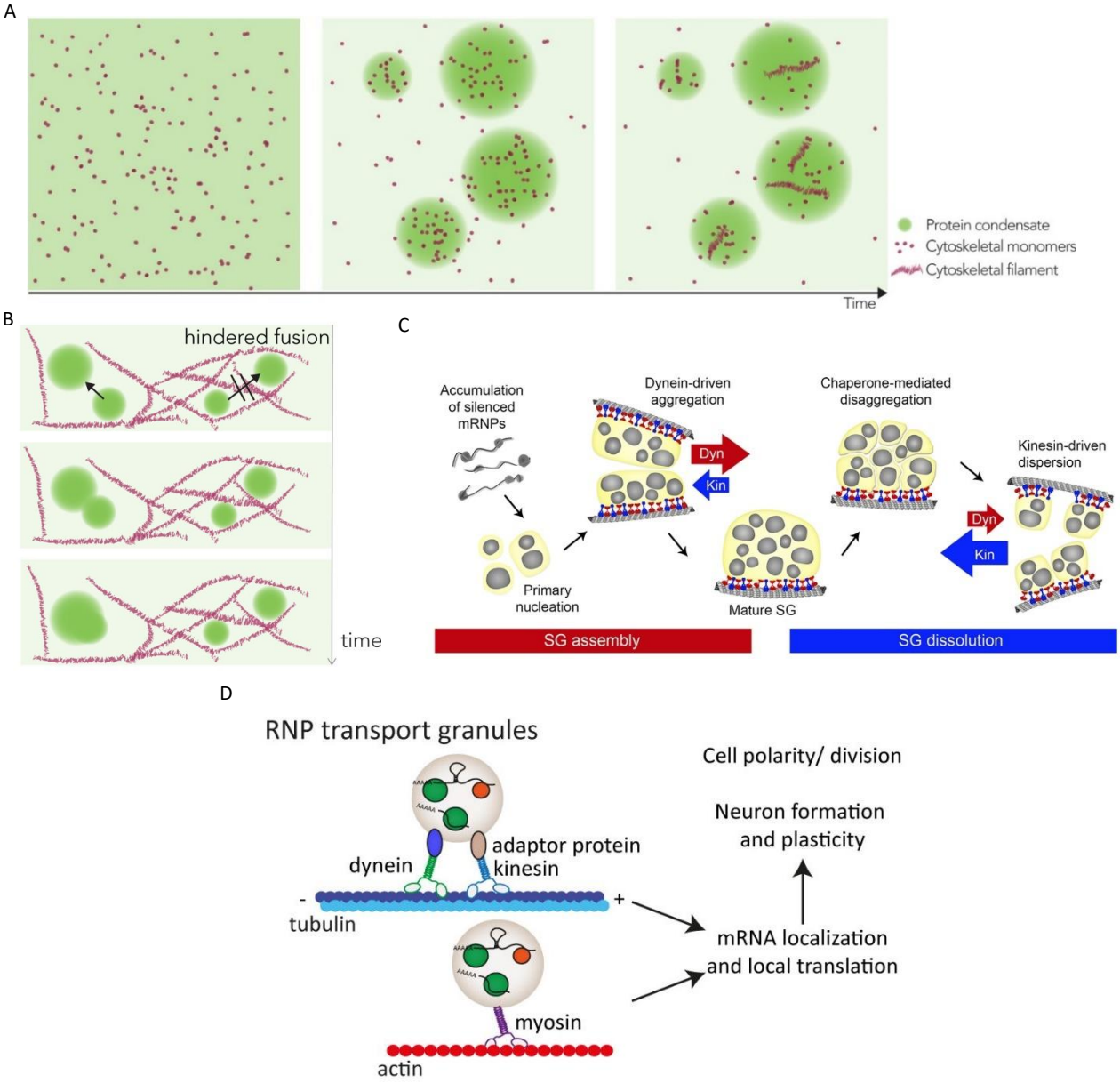

Figure I.26: A few examples illustrating the rich interplay between biomolecular condensates and the cytoskeleton. A. Upon condensation of cytoskeletal regulators (green), cytoskeletal monomers (pink dots) can get concentrated in the droplets to the point of overcoming the nucleation threshold and triggering fibers polymerization. Adapted from[116]. **B.** The dense cytoskeletal network can hinder fusion events by spatially segregating condensates from each other. Adapted from[116]. **C.** Model for transport-based assembly and disassembly of SGs: after translation abortion following acute stress, small complexes with among others silenced mRNPs are formed in the cytoplasm. They then undergo retrograde transport mediated by dynein motors (red), which facilitate their fusion into larger SGs. After a while, chaperones weaken SGs cohesion, which allow sub-units dispersion by anterograde kinesin (blue)-based transport and SGs disassembly. From[119] **D.** Some condensates in the cytoplasm, like here RNP transport granules, constituted of diverse biomolecules including mRNAs (grey), can associate directly or indirectly with motor proteins and are transported along microtubules or actin filaments to their final destination. Adapted from[115].

In addition to the passive interplay of cytoskeletal fibers with condensates compelled by the spatially limited cytosol, specific interactions between biomolecules in condensates and motors or motor adaptors can occur, resulting in motor-based transport of condensates with several biological outcomes. Microtubule-based transport is for example involved in the growth by fusion and disassembly by fission of SGs and PBs (Fig. I.26C)[119–124]. Furthermore, long-range active transport of condensates contributes to the spatial organization of the cellular space. Importantly, mRNAs transport and subcellular localization, often through transport of mRNA-containing condensates, allows localized translation and is involved in numerous cellular processes (Fig. I.26D)[125,126]. This mRNA localization through transport in condensates is highly conserved between species and type of cells. Indeed, localizing a mRNA, from which many proteins can be translated, is much more efficient than relocating individual proteins[127]. Biological processes regulated by mRNA transport include notably morphogen gradients in developing embryo[128–131], cell migration[132], neural development and synapse plasticity[11,133].

Altogether, biomolecular condensates and the cytoskeleton are intrinsically linked, both physically and biologically. New facets of the interplay between both cellular entities will undoubtedly be uncovered by further studies.

I.4. Ph.D. goals

The prime goal of my Ph.D. was to develop a minimal, versatile and robust reconstitution tool to study condensates in cells. To that end, the strategy applied consisted in designing and expressing in cells recombinant proteins, able to interact with each other and to phase separate into artificial condensates with controlled composition. Two systems were developed, the ArtiGranule and the linear 5Fm systems, which differ in the recombinant proteins used (see chapters II and III for a description of the two methods). Both were shown to be orthogonal to the cell environment, i.e., no interactions between the artificial condensates and the cell environment were observed. This specificity and the possibility to add proteins of interest in the scaffolds of the artificial condensates opens new possibilities to address various questions on cellular condensates. Below will be described some questions addressed during my Ph.D (Fig. I.27).

First, **how can we reduce the complexity in the RNA composition of condensates?** Indeed, native condensates count thousands of different biomolecules, and many condensates were shown to include RNAs. Recent advances have seen the development of tools to build mimics of biomolecular condensates in cells. Importantly, incorporation of RNA-binding domains of proteins found in native condensates in the design of iPOLYMER (TIA-1 from SGs), Corelet (G3BP1 from SGs) and ArtiGranule (Pumilio from PBs), have allowed for the reconstitution of truthful reconstitutions of protein-RNA condensates[75,78,84]. However, these RBPs can target thousands of different RNA species,

and unraveling the impact of RNA on the biogenesis of condensates and on the regulation of their material properties remains arduous. As will be further developed in Chapter II, we designed during my Ph.D. artificial condensates programmed to specifically recruit a single RNA species, by using an orthogonal RBP targeting a heterologously-expressed RNA.

Secondly, **what sets condensate size and number in cells?** The localization of RNAs at the surface of condensates has recently emerged as a common feature of different condensates, like PBs and SGs[18,134–137]. Importantly, the recruitment of endogenous components at the surface of ArtiGranules through interactions with the RNA-binding domain of Pumilio, including RNAs, has shown to directly regulate the size of the condensates. However, because of the RNA compositional complexity of condensates, a quantification of the impact of surface RNA on the biogenesis of condensates and on the regulation of their size and number was still out of reach. We showed that the heterologously expressed RNA specifically recruited in our system localized at the surface of our artificial condensates. By using a visualization method at the single molecule level (single molecule Fluorescence *In Situ* Hybridization (smFISH)), we were able to quantify the RNA surface recruitment, which allowed us to quantitatively link for the first time RNA surface density and condensate size and number (Chapter II).

Thirdly, **how molecular motors can impact the biogenesis of condensates?** Indeed, native cytosolic biomolecular condensates are part of the cell complex machinery and are not passively living their life independently of the cell environment. They can notably interact with the cytoskeleton tracks through molecular motors. However, no reconstitution approach has succeeded in engineering condensates that could be powered and positioned in specific area of cells by molecular motors. To bridge this gap, we developed during my Ph.D. a method to control the localization of our artificial condensates in cells via the addition in the scaffold of the condensates of motor or motor adaptor domain. Depending on the motor at play, condensates could be positioned either at the cell periphery or near the centrosome (Chapter III).

Finally, **can we reconstitute a mRNA localization system?** Indeed, while many studies have focused on revealing the spatial localization of mRNAs in cells, often via recruitment in biomolecular condensates that are subsequently shuttled in cells, there is no method to manipulate this localization. Such a tool would allow to investigate the effect of subcellular localization on RNA functions and processing, which up to now remains delicate. Therefore, we reconstituted a minimal RNA localization system by recruiting a specific target RNA in our artificial condensates with controlled localization (Chapter III).

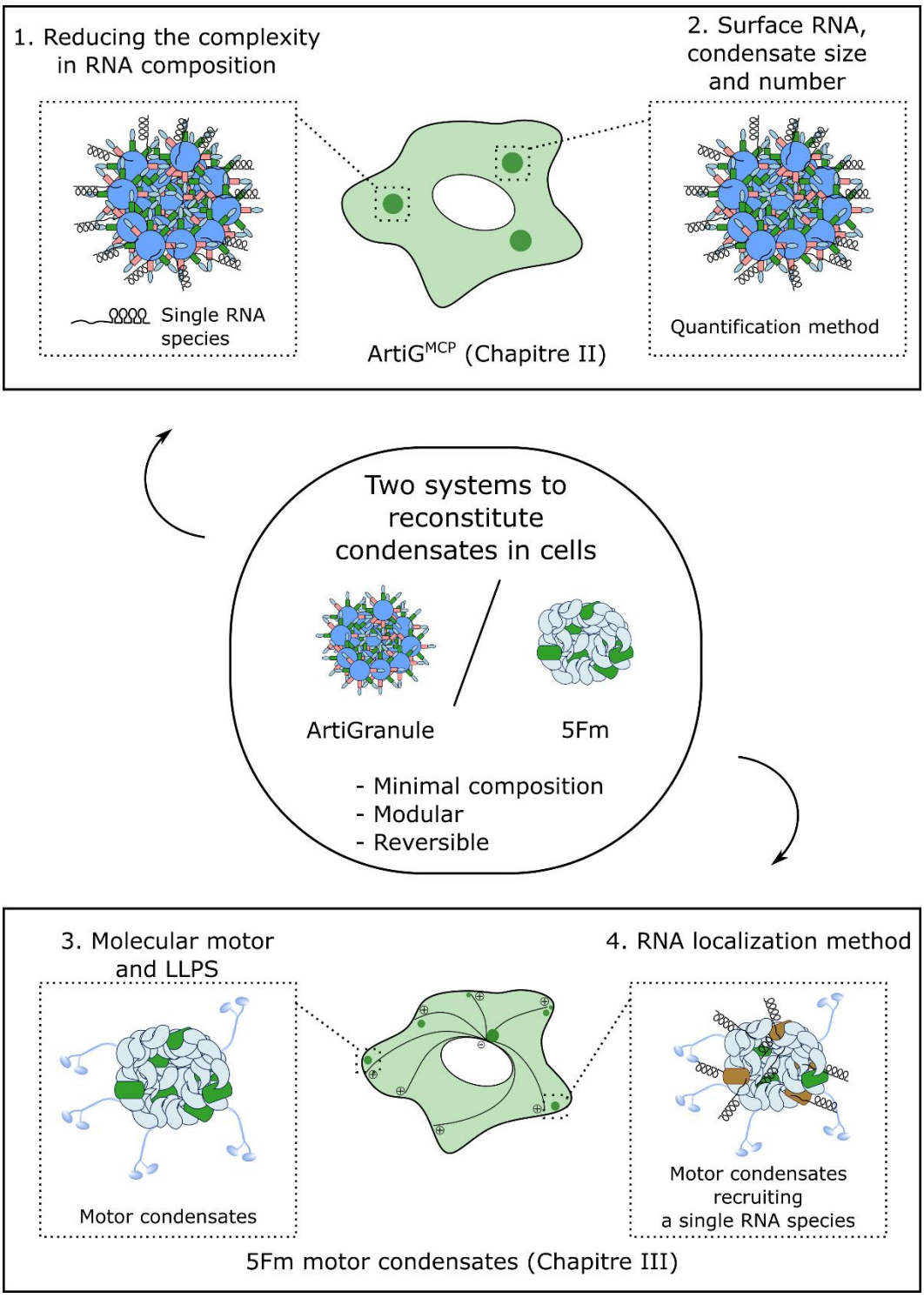

Figure I.27: Ph.D. goals. Chapter II will detail the method to build artificial condensates in cells specifically recruiting a single RNA species and the application of this method to quantify the impact of surface RNA on the biophysical properties of condensates (size, number and morphology). Chapter III will describe the method to build localized condensates in cells and its use in controlling the localization of target mRNAs.

CHAPTER II: RNA at the surface of phase-separated condensates impacts their size and number

This chapter is based on the following article:

RNA at the surface of phase-separated condensates impacts their size and number

Audrey Cochard, Marina Garcia-Jove Navarro, Leonard Piroska, Shunnichi Kashida, Michel Kress, Dominique Weil, Zoher Gueroui

Published in Biophysical Journal, April 12, 2022

doi: https://doi.org/10.1016/j.bpj.2022.03.032

Contents

II.1. Investigating the role of RNA in the biogenesis of biomolecular condensates

II.1.1 RNA contributes to the spatiotemporal control, the specificity, and the morphology of biomolecular condensates

Biomolecular condensates have a complex composition and often concentrate thousands of different species. The high molecular diversity of condensates raises the issue of how we can disentangle the contribution of a specific component from the intricate network. In particular, RNA is a common feature of cytosolic condensates and even of some nuclear ones such as the nucleolus. To examine the impact of RNA in the biogenesis of condensates, different approaches have been adopted[88,138,139]. Here I will provide three examples using *in vivo* or *in vitro* approaches.

To investigate the role of rRNA in nucleolus biogenesis, an elegant strategy was to compare wild-type and mutant *Drosophila melanogaster* embryos lacking rDNA repeats[138]. Interestingly, nucleolar proteins in mutant embryos still formed assemblies similar to nucleoli, but smaller, more numerous, and more broadly dispersed in the nucleoplasm (Fig. II.1A and B). Indeed, wild-type embryos displayed one of two nucleoli per nucleus, which are localized at a specific region of the rDNA repeats called the nucleolus organizer region and form at the same time for different embryos. In contrast, the assemblies in absence of rDNA did not seem to be associated with specific sequences of DNA, and the temporal precision of formation was lost. To investigate whether these discrepancies came from the lack of rDNA itself or the lack of rRNA transcripts, a complementary strategy was applied which consisted in blocking the synthesis of rRNA in wild-type embryos by knocking-down a subunit of RNA polymerase I through RNA interference. The observed delay in the formation of the nucleolus underlined the seeding effect that rRNA play in nucleolus formation, which would explain the spatiotemporal precision of formation. This study demonstrates the role of rDNA transcription in circumventing the instability of the nucleation step by seeding nucleolus formation and bringing spatiotemporal control over the formation process (Fig. II.1C).

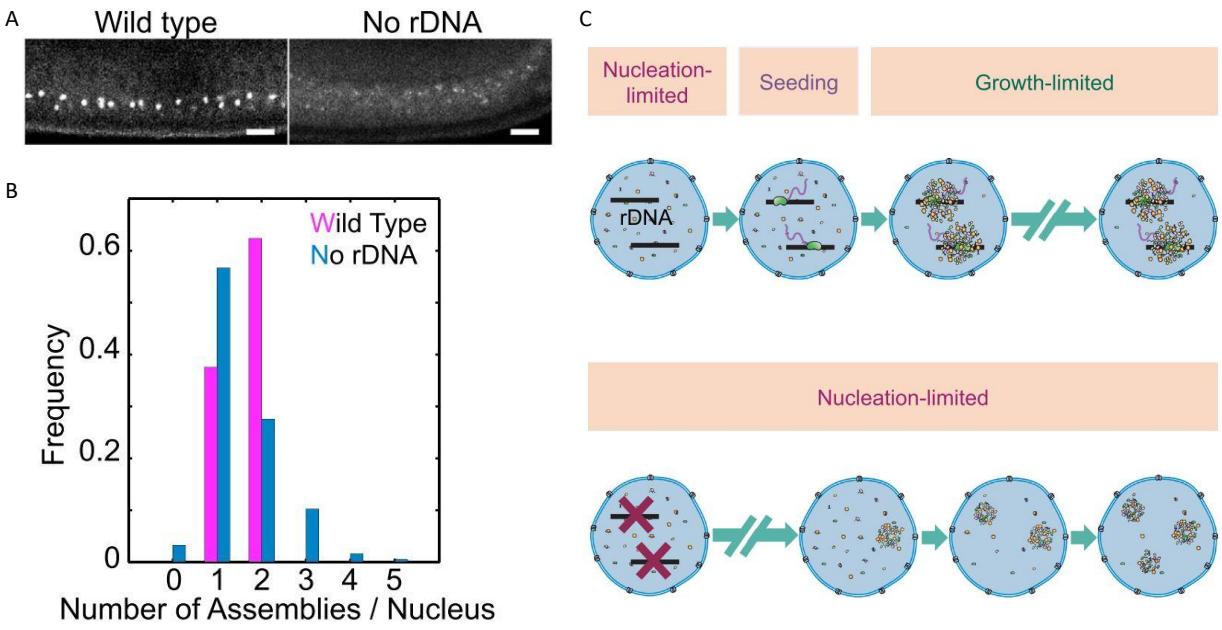

Figure II.1: rRNA seeds nucleolus formation. Adapted from[138]. A. Lateral view of a wild-type (left) and a mutant (lacking rDNA repeats, right) *Drosophila melanogaster* embryos at nuclear cycle 14, expressing an RFP-tagged fibrillarin, which is located in the dense fibrillar component of the nucleolus. **B.** Number of nucleoli per cell in the wild-type embryo (pink) and of nucleolus-like assemblies in the mutant embryo (blue). **C.** Schematic of the nucleolus nucleation model in *Drosophila melanogaster* embryos: rRNA transcription seeds the assembly of nucleoli at precise locations. In absence of rDNA, stochastic nucleation-limited assembly leads to randomly localized nucleolus-like assemblies.

Easier to implement, *in vitro* reconstitution approaches with purified RNA can also allow to investigate its role in the assembly or the control of the physical properties of condensates. *In vitro* reconstitution of fungus *Ashbya gossypii* Whi3 protein condensates with different Whi3-interacting RNAs thus showed the role of RNA structure in driving the coexistence of Whi3 condensates with different composition[88]. Indeed, in *Ashbya gossypii* cells, two different types of Whi3 droplets coexist and exhibit distinct Whi3 levels: perinuclear droplet enriched in the cyclin CLN3 mRNA and droplets at cell tips enriched in the formin BNI1 and SPA2 mRNAs. Protein-free, electrostatic-mediated phase transitions of the mRNAs *in vitro* showed no colocalization of CLN3 and BNI1 or SPA2 mRNAs, while BNI1 and SPA2 displayed significant co-localization (Fig. II.2A). Therefore, specificity of Whi3 phase separation seemed to be encoded by the mRNAs. Additional experiments implying modifications in the structures of the mRNAs showed the importance of mRNA structure in maintaining droplet identities. This study proposes a model whereby homo- and heterotypic RNA-RNA interactions drives compositional specificity of Whi3 droplets (Fig. II.2B). More broadly, RNA structure may promote coexistence of the diverse condensates found in a single cell.

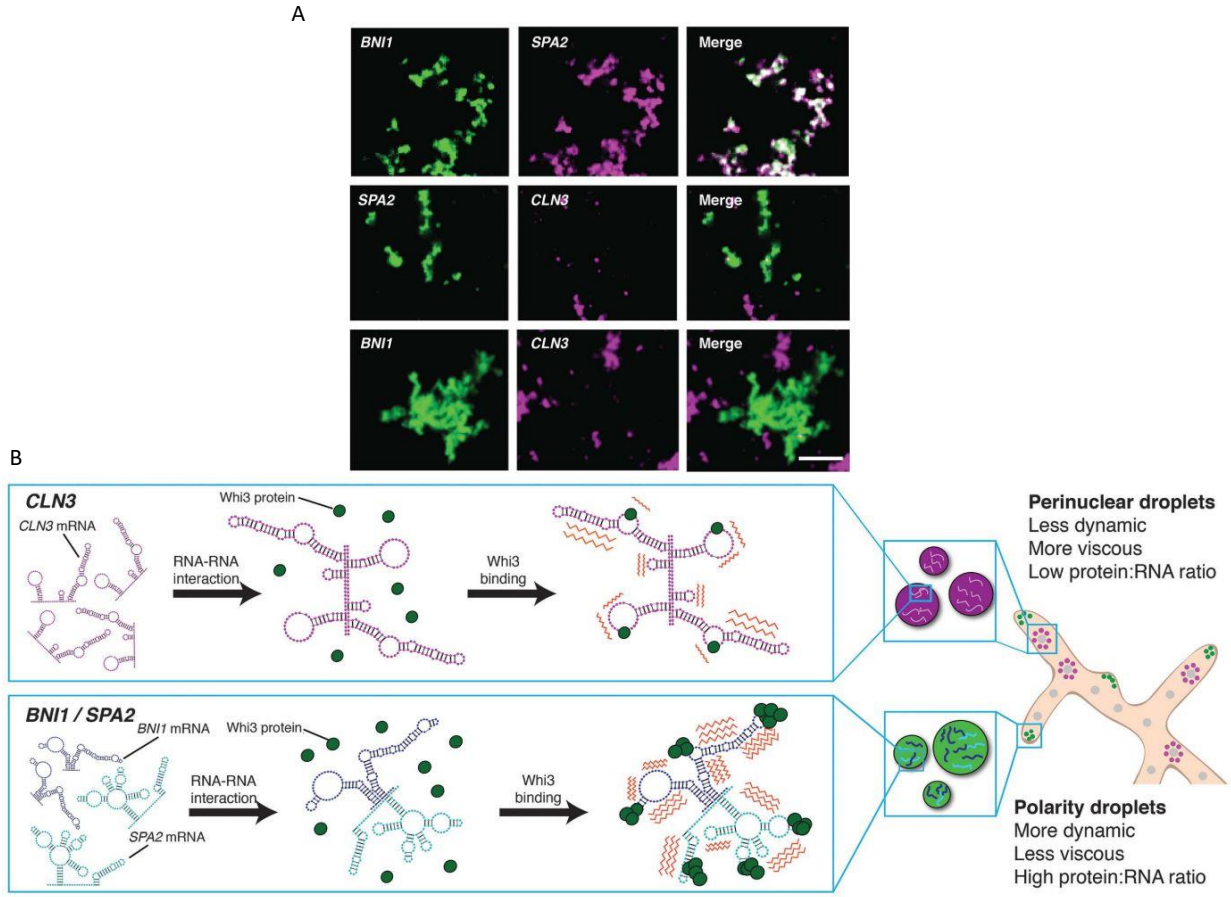

Figure II.2: mRNA structures drive specificity of Whi3 droplets. Adapted from[88]. A. *In vitro* fluorescence microscopy images showing co-localization of BNI1 and SPA2 mRNAs (green and pink, respectively, upper panel), but absence of co-localization of CLN3 mRNA (pink) and SPA2 or BNI1 mRNAs (green, middle and lower panel, respectively). Scale, 5 µm. **B.** Schematic of the proposed model: RNA-RNA interactions, dependent on RNA structures, promote the selective enrichment of distinct RNAs and proteins, which results in distinct dynamics (orange zigzags) and composition.

The role of RNAs on the shape of TIS granules, mesh-like condensates formed by assembly of the RBP TIS11B and intertwined with the tough endoplasmic reticulum (ER), was examined through both *in vitro* and *in vivo* reconstitution studies[139]. The mesh-like shape contradicts the spherical shape expected for liquid-like condensates, as surface tension favors a low surface to volume ratio. Moreover, the high dynamics of TIS granules protein components, revealed by FRAP experiments, are not consistent with gel-like properties that would explain the inability to relax into a spherical shape. In cells, expression of a mCherry-tagged TIS11B recombinant protein led to TIS granules that resemble endogenous TIS granules and have a mesh-like structure intertwined with the ER (Fig. II.3A, left). This contrasts with the expression of TIS11B with a mutated RNA binding domain (RBD), and thus unable to bind to RNAs, that gave rise to TIS granules with spherical shape and no longer intertwined with the ER (Fig. II.3A, right). These observations in cells were reinforced by *in vitro* reconstitution experiments, which showed the ability of unstructured RNAs to promote the mesh-like structure of TIS

granules, while in the presence of structured RNA, reconstituted condensates retain their spherical shape (Fig. II.3.B). These experiments allowed the development of a model whereby an underlying mRNA skeleton within TIS granules, constituted of mostly unstructured RNAs able to form intermolecular RNA-RNA interactions, would determine the shape of the granules. This RNA matrix would counteract the surface tension and induce the formation of mesh-like condensates (Fig. II.3.C).

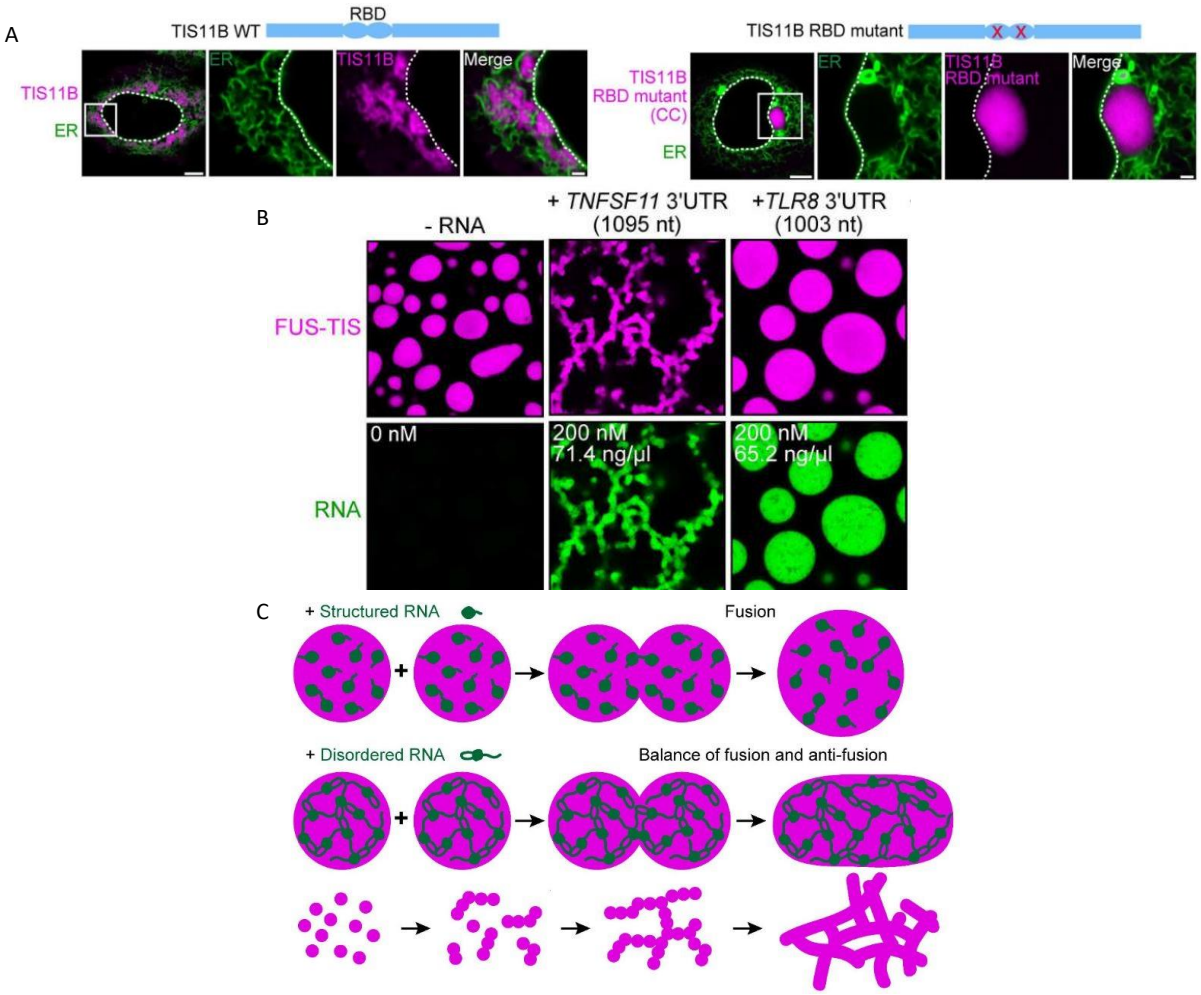

Figure II.3: RNA-RNA interactions define the mesh-like shape of TIS granules. Adapted from[139]. **A.** Confocal images of HeLa cells expressing mCherry-tagged TIS11B (left) or TIS11B with a mutated RNA-binding domain (RBD). GFP-labelled SEC61B was co-expressed to visualize the endoplasmic reticulum (ER). The area in the white square is magnified on the right of each panel. **B.** Confocal images of *in vitro* phase separation experiments with purified FUS-TIS (10 µM), where FUS plays the role of a multivalent domain, in the absence of RNA (left panel), or in the presence of the unstructured 3'UTR of TNFSF11 RNA (middle panel) or the structured 3'UTR of TLR8 RNA (right panel). **C.** Model to depict how structured RNAs, unable to engage in intermolecular RNA-RNA interactions, would not hinder the fusion and relaxation of granules, whereas unstructured RNAs able to interact with each other would form a stiff structure hindering the relaxation in spherical shapes, thus resulting in mesh-like condensates.

II.1.2. Investigating the role of RNAs in biomolecular condensates using bioengineered condensates

II.1.2.a. Bioengineered RNA-protein condensates

Similar to TIS11B that recruits RNAs in TIS granules, protein-RNA interactions were used to enrich RNAs in artificial condensates. Mimics of condensates, constituted of both proteins and RNAs have been developed via the addition of RNA-binding domains of RBPs found in native condensates in the design of iPOLYMER (RRM of the SG protein TiA-1), Corelet (the SG protein G3BP's dimerization domain NTF2, which acts as an interaction platform in addition to its ability to dimerize), and ArtiGranules (the RNA-binding domain (RBD) PUM.HD of the PB protein Pumilio 1)[75,84,140]. These mimics were shown to be enriched in SG or PB components (Fig. II.4A-C). However, these RBPs count thousands of RNA targets. For example, a database compiling crosslinking immunoprecipitation (CLIP)-seq from a large amount of publicly available data sets identifies more than 2500 RNA targets of Pumilio 1[141]. This complexity limits our understanding of the role of RNA in condensates biogenesis. Though the reconstitution studies introduced in Chapter I have allowed the simplification of the protein content of biomolecular condensates, none have succeeded in reducing the complexity of the RNA content.

Therefore, the first aim of my Ph.D. was to develop a method to build in cell artificial condensates containing a single RNA species, so that it would be possible to directly study the impact of RNA on condensate biogenesis. To do so, I used an adaptation of the ArtiGranule system, named ArtiG^{MCP} after the used RBP, and designed to recruit a single RNA species instead of the numerous binding partners of PUM.HD. The next sections will first further present the ArtiGranule system, secondly introduce the variant ArtiG^{MCP} and finally explain the workflow followed in this study.

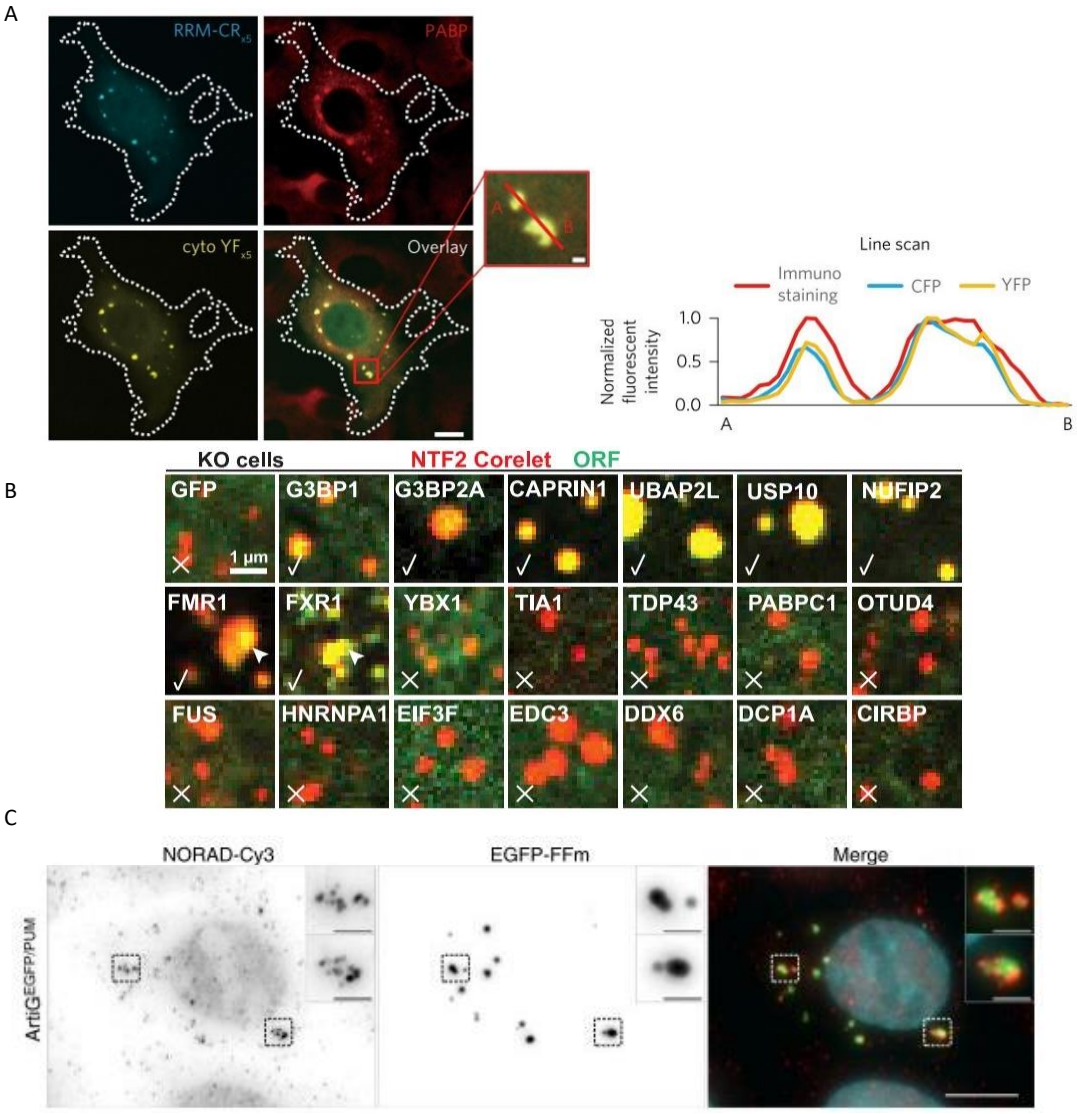

Figure II.4: Reconstitution of protein-RNA condensates via interaction of RBPs in the bioengineered scaffolds with endogenous RNAs and proteins. A. Addition of the RRM of TIA-1 in the iPOLYMER scaffold results in enrichment in the artificial condensates of SG components, like the endogenous poly(A)-binding protein (PABP), as revealed by immunofluorescence microscopy in COS-7 cells. Scale, 10 µm. The line-scan plot from A to B in the zoom image confirms the enrichment of PABP in iPOLYMER puncta. Adapted from[84]. **B.** In G3BP KO cells, NTF2-Corelets are enriched with several SG proteins (labeled with a check sign) like CAPRIN1, but some SG proteins like TIA1 do not partition into the artificial condensates, as revealed by co-expression of GFP-tagged proteins. The enriched proteins are putative binding partners of NTF2. Adapted from[140]. **C.** Epifluorescence imaging of a HeLa cell expressing PUM.HD-functionalized ArtiGranules condensates labeled with EGFP (ArtiG$^{EGFP/PUM}$, green in merge). The PB-enriched NORAD lncRNA is recruited on the condensates, as revealed by single fluorescence in situ hybridization (smFISH, red in merge). The nucleus is stained with DAPI (blue in merge). Scale, 10 µm. Zoom, 2 µm. Adapted from[75].

II.1.2.b. The ArtiGranule system

To reconstitute condensates in cells, I used for this project the ArtiGranule system introduced in part I.2.2.a, which was developed before my arrival in the lab and takes advantage of the auto-assembly of 24 ferritin monomers in nanocages of 12 nm (Fig. I.15). A highly multivalent core is obtained by functionalizing each ferritin monomer (Ft) with the self-interacting module F36M-FKBP (Fm). This mutant of the FKBP protein homodimerizes with a weak affinity (K_d in the µm range) which gives the multivalent cores the ability to undergo phase separation[142]. Indeed, 24 h after transfection of the module construct labelled with the mCherry fluorescent protein (Fm-mCherry-Ft) into HeLa or HEK293 cells, bright foci can be observed by epifluorescence microscopy in the cytoplasm of about 30% of the cells (Fig. II.5A). The granules recapitulate the hallmarks of condensates formed by LLPS. They are indeed spherical (Fig. II.5A), and time-lapse live confocal imaging showed their ability to coalesce (Fig. II.5B). FRAP experiments showed that a fraction of the fluorescent signal (35%) recovered with a timescale of 2 minutes, demonstrating that ArtiGranules have a mobile fraction that undergo fast exchange with the cytoplasm (Fig. II.5C-D). Moreover, time-lapse live imaging starting 8 h after transfection highlighted the existence of a C_{sat}, over which nucleation of several bodies could be observed (Fig. II.5E). Altogether, these observations suggest a mechanism of condensation by LLPS.

An asset of the ArtiGranule system is its reversibility. Indeed, the Fm-Fm interactions, whose weakness confers to our reconstituted condensates their liquid-like properties, are constantly done and undone, and condensates can thus be dissolved by the addition of a competitor of the homodimerization. The Fm protein is a point mutant of the FK506-binding protein (FKBP) that retains the ability to bind to FK506. The addition of FK506 to the cell milieu should thus compete with the Fm-Fm dimerization. Indeed, adding FK506 immediately after transfection prevents condensate formation and adding it after 24 h of expression readily dissolved ArtiGranules (Fig. II.5F). The ArtiGranule system thus allows for a controlled inhibition and disassembly of artificial condensates in cells.

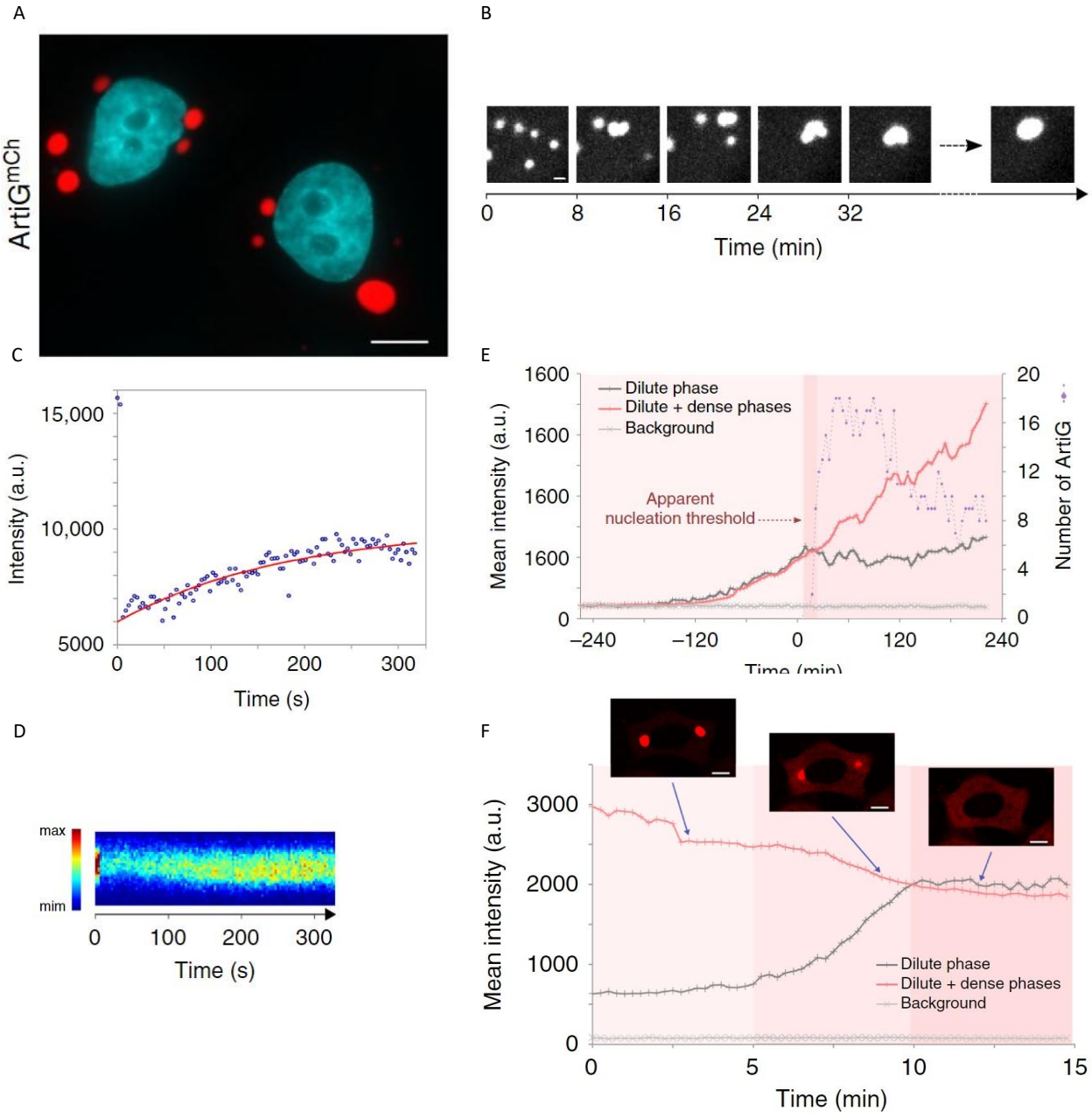

Figure II.5: ArtiGranules recapitulate the hallmarks of LLPS. Adapted from[75]. A. Representative confocal image of spherical ArtiGranules 24 h after transfection. Scale, 10 µm. **B.** Time-lapse confocal images of several ArtiGranules coalescing into one single larger condensate. Scale, 2 µm. **C.** Example of recovery of fluorescence intensity after photobleaching of an ArtiGranule. **D.** Kymograph representation of the fluorescence recovery analyzed in (C). **E.** Evolution of the total cytoplasmic fluorescence (dilute + dense phases, red) and of the dilute phase fluorescence (grey) of a HeLa cell. The dilute phase shows an increase in the fluorescence until reaching a plateau at the time of ArtiGranules nucleation, corresponding to a C_{sat}. The violet dots represent the number of granules over time, whose decrease reflects the coalescence events. **F.** The addition of the Fm-Fm homodimerization competitor FK506 dissolves ArtiGranules. Scale, 10 µm.

II.1.2.c. The ArtiG^{MCP} system

Addition of PUM.HD domain to the ArtiGranule design led to recruitment of numerous PBs components. To limit the recruitment at one single species of RNA and allow precise insights on the role of RNA in condensate biogenesis, we replaced PUM.HD in the ArtiGranule scaffold by the MS2 coat protein (MCP) of the MS2 bacteriophage (Fig. II.6). MCP is an orthogonal protein which binds with high specificity and affinity to RNA stem loops of the bacteriophage genome, called MS2 stem loops[143]. The resulting construct, Fm-MCP-Ft, consists in a fusion of the self-interacting domain Fm, of MCP and of a ferritin monomer Ft. To visualize the condensates, a second construct Fm-emGFP-Ft was used, where emGFP is the emerald GFP fluorescent protein. The assembly of ferritin monomers in nanocages gives rise to multivalent cores functionalized with Fm proteins, which can phase separate over a C_{sat} and form condensates hereafter called ArtiG$^{emGFP/MCP}$ (Fig. II.6). A third construct was designed to express a mRNA with four embedded MS2 stem loops in its 3'UTR (RNA-MS2, Fig. II.6). The co-transfection of the three constructs in cells should result in condensates specifically recruiting RNA-MS2.

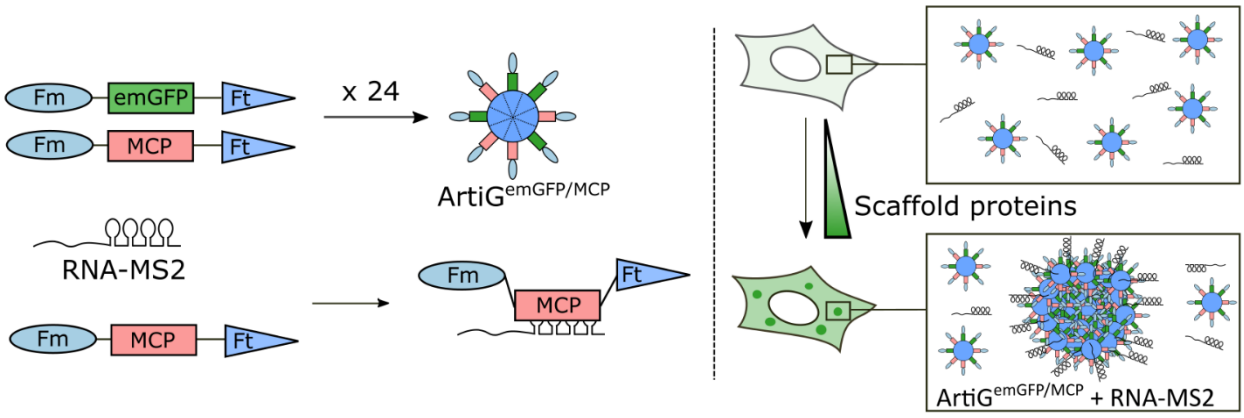

Figure II.6: Schematic of the ArtiG$^{emGFP/MCP}$ system. Adapted from Cochard et al., Biophysical Journal, 2022. The two fusion proteins Fm-emGFP-Ft and Fm-MCP-Ft assemble into fluorescent multivalent cores, which phase separate into ArtiG$^{emGFP/MCP}$ condensates over a C_{sat}. The MCP protein should allow the specific recruitment of RNA-MS2.

II.1.2.d. Workflow to investigate the relationship between RNA surface recruitment and biophysical properties of condensates

To reconstitute RNA-protein condensates in a cellular environment, we co-transfected HeLa cells with the three plasmids described above: Fm-MCP-Ft and Fm-emGFP-Ft, which should result in ArtiG$^{emGFP/MCP}$ condensates over a C_{sat}, and a plasmid expressing RNA-MS2 (Fig. II.6). To monitor the formation of the condensates, we used live confocal microscopy, which revealed nucleation and growth of several bright emGFP condensates per cell. Live imaging also allowed us to investigate the dynamic properties of the condensates by performing FRAP experiments and to assess the possibility to control the dissolution of the condensates via the addition of a competitor of the Fm-Fm homodimerization, FK506. We turned to experiments on fixed cells to visualize RNA-MS2 molecules via single molecule in situ hybridization (smFISH). The smFISH method is described in the annex (part II.3.1). Interestingly, RNA-MS2 was recruited exclusively at the surface of ArtiG$^{emGFP/MCP}$ condensates. Cell fixation, followed by immunofluorescence assays also provided information on the localization of endogenous components, especially PBs and SGs components, which were shown to not colocalize with the ArtiG$^{emGFP/MCP}$ condensates, and thus attested to the orthogonality of our reconstitution system.

Our bioengineered approach has several strengths. First, a single species of RNA is recruited in the condensates. The smFISH imaging method moreover allows the detection of RNA-MS2 at the individual molecule level. Secondly, RNA-MS2 localization at the surface of ArtiG$^{emGFP/MCP}$ condensates can bring insightful data on the importance of the surface composition in regulating condensates formation and biophysical properties. Finally, the transient transfection gives access to a library of cells with highly variable expression of RNA-MS2. These features offer the possibility to study the role that surface RNA could play in condensates biogenesis and in the control of their dynamic and material properties. To this end, we devised a pipeline, based on a Python-based smFISH-dedicated analysis[144], to perform extensive quantification and investigate potential relationships between condensate material properties, size and number, and RNA enrichment at the surface of biomolecular condensates (Fig. II.7). The quantification steps will be further detailed in the annex (part II.3.2).

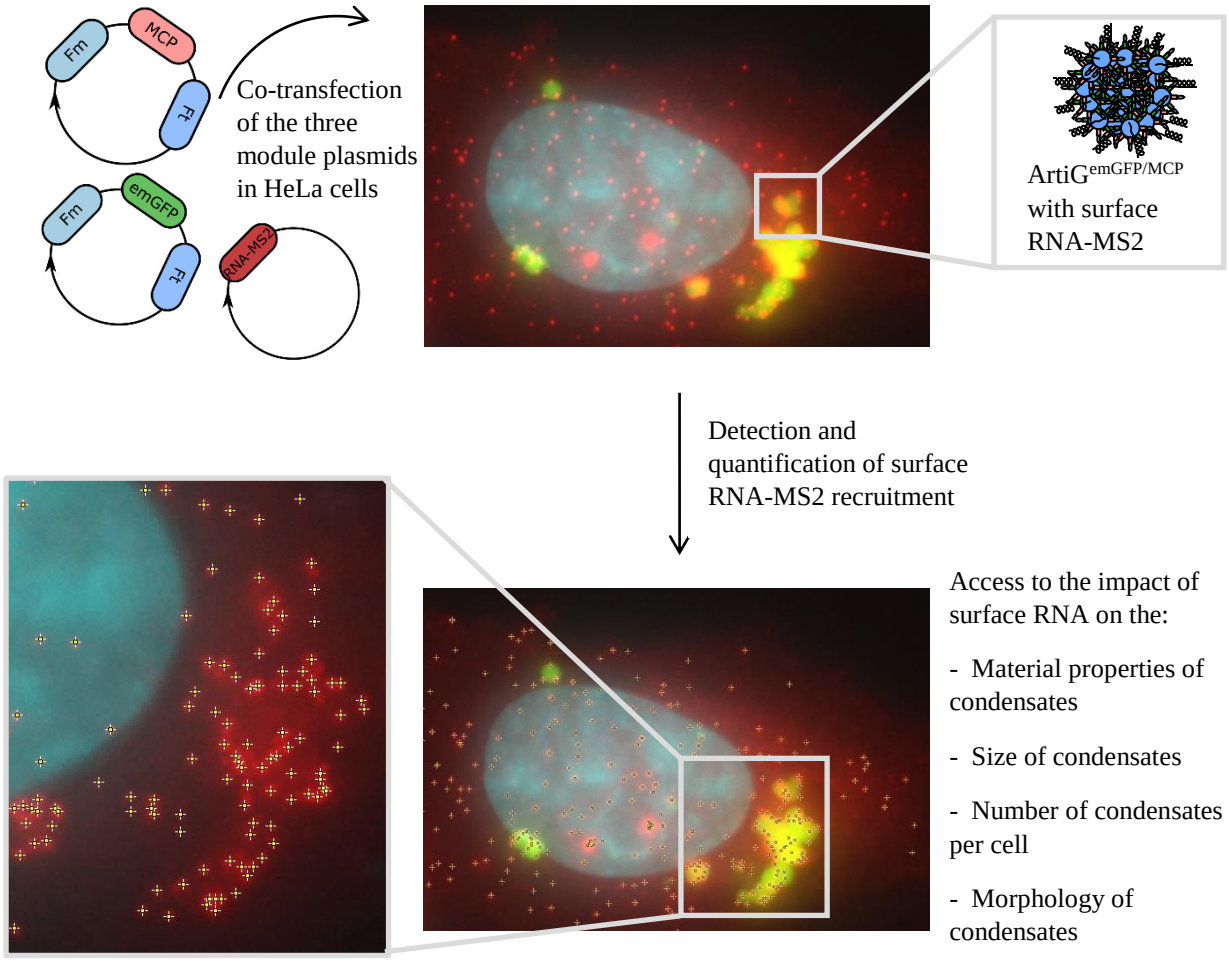

Figure II.7: Schematic of the strategy applied to investigate the relationship between RNA surface recruitment and biophysical properties of condensates.

II.2. Article and supplementary information

Biophysical Journal
Article

Biophysical Society

RNA at the surface of phase-separated condensates impacts their size and number

Audrey Cochard,[1,2] Marina Garcia-Jove Navarro,[1] Leonard Piroska,[1] Shunnichi Kashida,[1] Michel Kress,[2] Dominique Weil,[2,*] and Zoher Gueroui[1,*]

[1]PASTEUR, Department of Chemistry, École Normale Supérieure, PSL University, Sorbonne Université, CNRS, Paris, France and [2]Sorbonne Université, CNRS, Institut de Biologie Paris-Seine (IBPS), Laboratoire de Biologie du Développement, Paris, France

ABSTRACT Although it is now recognized that specific RNAs and protein families are critical for the biogenesis of ribonucleoprotein (RNP) condensates, how these molecular constituents determine condensate size and morphology is unknown. To circumvent the biochemical complexity of endogenous RNP condensates, the use of programmable tools to reconstitute condensate formation with minimal constituents can be instrumental. Here we report a methodology to form RNA-containing condensates in living cells programmed to specifically recruit a single RNA species. Our bioengineered condensates are made of ArtiGranule scaffolds composed of an orthogonal protein that can bind to a specific heterologously expressed RNA. These scaffolds undergo liquid-liquid phase separation in cells and can be chemically controlled to prevent condensation or to trigger condensate dissolution. We found that the targeted RNAs localize at the condensate surface, either as isolated RNA molecules or as a homogenous corona of RNA molecules around the condensate. The recruitment of RNA changes the material properties of condensates by hardening the condensate body. Moreover, the condensate size scales with RNA surface density; the higher the RNA density is, the smaller and more frequent the condensates are. These results suggest a mechanism based on physical constraints, provided by RNAs at the condensate surface, that limit condensate growth and coalescence.

SIGNIFICANCE It is increasingly recognized that biomolecular condensates contribute to organize cellular biochemistry by concentrating proteins and nucleic acids. How molecular constituents of condensates determine their size and morphology is unknown. To circumvent the biochemical complexity of endogenous condensates, the use of programmable tools to reconstitute condensate formation with minimal constituents can be instrumental. We report a methodology to form RNA condensates in cells programmed to specifically recruit a single RNA species. These ArtiGranule scaffolds undergo liquid-liquid phase separation in cells and can be chemically controlled to prevent condensation or to trigger condensate dissolution. Using this tool, we found that the condensate size scales with RNA surface density. This observation can be explained by physical constraints limiting condensate growth and coalescence.

INTRODUCTION

It is increasingly recognized that biomolecular condensates contribute to organize cellular biochemistry by concentrating and compartmentalizing proteins and nucleic acids. They include a broad range of nuclear and cytoplasmic ribonucleoprotein (RNP) granules, such as nucleoli, P-bodies (PBs), germ granules, and stress granules (SGs). Remarkably, abnormal condensate maturation into toxic aggregates is linked to viral infection, cancer, and neurodegenerative diseases (1). Cellular condensates harbor a large diversity in terms of biochemical composition as well as functions. Nevertheless, a unified model of formation via liquid-liquid phase separation (LLPS), where RNP constituents interact through multivalent and weak interactions, has been proposed to understand their biogenesis (2–6). In addition to their diverse compositions and functions, condensates are also diverse in size. Although PBs or PML bodies are often diffraction-limited puncta, other condensates such as germ granules, centrosomes, and nucleoli can reach a few micrometers in size (2,7–10). What sets condensate size and number in cells remains to be understood.

Mounting evidence based on in vitro reconstitutions and cellular approaches underlined the importance of

Submitted July 9, 2021, and accepted for publication March 28, 2022.

*Correspondence: dominique.weil@upmc.fr or zoher.gueroui@ens.fr

Editor: James Shorter.

https://doi.org/10.1016/j.bpj.2022.03.032

multivalent interactions between RNA-binding proteins (RBPs) and RNAs in shaping condensate biogenesis and morphology. In particular, RNA molecules have been shown to play fundamental roles in determining the structure, dynamic, and biophysical properties of condensates (11). For instance, RNAs act as molecular seeds to nucleate phase-separated condensates and regulate their assembly in a spatiotemporal manner (12–17). On the opposite, high RNA concentration can dissolve condensates and keep prion-like RBPs soluble in the cell nucleus (18,19). In addition to their formation or dissolution, RNA molecules can also impact the viscosity of the RNP condensates and the dynamics of their components in a sequence-dependent manner (20–22). The different structures of RNAs can also determine the molecular specificity of RNP condensates and thus explain the coexistence of separate condensates with distinct molecular compositions (23). Moreover, when RNAs are unstructured, RNA-RNA interactions can lead to the formation of nonspherical condensates (24). Finally, RNAs can take part in RNA-RBP interactions that drive the formation of multiphase condensates, whose structure relies on RNA concentration and on RNA-RBP interaction strength (22,25,26). In addition to the contribution of condensate constituents, extrinsic factors such as membrane, cytoskeleton, and chromatin can modulate LLPS and condensate biogenesis and coarsening (27–29).

Several bioengineering approaches have recently been developed to form condensates with specific properties in cells, and thus combine the control of condensate components achievable in in vitro experiments with the possibility to study LLPS within the cellular environment. These approaches often use optogenetic and chemical actuations based on protein-multimerization domains acting as scaffolds of artificial condensates. Engineering them with well-defined compositions, structures, and dynamic properties provides novel tools to correlate condensate biochemical functions with their material states, a link that is still difficult to reach by studying native RNP condensates. Such methods thus enabled quantitative studies of the dynamical properties of phase-separated condensates within cytoplasm and nucleus. For example, light-induced strategies based on optoDroplets allowed the actuation of model condensates that mimic pathological assemblies appearing in some age-related diseases (30,31). Alternative synthetic protein condensates were also designed with programmable material properties or functions (32–39). As a model for RNP condensates, iPOLYMER, Corelet, and our ArtiGranules (ArtiGs) were designed to induce condensation of RNA-binding motifs found in SGs (TIA-1, G3BP1) and PBs (Pumilio), respectively (40–42). Although these approaches provided a powerful mean to manipulate RNP condensate mimics in cells, they used RBP motifs that can bind thousands of RNA species, which could considerably limit our ability to interpret resulting observations in cells.

To overcome the inherent biochemical complexity of RBP-containing artificial condensates, our strategy has consisted in building a minimal RNP condensate, composed solely of an orthogonal protein that can bind a specific heterologously expressed RNA. To this aim, we relied on the widely used MCP/MS2 system, where MCP is the coat protein of the MS2 bacteriophage, which binds with high specificity and affinity to RNA stem loops of its genome, referred to as MS2 (43). We fused MCP to our previously developed ferritin-based ArtiG scaffold (42). When expressed in HeLa cells, the resulting ArtiG^{MCP} scaffolds underwent LLPS and formed micrometric bodies within the cytoplasm. When co-expressed with MS2-containing RNAs (MS2-RNAs), all condensates were decorated by MS2-RNA molecules. We found that MS2-RNAs localized at the condensates' surface, either as isolated RNA molecules or as a homogenous corona of RNA molecules around the condensates. Furthermore, fluorescent recovery after photobleaching experiments showed that RNA induced a hardening of the condensates toward a gel phase. We also found that cytosolic MS2-RNAs were depleted at the vicinity of large condensates, within a few micrometers range. The ArtiG^{MCP} condensates remained distinct from endogenous condensates, such as PBs or SGs. The assembly of ArtiG^{MCP} condensates is reversible: addition of a binding competitor of the self-interacting protein scaffolds enabled both dissolution and impediment of formation with a high efficiency. We first observed a negative correlation between the number of ArtiG condensates per cell and their mean diameter. The possibility to detect each individual RNA-MS2 molecule then allowed to quantitatively link RNA density to condensate size, which is not feasible for native condensates that recruit a large variety of RNAs. By quantifying the localization and number of individual RNA-MS2 molecules, we found that the higher the RNA density is, the smaller and more numerous the condensates are. Overall, our data indicated that the size of RNP condensate scales down with RNA surface density, which can be explained by physical constraints limiting condensate growth and coalescence.

MATERIALS AND METHODS

Experimental model

Human epithelioid carcinoma HeLa (ATCC, ccl-2) and embryonic kidney HEK-293 (ATCC, CRL-1573) cells were maintained in Dulbecco's modified Eagle's medium (with 4.5 g/L D-glucose, HyClone) supplemented with 10% fetal bovine serum (Gibco, 10,270,106) and antibiotics, at 37°C in a 5% CO_2 humidified atmosphere. Cells were routinely tested for mycoplasma contamination.

SGs were induced with 0.5 mM sodium arsenite (Sigma) for 30 min at 37°C.

For inhibition and reversibility experiments (Figs. 3 *B–E*), 2.5 μM of FK506 (Sigma F4679) was added to the cell culture medium.

Plasmids

All constructs were subcloned into pcDNA 3.1 plasmid (Invitrogen). The plasmids pcDNA3.1-F36M-FKBP(Fm)-emGFP-hFt, Fm-mCh-hFt, and

pcDNA3.1–Fm–hFt were previously described (42). The plasmid pcDNA3.1–Fm–MCP–hFt was obtained by replacing the emGFP coding sequence (CDS) between XhoI and BamHI restriction sites in pcDNA3.1–Fm–emGFP–hFt by a CDS encoding a tandem of two MS2-coat proteins (MCP). We used a tandem to enhance binding to MS2 stem loops (44). All three aforementioned plasmids contain a 6xHis sequence. RNA-MS2 was expressed from the plasmid pcDNA3.1–4xMS2, which was obtained by inserting the iRFP CDS in the pcDNA3.1 backbone along with a tandem of four MS2 stem loops in the 3′UTR.

The plasmid for cytoplasmic poly(A)-binding protein (PABP-GFP) expression is a gift from M. W. Hentze (45).

Transfection

For live experiments, HeLa cells were cultured on 35-mm μ-dishes with polymer coverslip bottom (ibidi, 1.5×10^5 cells/μ-dish). For other experiments, HeLa cells and HEK-293 cells were cultured on 22 × 22 mm glass coverslips (VWR) in 6-well plates (Falcon, 3.5×10^5 cells/well). 24 h after seeding, transient transfection using Lipofectamine 2000 (Invitrogen) was carried out according to the manufacturer's protocol. For live experiments, cells were transfected with a 1:1 ratio of pcDNA3.1–Fm–MCP–hFt and pcDNA3.1–Fm–emGFP–hFt (800 ng total per μ-dish) and 20 ng of pcDNA3.1–4xMS2. For other experiments, cells were transfected with a 1:0.7:0.3 ratio of pcDNA3.1–Fm–MCP–hFt, pcDNA3.1–Fm–emGFP–hFt and pcDNA3.1–Fm–hFt (2 μg total per well) and 50 ng (low RNA), 250 ng (high RNA), or indicated amount (Fig. S2 *B*) of pcDNA3.1–4xMS2. For PABP-GFP co-transfection experiment, the same plasmid ratio was transfected, with Fm-mCh-hFt instead of Fm-emGFP-hFt, along with 500 ng of the PABP-GFP plasmid.

Single-molecule fluorescence in situ hybridization (smFISH)

Single RNA molecule detection was performed according to the previously described smiFISH (single-molecule inexpensive FISH) method (46). For each target RNA (RNA-MS2, β-actin mRNA, and NORAD lncRNA), a set of 24 primary probes, composed of a distinct sequence and a common FLAP sequence (TTACACTCGGACCTCGTCGACATGCATT), was designed with the Oligostan R script (46). The primary probes and the Cy3 FLAP probe (sequences in the Table S1) were purchased from Integrated DNA Technologies. An equimolar mixture of the 24 primary probes (initial concentration of 100 μM) was prepared and diluted five times in TE buffer, for a final concentration of individual probes of 0.833 μM.

24 h after transfection, cells were fixed in 4% paraformaldehyde (PFA) for 20 min at RT, and permeabilized with 70% ethanol in phosphate buffer saline (PBS) at 4°C overnight. They were then washed once with PBS and incubated for 15 min at RT in 15% formamide freshly prepared in saline-sodium citrate (SSC) buffer. Primary and secondary probes were prehybridized by incubating 2 μL of the gene-specific probe set, 1 μL of the Cy3 FLAP probe, 1 μL of NEBuffer 3 and 6 μL of water, for 3 min at 85°C, 3 min at 65°C, and 5 min at 25°C, successively. Then, two mixes were prepared (quantities are given for six coverslips): Mix 1 contained 15 μL of 20x SSC buffer, 5.1 μL of 20 μg/μl *E. coli* tRNA (Merck 10109541001), 45 μL of 100% formamide (Merck F9037), 6 μL of the prehybridized probes, and 78.9 μL of water; Mix 2 contained 3 μL of 20 mg/mL Molecular Biology Grade BSA (NEB B9000S), 3 μL of 200 mM VRC (Merck R3380), 63.6 μL of 50% dextran sulfate (Merck S4031), and 80.4 μL of water. Both mixes were vortexed together, and 50 μL of the mixture was deposited on each coverslip before hybridization overnight at 37°C in a humidity chamber (a 10-cm Petri dish containing a 3.5-cm Petri dish filled with 1 mL of 15% formamide in SSC buffer). The next day coverslips were washed twice for 30 min at 37°C in 15% formamide in SSC buffer and rinsed twice in PBS. They were then either mounted with VECTASHIELD mounting medium containing DAPI (Vector Laboratories, H-1200) or processed through immunofluorescence steps.

Immunofluorescence

Cells were permeabilized with PBS 0.1% Triton X-100 for 10 min at RT, washed twice with PBS at RT, incubated with the primary antibody, washed three times with PBS at RT for 5 min, incubated with the secondary antibody, washed three times with PBS at RT for 5 min, and finally mounted with VECTASHIELD mounting medium (Vector Laboratories, H-1000). Primary antibodies were rabbit antibodies against DDX6 (Novus NB200-192, 1:1000 dilution), rabbit antibodies against ATXN2L (Bethyl A301-370A, 1:500 dilution), and rabbit antibodies against MCP (Merck ABE76-I, 1:333 dilution) diluted in PBS 0.1% BSA. The secondary antibody was F (ab')2-Goat anti-Rabbit IgG conjugated with Alexa Fluor 350 dye (Thermo Fisher Scientific A-11069, 1:500 dilution).

Imaging

For live experiments, cells were imaged on a Zeiss LSM 710 META laser scanning confocal microscope using an ×63 oil-immersion objective (PlanApochromatic, numerical aperture (NA) 1.4), at 37°C in a 5% CO_2 humidified atmosphere, either starting 8 h after transfection (ArtiG formation) or 24 h after transfection (ArtiG dissolution). Microscope hardware and image acquisition were controlled with LSM Software Zen 2012. Images were analyzed using Fiji (47).

For smFISH experiments, cells were imaged by epifluorescence microscopy performed on an inverted Zeiss Z1 microscope equipped with a motorized stage using a ×63 (NA 1.32) oil-immersion objective. Images were processed with open-source softwares Fiji and Icy (47,48).

Fluorescence recovery after photobleaching experiments

Fluorescence recovery after photobleaching (FRAP) experiments on ArtiG condensates in live HeLa cells were performed starting approximately 20 h after transfection. Bleaching experiments were performed in a humidified chamber maintained at 37°C and 5% CO_2, which was mounted on a Zeiss LSM 710 META laser scanning confocal microscope (using an 63x (NA 1.4) oil-immersion objective) and operated with the LSM Zen 2012 software. Each condensate was scanned 10 times to establish the average level of initial fluorescence, then bleached using 6 to 10 iterations at 100% 488-nm laser intensity. Subsequently, the fluorescence recovery was monitored using one acquisition per second (512*512 pixel images) for at least 120 s. The region of interest was circular for ArtiG^{emGFP} and ArtiG$^{emGFP/MCP}$, and traced by free-hand selection for the anisotropic ArtiG$^{emGFP/MCP/RNA}$. The average size of the bleached condensates was 2.75 μm ($\pm$1.25 μm). FRAP data analysis and fitting of the recovery curves were performed with MATLAB (Mathworks). To determine spatiotemporal FRAP patterns, kymographs were generated by measuring fluorescence evolution as a function of time across a line of interest, using Fiji.

Western blotting

24 h after transfection, cells were lysed in Laemmli 1X buffer. Proteins were denatured at 100°C for 5 min. After centrifugation at 15,000 *g* for 10 min at 4°C, soluble proteins were quantified using the Coomassie protein assay (Thermo Scientific). 25 μg of proteins were separated on a NuPAGE 4%–12% gel (Invitrogen, Thermo Fisher Scientific) and transferred to an Optitran BA-S83 nitrocellulose membrane (GE Healthcare Life Science). After blockage in PBS with 5% nonfat milk for 30 min, the membrane was incubated with the primary antibody (6x-His Tag Monoclonal Mouse Antibody, Thermo Fisher Scientific MA1-21315; or S6 Ribosomal Protein

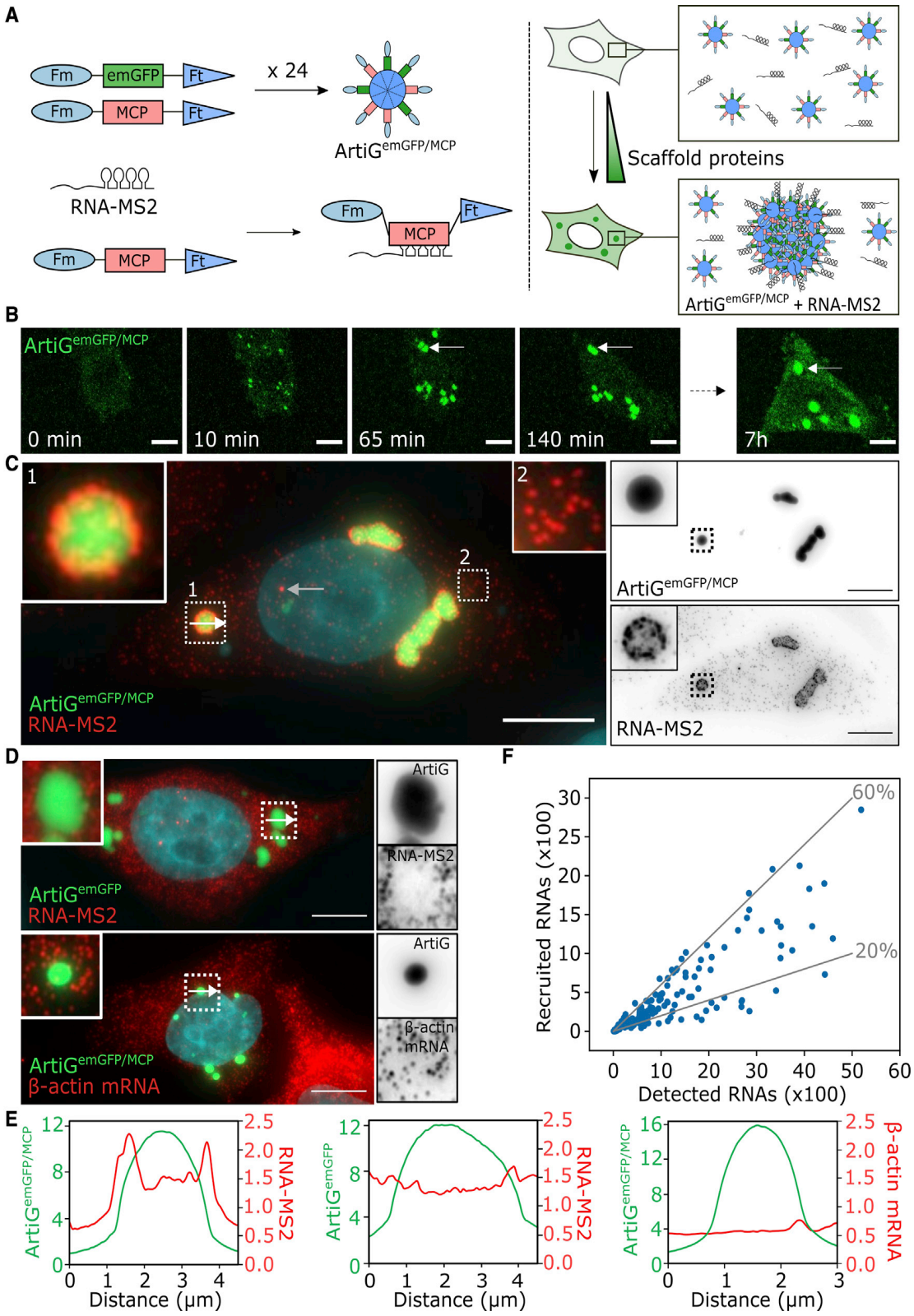

FIGURE 1 ArtiG^{MCP} condensates recruit a specific exogenous RNA. (*A*) Schematic of the ArtiG$^{emGFP/MCP}$ formation (Fm = F36M-FKBP, MCP = MS2 coat protein, Ft = ferritin, ArtiG = ArtiGranule). ArtiG$^{emGFP/MCP}$ form by LLPS driven by the homodimerization of Fm around ferritin nanocages. MCP protein enables the recruitment of RNA-MS2 molecules to the condensates. (*B*) Time-lapse confocal imaging of the formation of ArtiG$^{emGFP/MCP}$ in HeLa cells starting 8 h after transfection with plasmids Fm-emGFP-Ft and Fm-MCP-Ft (1:1 plasmid ratio). The white arrow highlights a coalescence event. Scale bar, 10 μm. (*C*) Epifluorescence imaging of ArtiG$^{emGFP/MCP}$ (green) and RNA-MS2 (red). Cells were fixed 24 h after transfection of scaffold and RNA-MS2 plasmids (low RNA condition in the methods, i.e., 50 ng RNA-MS2). Nuclei were stained with DAPI (blue in merge). The zoom in insert 1 shows the recruitment of RNA-MS2 around an ArtiG$^{emGFP/MCP}$ condensate. Insert 2 shows isolated RNA-MS2 molecules. The white arrow indicates where the intensity profile in (*E*) (left panel) was plotted. The gray arrow highlights a transcription focus. On the right panel, grayscale images correspond to separate channels. Scale bar, 10 μm. (*D*) Epifluorescence imaging of ArtiG^{emGFP} (green) and RNA-MS2 (upper panel) or *β*-actin mRNA (lower panel) (red). The white arrows

(legend continued on next page)

Rabbit mAb, Cell Signaling 2217) overnight at 4°C. Then the membrane was washed five times for 5 min with PBS, incubated for 30 min in PBS with 5% nonfat milk and then for 1 h at RT with horseradish peroxidase-conjugated secondary anti-mouse antibody (1:10,000 dilution in PBS with 5% nonfat milk, Jackson Immunoresearch Laboratories, Anti-Mouse 115,035-003 or Anti-Rabbit 111,035-003), and washed again. Proteins were detected with the chemiluminescence detection reagent Perkin Western Lightning plus ECL (PerkinElmer) and visualized using a radiology film processor (Curix 60, AGFA).

Data analysis

Detection and counting of RNA molecules were performed using version 0.4.0 of Python package Big-FISH (https://github.com/fish-quant/big-fish) (49). After nucleus segmentation from the DAPI channel, cells were segmented from the Cy3 FISH channel signal with a watershed algorithm. To detect RNA molecules, a Laplacian of Gaussian filter was applied to accentuate the spots signal and smooth the background. Then a maximum filter was applied, and local maxima were defined as pixels whose values were not modified by the filter. Local maxima under a threshold (determined by a function of Big-FISH) were considered as background noise and removed, and for each remaining maximum, single point coordinates were extracted. The next step was to detect maxima that could be clusters of RNA molecules and estimate the number of RNAs in those clusters. To do so, the background noise was first removed using a gaussian filter estimation of the background. Then the median spot intensity was computed, set as reference for a single RNA molecule and fitted with a gaussian function. Brighter spots were considered as clusters of RNAs, and the number of RNA molecules in each cluster was estimated based on the single RNA reference intensity.

To count the number of RNAs recruited on condensates in individual cells, a binary mask was first created on the emGFP channel (ArtiGs) using a manually set threshold. RNAs were considered in the condensates if their coordinates were within the mask coordinates.

For the analysis of RNA depletion at the vicinity of condensates (Figs. 2 and S3), first the binary mask on the emGFP channel was built as previously. Then it was repeatedly expanded by 5 pixels, and RNA molecules in the mask were counted at each step, which enabled the calculation of both the number and the density of RNA molecules in the last incremented area.

Condensate sizes were measured using Icy spot detector (Undecimated Wavelet Transform detector) (50). A lower size limit of 400 nm, corresponding to the diffraction limit of the microscope, was applied to exclude the condensates whose size could not be significantly measured. When close condensates were not discriminated, the detected regions of interest were adjusted manually. In Fig. 5, the size of individual condensates within intertwining clusters that were impossible to quantify were excluded from the statistics of size. For the correlation between condensate size and surface RNA density, the exterior surface was calculated from the condensate maximum projection. Then, for each cell, the sum of the surface of all condensates was calculated and used to determine the mean RNA density at the condensate surface (ratio of the total number of recruited RNAs to the total condensate surface).

Formatting of cell images was performed using the open-source software Fiji (47). For Figs. 2 and S3, the RNA coordinates were first saved from the Python workflow and then opened on Fiji. Graphics were generated using the shiny app PlotsOfData (51) (plots in Figs. 4 *B*, *D*, and 5 *A*) and OriginPro (OriginLab). For all violin plots, circles correspond to the mean. Schemas (Figs. 1 *A* and 5 *D*) were drawn with the open-source vector graphics editor Inkscape.

Statistical analysis

For Fig. 3 *C*, Student's t-tests (parametric test to compare two observed means) were performed using the *ttest2* MATLAB function (MathWorks). For Fig. 5 *A*, Wilcoxon rank-sum tests (nonparametric test to compare two distributions) were performed using the *ranksum* MATLAB function (MathWorks). For Fig. 5 *C*, Pearson's chi-squared test (nonparametric test for nominal variables) was performed using the Python's chi2_contingency function.

RESULTS

Reconstitution of RNA-protein condensates in human cells

Our first goal was to engineer artificial RNA-protein condensates that assemble through LLPS into cells. Our design combined two parts: a scaffold used to trigger the formation of protein condensates and a grafted RNA-binding domain to recruit specific RNA sequences (Fig. 1 *A*). As protein scaffold, we used ArtiGs that form liquid protein condensates in a concentration-dependent manner through weak multivalent interactions (42). The ArtiG scaffold developed previously was fused to a Pumilio-binding domain that recruits a large number of endogenous Pumilio RNA targets (42). To restrict the targeting to one single RNA species, we chose an orthogonal RNA-binding domain, the MS2-coat protein (MCP), that recognizes specific MS2 stem loops. The resulting plasmid construct, Fm-MCP-Ft, consisted of the fusion of an oligomeric ferritin (Ft) to MCP and a self-interacting domain F36M-FKBP (Fm), which spontaneously dimerizes without the need of a chemically induced dimerization molecule such as rapamycin (Fig. 1 *A*) (52).

In order to monitor condensate formation in cells, we co-transfected HeLa cells with the multivalent MCP self-interacting scaffold Fm-MCP-Ft, and Fm-emGFP-Ft as a fluorescent tracer. Live confocal imaging performed 8 h after transfection showed that, initially, emGFP fluorescence at low expression level was diffuse in the cytoplasm. As Fm-emGFP-Ft expression increased, several bright fluorescent bodies nucleated throughout the cytoplasm and grew to reach a micrometric size within an hour (Fig. 1 *B*). The emGFP-containing condensates, hereafter called ArtiG$^{emGFP/MCP}$, were very mobile and rapidly grew as a function of time. When two proximal condensates docked, they tended to coalesce and to relax into large spherical bodies, as generally observed for endogenous liquid-like condensates (Fig. 1 *B*, white arrow, and Fig. S1 *A*). To reconstitute RNA-protein condensates using ArtiG$^{emGFP/MCP}$, we first generated a plasmid to express a

indicate where the intensity profiles in (*E*) (middle and right panels) were plotted. Scale bar, 10 μm. (*E*) Intensity profiles across ArtiG condensates (white arrows in *C* and *D*). (*F*) Number of RNA-MS2 molecules recruited at the surface of ArtiGemGFP/MCP as a function of the total number of molecules detected in the cell, with each dot representing one cell (N = 140 from two independent experiments). Gray lines represent 20% and 60% recruitment. To see figure in color, go online.

mRNA equipped with MS2 stem loops in its 3′UTR (1250 nt long, called hereafter RNA-MS2, Fig. 1 *A*). We co-transfected this plasmid (RNA low condition in the methods, i.e., 50 ng) and the plasmids expressing the ArtiG$^{emGFP/MCP}$ scaffold (2 μg) and fixed the cells 24 h after transfection. We next monitored the intracellular localization of RNA-MS2 using smFISH (46). The majority of cells harbored micrometric ArtiG$^{emGFP/MCP}$ condensates in the cytoplasm, surrounded with a striking Cy3-FISH signal, indicating a localization of RNA-MS2 molecules at the condensates' surface (Fig. 1 *C*, insert 1, and Fig. 1 *E*, left panel). These RNAs were either present as isolated molecules or, when the number of recruited molecules was high, were more homogeneously distributed around the condensates, into a corona made of a single RNA molecule layer (see other examples in Fig. S1 *B*). Discrete Cy3 dots corresponding to individual mRNAs were also found dispersed throughout the cytosolic space (Fig. 1 *C*, insert 2), as well as brighter spots in the nucleus corresponding to transcription foci (Fig. 1 *C*, gray arrow). To verify if the RNA corona may result from some enrichment of MCP at the surface of the condensates, we performed an immunostaining of MCP. The antibody labeled the entirety of ArtiG$^{emGFP/MCP}$, indicating a homogeneous distribution of MCP within the condensates (Fig. S1 *C*). The efficient penetration of antibodies into the condensates also suggested that the smaller FISH probes should penetrate as well. Accordingly, rare RNA-MS2 molecules were observed inside condensates, as illustrated in Fig. S1 *D*, where an RNA-MS2 molecule seems to have been trapped during the coalescence of two condensates. Altogether, these results indicate that, despite the presence of MCP within the condensates, the RNA-MS2 molecules are restricted to their surface.

Next, to assess the specificity of RNA recruitment on the ArtiG$^{emGFP/MCP}$, we investigated the localization of RNA-MS2 in cells containing ArtiG^{emGFP} (devoid of the MCP domain) and found a complete absence of RNA-MS2 at the condensate periphery (Fig. 1 *D*, upper panel, and Fig. 1 *E*, middle panel). Experiments carried out in HEK293 cells showed the same results (Figs. S1 *E* and S1 *G* upper and middle panels). Similarly, ArtiG$^{emGFP/MCP}$ did not show any recruitment of the endogenous β-actin mRNA and NORAD lncRNA (devoid of MS2) (Fig. 1 *D*, lower panel, Fig. 1 *E*, right panel, Figs. S1 *F* and S1 *G*, lower panel). To investigate more broadly the specificity of the RNA recruitment, we co-transfected the plasmids of our artificial condensates with or without RNA-MS2 and with a PABP-GFP plasmid. PABP (poly-A binding protein), by binding to polyA tails, reports on all polyadenylated RNAs recruited to our condensates. We previously assessed this strategy using ArtiG^{PUMilio} condensates and found that those condensates recruited polyadenylated RNAs (42). Here, we found that ArtiG$^{mCh/MCP/RNA}$ also displayed a strong coronal PABP-GFP signal, which was not observed around control ArtiG^{mCh} and ArtiG$^{mCh/MCP}$ (Fig. S2 *A*). These data suggest that MCP does not significantly interact with other cellular polyadenylated RNAs than RNA-MS2, thus confirming the specificity of ArtiG$^{emGFP/MCP}$ for RNA-MS2. As an additional control, we verified by Western blotting that the expression level of the scaffold proteins is not altered by the co-transfection of RNA-MS2 (Fig. S2 *B*). When quantifying the total number of RNA-MS2 molecules dispersed in the cytoplasm and localized on ArtiG$^{emGFP/MCP}$, we found that 34% ± 19% of the cytoplasmic mRNAs were specifically recruited at the condensate surface (mean of 430 recruited RNAs and 1200 dispersed RNAs per cell) (Fig. 1 *F*). Altogether, these data show that ArtiG$^{emGFP/MCP}$ act as condensates localizing specific RNAs on their surfaces (ArtiG$^{emGFP/MCP/RNA}$).

RNAs modify the material properties of ArtiG condensates

The observation that RNAs only localized to the surface and not within the core of the condensates could be a consequence of the specific material properties of the condensates. To further characterize this aspect, we performed FRAP in cells expressing ArtiG condensates (ArtiG^{emGFP}, ArtiG$^{emGFP/MCP}$ without and with RNA-MS2 expression). In ArtiG^{emGFP} condensates, about 43% of the signal recovered with a half-recovery time of about 7 s (Fig. 2 *A* and *B*). This timescale reflects binding/unbinding states of the mobile fraction of the condensed phase, which dynamically exchanges with the cytosolic diluted phase. ArtiG$^{emGFP/MCP}$ (without RNA-MS2 transfection) displayed a reduced recovery amplitude with a signal that kept slowly increasing over 2 min without completely reaching a plateau, indicating that the mobile fraction reorganized and continuously exchanged with the cytosol at a minute scale. This indicates that MCP proteins increased the condensate viscosity (Figs. 2 *A–B*). In contrast, in the presence of RNA-MS2, ArtiG$^{emGFP/MCP/RNA}$ recovery rapidly reached a plateau regime corresponding to about 20% recovery. The initial fast recovery of those ArtiG$^{emGFP/MCP/RNA}$ lasted less than 1 s in most FRAP experiments, reflecting the rapid diffusion of the protein scaffold. Overall, the recovery curves of ArtiG$^{emGFP/MCP}$ with RNA are typical of gel-like phases, with the RNA-MS2 inducing a hardening of the condensates (Figs. 2 *A* and *B*). This hardening could in turn explain why RNA-MS2 molecules remain at the condensates' surface.

Cytosolic target RNAs are depleted at the vicinity of large condensates

As our data showed a robust recruitment of RNAs at the surface of ArtiG$^{emGFP/MCP}$ condensates, we next investigated whether this recruitment impacted the distribution of RNAs in the cytoplasm. Interestingly, we observed a depletion of cytoplasmic MS2-RNAs close to ArtiG$^{emGFP/MCP/RNA}$

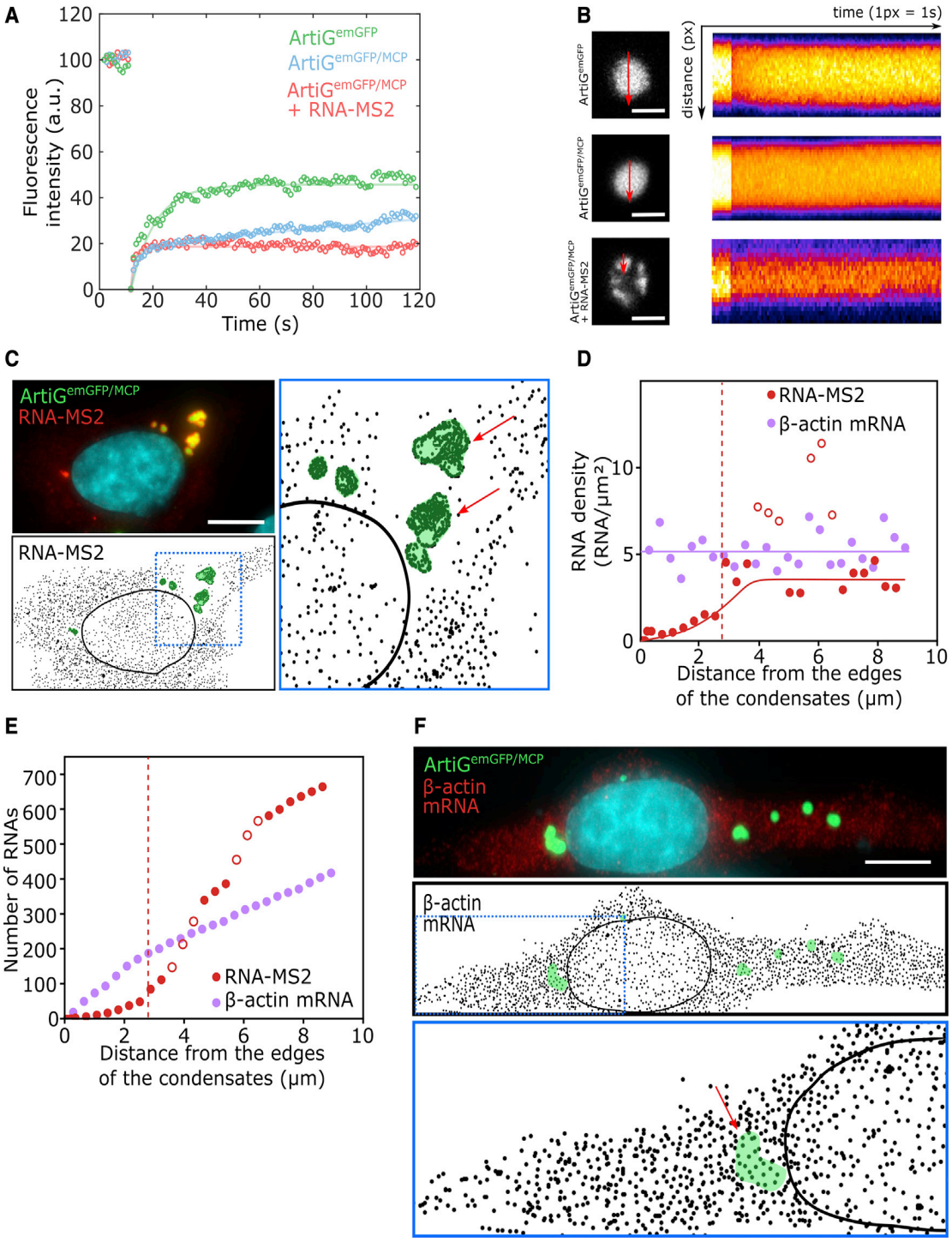

FIGURE 2 Fluorescence recovery after photobleaching and depletion of RNA-MS2 at the vicinity of ArtiG$^{emGFP/MCP}$ condensates. *(A)* Fluorescence recovery after photobleaching performed on ArtiG^{emGFP} (green, six cells), ArtiG$^{emGFP/MCP}$ (blue, eight cells), and ArtiG$^{emGFP/MCP/RNA}$ (red, eight cells). Scale bar, 2 µm. *(B)* Kymograph representation of three representative ArtiGs analyzed in *(A)*. *(C)* Upper panel: epifluorescence imaging of ArtiG$^{emGFP/MCP}$ (green) and RNA-MS2 (red) in a HeLa cell displaying a depletion of RNA-MS2 around the condensates. Scale bar, 10 µm. Lower panel: Binary mask of the RNA-MS2 molecules whose coordinates have been acquired as described in the methods. Isolated dots are single RNA molecules, and clustered dots overlap with ArtiG$^{emGFP/MCP}$ condensates (highlighted in green). The black solid line delineates the nucleus. The blue square is enlarged in the right panel. The red arrows point to the ArtiGs analyzed in *(D)* and *(E)*. *(D)* Density of RNA-MS2 (red) and *β*-actin mRNA (violet) as a function of the distance from the ArtiG$^{emGFP/MCP}$ condensates indicated by red arrows in *(C)* and *(F)*. *β*-actin mRNA density is constant, whereas RNA-MS2 density reaches a plateau after the depletion area indicated by the red dashed line. Empty red dots correspond to RNA densities when crossing neighboring condensates. *(E)* Cumulative representation of the data shown in *(D)*. *(F)* Upper panel: Epifluorescence imaging of ArtiG$^{emGFP/MCP}$ (green) and *β*-actin mRNAs (red). Scale bar, 10 µm. Middle and lower panels: Binary mask of the *β*-actin mRNAs, as in *(C)*. To see figure in color, go online.

condensates (Figs. 2 *C* and S3 *A*). This depletion was readily visible around large condensate clusters recruiting a high number of RNA molecules. On the examples shown in Figs. 2 *C* and S3 *A*, we quantified the density of RNAs as a function of the distance to the condensate edges. RNA density was almost zero in a large area ranging from the immediate vicinity of the cluster up to 3 μm from the condensate border. Then, RNA density increased until reaching a plateau at a distance of about 4 μm, with a value corresponding to the mean cytoplasmic RNA concentration of the cell (Fig. 2 *D*, red dots, and Fig. S3 *B*). The values over the plateau (Fig. 2 *D*, empty red dots) result from the analyzed area occasionally including neighboring condensates. Likewise, plotting the cumulative number of RNAs outside the condensates as a function of the distance to the condensates' edges showed first a very slow increase up to 3 μm from the condensates' edges (Fig. 2 *E*, red dots, and Fig S3 *C*). Beyond this depletion area, the increase sharpened with a steady slope corresponding to an even cytoplasmic RNA concentration, except when including neighboring condensates (Fig. 2 *E*, empty red dots). For comparison, we quantified the spatial distribution of β-actin mRNAs, which do not bind to ArtiG^{MCP}. We found a total absence of depletion of β-actin mRNAs around ArtiG clusters (Fig. 2 *F*), with an even RNA density around the condensates (Figs. 2 *D* and *E*, violet dots). Altogether, these results suggest that the RNA depletion was linked to the specific recruitment of RNA-MS2 on condensates rather than from potential nonspecific steric exclusion at the vicinity of condensates.

Artificial condensates are biochemically distinct from endogenous condensates

In a cellular context, biologically distinct RNP condensates that form in the same cytoplasm can interact with each other through shared proteins and RNAs, as described for PBs and SGs (53) or PBs and U-bodies (54). Therefore, we next sought to investigate whether the local enrichment of mRNAs on ArtiG$^{emGFP/MCP}$ may induce interactions with other cytoplasmic RNP granules. To this aim, we looked at the presence of PBs by immunostaining 24 h after transfection, using DDX6 as a PB marker. Our observations showed no particular physical proximity or docking between the two condensates (Fig. 3 *A*, left panel). Similarly, there was no proximity between ArtiG$^{emGFP/MCP}$ and SGs, using ATXN2L as an SG marker (Fig. S4 *A*). Moreover, no docking of ArtiG$^{emGFP/MCP/RNA}$ with SGs was observed after SG induction with an arsenite stress (Fig. 3 *A*, right panel). These results suggest that ArtiG$^{emGFP/MCP/RNA}$ is biochemically distinct and physically independent from both PBs and SGs.

Controlled dissolution of artificial condensates

Recent studies suggest that the formation and stability of biological condensates are tightly regulated by multiple stimuli, including posttranslational modifications, biochemical reactions, or physical parameters such as temperature or osmotic pressure changes (55,56). By design, the formation and stability of the ArtiG$^{emGFP/MCP}$ condensates are driven by multivalent interactions mediated by the Fm-Fm homodimer, and these interactions could in principle be disrupted by the addition of a chemical competitor, FK506 (52). We therefore assessed if FK506 addition could first prevent condensate formation and secondly dissolve already formed condensates (Fig. 3 *B*). In the absence of FK506, the majority of transfected cells exhibited ArtiG$^{emGFP/MCP/RNA}$ condensates (93% after 24 h of expression, Fig. 3 *C*). This percentage dropped to 15% upon addition of FK506 at the time of transfection, with the majority of cells displaying a diffuse emGFP fluorescence and a homogeneous MS2-RNA distribution in the cytosol (Fig. 3 *D*). Thus, FK506 efficiently inhibited the formation of the condensates. In a second experimental design, we examined the dissolution of fully formed ArtiGs by adding FK506 24 h after transfection (Fig. 3 *B*). After 2 h of FK506 incubation, we found that the majority of cells lacked ArtiGs and displayed diffuse emGFP with Cy3-labeled MS2-RNAs distributed throughout the cytoplasm (70%, Fig. 3 *C*). Thus, FK506 treatment induced the dissolution of the majority of preformed ArtiG$^{emGFP/MCP/RNA}$ condensates. To further characterize FK506 effect, we examined the timescale of dissolution using live confocal microscopy. Upon addition of FK506, some cells exhibited condensates dissolving within few seconds (Fig. 3 *E*), whereas in others, dissolution took up to 30 min (Fig. S4 *B*). These dissolutions were accompanied with a strong increase of the cytosolic fluorescence signal, corresponding to the release of the ArtiG scaffold (Fig. 3 *F*). We also observed a few cells with smaller condensates and a stronger cytosolic fluorescence, corresponding to incomplete condensate dissolution, in agreement with the observation of residual condensates in fixed cells (Fig. S4 *C*). Altogether, our data showed that pretreatment with the FK506 binding competitor of Fm proteins provides a means of preventing the formation of the ArtiG condensates, whereas it globally induces their disassembly when they are already formed. Our system thus allows for a controlled inhibition and disassembly (by adding FK506) of artificial condensates in living cells.

Linking condensate size and number of recruited RNAs

Determining how the primary constituents of condensates set the variety of condensate size and morphology naturally observed in cells remains very complex, since RNAs and proteins establish a large network of interactions. The ArtiG condensates potentially provide an important simplification to this problem, as only one RNA species is recruited to the condensates. We could therefore analyze how RNA contributes to ArtiG$^{emGFP/MCP/RNA}$ condensate morphology, by quantifying the recruitment of MS2-RNAs in condensates and condensate size in each cell. Within

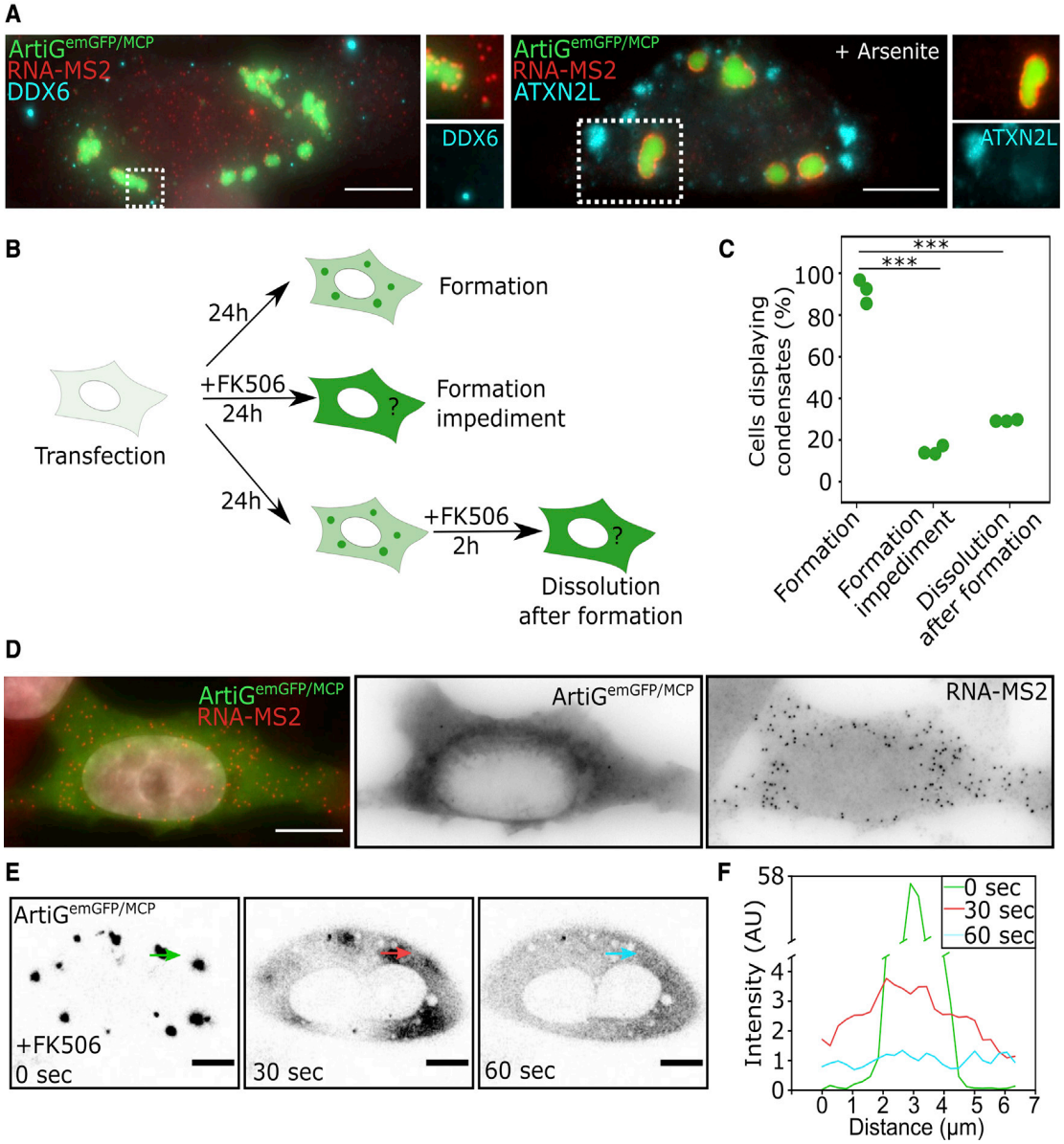

FIGURE 3 Absence of interaction of ArtiG$^{emGFP/MCP}$ with endogenous RNP granules, inhibition and reversibility. (*A*) Epifluorescence imaging of ArtiG$^{emGFP/MCP}$ (green) and RNA-MS2 (red) in HeLa cells, after immunostaining of DDX6 (blue) as a PB marker (left panel) or ATXN2L (blue) as an SG marker (right panel). In the right panel, SGs were induced with arsenite for 30 min. White dashed rectangles delineate the images zoomed on the right. Scale bar, 10 µm. (*B*) Experimental design to test the inhibition and reversibility of ArtiG$^{emGFP/MCP}$ formed in the presence of RNA-MS2, using FK506 in HeLa cells. FK506 was either added right after transfection to prevent condensation, or 24 h after transfection to dissolve the condensates. (*C*) Percentage of transfected cells displaying ArtiG$^{emGFP/MCP}$ condensates in the absence of FK506 (Formation), when adding FK506 at the time of transfection (Formation impediment) or 24 h later for 2 h (Dissolution after formation). Differences between conditions with and without FK506 were statistically significant (p-values $< 10^{-4}$ using a Student's t-test). (*D*) Epifluorescence imaging of ArtiG$^{emGFP/MCP}$ (green) and RNA-MS2 (red) after condensate dissolution with FK506. Nuclei were stained with DAPI (blue). Scale bar, 10 µm. (*E*) Confocal live imaging of ArtiG$^{emGFP/MCP}$ dissolution. FK506 was added at time zero. Colored arrows indicate where the intensity profiles in (*F*) were plotted. Scale bar = 10 µm. (*F*) emGFP intensity profile across an ArtiG$^{emGFP/MCP}$ condensate over time (colored arrows in (*E*). To see figure in color, go online.

the same transfection experiment, the size and number of ArtiG$^{emGFP/MCP/RNA}$ condensates were heterogeneous between cells, with some cells exhibiting few condensates and others a larger number (Fig. 4 *A*). The distribution of the mean diameter of ArtiG condensates roughly ranged from 0.4 to 4 µm depending on the cell (mean ± SD = 1.1 ± 0.6 µm, coefficient of variation CV = 58%, Fig. 4 *B*, left panel). Although 75% of the cells had condensates with a mean diameter below 1.5 µm, we observed particularly large condensates, up to 4 µm in diameter, in the other cells. The number of condensates per cell was also very diverse (mean number = 33, CV = 116%, Fig. 4 *B*, right panel). Interestingly, condensate mean size per cell was inversely related to their number (Fig. 4 *C*). Indeed, cells displaying large condensates (diameter >1.5 µm) always had a limited number of them (<25). In contrast, a higher number of condensates in a cell (>25) was correlated with a mean diameter of the condensates below 1.5 µm. In

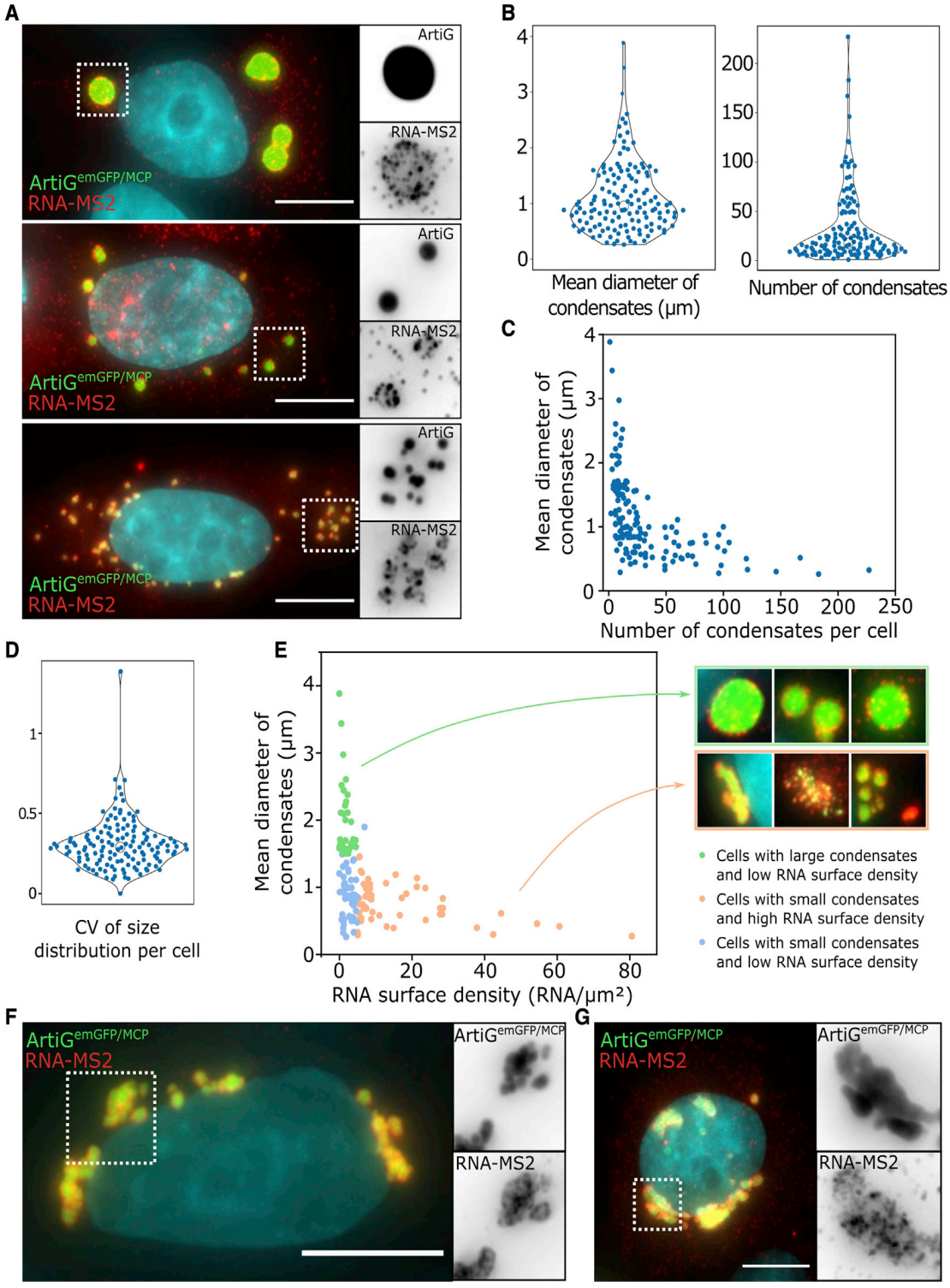

FIGURE 4 Heterogeneous morphology of ArtiG$^{emGFP/MCP}$ condensates. (*A*) Epifluorescence imaging of three HeLa cells displaying different sizes and numbers of ArtiG$^{emGFP/MCP}$ in the presence of RNA-MS2. Cells were fixed 24 h after transfection of scaffold and RNA-MS2 plasmids (low RNA condition in the methods, i.e., 50 ng RNA-MS2). Scale bar, 10 µm. (*B*) Distribution of the mean diameter of condensates per cell (left panel) and the number of condensates per cell (right panel), with each dot representing one cell (N = 140 from two independent experiments). (*C*) Mean diameter of the condensates as a function of the number of condensates. (*D*) Distribution of the coefficients of variation (CV) of the size distribution. (*E*) Mean diameter of the condensates as a function of RNA surface density. Green and orange dots highlight cells displaying a mean diameter above or below 1.5 µm, respectively, and an RNA surface density below or above 5 molecules/µm^2, respectively. Images on the right show representative examples of condensates for the green and orange cell categories. (*F* and *G*) Example of well-defined (*F*) and intertwining (*G*) condensate clusters. To see figure in color, go online.

contrast to the heterogeneity of condensates' size between cells, we found a homogeneity of size within a given cell (average CV = 30%, Fig. 4 *D*).

We next sought to examine whether there was a correlation between condensates' number and size, and RNA recruitment. To this aim, we computed, per cell, the density of RNAs recruited at the surface of ArtiG condensates and their mean diameter (Fig. 4 *E*). We could highlight two groups of cells. In cells displaying large condensates (mean diameter >1.5 μm, mean ± SD = 2.0 ± 0.6 μm), the RNA surface density was below 5 RNAs/μm^2 (mean = 2.0 RNAs/μm^2, Fig. 4 *E*, green dots). These condensates were generally spherical with a small number of RNAs at their periphery. In contrast, a higher RNA density (>5 RNAs/μm^2, mean = 16.0 RNA/μm^2) was associated with a mean diameter of ArtiG below 1.5 μm (mean ± SD = 0.79 ± 0.32 μm, Fig. 4 *E*, orange dots). In these cells, condensates were often found in close proximity to each other, forming cluster-like patterns (more than five condensates docking together) with RNA patches or corona separating individual condensates (Fig. 4 *F*). These clusters were reminiscent of coalescence events, but their high number suggested that the coalescence process was arrested, so that condensates did not relax into a sphere. We even observed a few cases where ArtiG$^{emGFP/MCP}$ and RNA molecules seemed intertwined, with frontiers between condensates becoming blurred and ArtiG$^{emGFP/MCP/RNA}$ losing its round shape (Fig. 4 *G*). To sum up, we found that all large spherical ArtiG condensates displayed few RNA molecules on their surfaces, whereas condensates with a high RNA surface density had a smaller size.

Evolution of condensate size and morphology as a function of RNA surface density

To refine our analysis of the role of RNA localization in the condensate morphology, we increased the expression of transcribed RNA-MS2 by transfecting a larger quantity of plasmids in cells (five-fold more, i.e., 250 ng). In this condition (RNA high) the mean number of RNA-MS2 transcripts per cell rose from about 1200 to around 2400, without affecting the expression of the ArtiG scaffold (Fig. S2 *B*). The mean number of RNA-MS2 recruited at the surface of the condensates rose from 430 to 1100 (Fig. 5 *A*, left panel). This was accompanied with changes in the condensate morphology. Firstly, the size of the condensates was drastically reduced compared to the RNA low condition (0.72 ± 0.32 μm instead of 1.26 ± 0.68 μm), and even more compared with conditions without RNA (Fig. 5 *A*, middle and right panels). This result is in line with our observation that higher RNA surface localization resulted in smaller condensates. Furthermore, in the RNA high condition, very few cells displayed large condensates (diameter >1.5 μm) (Fig. 5 *B*), whereas the incidence of cluster-like patterns was much higher: about 64% of cells in regard to 43% in the RNA low condition and 35% in the no RNA condition (Fig. 5 *C*). Among the clusters, condensate intertwining, which was a rare event in the low RNA condition (3.6%) and no RNA condition (4.6%), became more common (19%). Altogether these data confirm a direct relationship between RNA surface density and condensates' size and number.

DISCUSSION

RNA is more and more recognized as a driving force in cellular organization and functions. These polymers can interact and scaffold hundreds of proteins to generate high order organizations including RNP condensates. The first high-throughput biochemical studies of RNP condensates showed that their RNA and protein content is highly complex (57–60). Although these studies highlight that condensation is driven by the combination of multiple RNA-protein, protein-protein, and RNA-RNA interactions, the rules governing RNA and protein spatiotemporal co-assembly are still enigmatic. As a consequence, deciphering and manipulating RNP condensates in cellulo remains a difficult task. In this context, in vitro reconstitution using purified components has been a powerful strategy (11,22,25,61,62). Physicochemical parameters defining RNA polymers such as their length, chemical complexity, and sequence could thus be assessed in a reconstituted environment. Despite their obvious advantages, several limitations arose from these reductionist approaches. For instance, the physiological relevance of the protein concentration used in in vitro model condensates and their minimal composition can be questioned, as well as their simplified physicochemical environment compared with cells. Alternatively, the over-expression of recombinant proteins, often chosen among scaffolding proteins found to drive LLPS in test tube, was also widely used to identify the propensity of specific protein domains to undergo phase separation in a cellular environment (19,63,64). Complementary to these approaches, building RNP condensate mimics in cells using artificial condensates functionalized with a specific RBP (TIA-1, G3BP, or Pumilio) can be instrumental to establish a link between condensate biochemical functions and their material states, as illustrated by studies recapitulating the formation of physiological or pathological RNP condensates in cells (30,31,40,42). However, even with such engineered condensates, untangling the specific role of RNA from the large complex network of RBP-RNA interactions at work during condensate formation remains challenging (65–67). To overcome this limitation, our approach was to reconstitute in cells artificial RNP condensates recruiting a single RNA species, thus providing a unique system to question the link between RNA recruitment and condensate size.

Remarkably, the recruited RNA molecules localized at the condensates' surface, with two distinct patterns, either disperse or forming a corona around the condensates (Figs. 1 and S1). How do these patterns emerge from the

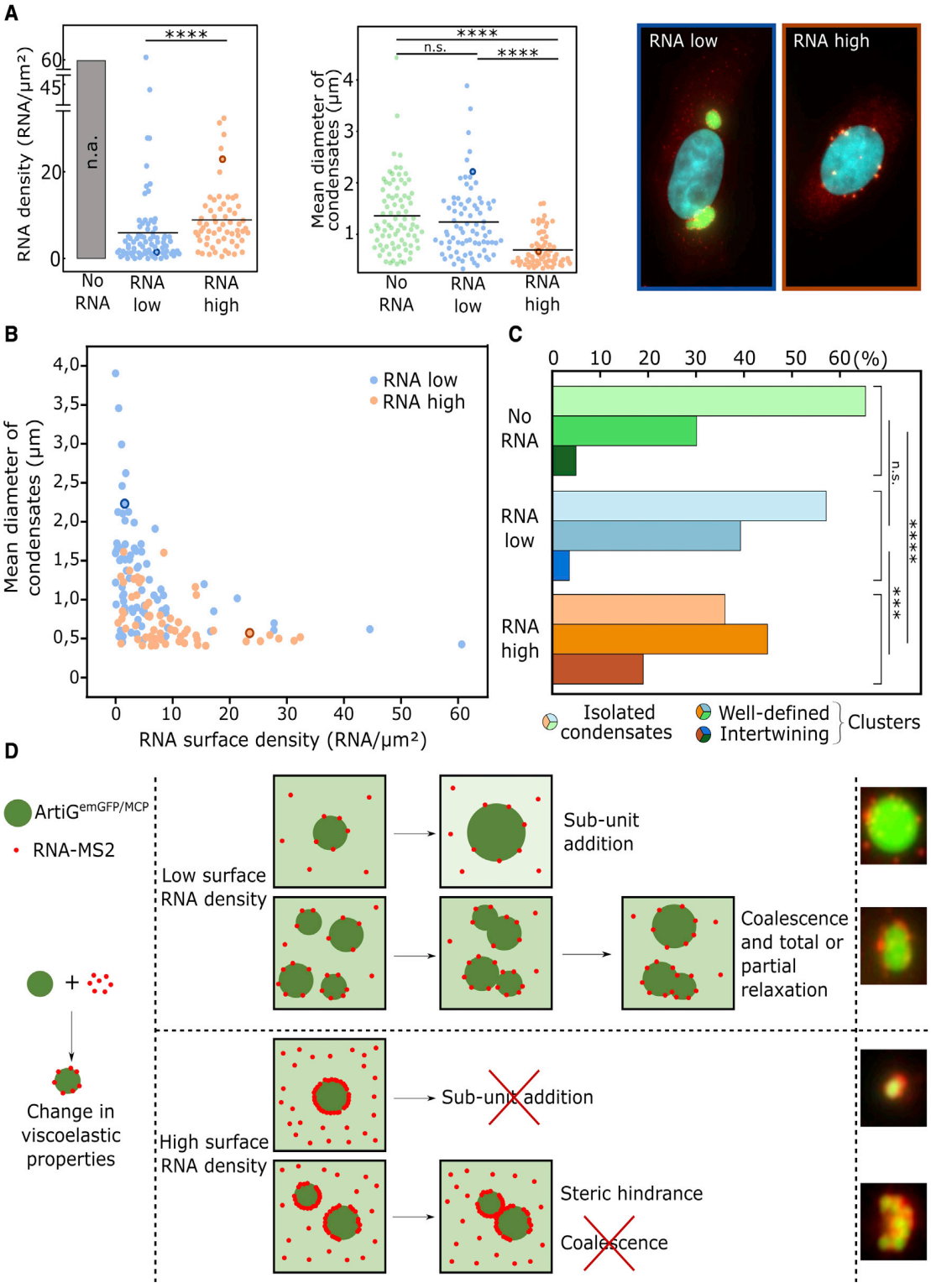

FIGURE 5 Impact of RNA density at the surface of condensates on condensate morphology. (*A*) Distribution of RNA-MS2 density at the surface of condensates (left panel) and of mean diameter of the condensates (middle panel) in no RNA, RNA low, and RNA high conditions, with each dot representing one cell (N = 82 for no RNA, N = 79 for RNA low, and N = 64 for RNA high conditions, each from two independent experiments). Differences between RNA low and RNA high conditions were statistically significant using a Wilcoxon rank-sum test (p-values < 10-5). Representative epifluorescence images for RNA low and RNA high conditions are shown on the right and correspond to the circled dots in the graphs. (*B*) Mean diameter of ArtiG$^{emGFP/MCP}$ in cells as a function of RNA-MS2 surface density in RNA low (blue dots) and RNA high (orange dots) conditions. (*C*) Percentage of cells with ArtiG$^{emGFP/MCP}$ that display isolated condensates, clusters of well-defined condensates, or intertwining condensates, in no RNA, low RNA, and high RNA conditions. Differences with and without RNA were statistically significant using a Pearson's chi-squared test (p-values < 10-6 and 10-4 for RNA low and RNA high, respectively). (*D*) Schematic model of the impact of surface RNA molecules on condensate growth, material properties, and coalescence. Illustrative examples of ArtiG$^{emGFP/MCP}$ (green) and RNA-MS2 (red) epifluorescence images are shown on the right. To see figure in color, go online.

interactions between ArtiG^{MCP} scaffolds and MS2-RNAs? Several in vitro studies and numerical simulations reported how multilayered organizations, such as core-shell droplets, assemble from ternary systems composed of protein-RNA interacting molecules (22,25,26,68–70). A possible mode of formation of these multiphase droplets results from competing intermolecular interactions between macromolecular constituents that drive differences in surface tension and coexisting liquid phases. In this regard, our RNP condensates differ from coexisting liquid phases that demix into core-shell droplets, since they generally displayed a single RNA molecule layer as a shell enveloping ArtiG condensates. Instead, the assembly pathway controlling the formation of condensates with an RNA corona could arise from a stepwise process: first, ArtiG^{MCP} scaffolds undergo LLPS, and subsequently, RNA molecules are recruited on the condensate surface, reaching a density that depends on the RNA expression level (Fig 5 *D*). Interestingly, the recruitment of RNA also changed the material properties of ArtiG$^{MCP/RNA}$, by hardening the condensate body, which can also explain why RNA-MS2 molecules remain at their surface (Figs. 2 *A* and *B*).

The robust formation of ArtiG condensates in cells provides a unique mean to examine basic questions such as how condensate size scales with RNA surface density. Indeed, the ability to count the RNA molecules recruited on ArtiGs allowed us to show that the RNA density at the surface of condensates was correlated to their size and number, with large condensates displaying only a few RNAs on their surface, whereas high RNA density always implied smaller and more numerous condensates. Furthermore, when we increased RNA expression in cells, and consequently RNA surface density on condensates, cells harbored smaller condensates, which supports a causal relationship between RNA surface density and condensate size.

Several examples in cell biology suggest the existence of a scaling of cellular organelles with cell volume, which could be understood if cells contain a limiting pool of structural components supporting the organelle assembly (9,71,72). In cells, native condensates such as PBs and PML nuclear bodies are generally found as submicrometric bodies that often do not grow over a certain size. This is generally in contradiction with the thermodynamical equilibrium picture of phase-separated systems predicting an evolution toward a single condensed phase coexisting with a dilute phase. Initial growth of phase-separated condensates generally occurs through subunit addition, and coarsening through coalescence or Ostwald ripening (73–75). Thus, a solution to regulate condensate size would be to tune one of these three pathways (subunit addition, coalescence, and Ostwald ripening), either through physicochemical parameters or by modifying interaction strengths and valences by biochemical reactions such as post-translational modifications (76,77). Recent theoretical studies suggest that both active and passive processes can be in play (78,79). For instance, it has been proposed that active processes within condensates could suppress Ostwald ripening and account for size selection (71,80–83). However, in the case of ArtiG$^{emGFP/MCP/RNA}$, the two main formation pathways are subunit addition and coalescence (Fig. 1 *B*). Client proteins acting like surfactants may reduce the energy required for the formation of an interface between the dense and dilute phase and lead to size-conserved multidroplet systems instead of the expected single large, condensed phase, with condensate size decreasing as a result of client concentration increasing (84). In this respect, the protein Ki-67, localized at the surface of chromosomes, may for instance form a steric barrier that prevents the chromosomes from collapsing into a single entity (85). A high surface charge density and thus a high electrostatic repulsion between biomolecular condensates may alter their propensity to fuse (86). In vitro observations of the co-assembly between RNA homopolymers and mRNAs showed multiphase assemblies, with RNAs localized at the droplet surface, suggesting that RNAs act as an interfacial shell stabilizing multiphase condensates (61). Thus, the biochemical and structural heterogeneity at the surface of condensates could also influence their stability. For instance in *C. elegans*, the adsorption of MEG-3 on PGL droplets drives the formation of a gel-like shell around a liquid core that eventually can stabilize P granules and trap RNAs (87,88). More precisely, MEG-3 clusters on P granules have been shown recently to behave like Pickering agents decreasing the surface tension of the P granules, slowing down their coarsening (89). These results remind us of our observations with ArtiGranules fused to Pumilio, as we showed that PBs docking at the surface of the condensates impacted their formation (42). Alternatively, a recent study explained how the RNA shell-forming domain of paraspeckles can modulate condensate shape and size and suggested a micellization-based model of assembly (90). Here we propose that the RNA present at the surface of ArtiG condensates cause a steric hindrance that may prevent the growth of condensates by both subunit addition and coalescence (Fig. 5 *D*). Additionally, the hardening of the condensate due to the presence of RNA could favor the arrested coalescence of the bodies and thus contribute to limit their growth during coarsening (Fig. 5 *D*). In this picture, RNAs, through their charges and length, could contribute to the colloidal stability of the condensates and thus regulate their size and number.

At a high RNA surface density, we found that ArtiG condensates can lose their sphericity and adopt a clustered morphology reminiscent of TIS granules (24). However, in contrast to TIS granules, where a skeleton made of RNA-RNA interactions between unstructured regions counterbalances the excess of surface energy generally driving fusion and relaxation, here RNAs at the condensate surface could impede coalescence by steric hindrance. We could also envision the existence of intermolecular interactions between RNAs that would bridge adjacent ArtiG condensates and enhance their stability.

Such an impact of surface RNA on condensate morphology may be relevant for native RNP condensates. Indeed, the spatiotemporal organization of RNAs at the surface of native condensates has recently been investigated using advanced imaging tools. For example, super-resolution imaging showed that the solid core of SGs is surrounded by a less concentrated RNA and protein layer (60,91). It has also been shown that RNAs exhibit diverse localization within PBs and at their surface (92). On SG or PB surfaces, RNAs can make transient contacts before stably associating inside the granules or leaving the granules for an alternative fate (92,93). Some of these RNAs are coding mRNAs, thus associating with ribosomes and other translation-related proteins when not in granules (94), whereas others are long noncoding RNAs with a regulatory function (92). These RNAs can partition bidirectionally between biologically different condensates (93,95). In the case of germ PBs, the association of the RNAs with the surface of the condensates can even be required for translation to happen (96). Along this line, our work suggests that localization of RNAs at the condensate surface could also feedback on condensate biogenesis.

In conclusion, our methodology to reconstitute biomolecular condensates in cells with controlled compositions and properties has proved powerful to reveal the role of surface RNA in condensate morphology and material properties. More generally, our study stresses the importance of an understudied aspect of condensates, which is the role of the biomolecules present at their surface, whether RNA or proteins. It illustrates how chemical and physical heterogeneities on condensate surface may determine granule morphology properties. Beyond this advance in the understanding of RNP condensate sizing, ArtiG-MCPs provide a powerful system, capable of recruiting any RNA of interest tagged with MS2. In addition, they can be chemically controlled to trigger their dissolution as well as to prevent their formation on demand. Due to its flexibility, we anticipate that our methodology will not only enable to address other basic biological issues in the future, but also be a means to engineer novel properties within cells.

DATA AVAILABILITY

All data are available from the corresponding authors upon request.

SUPPORTING MATERIAL

Supporting Material can be found online at https://doi.org/10.1016/j.bpj.2022.03.032.

AUTHOR CONTRIBUTIONS

A.C., D.W., and Z.G. conceived the project and analyzed results. A.C. carried out and analyzed most experiments. M.G.J.N. contributed to the design of protein scaffolds and performed initial experiments. L.P. performed FRAP experiments and analysis. S.K. and M.K. contributed to the design of synthetic RNAs. A.C., D.W., and Z.G. wrote the manuscript, and all authors were involved in revising it critically for important intellectual content.

ACKNOWLEDGMENTS

The authors acknowledge all the members of the Biophysical Chemistry group of the École normale supérieure for fruitful discussion. We thank A. Imbert, M. A. Plamont, M. Ernoult-Lange, M. N. Benassy, M. Bénard, H. Saito, and S. Matsumoto for their help along the project, as well as Adham Safieddine for carefully reading the manuscript.

A.C. was supported by IPV-SU PhD fellowship and ARC fellowship (ARCDOC42021020003470). M.G.J.N was supported by FRM (ING20150532742). This work was supported by the CNRS, École Normale Supérieure, and ARC (20181208003) to Z.G., FRM (MND202003011470) and iBio (SU) to Z.G. and D.W., and ANR (ANR-19-CE12-0024-01) to D.W.

REFERENCES

1. Buchan, J. R. 2014. mRNP granules. *RNA Biol.* 11:1019–1030.
2. Brangwynne, C. P., C. R. Eckmann, …, A. A. Hyman. 2009. Germline P granules are liquid droplets that localize by controlled dissolution/condensation. *Science.* 324:1729–1732.
3. Li, P., S. Banjade, …, M. K. Rosen. 2012. Phase transitions in the assembly of multivalent signalling proteins. *Nature.* 483:336–340.
4. Shin, Y., and C. P. Brangwynne. 2017. Liquid phase condensation in cell physiology and disease. *Science.* 357:20210255.
5. Boeynaems, S., S. Alberti, …, M. Fuxreiter. 2018. Protein phase separation: a new phase in cell biology. *Trends Cell Biol.* 28:420–435.
6. Banani, S. F., H. O. Lee, …, M. K. Rosen. 2017. Biomolecular condensates: organizers of cellular biochemistry. *Nat. Rev. Mol. Cell Biol.* 18:285–298.
7. Standart, N., and D. Weil. 2018. P-bodies: cytosolic droplets for coordinated mRNA storage. *Trends Genet.* 34:612–626.
8. Lallemand-Breitenbach, V., and H. de Thé. 2010. PML nuclear bodies. *Cold Spring Harbor Perspect. Biol.* 2:a000661.
9. Decker, M., S. Jaensch, …, A. A. Hyman. 2011. Limiting amounts of centrosome material set centrosome size in C. elegans embryos. *Curr. Biol.* 21:1259–1267.
10. Strom, A. R., and C. P. Brangwynne. 2019. The liquid nucleome – phase transitions in the nucleus at a glance. *J. Cell Sci.* 132:jcs235093.
11. Roden, C., and A. S. Gladfelter. 2020. RNA contributions to the form and function of biomolecular condensates. *Nat. Rev. Mol. Cell Biol.* 22:183–195. https://doi.org/10.1038/s41580-020-0264-6.
12. Shevtsov, S. P., and M. Dundr. 2011. Nucleation of nuclear bodies by RNA. *Nat. Cel. Biol.* 13:167–173.
13. Schwartz, J. C., X. Wang, …, T. R. Cech. 2013. RNA seeds higher-order assembly of FUS protein. *Cell Rep.* 5:918–925.
14. Jain, A., and R. D. Vale. 2017. RNA phase transitions in repeat expansion disorders. *Nature.* 546:243–247.
15. Yamazaki, T., S. Souquere, …, T. Hirose. 2018. Functional domains of NEAT1 architectural lncRNA induce paraspeckle assembly through phase separation molecular cell article functional domains of NEAT1 architectural lncRNA induce paraspeckle assembly through phase separation. *Mol. Cell.* 70:1038–1053.
16. Saha, S., C. A. Weber, …, A. A. Hyman. 2016. Polar positioning of phase-separated liquid compartments in cells regulated by an mRNA competition mechanism. *Cell.* 166:1572–1584.e16.
17. Falahati, H., B. Pelham-Webb, …, E. Wieschaus. 2016. Nucleation by rRNA dictates the precision of nucleolus assembly. *Curr. Biol.* 26:277–285.

18. Banerjee, P. R., A. N. Milin, …, A. A. Deniz. 2017. Reentrant phase transition drives dynamic substructure formation in ribonucleoprotein droplets. *Angew. Chem. - Int. Edition.* 56:11354–11359.

19. Maharana, S., J. Wang, …, S. Alberti. 2018. RNA buffers the phase separation behavior of prion-like RNA binding proteins. *Science.* 360:918–921.

20. Zhang, H., S. Elbaum-Garfinkle, …, A. S. Gladfelter. 2015. RNA controls PolyQ protein phase transitions. *Mol. Cell.* 60:220–230.

21. Elbaum-Garfinkle, S., Y. Kim, …, C. P. Brangwynne. 2015. The disordered P granule protein LAF-1 drives phase separation into droplets with tunable viscosity and dynamics. *Proc. Natl. Acad. Sci. United States America.* 112:7189–7194.

22. Boeynaems, S., A. S. Holehouse, …, P. S. Tompa. 2019. Spontaneous driving forces give rise to protein−RNA condensates with coexisting phases and complex material properties. *PNAS.* 116:7889–7898.

23. Langdon, E. M., Y. Qiu, …, A. S. Gladfelter. 2018. mRNA structure determines specificity of a polyQ-driven phase separation. *Science.* 360:922–927.

24. Ma, W., G. Zheng, …, C. Mayr. 2021. *In vivo* reconstitution finds multivalent RNA–RNA interactions as drivers of mesh-like condensates. *eLife.* 10:e64252.

25. Kaur, T., M. Raju, …, P. R. Banerjee. 2021. Sequence-encoded and composition-dependent protein-RNA interactions control multiphasic condensate morphologies. *Nat. Commun.* 12:872.

26. Feric, M., N. Vaidya, …, C. P. Brangwynne. 2016. Coexisting liquid phases underlie nucleolar subcompartments. *Cell.* 165:1686–1697.

27. Snead, W. T., T. M. Gerbich, …, A. S. Gladfelter. 2021. Membrane surfaces regulate assembly of a ribonucleoprotein condensate. Preprint at bioRxiv https://doi.org/10.1101/2021.04.24.441251.

28. Feric, M., C. P. Brangwynne, …, B. Author. 2013. A nuclear F-actin scaffold stabilizes RNP droplets against gravity in large cells HHS Public Access Author manuscript. *Nat. Cell Biol.* 15:1253–1259.

29. Lee, D. S. W., N. S. Wingreen, and C. P. Brangwynne. 2021. Chromatin mechanics dictates subdiffusion and coarsening dynamics of embedded condensates. *Nat. Phys.* 17:531–538.

30. Shin, Y., J. Berry, …, C. P. Brangwynne. 2017. Spatiotemporal control of intracellular phase transitions using light-activated optoDroplets. *Cell.* 168:159–171.e14.

31. Mann, J. R., A. M. Gleixner, …, C. J. Donnelly. 2019. RNA binding antagonizes neurotoxic phase transitions of TDP-43. *Neuron.* 102:321–338.e8.

32. Watanabe, T., T. Seki, …, A. Miyawaki. 2017. Genetic visualization of protein interactions harnessing liquid phase transitions. *Scientific Rep.* 7:1–13.

33. Bracha, D., M. T. Walls, …, C. P. Brangwynne. 2018. Mapping local and global liquid phase behavior in living cells using photo-oligomerizable seeds. *Cell.* 175:1467–1480.

34. Schuster, B. S., E. H. Reed, …, D. A. Hammer. 2018. Controllable protein phase separation and modular recruitment to form responsive membraneless organelles. *Nat. Commun.* 9:1–12.

35. Reinkemeier, C. D., G. Estrada Girona, and E. A. Lemke. 2019. Designer membraneless organelles enable codon reassignment of selected mRNAs in eukaryotes. *Science.* 363:e64252.

36. Dzuricky, M., B. A. Rogers, …, A. Chilkoti. 2020. De novo engineering of intracellular condensates using artificial disordered proteins. *Nat. Chem.* 12:814–825.

37. Heidenreich, M., J. M. Georgeson, …, E. D. Levy. 2020. Designer protein assemblies with tunable phase diagrams in living cells. *Nat. Chem. Biol.* 16:939–945.

38. Yoshikawa, M., T. Yoshii, …, S. Tsukiji. 2021. Synthetic protein condensates that inducibly recruit and release protein activity in living cells. *J. Am. Chem. Soc.* 143:6434–6446.

39. Lasker, K., S. Boeynaems, …, L. Shapiro. 2021. A modular platform for engineering function of natural and synthetic biomolecular condensates. Preprint at bioRxiv https://doi.org/10.1101/2021.02.03.429226.

40. Nakamura, H., A. A. Lee, …, T. Inoue. 2018. Intracellular production of hydrogels and synthetic RNA granules by multivalent molecular interactions. *Nat. Mater.* 17:79–88.

41. Sanders, D. W., N. Kedersha, …, C. P. Brangwynne. 2020. Competing protein-RNA interaction networks control multiphase intracellular organization. *Cell.* 181:306–324.e28.

42. Garcia-Jove Navarro, M., S. Kashida, …, Z. Gueroui. 2019. RNA is a critical element for the sizing and the composition of phase-separated RNA–protein condensates. *Nat. Commun.* 10:3230.

43. Coller, J. M., N. K. Gray, and M. P. Wickens. 1998. mRNA stabilization by poly(A) binding protein is independent of poly(A) and requires translation. *Genes Develop.* 12:3226–3235.

44. Wu, B., J. A. Chao, and R. H. Singer. 2012. Fluorescence fluctuation spectroscopy enables quantitative imaging of single mRNAs in living cells. *Biophysical J.* 102:2936–2944.

45. Strein, C., A. M. Alleaume, …, A. Castello. 2014. A versatile assay for RNA-binding proteins in living cells. *RNA.* 20:721–731.

46. Tsanov, N., A. Samacoits, …, F. Mueller. 2016. smiFISH and FISH-quant – a flexible single RNA detection approach with super-resolution capability. *Nucleic Acids Res.* 44:e165.

47. Schindelin, J., I. Arganda-Carreras, …, A. Cardona. 2012. Fiji: an open-source platform for biological-image analysis. *Nat. Methods.* 9:676–682.

48. de Chaumont, F., S. Dallongeville, …, J. C. Olivo-Marin. 2012. Icy: an open bioimage informatics platform for extended reproducible research. *Nat. Methods.* 9:690–696.

49. Imbert, A., W. Ouyang, …, F. Mueller. 2021. FISH-quant v2: a scalable and modular analysis tool for smFISH image analysis. Preprint at bioRxiv https://doi.org/10.1101/2021.07.20.453024.

50. Olivo-Marin, J.-C. 2002. Extraction of spots in biological images using multiscale products. *Pattern recognition.* 35:1989–1996.

51. Postma, M., and J. Goedhart. 2019. Plotsofdata—a web app for visualizing data together with their summaries. *PLoS Biol.* 17:e3000202.

52. Rollins, C. T., V. M. Rivera, …, T. Clackson. 2000. A ligand-reversible dimerization system for controlling protein-protein interactions. *Proc. Natl. Acad. Sci. U S A.* 97:7096–7101.

53. Wilczynska, A., C. Aigueperse, …, D. Weil. 2005. The translational regulator CPEB1 provides a link between dcp1 bodies and stress granules. *J. Cell Sci.* 118:981–992.

54. Liu, J. L., and J. G. Gall. 2007. U bodies are cytoplasmic structures that contain uridine-rich small nuclear ribonucleoproteins and associate with P bodies. *Proc. Natl. Acad. Sci. U S A.* 104:11655–11659.

55. Snead, W. T., and A. S. Gladfelter. 2019. The control centers of biomolecular phase separation: how membrane surfaces, PTMs, and active processes regulate condensation. *Mol. Cell.* 76:295–305.

56. Jalihal, A. P., A. Schmidt, …, N. G. Walter. 2021. Hyperosmotic phase separation: condensates beyond inclusions, granules and organelles. *J. Biol. Chem.* 296:100044.

57. Saitoh, N., C. S. Spahr, …, D. L. Spector. 2004. Proteomic analysis of interchromatin granule clusters. *Mol. Biol. Cell.* 15:3876–3890.

58. Hubstenberger, A., M. Courel, …, M. Daunesse. 2017. P-body purification reveals the condensation of repressed mRNA regulons. *Mol. Cel.* 68:144–157.e5.

59. Khong, A., T. Matheny, …, R. Parker. 2017. The stress granule transcriptome reveals principles of mRNA accumulation in stress granules. *Mol. Cell.* 68:808–820.e5.

60. Jain, S., J. R. Wheeler, …, R. P. Correspondence. 2016. ATPase-modulated stress granules contain a diverse proteome and substructure. *Cell.* 164:487–498.

61. Tauber, D., G. Tauber, …, R. Parker. 2020. Modulation of RNA condensation by the DEAD-box protein eIF4A. *Cell.* 180:411–426. https://doi.org/10.1016/j.cell.2019.12.031.

62. Guillé N-Boixet, J., A. Kopach, …, I. Poser. 2020. RNA-induced conformational switching and clustering of G3BP drive stress granule assembly by condensation article RNA-induced conformational

switching and clustering of G3BP drive stress granule assembly by condensation. *Cell.* 181:346–361.e17.

63. Banani, S. F., A. M. Rice, …, M. K. Rosen Correspondence. 2016. Compositional control of phase-separated cellular bodies in brief what are the general principles that define the composition of phase-separated cellular bodies? *Cell.* 166:651–663.
64. Nott, T. J., E. Petsalaki, …, A. J. Baldwin. 2015. Phase transition of a disordered nuage protein generates environmentally responsive membraneless organelles. *Mol. Cell.* 57:936–947.
65. van Treeck, B., and R. Parker. 2018. Emerging roles for intermolecular RNA-RNA interactions in RNP assemblies. *Cell.* 174:791–802.
66. Gomes, E., and J. Shorter. 2019. The molecular language of membraneless organelles. *J. Biol. Chem.* 294:7115–7127.
67. Adekunle, D. A., and A. Hubstenberger. 2020. The multiscale and multiphase organization of the transcriptome. *Emerging Top. Life Sci.* 4:265–280.
68. Harmon, T. S., A. S. Holehouse, and R. V. Pappu. 2018. Differential solvation of intrinsically disordered linkers drives the formation of spatially organized droplets in ternary systems of linear multivalent proteins. *New J. Phys.* 20:045002.
69. Mountain, G. A., and C. D. Keating. 2020. formation of multiphase complex coacervates and partitioning of biomolecules within them. *Biomacromolecules.* 21:630–640.
70. Lu, T., and E. Spruijt. 2020. Multiphase complex coacervate droplets. *J. Am. Chem. Soc.* 142:2905–2914.
71. Zwicker, D., M. Decker, …, F. Jülicher. 2014. Centrosomes are autocatalytic droplets of pericentriolar material organized by centrioles. *Proc. Natl. Acad. Sci. U S A.* 111:E2636–E2645.
72. Brangwynne, C. P. 2013. Phase transitions and size scaling of membrane-less organelles. *J. Cell Biol.* 203:875–881.
73. Berry, J., S. C. Weber, …, D. A. Weitz. 2015. RNA transcription modulates phase transition-driven nuclear body assembly. *Proc. Natl. Acad. Sci. U S A.* 112:E5237–E5245.
74. Berry, J., C. P. Brangwynne, and M. Haataja. 2018. Physical principles of intracellular organization via active and passive phase transitions. *Rep. Prog. Phys.* 81:046601.
75. Brangwynne, C. P., T. J. Mitchison, and A. A. Hyman. 2011. Active liquid-like behavior of nucleoli determines their size and shape in Xenopus laevis oocytes. *Proc. Natl. Acad. Sci. U S A.* 108:4334–4339.
76. Söding, J., D. Zwicker, …, J. Kirschbaum. 2019. Mechanisms for active regulation of biomolecular condensates trends in cell biology. *Trends Cell Biol.* 30:4–14. https://doi.org/10.1016/j.tcb.2019.10.006.
77. Kirschbaum, J., and D. Zwicker. 2021. Controlling biomolecular condensates via chemical reactions. *J. R. Soc. Interf.* 179:20210255.
78. Dar, F., and R. Pappu. 2020. Restricting the sizes of condensates. *eLife.* 9:1–3.
79. Ranganathan, S., and E. I. Shakhnovich. 2020. Dynamic metastable long-living droplets formed by sticker-spacer proteins. *eLife.* 9:1–25.
80. Weber, C. A., D. Zwicker, …, C. F. Lee. 2019. Physics of active emulsions. *Rep. Prog. Phys.* 82:064601.
81. Zwicker, D., A. A. Hyman, and F. Jülicher. 2015. Suppression of Ostwald ripening in active emulsions. *Physical Review E.* 92:12317.
82. Bressloff, P. C. 2020. Active suppression of Ostwald ripening: beyond mean-field theory. *Phys. Rev. E.* 101:42804.
83. David Wurtz, J., and C. F. Lee. 2018. Chemical-reaction-controlled phase separated drops: formation, size selection, and coarsening. *Phys. Rev. Lett.* 120:078102.
84. Sanchez-Burgos, I., J. A. Joseph, …, J. R. Espinosa. 2021. Size conservation emerges spontaneously in biomolecular condensates formed by scaffolds and surfactant clients. Preprint at bioRxiv https://doi.org/10.1101/2021.04.30.442154.
85. Cuylen, S., C. Blaukopf, …, D. W. Gerlich. 2016. Ki-67 acts as a biological surfactant to disperse mitotic chromosomes. *Nature.* 535:308–312.
86. Welsh, T. J., G. Krainer, …, T. P. Knowles. 2022. Surface electrostatics govern the emulsion stability of biomolecular condensates. *Nano Lett.* 22:612–621.
87. Putnam, A., M. Cassani, …, G. Seydoux. 2019. A gel phase promotes condensation of liquid P granules in Caenorhabditis elegans embryos. *Nat. Struct. Mol. Biol.* 26:220–226.
88. Lee, C. Y. S., A. Putnam, …, G. Seydoux. 2020. Recruitment of mRNAs to P granules by condensation with intrinsically-disordered proteins. *eLife.* 9:e52896.
89. Folkmann, A. W., A. Putnam, …, G. Seydoux. 2021. Regulation of biomolecular condensates by interfacial protein clusters. *Science.* 373:1218–1224.
90. Yamazaki, T., T. Yamamoto, …, T. Hirose. 2021. Paraspeckles are constructed as block copolymer micelles. *EMBO J.* 40:e107270.
91. Wheeler, J. R., T. Matheny, …, R. Parker. 2016. Distinct stages in stress granule assembly and disassembly. *eLife.* 5:e18413.
92. Pitchiaya, S., M. D. A. Mourao, …, N. G. Walter. 2019. Dynamic recruitment of single RNAs to processing bodies depends on RNA functionality. *Mol. Cell.* 74:521–533.e6.
93. Moon, S. L., T. Morisaki, …, T. J. Stasevich. 2019. Multicolour single-molecule tracking of mRNA interactions with RNP granules. *Nat. Cell Biol.* 21:162–168.
94. Mateju, D., B. Eichenberger, …, J. A. Chao. 2020. Single-molecule imaging reveals translation of mRNAs localized to stress granules. *Cell.* 183:1801–1812. https://doi.org/10.1016/j.cell.2020.11.010.
95. Wilbertz, J. H., F. Voigt, …, J. A. Chao. 2019. Single-molecule imaging of mRNA localization and regulation during the integrated stress response. *Mol. Cell.* 73:946–958.e7.
96. Davidson, A., R. M. Parton, …, I. Davis. 2016. Localized translation of gurken/TGF-α mRNA during Axis specification is controlled by access to orb/CPEB on processing bodies. *Cell Rep.* 14:2451–2462.

Biophysical Journal, Volume *121*

Supplemental information

RNA at the surface of phase-separated condensates impacts their size and number

Audrey Cochard, Marina Garcia-Jove Navarro, Leonard Piroska, Shunnichi Kashida, Michel Kress, Dominique Weil, and Zoher Gueroui

Supplementary information for:

RNA at the surface of phase-separated condensates impacts their size and number

Audrey Cochard[1,2], Marina Garcia-Jove Navarro[1], Leonard Piroska[1], Shunnichi Kashida[1], Michel Kress[2], Dominique Weil[2]*, Zoher Gueroui[1]*

1- PASTEUR, Department of Chemistry, École Normale Supérieure, PSL University, Sorbonne Université, CNRS, 75005 Paris, France.
2- Sorbonne Université, CNRS, Institut de Biologie Paris-Seine (IBPS), Laboratoire de Biologie du Développement, F-75005 Paris, France.

*Correspondence: zoher.gueroui@ens.fr, dominique.weil@upmc.fr

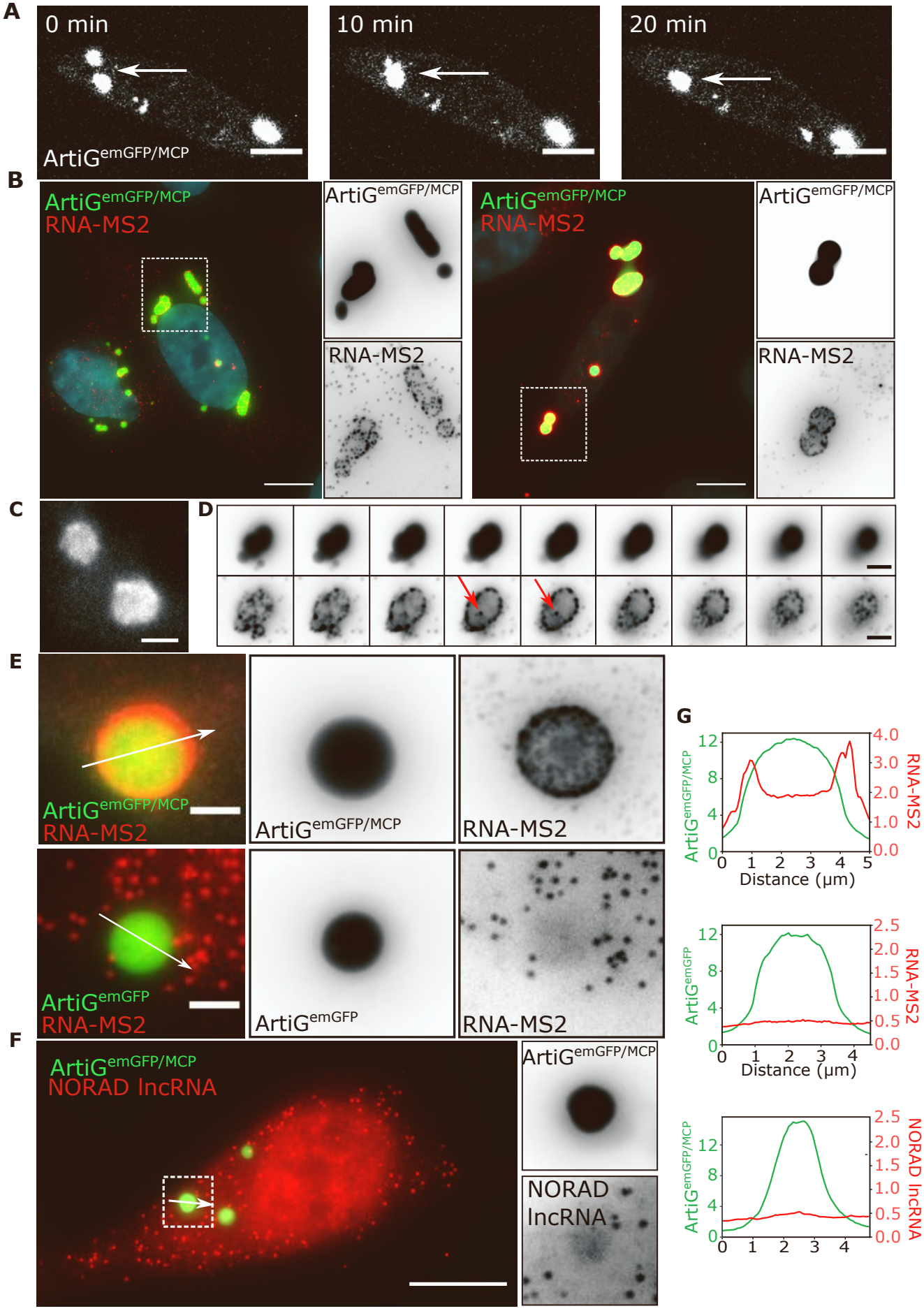

Figure S1: Validation of ArtiG$^{emGFP/MCP}$ specificity. **A.** Coalescence of two ArtiG$^{emGFP/MCP}$ condensates in a HeLa cell and relaxation into a spherical shape (white arrow). Scale bar = 10 µm. **B.** Epifluorescence imaging of two HeLa cells displaying the typical surface recruitment of MS2-RNA (red) around ArtiG$^{emGFP/MCP}$ (green). The white dashed rectangles delineate the images zoomed on the right. Nuclei were stained with DAPI (blue). Scale bars = 10 µm. **C.** Two ArtiG$^{emGFP/MCP}$ condensates in Hela cells immunostained with MCP antibodies. Scale bar = 2 µm. **D.** Z-stack images (step = 0.24 µm) of condensates with an RNA-MS2 molecule trapped in the middle (red arrows), as revealed by smFISH. Scale bar = 2 µm. **E.** Epifluorescence imaging of one ArtiG$^{emGFP/MCP}$ (upper panel) and one ArtiG^{emGFP} (lower panel) (green) and RNA-MS2 (red) in HEK293 cells. The white arrows indicate where the intensity profiles in **G.** (upper and middle panels) were plotted. Scale bars = 2 µm. **F.** Epifluorescence imaging of ArtiG$^{emGFP/MCP}$ (green) and NORAD lncRNA (red) in Hela cells. The white dashed square delineates the images zoomed on the right. The white arrow indicates where the intensity profile in **G.** (lower panel) was plotted. Scale bar = 10 µm. **G.** Intensity profiles across ArtiG condensates (white arrows in **E.** and **F.**).

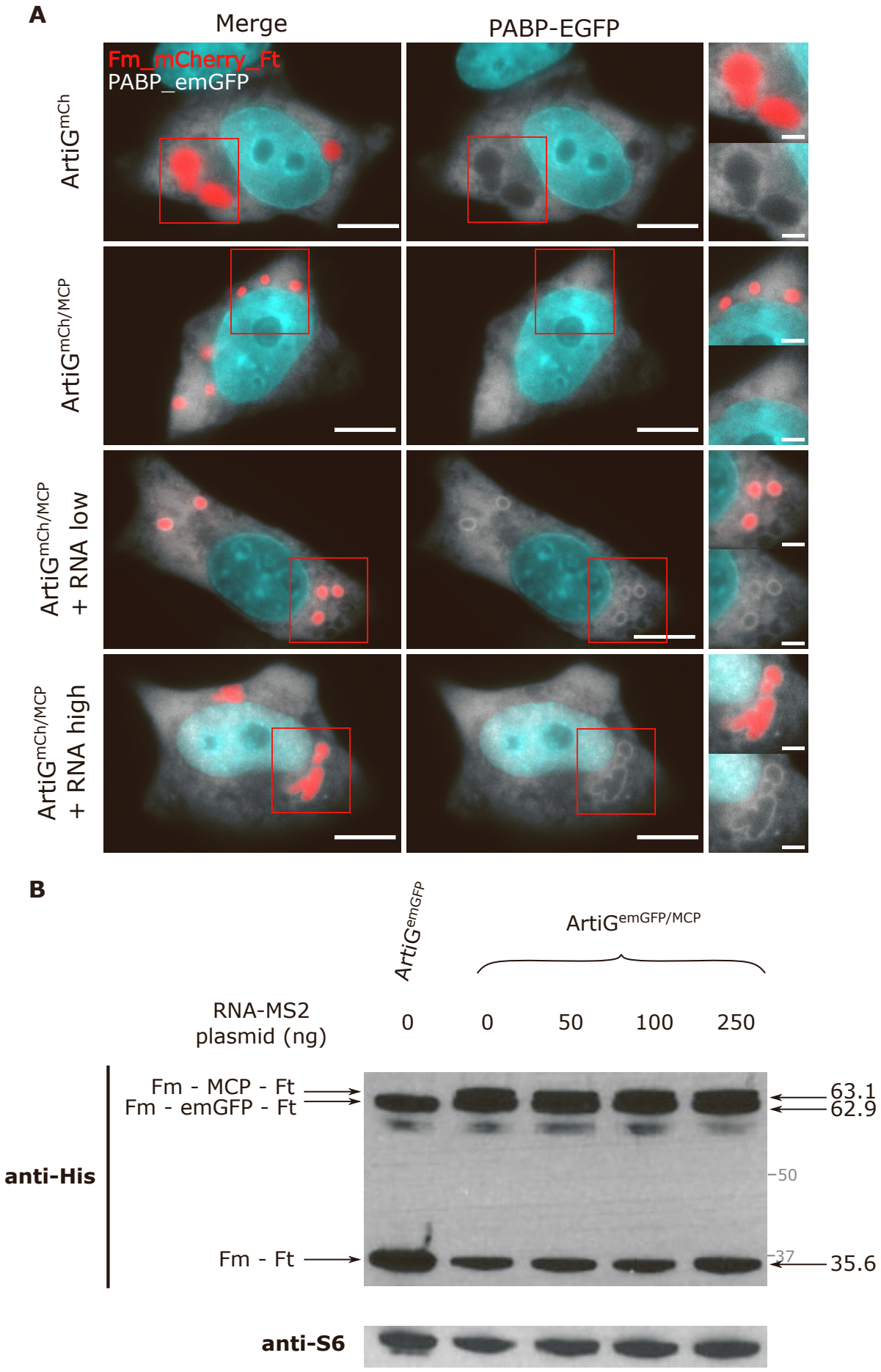

Figure S2: ArtiG$^{emGFP/MCP/RNA}$ but not ArtiG$^{emGFP/MCP}$ display a strong coronal PABP-GFP signal (**A**) and increasing the quantity of transfected RNA-MS2 plasmid has no impact on the expression of ArtiG$^{emGFP/MCP}$ scaffold proteins (**B**). **A.** Representative epifluorescence images of Hela cells expressing various ArtiG condensates (red) and PABP-GFP (white). Scale bar = 10 µm (zoom: 2 µm). Nuclei were stained with Hoechst (blue). **B.** Western blotting experiment showing scaffold protein expression 24 h after transfection with Fm–emGFP–Ft and Fm–Ft (ArtiG^{emGFP}, first column) or Fm–emGFP–Ft, Fm–MCP–Ft and Fm–Ft and increasing amount of RNA-MS2 plasmid (ArtiG$^{emGFP/MCP}$, 2nd to 5th columns). The size of the scaffold proteins (in kD) and the position of the MW markers are indicated on the right in black and grey, respectively.

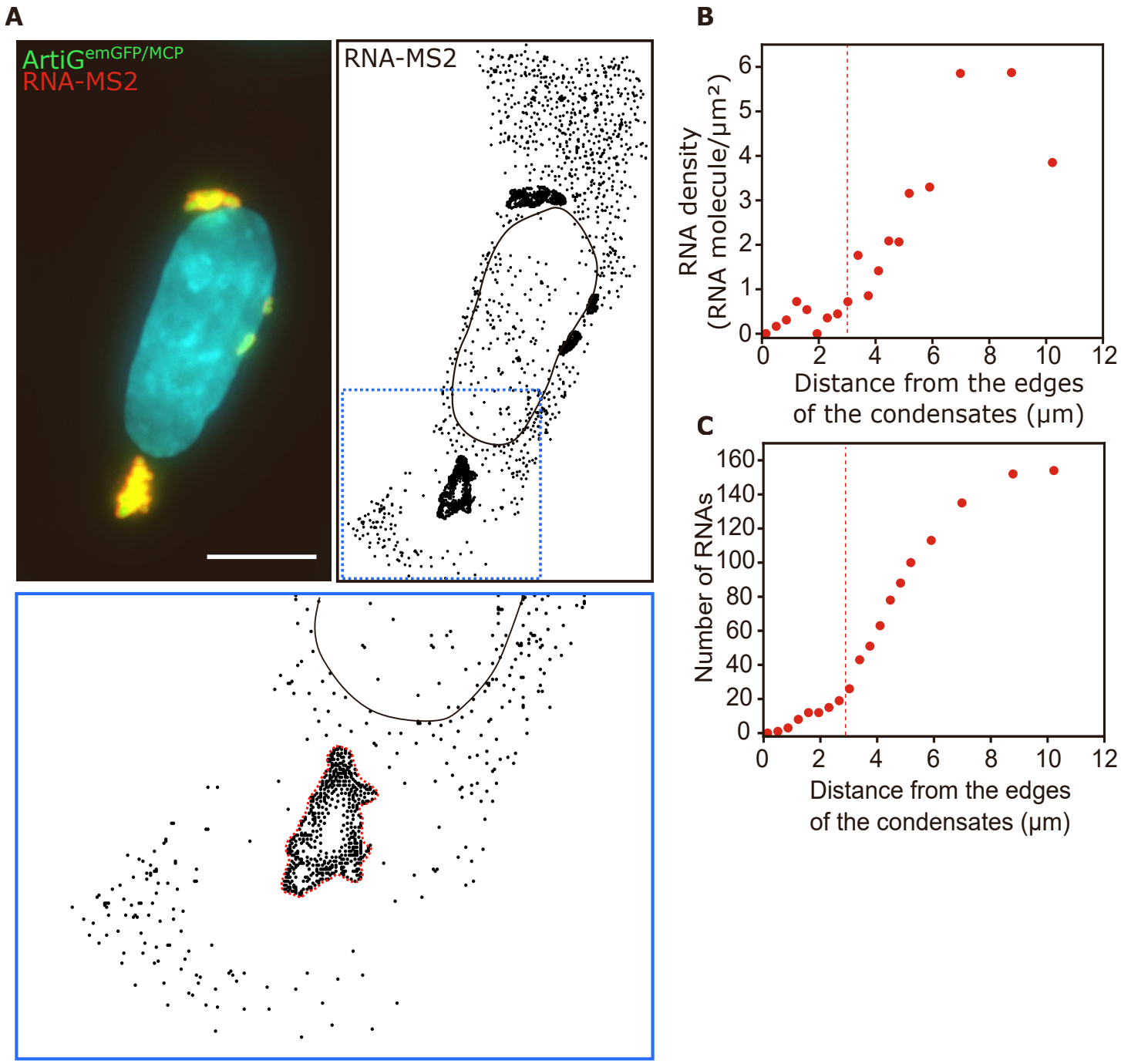

Figure S3: Depletion of RNA-MS2 around ArtiG$^{emGFP/MCP}$ condensates. Another example of RNA-MS2 depletion was analyzed as in Figure **2C. E. F.**

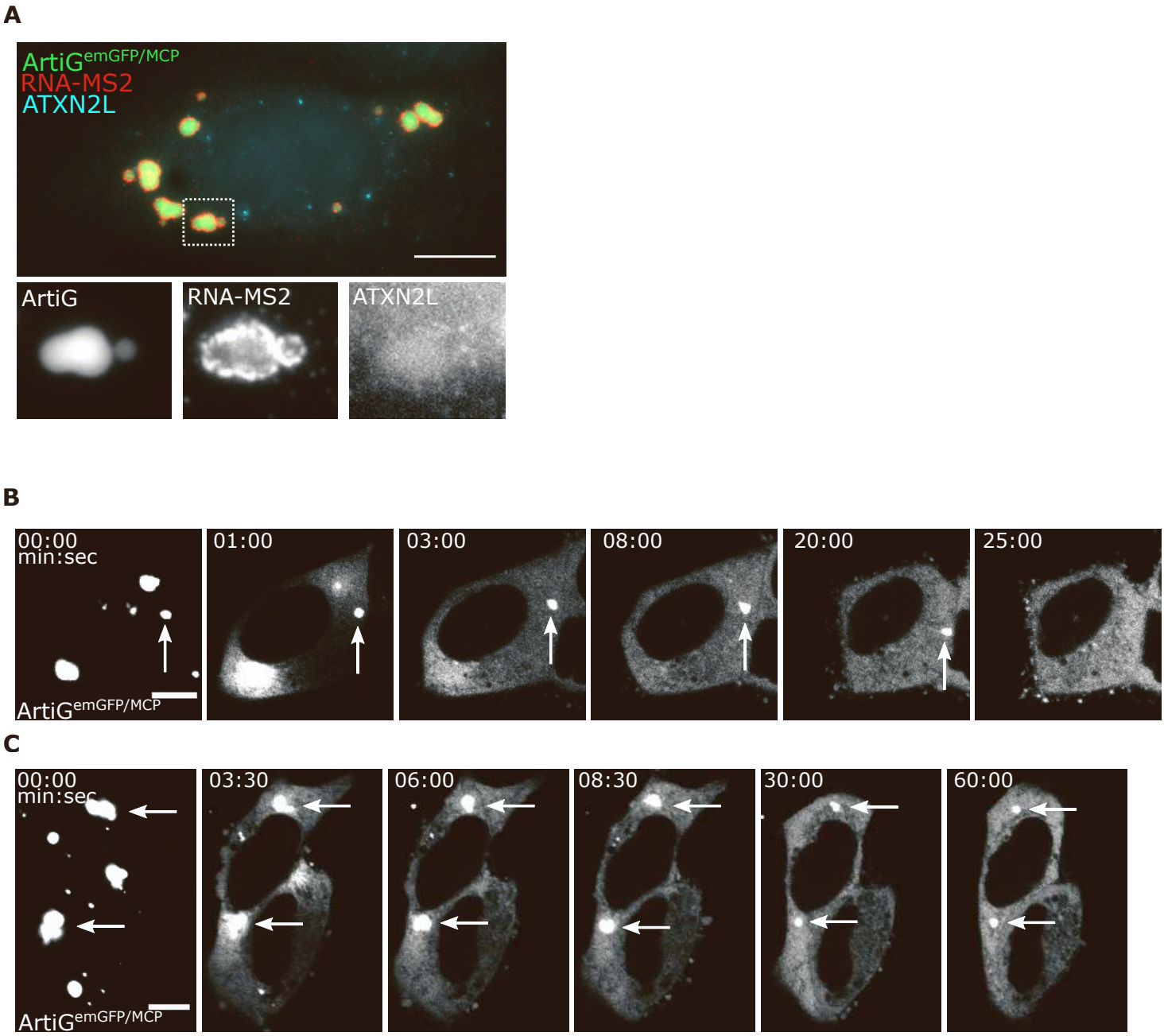

Figure S4: ArtiG$^{emGFP/MCP}$ do not induce SGs and dissolve upon FK506 treatment. **A.** Epifluorescence imaging of ArtiG$^{emGFP/MCP}$ (green) and RNA-MS2 (red) in HeLa cells, after immunostaining of ATXN2L (blue) as a SG marker (no arsenite treatment). The white dashed square delineates the images zoomed below. Scale bar = 10 µm. **B.** Time-lapse confocal imaging of an ArtiG$^{emGFP/MCP}$ that dissolved only after 25min FK506 treatment (white arrow). Scale bar = 10 µm. **C.** Time-lapse confocal imaging of two ArtiG$^{emGFP/MCP}$ whose dissolution was still incomplete after 60 min FK506 treatment (white arrows). Scale bar = 10 µm.

iRFP

Probe	Sequence
iRFP_FLAP-Y_p01	CCGCAGGCTCGAACTCGATGATCGATGTACTTACACTCGGACCTCGTCGACATGCATT
iRFP_FLAP-Y_p02	ACGCCCATGTTCCGCAGAAATTCGAGATGGCTTACACTCGGACCTCGTCGACATGCATT
iRFP_FLAP-Y_p03	TCTTCAAGTACAGTAGCCGCGCCTGCTGTTACACTCGGACCTCGTCGACATGCATT
iRFP_FLAP-Y_p04	GTGCGGCCATCTCTTCGAGCGACTTCAGTTTACACTCGGACCTCGTCGACATGCATT
iRFP_FLAP-Y_p05	TCATGGCGATGCAGTGAGATGTCGAAGGTGCGTTACACTCGGACCTCGTCGACATGCATT
iRFP_FLAP-Y_p06	GGTCTCGCCGAAGTAATCGGCGAGTAGCTCATTACACTCGGACCTCGTCGACATGCATT
iRFP_FLAP-Y_p07	CGGCATTTTCCGTAATGCGCGTGATCCGCATTACACTCGGACCTCGTCGACATGCATT
iRFP_FLAP-Y_p08	AGCGATAAGAAGTCGGCGAACATTTCGGCCGCTTACACTCGGACCTCGTCGACATGCATT
iRFP_FLAP-Y_p09	TCAATGATGATCGACAGCGACATCGAGGCGCTTACACTCGGACCTCGTCGACATGCATT
iRFP_FLAP-Y_p10	CGCGAAGCGGTACAACATCACGCGGTGATAGCTTACACTCGGACCTCGTCGACATGCATT
iRFP_FLAP-Y_p11	TGATGACAGATGATCAATCCCCATAGCGTGCTTACACTCGGACCTCGTCGACATGCATT
iRFP_FLAP-Y_p12	AGCATCGCCTGCAGATAGCGCGGCACTTACACTCGGACCTCGTCGACATGCATT
iRFP_FLAP-Y_p13	TGTTCGCGTTGGTGGTGGGCGGCGGTGAAGTTTACACTCGGACCTCGTCGACATGCATT
iRFP_FLAP-Y_p14	TGCTCGGGCACGATCCGGCTGCTGATTTACACTCGGACCTCGTCGACATGCATT
iRFP_FLAP-Y_p15	GAAAGCTCTCGAGGTCGCTGCGCTTCGCTTACACTCGGACCTCGTCGACATGCATT
iRFP_FLAP-Y_p16	TTTGGTGCGCGCGATGATCTGCCGCGTCTTACACTCGGACCTCGTCGACATGCATT
iRFP_FLAP-Y_p17	GACCCGCGGAGTTTCGCGTCCAAAGAACGCTTACACTCGGACCTCGTCGACATGCATT
iRFP_FLAP-Y_p18	ATCGGCTCGCGATCGCAGGAGGTGAGATCTTACACTCGGACCTCGTCGACATGCATT
iRFP_FLAP-Y_p19	GGACCAGCGACGCCGGAAAGTGCTGACCTTACACTCGGACCTCGTCGACATGCATT
iRFP_FLAP-Y_p20	CGGTCAGGCCGTCGCGCCAACCGAAGATTTACACTCGGACCTCGTCGACATGCATT
iRFP_FLAP-Y_p21	GCGCCGGTCGCTTTGGATCGGAGGACTGTTACACTCGGACCTCGTCGACATGCATT
iRFP_FLAP-Y_p22	CCAGTGCGTTGCGCAGCGCATGGGCTTTACACTCGGACCTCGTCGACATGCATT
iRFP_FLAP-Y_p23	CGCACGGCTGAATGCTGCCGGGGATGTTTACACTCGGACCTCGTCGACATGCATT
iRFP_FLAP-Y_p24	GGCGAGATGCTGCGCAGGTGCGCGAACTTACACTCGGACCTCGTCGACATGCATT

β-actin

Probe	Sequence
Beta-actine_FLAP-Y_p01	AAGGTGTGCACTTTTATTCAACTGGTCTCAAGTTACACTCGGACCTCGTCGACATGCATT
Beta-actine_FLAP-Y_p02	AGAAGCATTTGCGGTGGACGATGGAGGGGTTACACTCGGACCTCGTCGACATGCATT
Beta-actine_FLAP-Y_p03	GCTCAGGAGGAGCAATGATCTTGATCTTCTTACACTCGGACCTCGTCGACATGCATT
Beta-actine_FLAP-Y_p04	GGATGTCCACGTCACACTTCATGATGGAGTTACACTCGGACCTCGTCGACATGCATT
Beta-actine_FLAP-Y_p05	GAAGGTAGTTTCGTGGATGCCACAGGACTCTTACACTCGGACCTCGTCGACATGCATT
Beta-actine_FLAP-Y_p06	CAGCGGAACCGCTCATTGCCAATGGTTTACACTCGGACCTCGTCGACATGCATT
Beta-actine_FLAP-Y_p07	CAGCCTGGATAGCAACGTACATGGCTGTTACACTCGGACCTCGTCGACATGCATT
Beta-actine_FLAP-Y_p08	GTGTTGAAGGTCTCAAACATGATCTGGGTCATTTACACTCGGACCTCGTCGACATGCATT
Beta-actine_FLAP-Y_p09	TCGGGAGCCACACGCAGCTCATTGTATTACACTCGGACCTCGTCGACATGCATT
Beta-actine_FLAP-Y_p10	ACGAGCGCGGCGATATCATCATCCATTTACACTCGGACCTCGTCGACATGCATT
Beta-actine_FLAP-Y_p11	TTCTCCTTAGAGAGAAGTGGGGTGGCTTTTAGTTACACTCGGACCTCGTCGACATGCATT
Beta-actine_FLAP-Y_p12	CATTGTGAACTTTGGGGGATGCTCGCTCTTACACTCGGACCTCGTCGACATGCATT
Beta-actine_FLAP-Y_p13	GACTGCTGTCACCTTCACCGTTCCAGTTACACTCGGACCTCGTCGACATGCATT
Beta-actine_FLAP-Y_p14	GGACTCGTCATACTCCTGCTTGCTGATTACACTCGGACCTCGTCGACATGCATT
Beta-actine_FLAP-Y_p15	CAGTGATCTCCTTCTGCATCCTGTCGTTACACTCGGACCTCGTCGACATGCATT
Beta-actine_FLAP-Y_p16	GACAGCACTGTGTTGGCGTACAGGTCTTTTTACACTCGGACCTCGTCGACATGCATT
Beta-actine_FLAP-Y_p17	CGTGGCCATCTCTTGCTCGAAGTCCATTACACTCGGACCTCGTCGACATGCATT
Beta-actine_FLAP-Y_p18	GCGACGTAGCACAGCTTCTCCTTAATGTTTACACTCGGACCTCGTCGACATGCATT
Beta-actine_FLAP-Y_p19	AGGTGTGGTGCCAGATTTTCTCCATGTCGTTACACTCGGACCTCGTCGACATGCATT
Beta-actine_FLAP-Y_p20	CCAGTTGGTGACGATGCCGTGCTCGATTTACACTCGGACCTCGTCGACATGCATT
Beta-actine_FLAP-Y_p21	GGTACTTCAGGGTGAGGATGCCTCTCTTTACACTCGGACCTCGTCGACATGCATT
Beta-actine_FLAP-Y_p22	CCTCGTCGCCCACATAGGAATCCTTCTTACACTCGGACCTCGTCGACATGCATT
Beta-actine_FLAP-Y_p23	AAAAACAACAATGTGCAATCAAAGTCCTCGGCTTACACTCGGACCTCGTCGACATGCATT
Beta-actine_FLAP-Y_p24	TGCCCAGGAAGGAAGGCTGGAAGAGTGCTTACACTCGGACCTCGTCGACATGCATT

NORAD_FLAP-Y

Probe	Sequence
NORAD_FLAP-Y_p01	AGGATGTCTAGCTCCAAGGGGTGGACTAATTACACTCGGACCTCGTCGACATGCATT
NORAD_FLAP-Y_p02	CTGCAACTTCCGCCTCCCAAGTTCAATTACACTCGGACCTCGTCGACATGCATT
NORAD_FLAP-Y_p03	CGCTGTAAACAGGATGGCATAGAGCTCTCTTACACTCGGACCTCGTCGACATGCATT
NORAD_FLAP-Y_p04	TATCGCTTCCAGAGGCCGTCTTAACAACTTACACTCGGACCTCGTCGACATGCATT
NORAD_FLAP-Y_p05	CTCTTTCCATCTAGAAGGGCTAGATGTGACTTACACTCGGACCTCGTCGACATGCATT
NORAD_FLAP-Y_p06	AACGGGCCAAACGTGGCCTGTCATTCTTACACTCGGACCTCGTCGACATGCATT
NORAD_FLAP-Y_p07	CACAGCAGAGGCCTCCGTTATCTGCATTACACTCGGACCTCGTCGACATGCATT
NORAD_FLAP-Y_p08	AAGGTCACTCCCAGAGGACAGGCCTTTTACACTCGGACCTCGTCGACATGCATT
NORAD_FLAP-Y_p09	GTGGGCACCACCACGACCAGCTAATTTTACACTCGGACCTCGTCGACATGCATT
NORAD_FLAP-Y_p10	GATGGTCCTGATCTCTTGACCTCGTGATTACACTCGGACCTCGTCGACATGCATT
NORAD_FLAP-Y_p11	CCACTGCGACAGGCCGTTGTACACTTTTACACTCGGACCTCGTCGACATGCATT
NORAD_FLAP-Y_p12	CTCTCCACCACCAACCTGATGGATATTTACACTCGGACCTCGTCGACATGCATT
NORAD_FLAP-Y_p13	GCACGTGTCACTTAGAGCTGATGTTATCTCTTACACTCGGACCTCGTCGACATGCATT
NORAD_FLAP-Y_p14	CCCACCTCCCAGGTGGTTCAACAATTTTACACTCGGACCTCGTCGACATGCATT
NORAD_FLAP-Y_p15	CCTTCCCATCTCCATCAACCCAGAAGTTACACTCGGACCTCGTCGACATGCATT
NORAD_FLAP-Y_p16	GACTAGATGTTGTCAATTAGGACTCGTCTGTCTTACACTCGGACCTCGTCGACATGCATT
NORAD_FLAP-Y_p17	TTCTCTTCCTTCTCAGGTCTTCCAGCTTACACTCGGACCTCGTCGACATGCATT
NORAD_FLAP-Y_p18	AAGGTTGGGGTGGAGTTGAGAGCAGCTTTTTCTTACACTCGGACCTCGTCGACATGCATT
NORAD_FLAP-Y_p19	GTAAATCTTCCCAGAGGGTGGTGGGCATTTTTACACTCGGACCTCGTCGACATGCATT
NORAD_FLAP-Y_p20	CCATTTCTCTCTTCCGACAGCAAAGTCTGTTACACTCGGACCTCGTCGACATGCATT
NORAD_FLAP-Y_p21	TTGAGTGTCTTCTAAATAGGAACATTCTGGCCTTACACTCGGACCTCGTCGACATGCATT
NORAD_FLAP-Y_p22	CTCAGCCTCTCGAGTAACTGGGGCTATTACACTCGGACCTCGTCGACATGCATT
NORAD_FLAP-Y_p23	CCATCTGTAATGCTTAGGGGGGGTTTTAACAATTACACTCGGACCTCGTCGACATGCATT
NORAD_FLAP-Y_p24	CCTTCCTTCTCTGCCTTCAATCCAGTTTACACTCGGACCTCGTCGACATGCATT

FLAP-Y-Cy3	/5Cy3/AA TGC ATG TCG ACG AGG TCC GAG TGT AA/3Cy3Sp/

II.3. ANNEX - Visualization and quantification of RNA-MS2 molecules

II.3.1. SmFISH

To be able to screen a lot of cells and have quantitative data, we turned to observations of fixed cells. Single molecule fluorescence *in situ* hybridization (smFISH) is a technique that allows for the visualization of individual RNAs in single cells, via the hybridization on a target RNA of 40 to 50 DNA probes, all conjugated with a fluorophore[145]. The combination of the numerous fluorescent probes enables the visualization of the single molecules of RNA as bright, diffraction limited spots. Therefore, the smFISH method opens the possibility to count RNA molecules and analyze their localization of RNA in cells.

The high number of oligonucleotide probes increases the signal to noise ratio. However, this large number of modified fluorescent oligonucleotide probes has a cost. Therefore, alternative smFISH techniques have been developed, including the single molecule inexpensive FISH (smiFISH), which has the simplest design[146]. Here, two types of probes are used: first 12 to 48 unlabeled primary probes (usually 24), composed of a 26 to 32 nucleotides target-specific sequence and of a shared 28-nucleotides sequence called FLAP; secondly, secondary probes complementary to the FLAP sequence and labeled with two fluorophores (Fig. II.8). Primary and secondary probes are first hybridized *in vitro*, and the complex is then hybridized on target RNAs in cell overnight. The smiFISH technique is much cheaper that the smFISH method as the unlabeled primary probes are inexpensive and the same secondary probe is used for all the primary probes and thus can be synthesized at large scale. Furthermore, different fluorophores can be used for the secondary probes, allowing for multicolor imaging without extra cost. Hereafter, for simplification, smiFISH will be called smFISH.

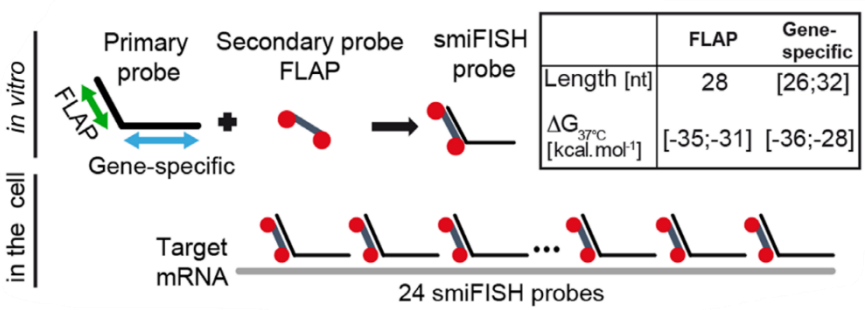

Figure II.8: mRNA detection using smiFISH. Adapted from[146]. 24 primary probes are first hybridized *in vitro* with the fluorescent secondary probe via the FLAP sequence. The duplexes are then hybridized on the target mRNA in cells. Red circles: Cy3 moieties.

The visualization of RNA-MS2 with the smFISH method, using Cy3-labeled secondary probes, in cells expressing ArtiG$^{emGFP/MCP}$ condensates, showed that the RNA was exclusively recruited at the surface of the condensates (Fig. II.9A). Interestingly, it seemed that the RNA surface density on the condensates was linked to their size. To test that hypothesis, a detection tool able to evaluate the number of recruited RNAs, which appear as clusters on the surface of condensates and are undiscernible for the unaided eyes, was required.

Dedicated tools for smFISH image analysis have been developed. A tricky part of the analysis consists in quantifying the number of RNAs in clusters, for example at transcription sites, or here at the surface of condensates, which is harder than detecting and counting individual RNAs in cells. FISH-QUANT was developed to address this issue and was added in Matlab[147]. Very recently, a Python-based improved version of FISH-QUANT, free, open-source, more user-friendly, and integrating the latest open-source tools for data analysis, was devised[144]. Its code is available under the name of Big-FISH. We thus used the Big-FISH workflow to perform extensive quantitative analysis of RNA-MS2 localization in cells. The next part will describe the analysis steps illustrated with the example of a cell expressing ArtiG$^{emGFP/MCP}$ condensates, recruiting RNA-MS2 at their surfaces.

II.3.2. Big-FISH

Here will be described the outlines of the Big-FISH workflow applied on a cell expressing ArtiG$^{emGFP/MCP}$ condensates, without going into details in the algorithms. For a more detailed description of the method and of the algorithms, tutorials are made available online by the FISH-quant method developers (https://github.com/fish-quant/big-fish-examples).

Cells were imaged with an epifluorescence microscope, and for each field of view, a z-stack acquisition was performed to consider the entirety of the cells. To analyze the RNA localization in cells, I projected the 3D-acquisitions in 2D using a maximum intensity projection method, that keeps for each pair of coordinates (x,y) the pixel along the z-stack with the highest intensity (Fig. II.9A).

The first step to analyze the RNA-MS2 content of a cell was cell segmentation, i.e., detecting the outline of the cell (Fig. II.9B). Briefly, first the nucleus was segmented by applying a manually set threshold, and in second step a watershed algorithm was applied to detect the cell boundaries.

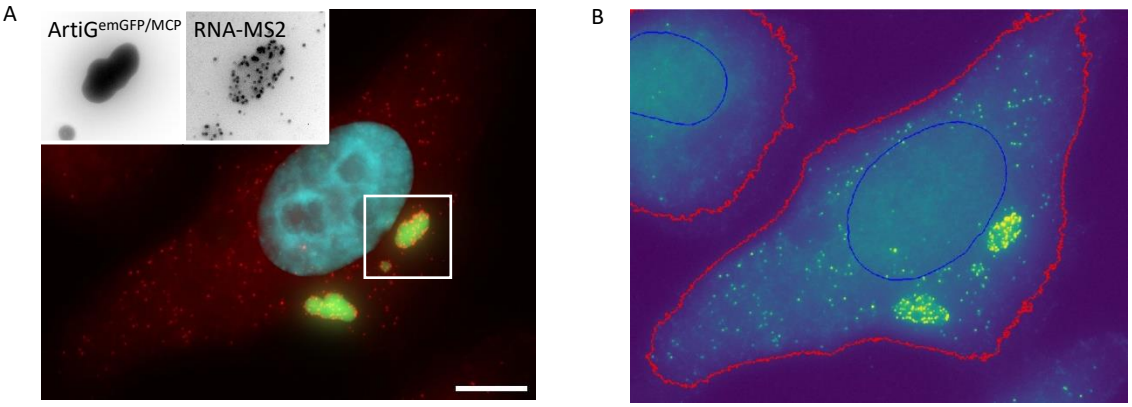

Figure II.9: Cell segmentation. A. Representative example of a HeLa cell expressing ArtiG$^{emGFP/MCP}$ condensates (green) and RNA-MS2 (red). The image is a 2D maximum projection of a z-stack acquisition. Bright dots in the cytoplasm correspond to individual RNA molecules. Numerous RNA molecules are recruited at the surface of the condensates. The region delimited by a white square is enlarged on the top left. Scale, 10 µm. **B.** Segmentation of the nucleus (blue line) and of the cell (red line) on the Cy3 channel (RNA-MS2 signal).

The second step consisted in detecting all the RNA molecules. First, all the local maxima (spots), which could be either individual or clustered RNA molecules, were detected (Fig. II.10A). RNA clusters were then decomposed: in a simplified view, a reference median spot was built from the predetected spots and the brighter regions were filled with as many reference spots as possible until matching the regions intensity (Fig. II.10B).

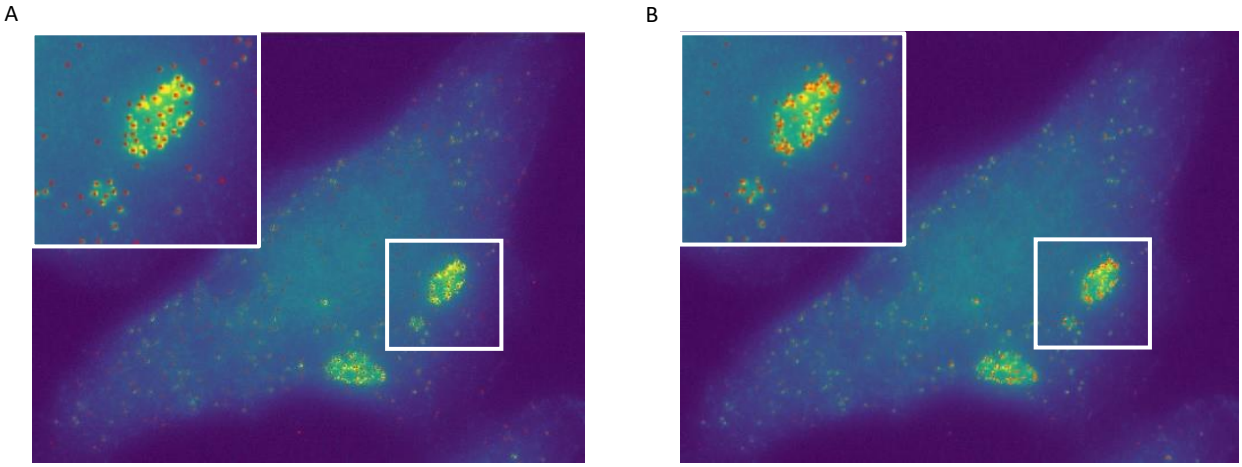

Figure II.10: Detection of RNA molecules. A. Detection of all local maxima, labeled by red dots. **B.** Decomposition of bright clusters in individual molecules of RNA, labeled by red dots. In (A) and (B), the area delimited by a white square is enlarged on the top left of the image.

The third step, once we had access to the total number of RNA molecules in the cell, was to count the number of recruited molecules on the condensates. The Big-FISH workflow was of course not particularly designed to do that, but I took advantage of the segmentation function that is used for the nucleus to segment the condensates. For each instance, I manually modified the threshold to fit to the cell expression. (Fig. II.11A). As the RNA molecules are at the surface of the condensates, I enlarged the detected condensates from a few pixels and then I compared the coordinates of each detected RNA molecule in the image to the condensates' coordinates, to keep only the recruited RNAs (Fig. II.11B).

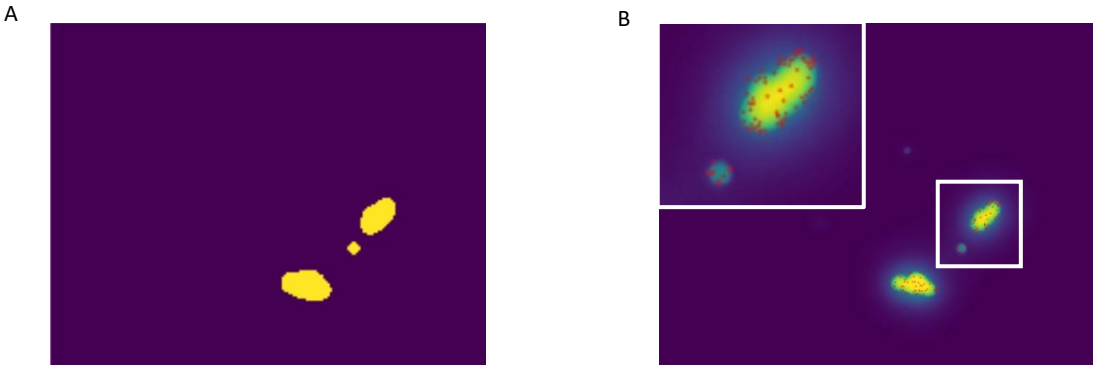

Figure II.11: Counting recruited RNA molecules. A. Detected condensates are marked in yellow. **B.** RNA molecules considered as recruited are marked with red dots on the emGFP channel (ArtiG$^{emGFP/MCP}$). The region delimited by a white square is enlarged on the top left.

Therefore, this workflow gives access to the number and the proportion of recruited RNA molecules on ArtiG$^{emGFP/MCP}$ condensates. By measuring the surface of the condensates, I could then calculate the RNA surface density.

CHAPTER III: Condensate functionalization with motors directs their nucleation in space and allows manipulating RNA localization

This chapter is based on the following pre-print:

Condensate functionalization with motors directs their nucleation in space and allows manipulating RNA localization

Audrey Cochard, Adham Safieddine, Pauline Combe, Marie-Noëlle Benassy, Dominique Weil, Zoher Gueroui

Posted on BioRxiv, July 10, 2022

doi: https://doi.org/10.1101/2022.07.10.499452

Contents

III.1. Examining the importance of subcellular localization of organelles and RNA

III.1.1. Repositioning assays to study membrane-bound organelles

Repositioning assays of organelles are interesting to investigate organelle dynamics, and establish causal relations between positions in cells and functions[148,149]. Positioning of organelles rely on cytoskeleton-based transport. Therefore, a first method to study the importance of organelles positioning consists in disrupting the microtubule network, for example by treating cells with nocodazole, an agent that binds to β-tubulin and disrupts microtubule assembly[150,151]. However, such action has broad effects on cell morphology and not only in the modification of organelles positioning. Fusion of a cytoskeleton-interacting element to an organelle-enriched membrane protein circumvents that issue and forces the transport of a specific organelle[152,153]. This strategy was applied to restore mitochondria presence in the axons of *ric-7 C. elegans* mutant, in which mitochondria are unable to exit the neuron cell bodies and axons show enhanced degeneration[153]. Fusing the Kinesin-1 motor to the Tom7 protein, that localized on the outer mitochondrial membrane (Fig. III.1A), rescued mitochondrial localization in the axons of *ric-7* mutants and suppressed the degeneration phenotype, thus demonstrating that mitochondria absence causes rapid axon degeneration[153].

To add temporal control, dimerization assays either based on chemical induction or on optogenetics were developed[149]. Chemically-induced dimerization (CID) using the FKBP-rapalog-FRB heterodimerization system[154], where FKPB or FRB is fused to an organelle-enriched protein while the other is fused to a motor protein or an adaptor of a motor protein, has been extensively used to induce irreversible delocalization of various organelles like mitochondria, peroxisomes, early or recycling endosomes, and lysosomes[152,155–162]. An example of application of this strategy is the rescue of peroxisome dynamics in mutant hTERT-RPE1 cells showing defects in contacts between peroxisomes and primary cilia and reduced ciliary cholesterol levels compared to non-mutant cells[161]. Addition of rapamycin in the mutant cells expressing fusions of FRB to the peroxisomal membrane protein Peroxisomal Biogenesis Factor 3 (PEX3-GFP-FRB), and of FKBP to the dynein adaptor BICD2 (tdTomato-BICD2-FKBP), targeted peroxisomes to the ciliary pocket and restored the ciliary pocket cholesterol level (Fig. III.1B). This study pointed out the peroxisome as a direct source of ciliary membrane cholesterol[161].

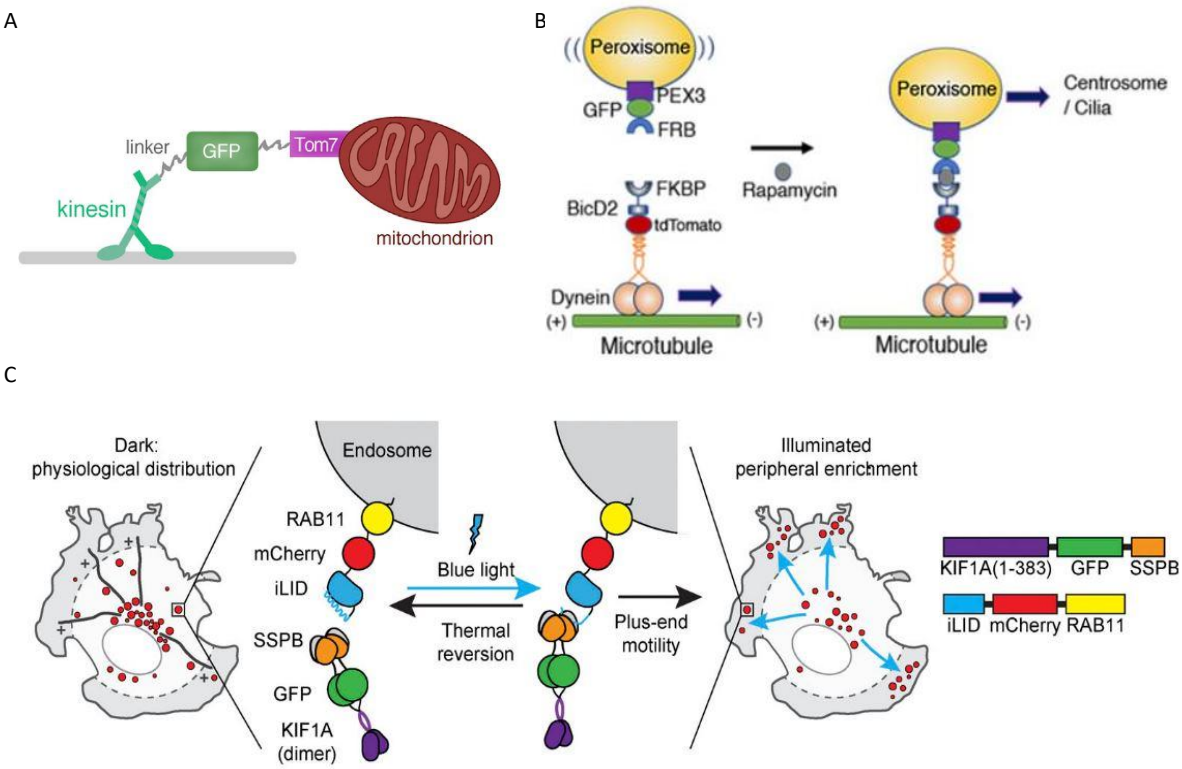

Figure III.1: Methods to reposition membrane-bound organelles in cells. A. Direct fusion of an organelle-enriched membrane protein, like here the Tom7 mitochondria protein, with a motor or motor adaptor protein, here Kinesin-1 motor. Adapted from[153]. **B.** FKBP-rapalog-FRB heterodimerization system: the addition of rapamycin or a rapalog induces the interaction between an organelle, here the peroxisome, and a motor, here the dynein via the dynein adaptor BicD2. Adapted from[161]. **C.** Optogenetics systems: light-induced dimerization of two binding partners, here iLID and SspB, one fused to an organelle membrane-protein, here the recycling endosome RAB11 protein, and the other to a motor, here the plus-end KIF1A motor. Adapted from[163].

The combination with an orthogonal dimerization system based on the plant hormone gibberellin allowed for the recruitment of two different motors on the same cargo[164,165]. A recently-developed split FKBP/FRB system opened new possibilities by allowing chemically-induced trimerization[166].

While CID enables a sustained motor activity, optogenetics enables spatiotemporal control of organelle transport in cells, with a rapid dissociation of the motor and the organelle after light extinction. Among the principal optogenetic strategies, TULIP tags rely on the fusion of the photoreceptor LOV2 domain of Avena sativa phototropin 1 to a peptide epitope. Caged in the dark, the peptide is freed by the unfolding of the LOV2 domain under blue light excitation and can then interact with a cognate domain[167]. Similarly, the LOV2-derived improved light inducible dimer (iLID) cages the bacterial SsrA peptide in the dark and prevents its binding to its partner SspB, while blue-light illumination allows for a > 25-fold affinity increase. TULIPs and iLID systems were successfully used to induce delocalization of organelles (Fig. III.1C)[158,163,168–171].

As with CID, the development of orthogonal systems enables the tethering of two different motors[172]. A recent study combined the sustained motor recruitment of CID with the reversibility of optogenetics by using a photolyzable dimerizer[173].

Repositioning studies have proven to be insightful. Indeed, in addition to the already discussed roles of mitochondria in preventing axon degeneration[153] and of peroxisomes in bringing cholesterol to the ciliary membranes[161], repositioning of organelles have brought to light other important cellular functions of organelles, like the roles of endosomes in axon growth[168] and of lysosomes in regulating ER distribution and morphology[171]. Besides uncovering links between mislocalization of organelles and pathologies, repositioning studies have also enabled to decipher how specific proteins and RNAs are transported, like AMPA receptors by recycling endosomes[156] and EEA1 mRNA by early endosomes[162], and to investigate the motile properties of endogenous or engineered motors[155,159,174], the motility of organelles linked to different motors[158,160,165], and the mechanisms of motor recruitment to organelles[157].

Though a plethora of membrane-bound repositioning studies have been carried out, no similar strategies have been applied to biomolecular condensates. In particular, such methods applied to artificial RNA-containing condensates could help investigate the localization of RNAs in cells through motor-based transport.

III.1.2. Examples of studies investigating the importance of RNA localization in cell

Different pathways underlie mRNA positioning in cells. Most of the time, mRNA localization relies on recognition of localization elements, or ZIP-codes, in the mRNA sequence by specific RBPs, and subsequent incorporation into ribonucleoprotein (RNP) complexes or larger granules that are then actively transported across cells by molecular motors. The ZIP code recognition is based on the primary sequence of the mRNA and on its secondary structure[175–177]. For example, the yeast *Saccharomyces cerevisiae* ASH1 mRNA accumulates at the bud tip during anaphase via co-transcriptional recognition of its four ZIP codes by the RBP She2, and then binding in the cytosol to She3, an adaptor of the myosin motor Myo4, which induces the transport to the bud of the complex along actin filaments (Fig. III.2, left panel)[178]. The She2-She3 complex similarly promotes the active transport of tens of mRNAs along actin filaments[175]. The β-actin mRNA in mammalian cell undergoes a similar active transport along both actin filaments and microtubules: it displays a bipartite motif recognized by the RBP zipcode-binding protein 1, which associates with still unidentified motors. mRNA can be transported as single mRNAs, as it is the case for example for a great majority of β-actin mRNAs in growing retinal ganglion cell axons in *Xenopus laevis* [179], or may belong to larger assemblies, that can be homotypic or heterotypic, i.e., they can contain several copies of one mRNA species or gather different mRNA species[175]. Because of the inherent ability of many RBPs to form multivalent interactions and drive LLPS (see Chapter I), mRNA transport often relies on incorporation into phase-separated condensates[175].

In addition to mRNA localization by integration into RNP complexes or into larger phase-separated assemblies directly associating with motors ensuing their directed transport in cells, other translocation strategies are at play. mRNAs can be recognized by RBPs that associate with moving vesicles like lysosomes and endosomes[11,180]. This “hitchhiking” phenomenon regulates for example the transport of the septin *cdc3* mRNA in the fungus *Ustilago maydis*, which associates with endosomes as part of an RNP complex (Fig. III.2, second to left panel)[181]. mRNA can also be localized by random active motor-based transport of RNP complexes or mRNA diffusion in cells, followed in both instances by a local anchorage at polarity sites. The *bicoid* mRNA thus localizes to the *Drosophila* oocyte anterior by random active transport mediated by dynein motors, towards the minus-end extremity of randomly orientated microtubules, followed by anterior anchoring (Fig. III.2, second to right panel)[182]. This localization provides a local source of bicoid proteins that diffuse to form a morphogen gradient required for embryonic patterning[182]. Nanos proteins also play a crucial role in the patterning of the anterior-posterior body axis of *Drosophila* oocytes, via local translation of *nanos* mRNAs at the posterior pole[183]. The localization of the *nanos* mRNAs relies here on diffusion processes and trapping at the oocyte posterior (Fig. III.2, right panel)[183]. These two last examples, *bicoid* and *nanos* mRNAs,

demonstrate the ability of cells lacking cytoskeletal polarity to still generate asymmetric RNA distribution.

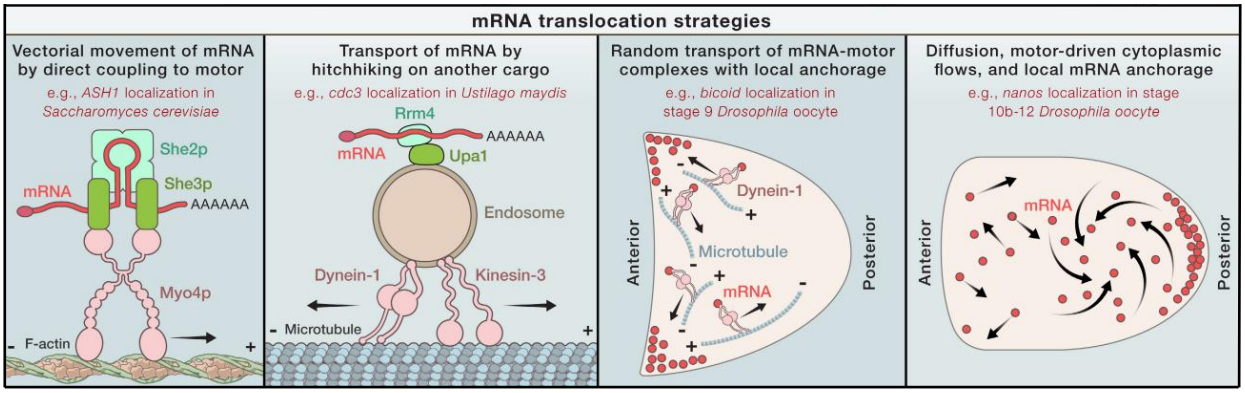

Figure III.2: Different translocation strategies to localize mRNA in cells. Adapted from[184]. A. Some mRNAs, like the yeast *Saccharomyces cerevisiae* ASH1 mRNA are localized via directed transport of RNP complexes by direct coupling to motor proteins. **B.** Some mRNAs, like the septin cdc3 in the fungus *Ustilago maydis*, are "hitchhiking" on moving organelles like endosomes. **C.** Some mRNAs, like the *Drosophila* oocyte *bicoid* mRNA, undergo random motor-based transport followed by local anchoring. **D.** Some mRNAs, like the *Drosophila* oocyte *nanos* mRNA, are localized via diffusion followed by local anchoring.

One pathway of mRNA mislocalization, consisting in mutating the ZIP code sequence or modifying its secondary structure to impede its recognition by RBP partners, was successfully applied in various organisms, like the yeast and the drosophila, and cell types, like neurons[129,178,185,186]. By using this method, a recent study highlighted for the first time in the yeast *Saccharomyces cerevisiae* cyclin CLB2 mRNA as an example of mRNA localized translation that does not lead to protein co-localization[185]. On the contrary to ASH1 mRNA, whose local translation in the yeast bud allows local translation and segregation of the protein in the bud, CLB2 protein is localized in the mother nucleus. In this study, mutagenesis of the coding sequence was used to destroy the ZIP code structure without altering the protein sequence (Fig. III.3.A)[185]. As expected, the CLB2 mRNA localization in the yeast bud was lost (Fig. III.3.B). Interestingly, the loss of mRNA localization had an impact on protein synthesis, which was significantly reduced for the mutant mRNA compared with the wild-type mRNA. This suggested that CLB2 mRNA localization was required for efficient translation in the bud, followed by translation of the protein back to the mother nucleus. The authors proposed that the shuttling back of CLB2 proteins to the mother nucleus acts as a sensor of the bud translation capacity and signals to the mother cell when the bud is ready for mitosis. This study thus revealed a novel function for mRNA localization.

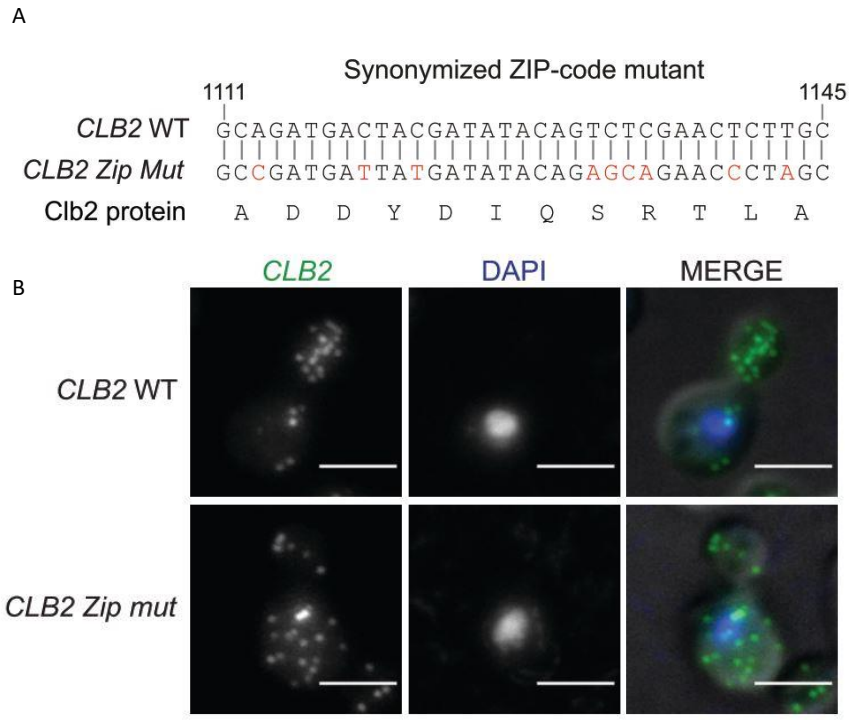

Figure III.3: Mutating the ZIP code sequence of the yeast *Saccharomyces cerevisiae* cyclin CLB2 mRNA successfully impedes its bud localization. Adapted from[185]. A. Nucleotide sequences of the wild-type and mutant CLB2 (top and bottom sequences, respectively), which have an identical corresponding amino acid sequence, given below. **B.** Visualization of CLB2 mRNAs for the wild-type and mutant strain via smFISH (green in merge). Nuclei are stained with DAPI (blue in merge). Scale, 3 µm.

As illustrated by the study on the yeast CLB2 mRNA, ZIP code mutations can be very powerful to impede proper mRNA localization and decipher the consequences of mRNA localization. However, this method results in a dispersion of the target RNA, unable to interact with its partner RBPs, but does not allow for a precise repositioning of the RNA in cell. Controlling localization of a target RNA in cells would facilitate the assessment of the importance of subcellular RNA localization. In that spirit, the PUF (Pumilio and FBF homology domain)-assisted localization of RNA (PULR) system was developed to induce the transport of a heterelogously-expressed or endogenous PUF target mRNA[187]. The system takes advantage of the PUF RBD of human Pumilio 1 protein, which was prevented from binding its hundreds of endogenous mRNA partners by modifying its recognition sequence so that it would have a significantly smaller number of partners. The PUF domain was subsequently fused with one or two consecutive FKBP protein(s) and the enhanced green fluorescent protein (eGFP) (Fig. III.4A). The FRB protein, which very efficiently dimerizes with FKBP in presence of rapamycin or a rapalog, was fused to either a truncated plus-end kinesin-1 KIF5B or the N-terminal of the Bicaudal D2 (BICDN), an adaptor of the dynein motor protein (Fig. III.4A). The system was first assessed with a

heterologous mRNA, the Firefly luciferase (FLuc) mRNA, on which 10 PUF-binding sites were added in the 3'UTR (Fig. III.4A). Upon addition of a rapalog, the induced dimerization of FKBP and FRB proteins successfully led to the transport and accumulation of the target FLuc mRNA to the cell periphery for KIF5B (Fig. III.4B and C) or to the centrosome for BICDN (Fig. III.4D and E). Then, the PUF sequence was mutated to recognize a sequence in β-actin mRNA. The KIF5B-based transport system successfully increased the level of β-actin mRNA in the growth cone of embryonic rat hippocampal neurons. The PULR system can thus localize both tagged mRNA and endogenous untagged mRNA.

Another interesting strategy would be to reconstitute an mRNA transport system by incorporation of a target mRNA into a phase-separated condensate. In that spirit, the second part of my Ph.D. aimed first at building for the first time artificial phase-separated condensates with controlled localization in cells, and in a second time at recruiting a target mRNA in the condensates to obtain its reposition.

To do so, we first developed a derivative of the ArtiGranule system. Indeed, the ArtiGranule system is very robust and can be functionalized by fusion of proteins of interest at the N-terminal of the Ferritin monomers. However, the C-terminal is not available for fusion, as it would prohibit the formation of the nanocage. We thus designed a linear system based on five repetitions of the Fm protein, and thus called 5Fm, in order to expand our toolbox and to have a more versatile system (Fig. III.5). In the next sections, the linear 5Fm system will be detailed, and the workflow of the study will be explained.

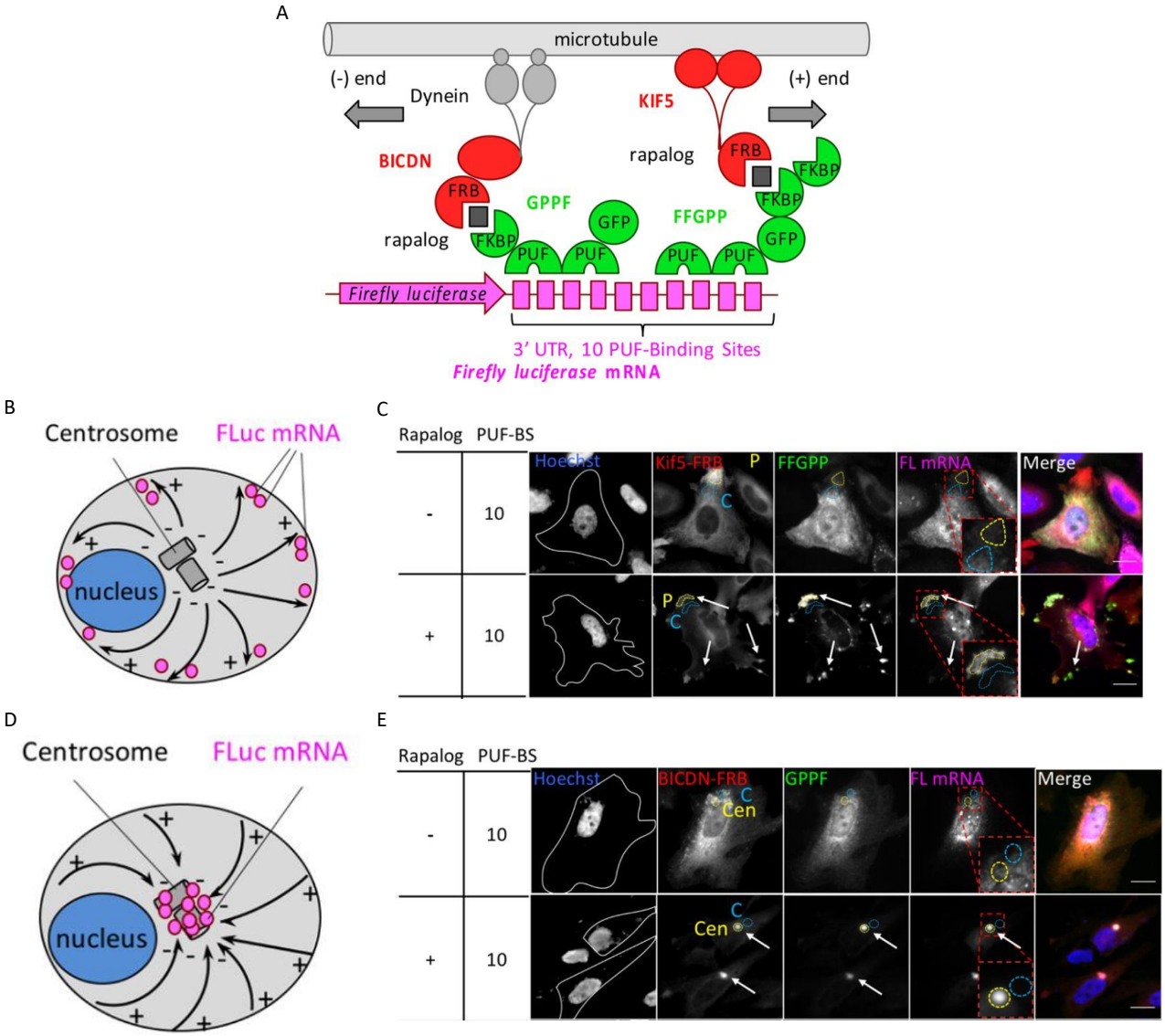

Figure III.4: PULR system can localize a target mRNA in cells. Adapted from[187]**. A.** Schematic of the PULR system: in the presence of a rapalog (black squares), the PULR module proteins transport the reporter FLuc mRNA to the plus (+) or minus (-) ends of microtubules, depending on the involved motor protein. **B.** Schematic of the KIF5B-mediated transport, with microtubules represented as black arrows pointing to their (+) ends. **C.** Fluorescence images of Hela cells expressing the KIF5B-based PULR modules in the absence or presence of rapalog (top and bottom panels, respectively). The mRNA is imaged by smFISH (pink in merge). Arrows indicate enriched spots. Nuclei are stained with Hoechst (blue in merge). Scale, 20 µm. **D.** Schematic of the BICDN-mediated transport, with microtubules represented as black arrow pointed to their (-) ends. **E.** Same as (C) for the BICDN-based PULR system.

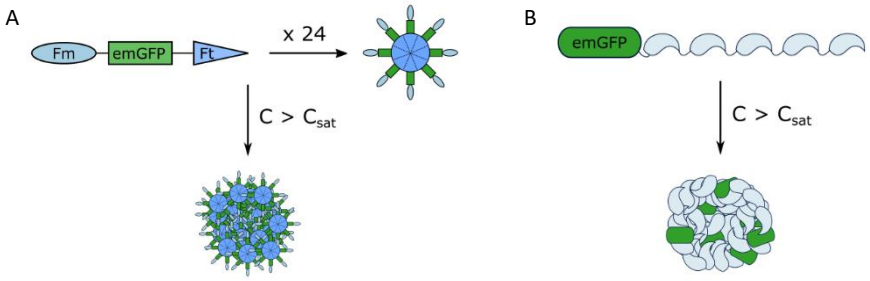

Figure III.5: Comparison of the scaffolds of the ArtiGranule (left) and 5Fm (right) systems.

III.1.3. The linear 5Fm system

The 5Fm system was inspired by reconstitution studies *in vitro* or in cells of condensates based on linear repeats of folded domains able to heterodimerize, like SH3/PRM and SUMO/SIM, and by the iPOLYMER system[21,37,84]. On the contrary to the latter approach that requires rapamycin to induce FKBP/FRB interactions, here we used five repeats of the self-dimerizing Fm protein, separated by flexible linkers to facilitate Fm-Fm interactions (5Fm, Fig. III.6A). Transfection of the 5Fm construct, labeled with fluorescent proteins for visualization, led, like for ArtiGranules, to condensates displaying liquid-like properties, as expected for phase separated condensates: they are spherical (Fig. III.6B), have the ability to coalesce, contain a mobile fraction pointed out by FRAP experiments (a fraction of the fluorescent signal (40%) recover with a timescale of about 2 minutes, Fig. III.6C), and buffer the dilute phase as revealed by the existence of a C_{sat}. The divergence of material properties between these condensates, that exhibit a liquid-like behavior, and the bodies obtained with the iPOLYMER method, that are gel-like, can be explained by the difference in the strength of interaction of the modules. The FKBP/FRB interaction (K_d in the nm range) is indeed much stronger than the homodimerization of Fm proteins (K_d in the µm range)[188].

Like the ArtiGranule system, the formation of 5Fm condensates is based on the Fm-Fm dimerization. Thus, condensate formation can be impeded by the addition of FK506 right after transfection, and addition of the chemical competitor after formation of the condensates very efficiently dissolves them.

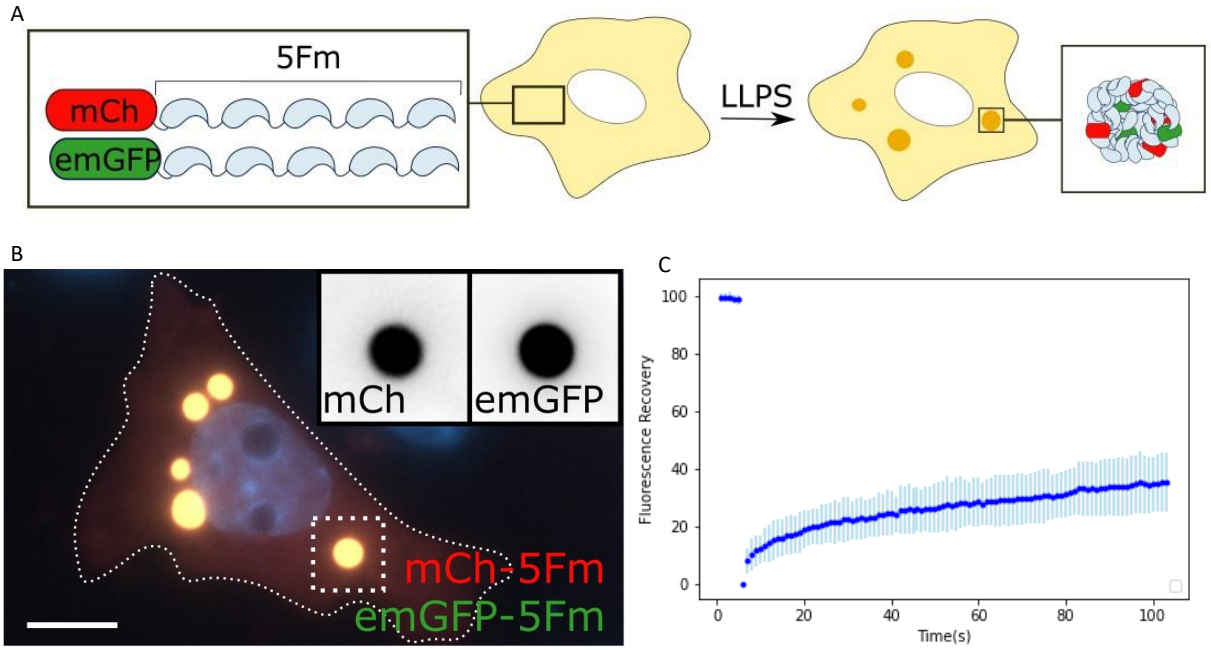

Figure III.6: The 5Fm system. Adapted from Cochard et al., BioRxiv, 2022. A. Schematic of the 5Fm system. **B.** Representative epifluorescence image of a HeLa cell expressing spherical 5Fm condensates 24 h after transfection of mCh-5Fm and emGFP-5Fm. The nucleus was stained with DAPI (blue in merge). Grayscales inserts correspond to separate channels of the zone delineated by a white dashed square. Scale bar, 10 µm. **C.** Mean of fluorescence recovery after photobleaching (N = 9 condensates, unpublished).

III.1.4. Workflow to build RNA-containing artificial condensates localized in cells

To build artificial biomolecular condensates with controlled localization in cells, we fused motor or motor adaptor domains to the scaffold of our linear 5Fm system. We investigated two plus-end kinesin motor proteins (KIF1A and KIF5B), one minus-end motor (KIFC1) and one adaptor of the dynein motor protein (BICD2). Fixed cell imaging and immunofluorescence assays to image the centrosome were used to investigate the localization of our artificial condensates, which showed robust asymmetrical localization either at the cell periphery or near the centrosome, depending on the motor at play (Fig. III.7A). To investigate the pathway of localization, we turned to live imaging by confocal microscopy, which revealed a localized nucleation. In addition to this system, we developed a method to induce the transport and localization of preformed condensates in cells. To do so, we took advantage of the FKBP/FRB chemically-induced dimerization to bridge motor domains and condensates.

In a second time, we investigated the possibility to use our system to localize a mRNA in cell. We used the MCP RBP, which, as a reminder of the previous chapter, specifically binds to RNA stem loops of the MS2 bacteriophage genome, called MS2 stem loops. We first targeted the same heterelogously-expressed RNA-MS2 as in Chapter II, that we visualized by smFISH. In a second step, our collaborator A. Safieddine made use of a stable cell line he developed previously to target a MS2-tagged endogenous ASPM mRNA, which normally localizes at the centrosome during mitosis (Fig. III.7B)[189].

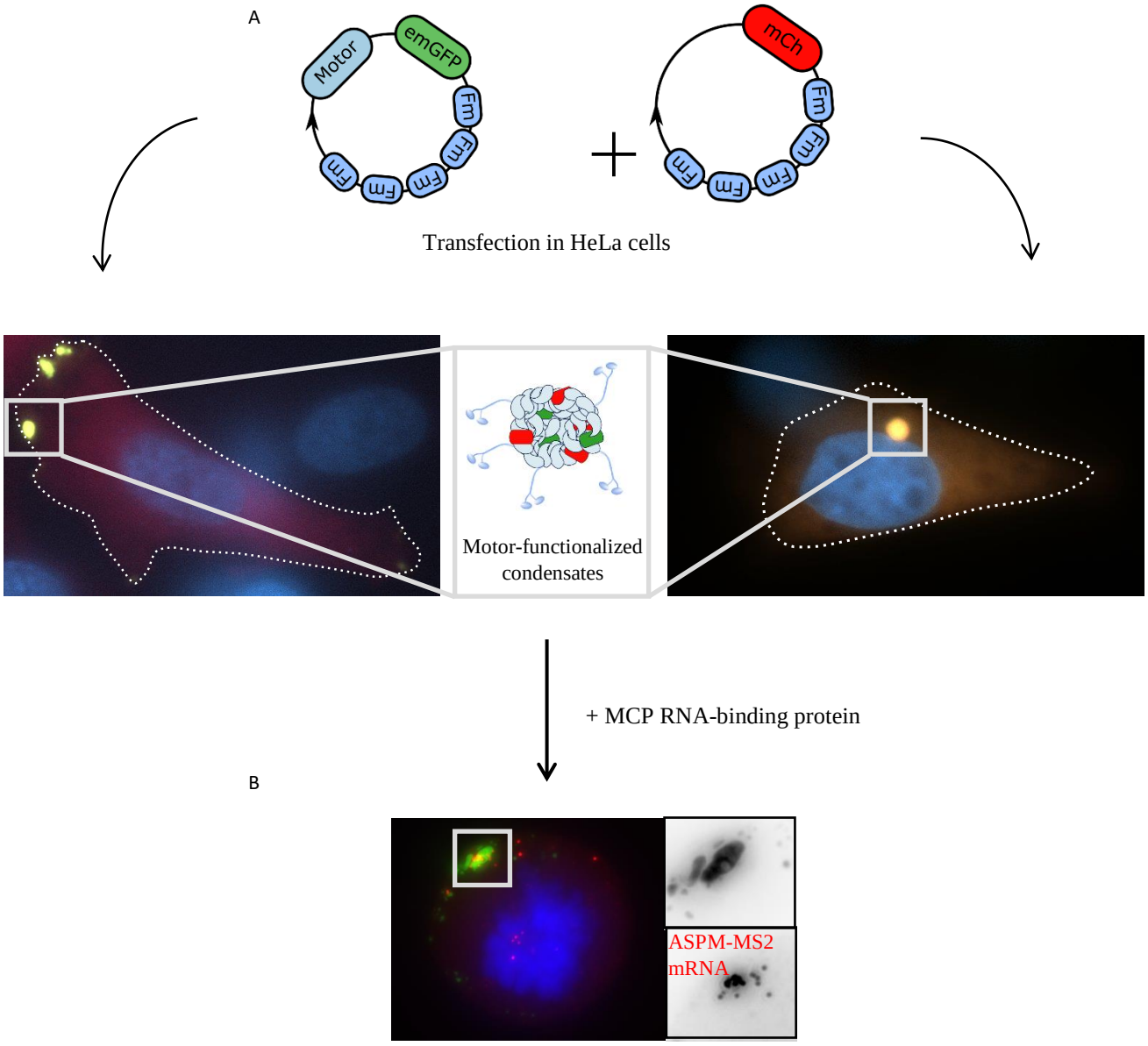

Figure III.7: Schematic of the strategy to reconstitute RNA-containing localized condensates in cells. Adapted from Cochard et al., BioRxiv, 2022. A. Transfection of fusions of the 5Fm module with motor domains to localize artificial condensates in cells. **B.** Condensates functionalized with plus-end motor domains and MCP (green in merge) delocalizes ASPM-MS2 mRNA (labeled by smFISH, red in merge) from the centrosome to the cell periphery in mitotic cells.

III.2. Article and supplementary information

Condensate functionalization with motors directs their nucleation in space and allows manipulating RNA localization

Audrey Cochard[1,2], Adham Safieddine[2], Pauline Combe[1], Marie-Noëlle Benassy[2], Dominique Weil[2], Zoher Gueroui[1]*

1- Department of Chemistry, École Normale Supérieure, PSL University, Sorbonne Université, CNRS, 75005 Paris, France.
2- Sorbonne Université, CNRS, Institut de Biologie Paris-Seine (IBPS), Laboratoire de Biologie du Développement, F-75005 Paris, France.

* zoher.gueroui@ens.fr

ABSTRACT

The localization of RNAs in cells is critical for many cellular processes. Whereas motor-driven transport of RNP condensates plays a prominent role in RNA localization in cells, their studies remain limited by the scarcity of available tools allowing to manipulate condensates in a spatial manner. To fill this gap, we reconstitute *in cellula* a minimal RNP transport system based on bioengineered condensates which were functionalized with kinesins and dynein-like motors, allowing for their positioning at either the cell periphery or centrosomes. This targeting mostly occurs through the active transport of the condensate scaffolds, which leads to localized nucleation of phase-separated condensates. Then, programming the condensates to recruit specific mRNAs is able to shift the localization of these mRNAs towards the cell periphery or the centrosomes. Our method opens novel perspectives to examine the role of RNA localization as a driver of cellular functions.

INTRODUCTION

The spatial organization of signaling network and biochemical reactions is of vital importance for many cellular functions. To organize the cell inner space, biomolecules and subcellular structures can be dispatched by active transport mechanisms. Long-range motor-based transport of cellular compartments along cytoskeletal networks is essential for rapid reorganization of the cellular space in response to environmental changes[1]. Microtubule-based transport is for instance necessary for the endocytic pathway, for long-distance transport of mitochondria and for lipid droplets contacts with organelles[2–4]. Although less documented than membrane-bound organelles, biomolecular condensates are also prone to interact with cytoskeletal fibers in various ways. As the main microtubule organizing center, the centrosome can be viewed as a condensate facilitating microtubule nucleation by concentrating tubulins[5]. Other examples include RNA-containing condensates such as stress granules and P-bodies, whose growth by fusion and disassembly by fission involves by microtubule-based transport[6–11]. The functional importance of condensate-microtubule interactions is also exemplified by the transport and localization of mRNAs through RNP granule transport.

Subcellular mRNA localization is a widespread process that involves mRNA transport as isolated molecules or as part of phase-separated RNP condensates[12,13]. This localization is vital for many developmental and cellular processes, from the establishment of embryo polarization to local protein synthesis at the synapses[14,15]. Motor-based positioning of specific mRNAs and subsequent local translation has for instance been described during the establishment of asymmetrical processes such as morphogen gradients in developing embryo[16–19], cell migration[20], neural development and synaptic plasticity[21,22]. Additionally, disruption of axonal RNP granule transport is associated with a broad range of neurodegenerative diseases[23,24]. Localizing mRNAs and RNP granules, rather than proteins, into subcellular compartments before translation favors spatially restricted protein synthesis and provides 'outposts' operating far from the soma[25,26]. In addition, localizing mRNAs is likely to be more energy-efficient than moving separately each protein to the right location[25].

Due to the critical importance of RNA localization to cell fate determination, numerous methods were recently developed to describe how RNAs find their way to distinct subcellular compartments, and how this impacts RNA functions and processing. For example, the direct visualization of RNA molecules in living cells and organisms has been instrumental to elaborate our current understanding of RNA localization mechanisms[27,28]. Complementary to imaging approaches, transcriptomic RNA sequencing-based methods also described a variety of RNAs enriched in specific subcellular areas[29–31]. Motor proteins from all three families, i.e., kinesin, dynein, and myosin, have been identified as the drivers of short- and long-range mRNA transport along the cytoskeleton[32,33]. Though further studies are necessary to decipher the building blocks required to recruit, direct and release specific mRNAs to a particular destination, one recurrent scenario involves RNA binding proteins (RBP) and motor adaptors, linking mRNAs and motor proteins[12,34–37].

Beside its role in guiding long-range transport, the cytoskeleton also contributes to the mechanical integrity of cells. Due to its inherent heterogeneity and dynamic nature, determining how such a meshwork impacts RNP condensation remains difficult to quantify. Yet, some biophysical implications of the cytoskeleton meshwork on phase separation mechanisms have

recently started to be investigated both theoretically or experimentally. For example, the cytoskeleton modeled as an elastic meshwork, and acting at length scales comparable to condensate sizes, has been seen to modify nucleation and coarsening of phase separation systems[38–40]. In the very large *Xenopus* oocytes, the actin meshwork provides steric hindrance limiting nucleolar fusion as well as counter balancing sedimentation by gravity[41]. In epithelial cells, it has been shown that weak and non-specific interactions between cytoskeleton elements and the condensate surface may account for mutual influences[42]. One missing element in this description is the effect of molecular motors on phase-separated condensates to explore how transport could shape condensate formation and localization. To fill this gap, and examine how motor proteins could impact RNP phase separation, we adopted an approach allowing the reconstitution in cells of motor-functionalized condensates.

Novel tools have been developed allowing the formation of artificial condensates with programmable properties in cells. Indeed, such technologies bring novel perspectives both for addressing new biological questions and for further biotechnological improvements[43–54]. In this context, we engineered artificial condensates made of protein scaffolds that are prone to phase separate and functionalized them to interact with microtubule-bound motor proteins. Our first aim was to examine how motor proteins would affect condensate formation and localization. A second goal was to build minimal RNP condensates recruiting a unique RNA, making it possible to explore condensate-mediated RNA delocalization.

Condensates are thought to form through liquid-liquid phase separation (LLPS) induced by weakly interacting multivalent biomolecules. Based on this observation, our system relies on a self-interacting multivalent protein driving the formation of the condensates and fused to microtubule-interacting domains (from either a motor protein or a motor adaptor). We previously developed the ArtiGranule system, which relies on multivalent cores of ferritin monomers cross-linked by the self-interacting domain F36M-FKBP (Fm)[46,54]. Here, we replaced the ferritin core by a multimerization domain consisting of five consecutive Fm repeats (5Fm)[55]. We investigated two plus-end motors (KIF1A and KIF5B), one minus-end motor (KIFC1) and one adaptor of the dynein motor protein (BICD2). We first showed that the resulting scaffold proteins underwent LLPS in cells and that condensates functionalized with plus-end kinesins (thereafter called plus-end motor-condensates) were robustly positioned at the edge of cells. In contrast, condensates functionalized with the minus-end kinesin or the dynein adaptor (thereafter called minus-end motor-condensates) eventually formed a unique body at the centrosome. Interestingly, the localization of condensates was determined at the nucleation step. Our observations support a two-step process; first, motors moved quickly either towards the cell periphery or the centrosome, depending on the motor; then this led to the local accumulation of the multivalent protein on microtubules, and eventually to the formation of asymmetrically positioned large condensates through phase separation. In the case of BICD2, we additionally observed some condensate nucleation throughout the cytosol, followed by their directed transport to the vicinity of the centrosome and their coalescence.

In addition to our assay based on constitutive interactions between condensates with microtubules, we also developed a system where condensate interaction with motors or dynein adaptors could be chemically triggered using a chemically-inducible dimerization strategy[56]. Here, we observed that, upon induction of their interaction with the cytoskeleton, preformed

condensates re-localized at the cell periphery or at the centrosomes, depending on the directionality of the motors.

Finally, we engineered motor condensates programmed to recruit either exogenous or endogenous mRNAs, using the MS2-MCP (MS2 Coat Protein) system. We found that bi-functionalized condensates, with both MCP and motor proteins (motor/MCP condensates), were asymmetrical positioned in cells and recruited heterologous MS2-containing mRNAs. We then studied the ASPM mRNA, which normally localizes at the centrosome during mitosis[57] and showed that our motor/MCP condensates successfully perturb the spatial distribution of endogenous MS2-tagged ASPM mRNA.

RESULTS

Plus-end motor condensates localize at the periphery of cells

To build model condensates functionalized with plus-end kinesin motors in living cells, we generated a chimeric construct composed of two functional parts: a multivalent protein domain triggering LLPS in cells, fused to a kinesin motor domain to ensure trafficking along microtubule tracks. As a multivalent protein domain, we designed the 5Fm module, composed of five repetitions of the dimerizable mutant F36M of the FKBP protein (Fm) (Fig. 1A)[55]. Expression of emGFP-5Fm and mCh-5Fm in HeLa cells for 24h led to the formation of hybrid micrometric condensates composed of both emGFP and mCherry fusion proteins and randomly localized throughout the cytosolic space (Fig. 1B, left panel). For the kinesin motor domain, we first considered a truncation of the human kinesin-3 KIF1A (aa 1-383), which ensures the processivity of the motor (Fig. 1A)[58,59]. KIF1A(1-383) was fused to emGFP-5Fm (giving rise to the KIF1A-emGFP-5Fm plasmid), and the localization of the fusion protein was compared to the control LLPS scaffold emGFP-5Fm lacking any motor. Interestingly, when both the motor-LLPS scaffold (KIF1A-emGFP-5Fm) and the LLPS scaffold (mCh-5Fm) were co-expressed in HeLa cells during 24h, chimeric condensates were mostly found localized at the vicinity of the cell periphery, next to the membrane. In these conditions, almost all cells displayed highly asymmetrical localization patterns, often consisting of 3-5 micrometric condensates per cell (Fig. 1B, middle panel). To quantify the degree of asymmetry among cells, we measured the fraction of mCherry fluorescence, *i.e.* of the non-motor part of the scaffold, in the 25% peripheral area of the cells (I_{25}) (Methods)[58]. Using the motor-less scaffold, as expected, condensates did not display any asymmetrical positioning and gave a I_{25} value of 20% +/- 9% (mean +/- SD, Fig. 1C). In contrast, for the chimeric condensates containing the KIF1A(1-383) motor, the I_{25} value was higher (34 +/- 9 %), in accordance with the visualization of asymmetric patterns. Therefore, KIF1A condensates are efficiently localized at the cell periphery.

In order to extend our assay, we next examined cells expressing a second plus-end directed motor domain fused to LLPS scaffolds, KIF5B(1-555)-emGFP-5Fm (Fig. 1A). The KIF5B(1-555) truncated proteins contains the motor and neck domains and part of the coiled-coil domain of mouse KIF5B[60]. As with KIF1A-LLPS scaffolds, epifluorescence imaging of

HeLa cells 24 h after co-transfection of KIF5B-LLPS scaffolds (KIF5B-emGFP-5Fm) and LLPS scaffolds (mCh-5Fm) showed an asymmetrical localization of condensates at the periphery of cells (Fig. 1B, right panel). In accordance with these observations, the I_{25} value was 32% +/- 8% (mean +/- SD, Fig. 1C). Altogether our data showed that plus-end kinesin condensates are robustly positioned at the edge of cells.

To verify that the motor domain needs to be part of the LLPS scaffold for the condensate to be relocated, we examined the localization of non-functionalized LLPS scaffold (mCh-5Fm) in the presence of motor domains lacking the 5Fm multivalent domain (KIF1A-emGFP or KIF5B-emGFP). In these conditions, mCherry condensates were randomly dispersed throughout the cytosol, (Fig. S1A, red), whereas the motor domains accumulated in some regions of the cell periphery as expected (Fig. S1A, green). As a second control, we assessed the importance of multivalent LLPS scaffold interactions in the localization of plus-end motor condensates. By design, condensates should be disrupted by adding a competitive ligand of Fm dimerization (FK506). HeLa cells were transfected with KIF1A-emGFP-5Fm and mCh-5Fm, and FK506 was added at micromolar range either directly after transfection (to probe condensate formation) or 24 hours after transfection (to probe condensate dissociation). In both situations, after 26 hours of transfection, we found an absence of condensates (Fig. S1B, red) and a motor domain signal that either formed a gradient of concentration towards some regions of the cell periphery or was homogeneously diffuse in the cytoplasm (Fig. S1B, green). Time-lapse microscopy following addition of FK506 24 h after transfection showed a very fast dissolution of the condensates, with the LLPS scaffold (mCherry signal) diffusing in the whole cell in a few seconds and the motor-LLPS scaffold (emGFP signal) losing its condensed state but remaining at the cell periphery. Our method thus allows for the controlled inhibition and disassembly of plus-end motor condensates upon drug addition.

Dynamics of formation and localization of plus-end motor condensates

While condensate positioning at the cell periphery is consistent with an active transport mediated by plus-end motors along microtubules, the localization kinetics remained to be determined. One possible chronology is, first, condensate nucleation throughout the cytosol, followed by condensate transport along microtubules. Alternatively, transport of LLPS scaffolds powered by motors could first induce their accumulation at peripherical sites, which would then trigger local condensate nucleation. To distinguish between the two scenarios, we monitored the early times of condensate formation using time-lapse microscopy (Supplementary movie 1). 4 h after co-transfection of KIF1A-LLPS and LLPS scaffolds (KIF1A-emGFP-5Fm and mCh-5Fm), we firstly noticed the strong accumulation of the motor scaffolds at the tips of the cells, illustrating the capacity of kinesins to localize within short time scales (Fig. 1D). Very often, the fast peripheral nucleation of KIF1A condensates occurred as soon as fluorescent KIF1A-LLPS scaffolds became detectable in the cytosol (Fig. 1E). These condensates tended to grow to eventually form large spherical bodies that could reach few micrometers. In addition, nearby condensates tended to coalesce (Fig. 1F).

Interestingly, we found that KIF1A-LLPS scaffolds condensed systematically ahead of LLPS scaffolds, with LLPS scaffolds then accumulating in preformed KIF1A condensates (Fig. 1D). This contrasts with the intrinsic ability of LLPS scaffolds to form randomly localized condensates, as seen in cells expressing KIF1A-emGFP lacking the LLPS domain (Fig. S1A).

Altogether, these observations indicate that KIF1A condensates recruit the non-functionalized LLPS scaffolds, thus preventing their independent phase separation. In addition to peripheral condensate nucleation, we also observed rare events of long-ranged (2 to 5 µm/min) condensate transports towards the periphery (Fig. S1C).

The same dynamic characteristics were found when observing the formation of KIF5B condensates (KIF5B-emGFP-5Fm and mCherry-5Fm) (Supplementary movie 2). Early observations of KIF5B-LLPS scaffolds showed an immediate asymmetrical pattern, with a sharp gradient of fluorescence forming at the membrane and shortly preceding nucleation events (Fig. 1G). The condensation of KIF5B-LLPS scaffolds at the cell periphery also occurred ahead, followed by the recruitment of LLPS scaffolds (Fig. 1H). Condensates in close proximity tended to coalesce (Fig. 1I). As for KIF1A condensates, rare directed transport events were observed (Fig. S1D).

Taken together, our observations showed that condensate positioning at the cell periphery occurred predominantly by nucleating phase separation directly at the final sites rather than by transporting already formed condensates to their destination.

Minus-end motor condensates localize at the centrosomes

We next examined the positioning of condensates using minus-end motors conjugated to LLPS scaffolds. We first used the human KIFC1(125-673) truncation that includes the coiled coil and motor domains required for motor processing[60]. KIFC1(125-673) was fused to emGFP-5Fm, and the resulting emGFP-5Fm-KIFC1 scaffold was co-transfected along with the LLPS scaffold (mCh-5Fm) in HeLa cells (Fig. 2A). Strikingly, after 24 h of expression, most cells displayed a single condensate in the cytosol near the nucleus (mean number of condensates per cell = 1.4 +/- 0.9, Fig. 2B, middle panel, and Fig. 2C). This contrasted with control cells transfected only with LLPS scaffolds (emGFP-5Fm and mCh-5Fm), which displayed in average 4 condensates per cell (mean +/- SD = 4.0 +/- 3.0, Fig. 2B, left panel, and Fig. 2C). As an alternative to minus-end kinesin motor, we also assessed the mouse dynein adaptor BICD2 (aa 15-595)[60]. We co-transfected BICD2-emGFP-5Fm along with the LLPS scaffold (mCh-5Fm) in HeLa cells (Fig. 2A). As observed with KIFC1, most cells displayed after 24 h a single condensate localized near the nucleus (mean number per cell = 1.2 +/- 0.6, Fig. 2B, right panel, and Fig. 2C). Interestingly, for both KIFC1 and BICD2, the single condensates docked at the centrosomes, as demonstrated by immunostaining of pericentrin (Fig. 2D). Altogether, minus-end motor functionalization of LLPS scaffold robustly led to the formation of a single condensate at the centrosome.

As expected, the control co-expression of motor constructs lacking the LLPS multivalent domain (emGFP-KIFC1 or BICD2-emGFP) and non-functionalized LLPS scaffold (mCh-5Fm) led to cells displaying mCherry condensates randomly distributed though the cytosol (Fig. S2A). Of note, unlike the efficient peripheric localization of KIF1A-emGFP and KIF5B-emGFP, we observed little centrosomal accumulation of emGFP-KIFC1 or BICD2-emGFP. As for the plus-end kinesin scaffolds, adding the Fm competitor ligand FK506, immediately or 24h after transfection, suppressed condensates (Fig. S2B). These controls demonstrated the requirement of motor-LLPS scaffolds to localize condensates, as well as the need of a multivalent scaffold to trigger LLPS.

Dynamics of formation and localization of minus-end motor condensates

To examine the pathway leading to the emergence of single condensates at the centrosomes, we monitored the early steps of their formation, starting 4 hours after transfection of emGFP-5Fm-KIFC1 or BICD2-emGFP-5Fm along with mCh-5Fm (Supplementary movies 3 and 4). In both cases, we found that condensates primarily nucleated at the vicinity of the nucleus (Fig. 2E-F). This led to the emergence of a single condensate that kept on growing, including by coalescence of smaller condensates appearing nearby. As observed with the plus-end motors, the non-functionalized scaffold accumulated exclusively at the site of motor condensates (Fig. 2E-F). In the case of BICD2 condensates, we also observed long-range transport of condensates nucleated far from the nucleus, coalescing into one large condensate during transport (Fig. 2F and S2C).

Taken together, our observations showed that minus-end motor condensates mainly nucleate at the vicinity of the nucleus, and then recruit non-functionalized scaffolds.

The timing of non-functionalized scaffold enrichment into motor condensates depends on their localization in cells

One interesting feature shared by the four motor condensates is their ability to capture the non-functionalized LLPS scaffolds. Yet, the intracellular space being very heterogenous in term of physical properties, such as crowding and geometry, condensates' subcellular location may impact some of their characteristics. To examine further this aspect, we studied more closely the enrichment of non-functionalized scaffolds into condensates depending on their localization in cells. We quantified the delay between the initial nucleation of motor condensates and the first discernible enrichment of the non-functionalized LLPS scaffold. We found that co-localization occurred after 1 to 2 hours using the plus-end motors (mean 83 min with a coefficient of variation CV of 40% and 74 min with a CV of 39% for KIF1A and KIF5B, respectively, Fig. 3A and 3B), contrasting with less than 20 min using the minus-end motors (mean 8 min with CV of 163% and 18 min with CV of 89% for KIFC1 and BICD2, respectively, Fig. 3A and 3C). Therefore, the delay of LLPS scaffold enrichment into preformed motor condensates was much longer for plus-end than minus-end motors. This difference in temporality may result from two non-exclusives factors: first, plus-end and minus-end motor condensates localized in two different areas of the cell where the pool of available LLPS scaffold may strongly differ because of the cell geometry, narrower at the periphery than close to the nucleus (Fig. 3D). Additionally, molecular crowding may strongly vary between the centrosome and the cell membrane area. Secondly, the processivity of our plus-end and minus-end motor differ, with only the plus-end motor scaffolds leading a rapid leap in concentration and condensate nucleation (Fig. 1E and 1G). Nucleation could thus occur before the non-functionalized LLPS scaffold reaches a sufficient concentration for enrichment. Altogether our data show that the timing of the enrichment of non-functionalized scaffolds into motor condensates depends on their localization in cells.

Chemical induction of condensate transport and localization

Several endogenous condensates were found to interact and undergo transport along the cytoskeleton tracks[61]. Our motor-LLPS scaffolds could, by design, constitutively interact with microtubule fibers as soon as they are translated. We thus sought to examine the consequence

of a sudden induction of the interaction between condensates randomly distributed through the cytosol and molecular motors. To this end, we devised an assay based on the rapamycin-dependent heterodimerization of FRB and FKBP (Fig. 4A). On one side we fused plus-end and minus-end motors to mCh-FRB (giving rise to KIF1A-mCh-FRB and BICD2-mCh-FRB, respectively) (Fig. 4A). On the other side, we fused our LLPS scaffold emGFP-5Fm to FKBP (FKBP-emGFP-5Fm) (Fig. 4A). We first analyzed the behavior of these proteins in the absence of rapamycin. After 24 h co-expression of FKBP-emGFP-5Fm and either KIF1A-mCh-FRB or BICD2-mCh-FRB, cells displayed several FKBP condensates, randomly dispersed in the cytosol and coexisting without interactions with FRB-fused motors (Fig. 4B). In some cells KIF1A-mCh-FRB accumulated at the cell periphery, while no particular enrichment of BICD2-mCh-FRB could be observed close to the nucleus (Fig. 4B).

We then added rapamycin (24 h after transfection) to induce interaction between the FKBP-condensates and KIF1A-mCh-FRB, and monitored the consequences using time-lapse microscopy. Within a couple of minutes, we could observe some events of long-range condensate transport toward the cell periphery. On Fig. 4C, we report an example of converging motions of condensates, which coalesced together at the cell extremity within a few minutes (Fig. 4D). The other cells, however, did not display obvious transport of condensates, which may be explained if initially the distribution of KIF1A motors was highly polarized towards the plasma membrane, making them unavailable for interaction with disperse condensates.

With BICD2-mCh-FRB, upon addition of rapamycin, we first observed the recruitment of the FRB-fused motor on the surface of the FKBP-emGFP-5Fm condensates, with a distinct mCherry corona forming in less than 1 min (Fig. 4E). Then, BICD2-mCh-FRB diffused towards the inner part of the FKBP condensates, driven by an internal mixing of the components, which occurred within 10 to 30 minutes (depending on the condensate size) (Fig. 4E and 4F). Subsequently, two types of directed motions towards the cell center were observed: some condensates were transported in a few minutes with no morphological change (Fig. 4G), while others underwent a striking deformation consistent with the rheological properties of a cytoplasm acting as a stiff and porous meshwork (Fig. 4H)[62].

In conclusion, this assay allowed to chemically induce the rapid transport of condensates to either the cell periphery or the cell center.

Localizing exogenous RNAs through the spatial positioning of condensates

The co-assembly of RNAs and RBPs into membrane-less organelles could potentially play a role in RNA trafficking to specific subcompartments or distal positions. Using a biomimetic approach, we thus sought to localize mRNAs by engineering motor condensates programmed to recruit a specific mRNA. Our strategy consisted of fusing MCP to our LLPS scaffold to enable the recruitment of RNAs with MS2 stem loops (Fig. 5A) [40]. MCP scaffolds (MCP-5Fm) were then co-transfected with motor-LLPS scaffolds (KIF1A-emGFP-5Fm or BICD2-emGFP-5Fm), and with a plasmid expressing an RNA containing four MS2 repeats (RNA-MS2) (Fig. 5A).

We found that after 24 h of expression, bi-functionalized motor/MCP condensates were efficiently positioned at the cell periphery or at the centrosome depending on the motor's directionality. Using single molecule FISH (smFISH), we demonstrated the recruitment of RNA-MS2 molecules in the motor condensates (each Cy3 dot corresponds to individual RNA

molecule) (Fig. 5B). As specificity controls, the endogenous β-actin mRNA lacking MS2 stem loops was not recruited to MCP condensates (Fig. 5C), and the RNA-MS2 was not recruited on condensates lacking MCP (Fig. 5D). Therefore, condensates formed using a combination of motor- and MCP-LLPS scaffolds efficiently and specifically recruit MS2-containing RNAs.

Overall, these results demonstrate the specific localization of RNA via artificial condensates.

Delocalizing endogenously tagged ASPM mRNA using motor condensates

To highlight a second application of our condensates, we aimed to use them as a tool to alter the subcellular localization of an endogenous RNA. To this end, we used a HeLa cell line in which 24 MS2 repeats were inserted in the 3'UTR of the Abnormal Spindle-like Microcephaly-associated (*ASPM*) gene using CRISPR-Cas9 (HeLa/ASPM-MS2). The resulting clone thus expresses the ASPM-MS2 mRNA in a stable manner, under the control of its endogenous promoter, which can be visualized by smFISH using a probe directed against the MS2 sequence[57]. Like untagged ASPM mRNA, ASPM-MS2 mRNA was weakly expressed during interphase and its expression increased during mitosis, with the mRNA localizing to centrosomes, particularly from early mitotic stages till metaphase (Fig. 6A)[57,63]. This created a striking local concentration of ASPM-MS2 mRNA on centrosomes making it an ideal candidate for delocalization attempts.

To test this delocalization, we transiently transfected HeLa/ASPM-MS2 cells with our MCP and KIF1A scaffolds (MCP-5Fm with KIF1A-emGFP-5Fm). Remarkably, the KIF1A/MCP condensates successfully delocalized ASPM-MS2 mRNAs away from centrosomes towards the cell membrane across mitosis (Fig. 6B). As a negative control, we expressed condensates without MCP (5Fm only) functionalized with the KIF1A motor (KIF1A-emGFP-5Fm). In this condition, condensates localized at the cell periphery without recruiting ASPM-MS2 mRNA (Fig. 6C, D), thus confirming the specificity of the system. Moreover, we observed three patterns of KIF1A condensates in mitotic cells: local clustering of condensates at the membrane (i); or condensates distributed under the cell membrane producing either a half (ii) or a full (iii) crown pattern (Fig. S3). Interestingly, the ASPM-MS2 mRNA tended to distribute like the condensates, demonstrating the robustness of this tool (Fig. S3).

Conversely, we tested the possibility of forcing centrosomal localization of ASPM-MS2 mRNA in interphasic cells. First, as expected, condensates without motor (formed using emGFP-5Fm) were randomly localized in the cytoplasm and were able to recruit ASPM-MS2 mRNAs only in the presence of MCP-5Fm (Fig. S4A, B). In contrast, the BICD2 scaffold (BICD2-emGFP-5Fm) led to a single condensate at the centrosome, which was able to artificially localize some ASPM-MS2 mRNAs at the vicinity of centrosomes during interphase (Fig. S4C, D), at a time where the mRNA should not localize there.

Taken together, motor condensates are a versatile tool for altering the subcellular localization of RNA in living cells.

DISCUSSION

How is the spatial positioning of biomolecular condensates orchestrated in cells? Whereas many mechanisms of spatial regulation have been described for membrane-bound organelles and other cargos, much less is known for condensates. Yet, despite the diversity of cytoplasmic RNP condensates, including RNA transport granules, stress granules, and P-bodies, one common feature relies on their interactions with microtubule-based cytoskeleton. In this study, we engineered artificial condensates functionalized with kinesin motor and dynein adaptor domains in order to examine their interplay with microtubules and its consequences on condensate formation and localization. We found that motor condensates were robustly positioned at the periphery of cells or at the vicinity of the centrosomes, as predicted from the direction of processivity of the motors. Next, we asked whether one could reconstitute a minimal RNP transport system to localize RNAs in cells. By incorporating MCP proteins into our motor condensates, we succeeded in recruiting MS2-tagged RNAs in asymmetrically positioned condensates.

In a first setting, LLPS scaffolds were directly fused to plus-end motors (KIF1A or KIF5B), or to minus-end motor / motor adaptor (KIFC1 or BICD2) and constitutively expressed in cells. Using this approach, we could investigate the formation of condensates made of proteins prone to phase-separate while interacting with microtubule fibers. Indeed, at early stage, motor-LLPS scaffolds underwent phase separation on microtubule fibers due to motor accumulation at the cell periphery or near the centrosome. One hypothesis is that the accumulation of motor-LLPS scaffolds on microtubule increases their local concentration which may account for their local condensation on microtubule surface lattice. The cooperative binding of the motor-LLPS scaffold on fibers, mediated by the repetitive nature of the LLPS scaffolds, could therefore favor prewetting on microtubules and phase separation below the expected saturation concentration [64]. This process has recently been proposed for Tau and TPX2, two microtubule-associated proteins involved in the stabilization/nucleation of microtubule fibers[64], or in a different context for the condensation of the transcription factor Klf4 on DNA molecules[65].

To infer how nucleation of condensates was dependent on the capacity of the scaffolds to interact with microtubules, we monitored both motor-functionalized and non-functionalized LLPS scaffolds. Interestingly, we found that the condensation of the two LLPS scaffolds was sequential, with motor-LLPS scaffolds condensing systematically ahead of non-functionalized LLPS scaffolds. Non-functionalized scaffolds predominately accumulated at the sites of preformed motor condensates (Fig. 1D, 1F, 2E, 2F).

Classical nucleation theory predicts that phase-separated condensates can either form with no specific localization or, in contrast, at specific sites acting as seeds overcoming the kinetic barrier of nucleation. Recent studies showed how specific biomolecules can act as seeds and govern condensate nucleation at specific sites, such as DNA break sites[66], the membrane[67–69], or the apical side of the nucleus for nucleolus[70]. Our study provides an alternative scheme for the spatial positioning of nucleation. Here, we highlighted the positioning of condensates at polarity sites powered by microtubule-based motor proteins. In our system, condensate positioning occurred predominantly by nucleating phase separation at the destination sites of transported molecules rather than by transporting already formed condensates to their

destination. This suggests a two-step mechanism (Fig. 7A): (i) active transport of the condensate scaffolds leading to their localization at polarity sites (microtubules extremities), (ii) nucleation of motor condensates through a mechanism possibly mediated by prewetting or cooperative binding. The pathway to such condensate localization is similar for the four motor domains studied. However, and in contrast to kinesin condensates, we also observed some events of nucleation of BICD2 condensates dispersed throughout the cytosol, which then were transported to the cell centrosome to eventually coalesce into a large condensate (Fig. 2F and S2C). This formation of BICD2 condensates in the cytosol prior to their transportation may be due to the requirement to assemble a high number of dyneins on the condensate surface to generate large collective forces and efficient transport[71]. Subsequently, recruitment of non-functionalized scaffolds in the preformed condensates could be observed.

Coalescence of smaller BICD2 condensates into one larger condensate is reminiscent of the coalescence of stress granules upon transport along microtubules mediated by the dynein adaptor BICD1[6–8,10]. Previous studies on stress granules emphasized that their assembly follows distinct temporal steps, with first the formation of stable cores through multiple stable interactions, and secondly evolution into larger assemblies by recruiting a less dense shell[72]. Here, our studies highlight a simple mechanism based on LLPS where compositional complexity of granules builds during assembly processes in a sequential fashion. In our system, the localized nucleation of motor condensates provides a platform for the subsequent enrichment of non-functionalized LLPS scaffolds. This is reminiscent of the sequential localization of mRNAs observed during P-body formation in yeast[73]. Interestingly, in our system, the timing of enrichment of non-functionalized scaffolds into motor condensates depends on their localization in cells (Fig. 3). Therefore, site-specific nucleation combined with sequential enrichment provides a simple mechanism to build, in an ordered fashion, multicomponent condensates.

Other the last years, several chemical and optogenetic tools have been developed to perturb and control organelles positioning, interactions, and trafficking. Here, inspired by repositioning assays of membrane-bound organelles using chemically-induced dimerization strategy[74], we extended our system to chemically trigger the interactions between dispersed condensates and microtubule motor proteins. With this approach, we obtained a temporal control of induction of condensate transport and localization at the cell periphery or at the vicinity of the centrosome (Fig. 4). Harnessing the trafficking of artificial condensates is a first step towards the assembly of biomimetic RNP transport system in cells.

Many RNAs are found localized in specific area of cells, and local translation is thought to participate to many functions dictating cell fate[13]. Complementary, mislocalization of RNA is reported to be associated with disease development[24]. There is consequently a strong emphasis to enlarge the current toolbox to analyze and study RNA localization and translation. The methodologies developed so far range from the visualization of RNP transport and translation with single molecule resolution, to spatial transcriptomics to map RNP interactomes[21,27,28,30,75,76]. In this context, we extended our assay to use it for the spatial manipulation of RNAs in cells. We showed that artificial condensates, functionalized with both motor domains and MCP proteins could be used as minimal RNP condensates recruiting a unique RNA, making it possible to explore condensate-mediated RNA delocalization. As a first proof-of-concept, we demonstrated the efficient recruitment of exogenous RNAs on motor

condensates that were positioned at the cell periphery or at the centrosome depending on the motor directionality (Fig. 5). Combined with a temporal control of assembly/disassembly, one could anticipate future developments, where these artificial structures could act as platform organizing biochemistry in space and time.

Then, we demonstrated the ability of our system to strongly perturb the spatial distribution of endogenously tagged mRNAs. Artificial condensates drove the delocalization of individual ASPM-MS2 mRNAs at the cell periphery (Fig. 6,7B). This demonstrates how our system could outperform endogenous mRNA localization mechanisms by rewiring the transport machinery between the cytoplasm, the centrosome and the cell periphery. Competing with endogenous ASPM mRNA localization using artificial condensates provides interesting insights. On one hand, it has been shown that the ASPM RNA (as well as other centrosomal transcripts) naturally localizes to centrosomes through an active transport mechanism involving the microtubules and molecular motors[57]. This trafficking is dependent on the encoded nascent peptide and occurs rapidly at the onset of mitosis: within a couple of minutes, scattered RNA readily concentrates on centrosomes, as revealed by live imaging[57]. On the other hand, KIF1A condensates traffic away from the centrosomes and thus drag ASPM-MS2 mRNA. Since both the natural and artificial transport systems share microtubules for transit, the location where the RNA ends up provides an estimation of which localization process is more efficient. In most cells, the artificial condensates won the contest.

Several non-exclusive processes, that all rely on the capacity of KIF1A condensates to generate mechanical forces, could account for ASPM mRNA delocalization at the cell periphery: (i) Pulling forces applied by the condensates on individual ASPM mRNAs accumulated at the centrosome, allowing to convey RNAs along microtubule tracks. This suggests KIF1A forces are stronger than the cohesive forces bridging ASPM mRNA to centrosomal material. (ii) A tug-of-war between the KIF1A condensates and the endogenous transport machinery of ASPM mRNA to the centrosomes. For instance, KIF1A condensates can link individual RNAs to many more motors than a single nascent peptide or an endogenous adapter canonically would. They can be seen as a transport particle pulled by several molecular motors in a cooperative manner, allowing them to surpass the natural mechanism of ASPM mRNA transport. (iii) The direct capture and transportation of freely-diffusing ASMP RNAs by KIF1A condensates, upstream of their transport to the centrosome.

Interestingly, ASMP mRNA delocalization experiments provide a first benchmarking of the performance of our artificial condensates. This approach could open novel perspectives to examine the importance of RNA localization for cellular functions and may be extended to rewire the trafficking of other biomolecules of interest.

MATERIAL AND METHODS

Experimental model

Human epithelioid carcinoma HeLa cells (ATCC, ccl-2) were kept in Dulbecco's modified Eagle's medium (with 4.5 g/L D-glucose, HyClone) with 10% fetal bovine serum (Gibco, 10,270,106) and 1% Penicillin-Streptomycin (Sigma, P4333), at 37°C in a 5% CO_2 humidified atmosphere. Tests for mycoplasma contamination were routinely carried out.

Plasmids

To generate the constructs containing 5 repeats of FKPB-F36M, a first plasmid puCIDT-Amp-5Fm was designed containing five repeats of FKBP-F36M separated by sequences coding for linkers of four GGS repeats (12 amino acids total). To avoid recombination, degenerate repeats were used. The first repeat was preceded by a Nhe and an AfeI restriction sites and the last one was followed by a Xba1 restriction site. This plasmid was purchased from IDT. To obtain the pcDNA3.1-5Fm plasmid (called hereafter 5Fm), puCIDT-Amp-5Fm was digested with NheI and XbaI, and the 5Fm containing fragment was subcloned between NheI and XbaI sites in the pcDNA3.1 (+) vector (Invitrogen). pcDNA3.1-emGFP-5Fm, pcDNA3.1-mCh-5Fm (called hereafter mCh-5Fm) and pcDNA3.1-MCP-5Fm (called hereafter MCP-5Fm) were then obtained by inserting emGFP, mCherry or a tandem MCP coding sequence, respectively, between HindIII and AfeI restriction sites.

Coding sequences for human KIF1A(1-383), mouse KIF5B(1-555), human KIFC1(125-673) and mouse BICD2(15-595) were obtained from Addgene (plasmids #133242, #120170 #120169, and #120168 respectively)[60,77]. KIF1A and KIF5B coding sequences were inserted in pcDNA3.1-5Fm between NheI and AfeI restriction sites, with respectively EcoR1 and Not1 restriction sites ahead of AfeI for subsequent sub-cloning. Then emGFP was inserted in pcDNA3.1-KIF1A-5Fm between EcoRI and AfeI, and in pcDNA3.1-KIF5B-5Fm between NotI and AfeI restriction sites. KIFC1 coding sequence was inserted in pcDNA3.1-emGFP-5Fm between XbaI and AgeI restriction sites. pcDNA3.1-BICD2-emGFP-5Fm plasmid was obtained by adding a NheI restriction site ahead of emGFP in pcDNA3.1-emGFP-5Fm, and inserting the BICD2 coding sequence between HindIII and NheI restriction sites. The four pcDNA3.1 constructs KIF1A-emGFP-5Fm, KIF5B-emGFP-5Fm, emGFP-KIFC1-5Fm and BICD2-emGFP-5Fm, are hereafter called the motor-LLPS scaffolds.

Transfection

For imaging after cell fixation, HeLa cells were cultured on 22x22 mm glass coverslips (VWR) in 6-well plates (Falcon, $3.5x10^5$ cells per well). For live imaging, HeLa cells were seeded on 35-mm-dishes with polymer coverslip bottom (Ibidi, $1.5x10^5$ cells per dish). For both, cells were transfected 24 hours later using Lipofectamine 2000 (Invitrogen) according to the manufacturer's protocol. For fixed cell imaging, cells were transfected with a 2:1:1 ratio of 5Fm, mCh-5Fm and motor-LLPS scaffold (2 µg total per well). The same conditions were followed for control experiments with motors lacking the LLPS 5Fm domain. In the case of KIFC1, cells were transfected with a modified ratio of 2.5:1:0.5. For live imaging (formation, dissolution and induction acquisitions), cells were transfected with a 1:1 ratio of motor-LLPS and 5Fm scaffolds (800 ng total per µ-dish). For smFISH experiments, cells were transfected with a 1:1:2

ratio of motor-5Fm scaffold, 5Fm, and MCP-5Fm (2 µg total per well) and 50 ng of RNA-MS2 plasmid. The ratio was modified to 0.5:1.5:2 in the case of KIFC1.
To probe condensate inhibition and dissolution (Fig. S1 and S2), FK506 (Sigma, F4679) was used at 2.5 µM. For chemical induction experiments of condensate transport (Fig. 3), rapamycin was used at 0.4 µM.

ASPM-MS2 cell line generation
HeLa Kyoto cells were transfected with a combination of plasmids expressing the Cas9-nickase protein, two guide RNAs targeting the end of the ASPM gene, and a repair template harbouring 500 nucleotide homology arms. Homology arms flanked 3 HA tags, a stop codon, 24 MS2 repeats and an IRES-NeoR-stop codon sequence. This repair template was designed to allow insertion at the endogenous ASPM stop codon. Following neomycin selection at 400 µg/ml for 7-10 days, clones were isolated and characterized by PCR genotyping and smFISH to ensure proper cassette insertion and edited RNA localization. The clone used in this study is heterozygous as described in detail in Safieddine et al[57]. The sequences targeted by the guide RNAs are: TCTCTTCTCAAAACCCAATCtgg for guide 1, and GCAAGCTATTCAAATGGTGAtgg for guide 2, where lowercase corresponds to PAM sequences.

Single-molecule fluorescence in situ hybridization
Single RNA molecule detection of the heterelogously expressed RNA-MS2 was performed according to the previously described smiFISH (single-molecule inexpensive FISH) method[78]. Briefly, cells were fixed in 4% paraformaldehyde (PFA) for 20 min at RT, and permeabilized with 70% ethanol in phosphate buffer saline (PBS) at 4°C overnight. A mix of gene specific (described previously[54]) and Cy3 FLAP probes in hybridization buffer (50 µl/coverslip) was used for overnight hybridization at 37°C in a humidity chamber. After washing twice for 30 min at 37°C in 15% formamide in SSC buffer and rinsing twice in PBS, cells were either mounted with VECTASHIELD mounting medium containing DAPI (Vector Laboratories, H-1200) or processed through immunofluorescence steps.
smFISH against the MS2 sequence in HeLa/ASPM-MS2 cells was done using a single probe (25 ng of probe per 100 µl of hybridization mixture) that had the following sequence: 5'AT*GTCGACCTGCAGACAT*GGGTGATCCTCAT*GTTTTCTAGGCAATT*A where * denotes a thymidine conjugated with a Cy3 molecule. Hybridization was done on cells grown on a glass coverslip in a buffer containing 20% formamide (Sigma-Aldrich), 1x SSC, 0.34 mg/ml tRNA (Sigma-Aldrich), 2 mM VRC (Sigma-Aldrich), 0.2 mg/ml RNAse-free bovine serum albumin (BSA, Roche Diagnostics) and 10% dextran sulfate (MP Biomedicals). Hybridization was done overnight at 37°C and coverslips were washed the next day in a 20% formamide 1x SSC solution twice, each at least for 40 mins at 37°C. Coverslips were then mounted using VECTASHIELD containing DAPI (Vector Laboratories, H-1200).

Immunofluorescence
For centrosome imaging in Figure 2, cells were fixed 24 h after transfection in methanol at -20°C for 10 minutes. They were then permeabilized with a solution of 0.2% Triton X-100 and 0.1% BSA in PBS for 30 min, incubated for 1 h with the primary antibody (rabbit anti-

pericentrin, Covance PRB-432C, 1:500 dilution), washed three times with PBS at RT for 5 min, incubated for 1 h with the secondary antibody (AffiniPure Goat Anti-Rabbit conjugated with Alexa Fluor 488 dye), washed three times with PBS at RT for 5 min, and finally mounted with VECTASHIELD containing DAPI (Vector Laboratories, H-1200).

Imaging

For live imaging, cells were imaged on a Zeiss LSM 710 META laser scanning confocal microscope using an x63 oil-immersion objective (PlanApochromatic, numerical aperture (NA) 1.4), at 37°C in a 5% CO2 humidified atmosphere, starting 4 h after transfection (formation). Microscope hardware and image acquisition were controlled with LSM Software Zen 2012. For fixed experiments, cells were imaged using an IX81 microscope (Olympus) and 60x oil immersion objective (PlanApo, NA 1.42), equipped with a CMOS camera, Orca-Fusion (Hamamatsu, Corporation), and a LED system of illumination (Spectra X, Lumencor). Microscope settings were controlled using Micro-manager on ImageJ. Images were analyzed using Fiji.

Data analysis

To quantify the degree of asymmetry of the condensate distribution, the fraction of mCh-5Fm fluorescence in the peripheral 25% of the cells (I_{25}) was measured by adapting a previously published method[58]. For each cell, a first circle encompassing the entire cell and having for center a point in the nucleus was drawn. A concentric circle with a 10-pixel diameter was then drawn, from which a series of concentric circles were derived by iteratively enlarging the diameter by 10 pixels until reaching the first circle size. 5-pixel rings were then built by subtracting each circle to the next one in the series. Final regions of interest (ROI) were defined as the overlap between each ring and the cytoplasm. The images were subsequently processed by applying Gaussian blur (5-pixel radius) to eliminate strong local variations in intensity. For each ROI, the area and the mean and minimal intensities were measured. Minimal intensities were subtracted to mean values to remove background, and integrated intensity were calculated for each ROI. The peripheral 25% of a cell was defined as the sum of consecutive ROI, starting from the most peripheral one, reaching 25% of the total cell area. For each cell, I_{25} was obtained by calculating the ratio between the integrated fluorescence of the mCherry signal in the peripheral 25% over the integrated fluorescence of the entire cell.

Statistical analysis

For Fig. 1C and 3A, Wilcoxon rank-sum tests (nonparametric test to compare two distributions) were performed using the ranksum MATLAB function (MathWorks). For Fig. 2C, Pearson's chi-squared tests (nonparametric test for nominal variables) were performed using the Python's chi2_contingency function.

Legends of supplementary movies

Movie S1: Time-lapse confocal microscopy of the formation of KIF1A condensates in a Hela cell after transfection of KIF1A-emGFP-5Fm (green) and mCh-5Fm (red). Acquisitions were taken every 4 minutes.

Movie S2: Time-lapse confocal microscopy of the formation of KIF1A condensates in two Hela cells after transfection of KIF5B-emGFP-5Fm (green) and mCh-5Fm (red). Acquisitions were taken every 4 minutes.

Movie S3: Time-lapse confocal microscopy of the formation of a KIFC1 condensate in a Hela cell after transfection of emGFP-5Fm-KIFC1 (green) and mCh-5Fm (red). Acquisitions were taken every 4 minutes.

Movie S4: Time-lapse confocal microscopy of the formation of a BICD2 condensate in a Hela cell after transfection of BICD2-emGFP-5Fm (green) and mCh-5Fm (red). Acquisitions were taken every 4 minutes.

Acknowledgments

We thank M.A. Plamont for her help along the project and C. Amari for his help in the implementation of the quantification process. We thank A. Meunier for providing the pericentrin antibodies and E. Bertrand for sharing HeLa/ASPM-MS2 cells.

Funding

A.C was supported by an IPV-SU PhD fellowship. A. S. was supported by ANR (ANR-19-CE12-0024-01). P.C was supported by a FRM (MND202003011470) grant. This work was supported by the CNRS, Ecole Normale Supérieure, and ARC (20181208003) to Z.G, FRM (MND202003011470) and iBio (SU) to Z.G and D.W, and ANR (ANR-19-CE12-0024-01) to D.W.

Author Contributions

A.C and Z.G conceived the project. A.C and P.C designed the motor condensate toolbox, as well as performed and analyzed motor-condensate experiments. A.S, M-N.B and D.W performed and analyzed ASPM-related experiments. A.C and Z.G prepared the manuscript with contributions from A.S, P.C and D.W. All authors discussed the results and commented on the manuscript.

Declaration of Interests

The authors declare that they have no competing interests.

Supporting Information

4 Supplementary Figures and 4 Supplementary Movies.

All data are available from the corresponding author upon request.

REFERENCES

1. Barlan, K. & Gelfand, V. I. Microtubule-Based Transport and the Distribution, Tethering, and Organization of Organelles. *Cold Spring Harbor Perspectives in Biology* **9**, a025817 (2017).

2. Granger, E., McNee, G., Allan, V. & Woodman, P. The role of the cytoskeleton and molecular motors in endosomal dynamics. *Seminars in Cell & Developmental Biology* **31**, 20–29 (2014).

3. Kilwein, M. D. & Welte, M. A. Lipid Droplet Motility and Organelle Contacts. *Contact* **2**, 1–13 (2019).

4. Melkov, A. & Abdu, U. Regulation of long-distance transport of mitochondria along microtubules. *Cell Mol Life Sci* **75**, 163–176 (2018).

5. Woodruff, J. B. *et al.* The Centrosome Is a Selective Condensate that Nucleates Microtubules by Concentrating Tubulin. *Cell* **169**, 1066-1077.e10 (2017).

6. Chernov, K. G. *et al.* Role of microtubules in stress granule assembly: Microtubule dynamical instability favors the formation of micrometric stress granules in cells. *Journal of Biological Chemistry* **284**, 36569–36580 (2009).

7. Tsai, N.-P., Tsui, Y.-C. & Wei, L.-N. DYNEIN MOTOR CONTRIBUTES TO STRESS GRANULE DYNAMICS IN PRIMARY NEURONS. *NSC* **159**, 647–656 (2009).

8. Loschi, M., Leishman, C. C., Berardone, N. & Boccacio, G. L. Dynein and kinesin regulate stress-granule and P-body dynamics. *Journal of Cell Science* **122**, 3973–3982 (2009).

9. Nadezhdina, E. S., Lomakin, A. J., Shpilman, A. A., Chudinova, E. M. & Ivanov, P. A. Microtubules govern stress granule mobility and dynamics. *Biochimica et Biophysica Acta (BBA) - Molecular Cell Research* **1803**, 361–371 (2010).

10. Perez-Pepe, M., Fernández-Alvarez, A. J. & Boccaccio, G. L. Life and Work of Stress Granules and Processing Bodies: New Insights into Their Formation and Function. *Biochemistry* **57**, 2488–2498 (2018).

11. Aizer, A. *et al.* The Dynamics of Mammalian P Body Transport, Assembly, and Disassembly In Vivo. *Molecular Biology of the Cell* **19**, 4154–4166 (2008).

12. Engel, K. L., Arora, A., Goering, R., Lo, H. Y. G. & Taliaferro, J. M. Mechanisms and consequences of subcellular RNA localization across diverse cell types. *Traffic* **21**, 404–418 (2020).

13. Ryder, P. v. & Lerit, D. A. RNA localization regulates diverse and dynamic cellular processes. *Traffic* vol. 19 Preprint at https://doi.org/10.1111/tra.12571 (2018).

14. Martin, K. C. & Ephrussi, A. mRNA Localization: Gene Expression in the Spatial Dimension. *Cell* **136**, 719–730 (2009).

15. Eliscovich, C. & Singer, R. H. RNP transport in cell biology: the long and winding road. *Current Opinion in Cell Biology* **45**, 38–46 (2017).

16. Zimyanin, V. L. *et al.* In Vivo Imaging of oskar mRNA Transport Reveals the Mechanism of Posterior Localization. *Cell* **134**, 843 (2008).

17. Jambor, H., Mueller, S., Bullock, S. L. & Ephrussi, A. A stem-loop structure directs oskar mRNA to microtubule minus ends. *RNA* (2014) doi:10.1261/rna.041566.113.

18. Driever, W. & Nüsslein-Volhard, C. The bicoid protein determines position in the Drosophila embryo in a concentration-dependent manner. *Cell* **54**, 95–104 (1988).

19. Ephrussi, A., Dickinson, L. K. & Lehmann, R. oskar organizes the germ plasm and directs localization of the posterior determinant nanos. *Cell* **66**, 37–50 (1991).

20. Herbert, S. P. & Costa, G. Sending messages in moving cells: mRNA localization and the regulation of cell migration. *Essays Biochem* (2019) doi:10.1042/EBC20190009.

21. Holt, C. E., Martin, K. C. & Schuman, E. M. Local translation in neurons: visualization and function. *Nature Structural & Molecular Biology 2019 26:7* **26**, 557–566 (2019).

22. Dalla Costa, I. *et al.* The functional organization of axonal mRNA transport and translation. *Nature Reviews Neuroscience 2020 22:2* **22**, 77–91 (2020).

23. Mofatteh, M. Neurodegeneration and axonal mRNA transportation. *Am J Neurodegener Dis* **10**, 1–12 (2021).

24. Lin, J. Q., van Tartwijk, F. W. & Holt, C. E. Axonal mRNA translation in neurological disorders. *RNA BIOLOGY* (2020) doi:10.1080/15476286.2020.1822638.

25. Jansen, R. P. mRNA localization: message on the move. *Nature Reviews Molecular Cell Biology 2001 2:4* **2**, 247–256 (2001).

26. Holt, C. E. & Schuman, E. M. The Central Dogma Decentralized: New Perspectives on RNA Function and Local Translation in Neurons. *Neuron* **80**, 648–657 (2013).

27. Weil, T. T., Parton, R. M. & Davis, I. Making the message clear: visualizing mRNA localization. *Trends Cell Biol* **20**, 380–90 (2010).

28. Pichon, X., Lagha, M., Mueller, F. & Bertrand, E. A Growing Toolbox to Image Gene Expression in Single Cells: Sensitive Approaches for Demanding Challenges. *Molecular Cell* **71**, 468–480 (2018).

29. Lécuyer, E. *et al.* Global Analysis of mRNA Localization Reveals a Prominent Role in Organizing Cellular Architecture and Function. *Cell* **131**, 174–187 (2007).

30. Fazal, F. M. *et al.* Atlas of Subcellular RNA Localization Revealed by APEX-Seq. *Cell* **178**, 473–490 (2019).

31. Taliaferro, J. M., Wang, E. T. & Burge, C. B. Genomic analysis of RNA localization. *RNA Biology* **11**, 1040–1050 (2014).

32. Kanai, Y., Dohmae, N. & Hirokawa, N. Kinesin transports RNA: Isolation and characterization of an RNA-transporting granule. *Neuron* **43**, 513–525 (2004).

33. Gagnon, J. A. & Mowry, K. L. Molecular Motors: Directing Traffic during RNA Localization. *Crit Rev Biochem Mol Biol* **46**, 229 (2011).

34. Rodrigues, E. C., Grawenhoff, J., Baumann, S. J., Lorenzon, N. & Maurer, S. P. Mammalian Neuronal mRNA Transport Complexes: The Few Knowns and the Many Unknowns. *Frontiers in Integrative Neuroscience* **15**, 13 (2021).

35. Das, S., Vera, M., Gandin, V., Singer, R. H. & Tutucci, E. Intracellular mRNA transport and localized translation. *Nature Reviews Molecular Cell Biology* 1–22 (2021) doi:10.1038/s41580-021-00356-8.

36. Buxbaum, A. R. In the right place at the right time: visualizing and understanding mRNA localization. *Nature Reviews Molecular Cell Biology* **16**, 95–109 (2015).

37. Baumann, S. *et al.* A reconstituted mammalian APC-kinesin complex selectively transports defined packages of axonal mRNAs. *Science Advances* **6**, (2020).

38. Rosowski, K. A. *et al.* Elastic ripening and inhibition of liquid–liquid phase separation. *Nature Physics 2020 16:4* **16**, 422–425 (2020).

39. Vidal-Henriquez, E. & Zwicker, D. Cavitation controls droplet sizes in elastic media. *Proc Natl Acad Sci U S A* **118**, (2021).

40. Martin, D. R. *et al.* Liquid demixing in elastic networks: Cavitation, permeation, or size selection? *Europhysics Letters* **137**, 67001 (2022).

41. Feric, M., Brangwynne, C. P., Cell, N. & Author, B. A nuclear F-actin scaffold stabilizes RNP droplets against gravity in large cells. *Nat Cell Biol* **15**, 1253–1259 (2013).

42. Böddeker, T. J. *et al.* Non-specific adhesive forces between filaments and membraneless organelles. *Nature Physics 2022* 1–8 (2022) doi:10.1038/s41567-022-01537-8.

43. Shin, Y. *et al.* Spatiotemporal Control of Intracellular Phase Transitions Using Light-Activated optoDroplets. *Cell* **168**, 159-171.e14 (2017).

44. Bracha, D. *et al.* Mapping Local and Global Liquid Phase Behavior in Living Cells Using Photo-Oligomerizable Seeds. *Cell* **175**, 1467–1480 (2018).

45. Nakamura, H. *et al.* Intracellular production of hydrogels and synthetic RNA granules by multivalent molecular interactions. *Nature Materials* **17**, 79–88 (2018).

46. Garcia-Jove Navarro, M. *et al.* RNA is a critical element for the sizing and the composition of phase-separated RNA–protein condensates. *Nature Communications* **10**, 3230 (2019).

47. Zhao, E. M. *et al.* Light-based control of metabolic flux through assembly of synthetic organelles. *Nature Chemical Biology* **15**, 589–597 (2019).

48. Reinkemeier, C. D., Estrada Girona, G. & Lemke, E. A. Designer membraneless organelles enable codon reassignment of selected mRNAs in eukaryotes. *Science (1979)* **363**, (2019).

49. Heidenreich, M. *et al.* Designer protein assemblies with tunable phase diagrams in living cells. *Nature Chemical Biology* **16**, 939–945 (2020).

50. Dzuricky, M., Rogers, B. A., Shahid, A., Cremer, P. S. & Chilkoti, A. De novo engineering of intracellular condensates using artificial disordered proteins. *Nature Chemistry* **12**, 814–825 (2020).

51. Yoshikawa, M., Yoshii, T., Ikuta, M. & Tsukiji, S. Synthetic Protein Condensates That Inducibly Recruit and Release Protein Activity in Living Cells. *J Am Chem Soc* **143**, 6434–6446 (2021).

52. Lasker, K. *et al.* A modular platform for engineering function of natural and synthetic biomolecular condensates. *bioRxiv* 2021.02.03.429226 (2021) doi:10.1101/2021.02.03.429226.

53. Garabedian, M. v. *et al.* Designer membraneless organelles sequester native factors for control of cell behavior. *Nature Chemical Biology 2021 17:9* **17**, 998–1007 (2021).

54. Cochard, A. *et al.* RNA at the surface of phase-separated condensates impacts their size and number. *Biophysical Journal* **121**, (2022).

55. Rollins, C. T. *et al.* A ligand-reversible dimerization system for controlling protein-protein interactions. *Proc Natl Acad Sci U S A* **97**, 7096–101 (2000).

56. Fegan, A., White, B., Carlson, J. C. T. & Wagner, C. R. Chemically Controlled Protein Assembly: Techniques and Applications. doi:10.1021/cr8002888.

57. Safieddine, A. *et al.* A choreography of centrosomal mRNAs reveals a conserved localization mechanism involving active polysome transport. *Nature Communications 2021 12:1* **12**, 1–21 (2021).

58. Nijenhuis, W., van Grinsven, M. M. P. & Kapitein, L. C. An optimized toolbox for the optogenetic control of intracellular transport. *Journal of Cell Biology* **219**, (2020).

59. Hammond, J. W. *et al.* Mammalian Kinesin-3 Motors Are Dimeric In Vivo and Move by Processive Motility upon Release of Autoinhibition. doi:10.1371/journal.pbio.1000072.

60. Guardia Id, C. M. *et al.* Reversible association with motor proteins (RAMP): A streptavidin-based method to manipulate organelle positioning. *PLOS Biology* **17**, 1–27 (2019).

61. Rajgor, D. & Shanahan, C. M. RNA granules and cytoskeletal links. *Biochemical Society Transactions* **42**, 1206–1210 (2014).

62. Moeendarbary, E. *et al.* The cytoplasm of living cells behaves as a poroelastic material. (2013) doi:10.1038/NMAT3517.

63. Chouaib, R. *et al.* A Dual Protein-mRNA Localization Screen Reveals Compartmentalized Translation and Widespread Co-translational RNA Targeting. *Developmental Cell* **54**, 773-791.e5 (2020).

64. Wiegand, T. & Hyman, A. A. Drops and fibers — how biomolecular condensates and cytoskeletal filaments influence each other. *Emerging Topics in Life Sciences* **4**, 247 (2020).

65. Morin, J. A. *et al.* Sequence-dependent surface condensation of a pioneer transcription factor on DNA. *Nature Physics 2022 18:3* **18**, 271–276 (2022).

66. Altmeyer, M. *et al.* Liquid demixing of intrinsically disordered proteins is seeded by poly(ADP-ribose). *Nature Communications* **6**, (2015).

67. Banjade, S. & Rosen, M. K. Phase transitions of multivalent proteins can promote clustering of membrane receptors. *Elife* **3**, (2014).

68. Snead, W. T. *et al.* Membrane surfaces regulate assembly of ribonucleoprotein condensates. *Nature Cell Biology 2022 24:4* **24**, 461–470 (2022).

69. Ma, W. & Mayr, C. A Membraneless Organelle Associated with the Endoplasmic Reticulum Enables 3'UTR-Mediated Protein-Protein Interactions. *Cell* **175**, (2018).

70. Falahati, H., Pelham-Webb, B., Blythe, S. & Wieschaus, E. Nucleation by rRNA Dictates the Precision of Nucleolus Assembly. *Current Biology* **26**, 277–285 (2016).

71. Rai, A. K., Rai, A., Ramaiya, A. J., Jha, R. & Mallik, R. Molecular adaptations allow dynein to generate large collective forces inside cells. *Cell* **152**, 172–182 (2013).

72. Wheeler, J. R., Matheny, T., Jain, S., Abrisch, R. & Parker, R. Distinct stages in stress granule assembly and disassembly. *Elife* **5**, (2016).

73. Simpson, C. E., Lui, J., Kershaw, C. J., Sims, P. F. G. & Ashe, M. P. mRNA localization to P-bodies in yeast is bi-phasic with many mRNAs captured in a late Bfr1p-dependent wave. *Journal of Cell Science* doi:10.1242/jcs.139055.

74. Passmore, J. B., Nijenhuis, W. & Kapitein, L. C. From observing to controlling: Inducible control of organelle dynamics and interactions. *Current Opinion in Cell Biology* **71**, 69–76 (2021).

75. Turner-Bridger, B. *et al.* Single-molecule analysis of endogenous β-actin mRNA trafficking reveals a mechanism for compartmentalized mRNA localization in axons. *Proc Natl Acad Sci U S A* **115**, E9697–E9706 (2018).

76. Cassella, L. & Ephrussi, A. Subcellular spatial transcriptomics identifies three mechanistically different classes of localizing RNAs. *bioRxiv* 2021.12.05.471303 (2021) doi:10.1101/2021.12.05.471303.

77. Chiba, K. *et al.* Disease-associated mutations hyperactivate KIF1A motility and anterograde axonal transport of synaptic vesicle precursors. doi:10.1073/pnas.1905690116.

78. Tsanov, N. *et al.* smiFISH and FISH-quant – a flexible single RNA detection approach with super-resolution capability. *Nucleic Acids Research* **44**, e165–e165 (2016).

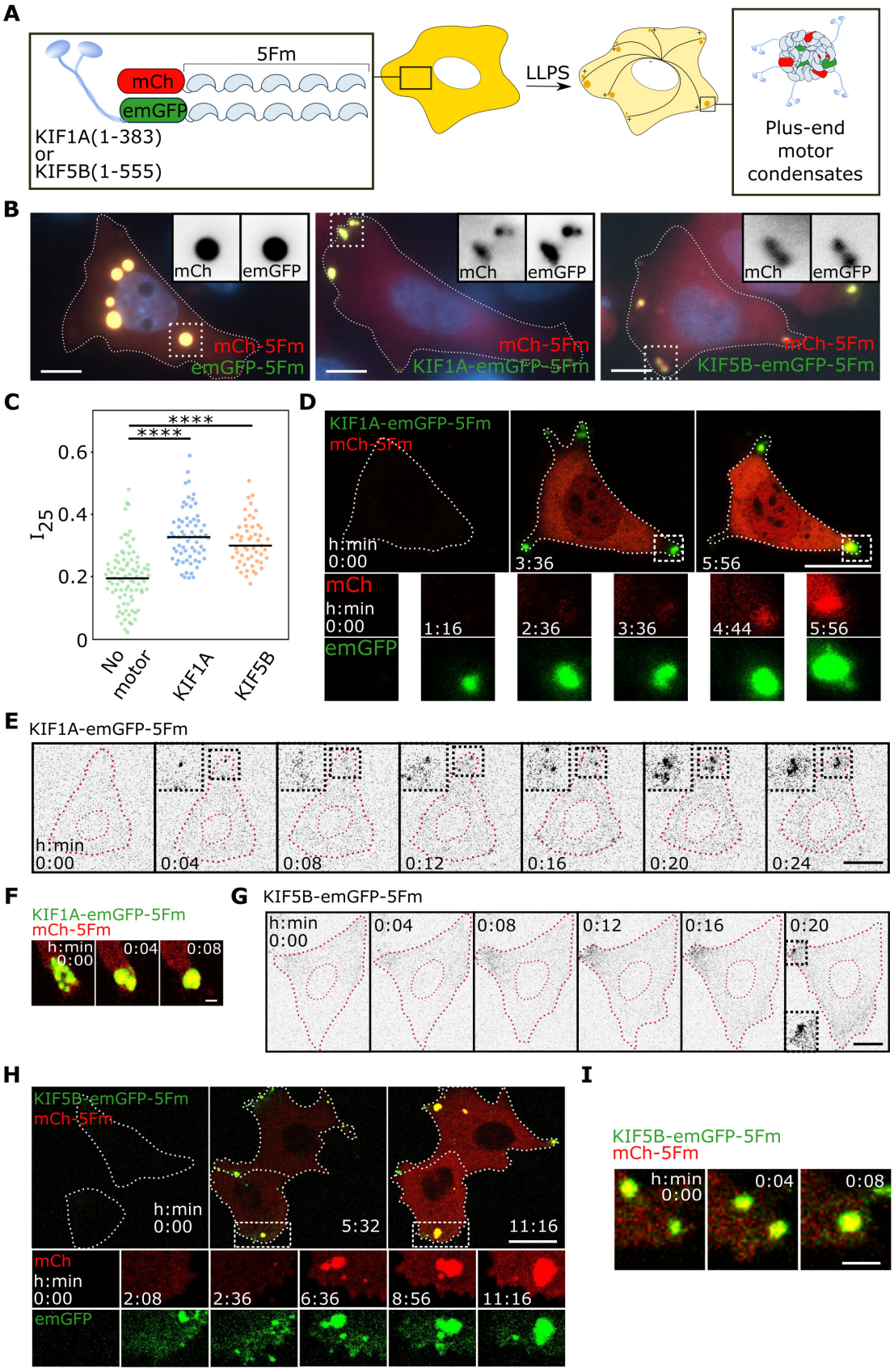

Figure 1: Functionalization of artificial condensates with plus-end motors drives their localization at the cell periphery. A. Schematic of the expected peripheral localization of condensates following transfection of mCh-5Fm and KIF1A-emGFP-5Fm or KIF5B-emGFP-5Fm (Fm = F36M-FKBP) in HeLa cells. **B.** Representative epifluorescence imaging of three cells expressing non-functionalized condensates (left panel), and KIF1A of KIF5B condensates (middle

and right panel, respectively). Nuclei were stained with DAPI (blue). Grayscales inserts correspond to the red (mCh) and green (emGFP) channels of the regions delineated by dashed squares. Scale bar, 10 µm. **C.** Distribution of the fraction of mCherry fluorescence in the peripheral 25% of the cell (I_{25}) for cells displaying non-functionalized condensates (left), and KIF1A or KIF5B condensates (middle and right, respectively), with each dot representing one cell (N = 87, 67 and 53, respectively, each from three independent experiments). Differences between no motor and KIF1A or KIF5B were statistically significant using a Wilcoxon rank-sum test (****: p-values < 10^{-11}). **D.** Time-lapse confocal imaging of the formation of KIF1A condensates in a cell (delineated by a dashed line), starting 4 h after transfection. The dashed squares indicate the region enlarged in the time-lapse images below (separate red and green channels). Scale bar, 20 µm. **E.** Epifluorescence imaging of the early time points of KIF1A-LLPS scaffold expression. Scale bar, 10 µm. **F.** Confocal imaging of coalescence events of KIF1A condensates. Scale bar, 2 µm. **G.** Epifluorescence imaging of the early time points of KIF5B-LLPS scaffold expression. Scale bar, 10 µm. **H.** Same as (D**)** for KIF5B condensates. **I.** Confocal imaging of coalescence events of KIF5B condensates. Scale bar, 2 µm.

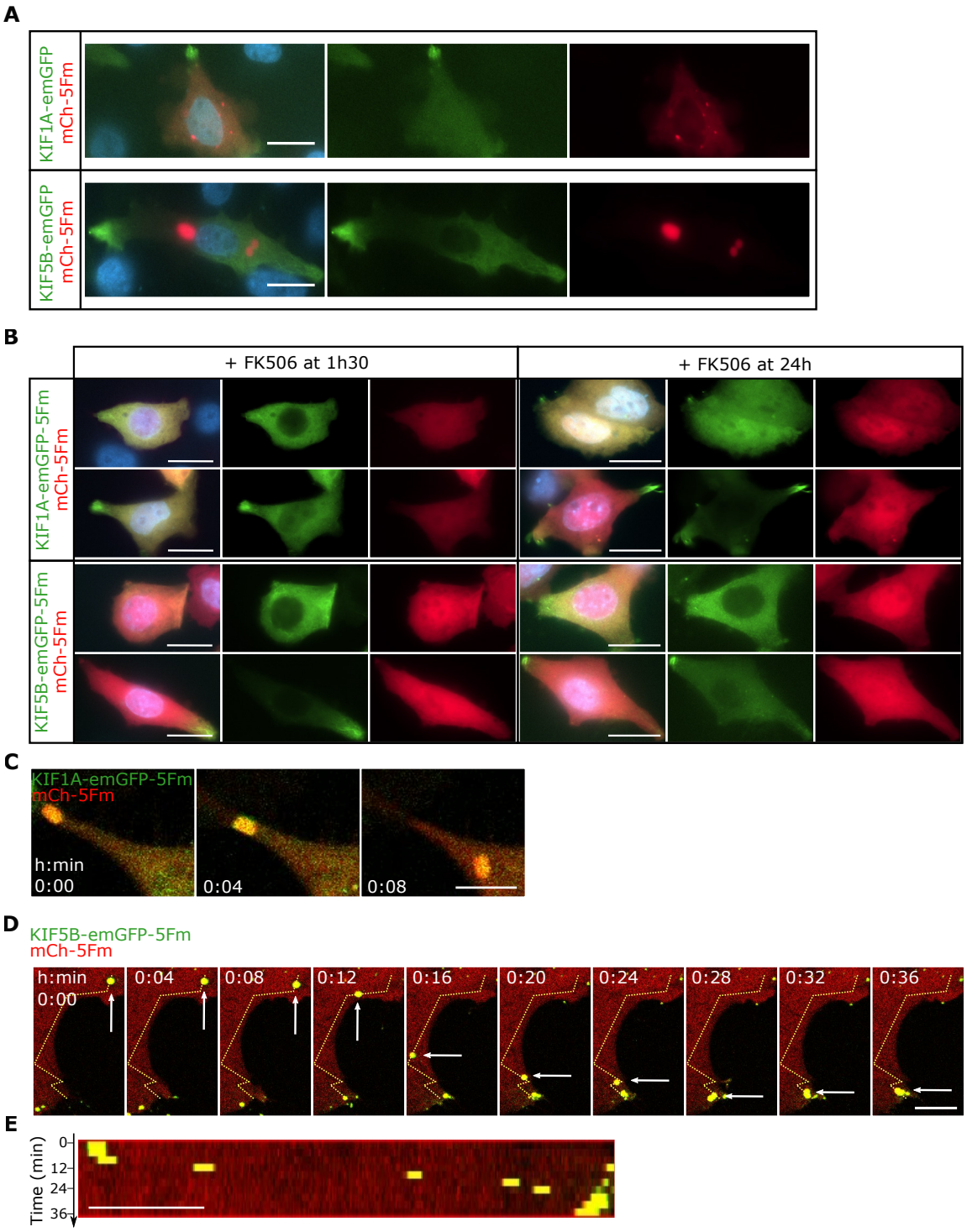

Figure S1: Cells expressing plus-end motors lacking the LLPS domain; chemical inhibition of condensates; and directed transport of condensates. A. Representative epifluorescence imaging of HeLa cells transfected with KIF1A-emGFP or KIF5B-emGFP (without LLPS domain) and mCh-5Fm. Nuclei were stained with DAPI (blue in merge). Scale bar, 20 µm. **B.** Epifluorescence imaging of HeLa cells expressing KIF1A- or KIF5B-emGFP-5Fm and mCh-5Fm after FK506 addition either right after transfection to forestall the formation of condensates (left) or 24 h after transfection to dissolve the condensates (right) (two examples for each condition). Nuclei were stained with DAPI (blue in merge). Scale bar, 20 µm. **C.** Directed transport of a KIF1A condensate. Scale bar, 10 µm. **D.** Directed transport of a KIF5B condensate (white arrows). The dashed yellow line represents the condensate trajectory. Scale bar, 10 µm. **E.** Kymograph analysis along the condensate trajectory shown in (C). Scale bar, 10 µm.

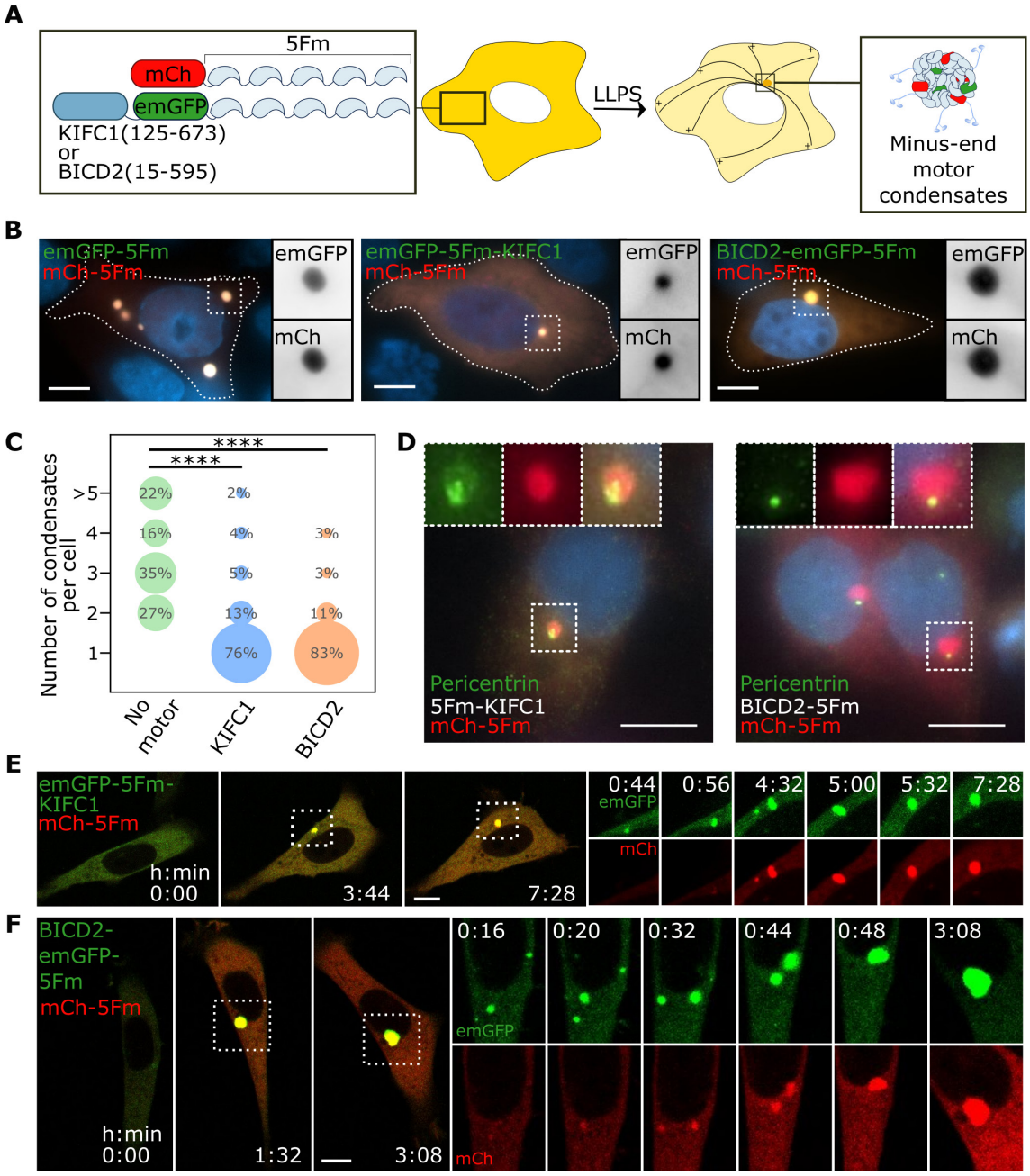

Figure 2: Functionalization of artificial condensates with a minus-end motor or a dynein adaptor drives their localization at the centrosome. A. Schematic of the expected centrosomal localization of condensates following transfection of mCh-5Fm and emGFP-5Fm-KIFC1 or BICD2-emGFP-5Fm (Fm = F36M-FKBP) in HeLa cells. **B.** Representative epifluorescence imaging of three cells expressing non-functionalized condensates (left panel), and KIFC1 or BICD2 condensates (middle and right panel, respectively). Nuclei were stained with DAPI (blue). Grayscale inserts correspond to the red (mCh) and green (emGFP) channels of the region delineated by dashed squares. Scale bar, 10 µm. **C.** Percentage of cells displaying 1, 2, 3, 4 or more than 5 condensates, for cells expressing non-functionalized condensates (left, N = 89 cells from three independent experiments), and KIFC1 or BICD2 condensates (middle, N = 85, and right, N = 73, respectively, each from three independent experiments). Differences between no motor and KIFC1 or BICD2 were statistically significant using a Pearson's chi-squared test (****: p-values < 10^{-25}). **D.** Epifluorescence imaging of cells displaying a KIFC1 or BiCD2 functionalized condensate (red, left and right, respectively) after immunostaining of pericentrin (green) as a centrosome marker. Nuclei were stained with DAPI (blue). Scale bar, 10 µm. **E.** Time-lapse confocal imaging of the formation of a KIFC1 condensate in a cell, starting 4 h after transfection. The dashed squares indicate the region enlarged on the right. Scale bar, 10 µm. **F.** Same as (E) for a BICD2 condensate. Scale bar, 10 µm.

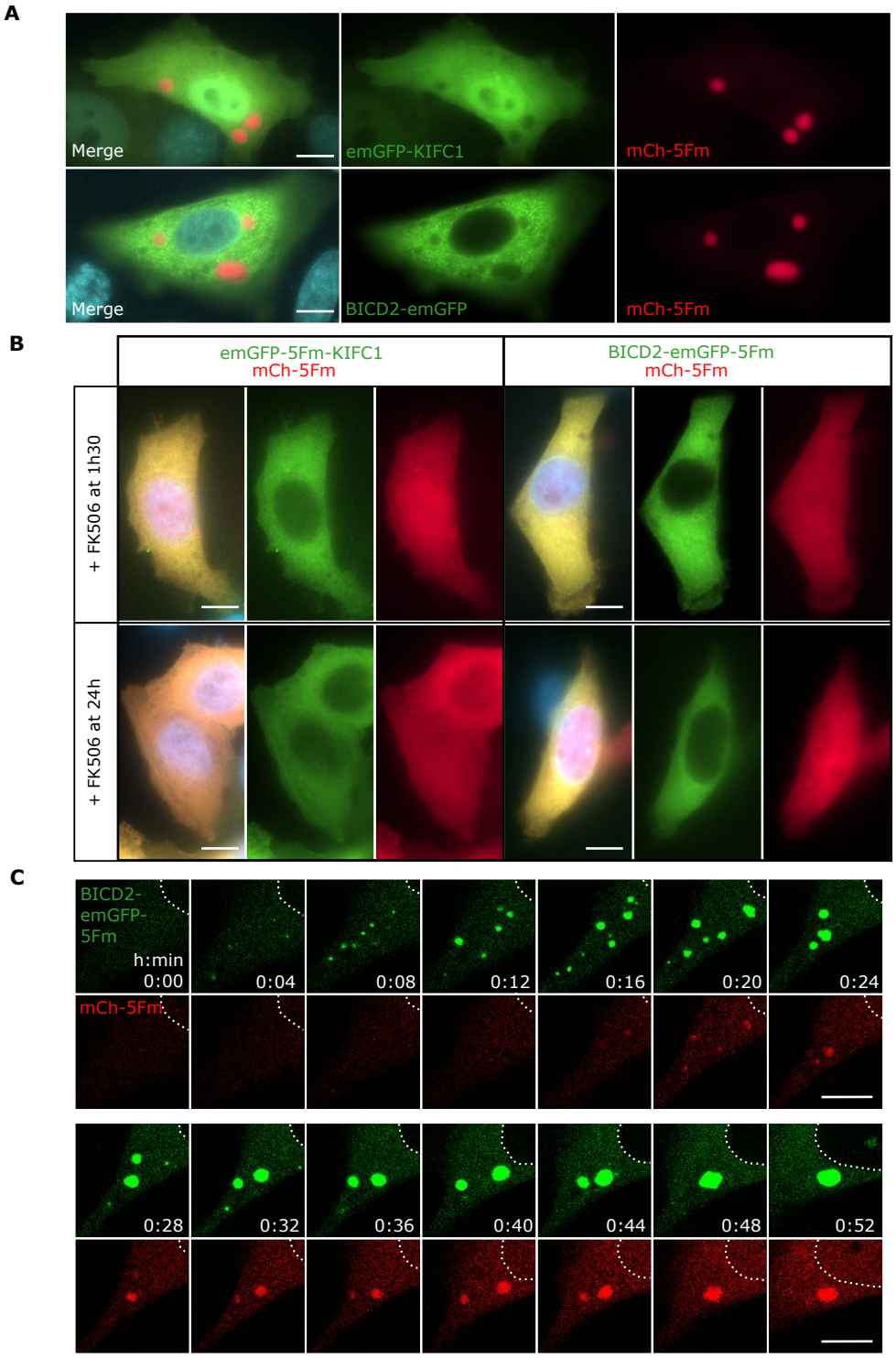

Figure S2: Cells expressing minus-end motors lacking the LLPS domain; chemical inhibition of condensates; and coalescence of BICD2 condensates. A. Representative epifluorescence imaging of HeLa cells transfected with emGFP-KIFC1 (upper panel) or BICD2-emGFP (lower panel) and mCh-5Fm. Nuclei were stained with DAPI (blue in merge). Scale bar, 10 µm. **B.** Epifluorescence imaging of HeLa cells expressing emGFP-5Fm-KIFC1 (left) or BICD2-emGFP-5Fm (right) and mCh-5Fm after FK506 addition either right after transfection to forestall the formation of condensates (top) or 24 h after transfection to dissolve the condensates (bottom). Nuclei were stained with DAPI (blue in merge). Scale bar, 10 µm. **C.** Time-lapse confocal imaging of occasionally dispersed nucleation of BICD2 condensates, followed by a delayed enrichment of the non-functionalized LLPS scaffold, directed transport towards the centrosome and coalescence. The white dashed line delineates the nucleus. Scale bar, 10 µm.

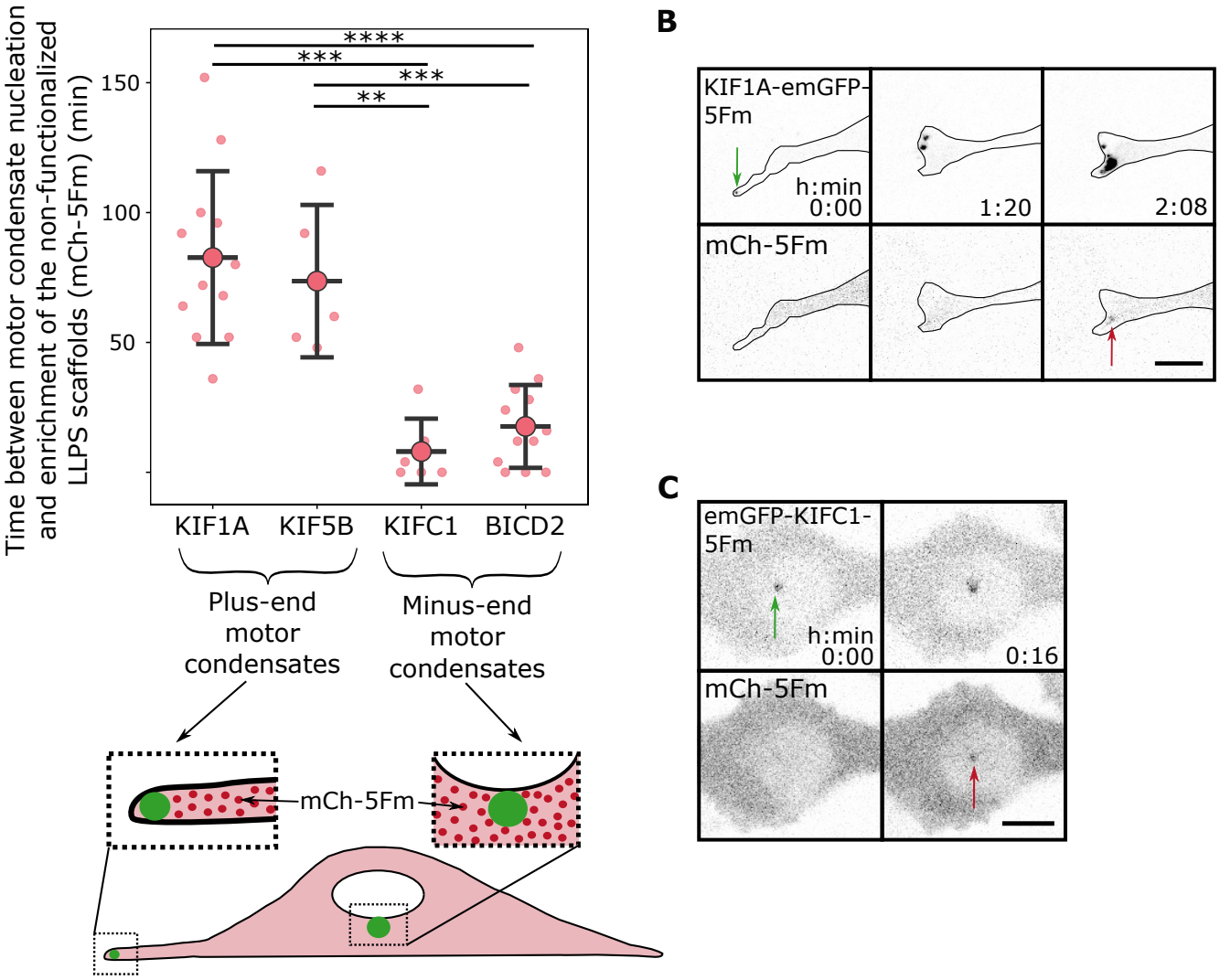

Figure 3: The enrichment of non-functionalized scaffolds in motor condensates differs depending on their cellular localization. A. Top: Delays between nucleation of the motor-LLPS scaffold and first detectable non-functionalized scaffold (mCherry signal) enrichment in condensates, for plus-end motors KIF1A (N = 12 cells) and KIF5B (N = 5), minus-end motor KIFC1 (N = 12) and dynein adaptor BICD2 (N = 6). Measurements were carried out on at least three independent experiments for each condition. Differences between plus-end motors and minus-end motor / motor adaptor were statistically significant using a Wilcoxon rank-sum test (**: $p < 10^{-2}$; ***: $p < 10^{-3}$; ****: $p < 10^{-4}$). Bottom: Schematic of the subcellular location of condensates at the centrosome and at the cell periphery. **B.** Time lapse epifluorescence images of the delayed enrichment of mCh-5Fm in KIF1A condensates in a representative cell. The green and red arrows correspond to the nucleation of the condensate and the first visible enrichment of mCh-5Fm, respectively. Scale bar, 10 µm. **C.** Same as (B) for a KIFC1 condensate.

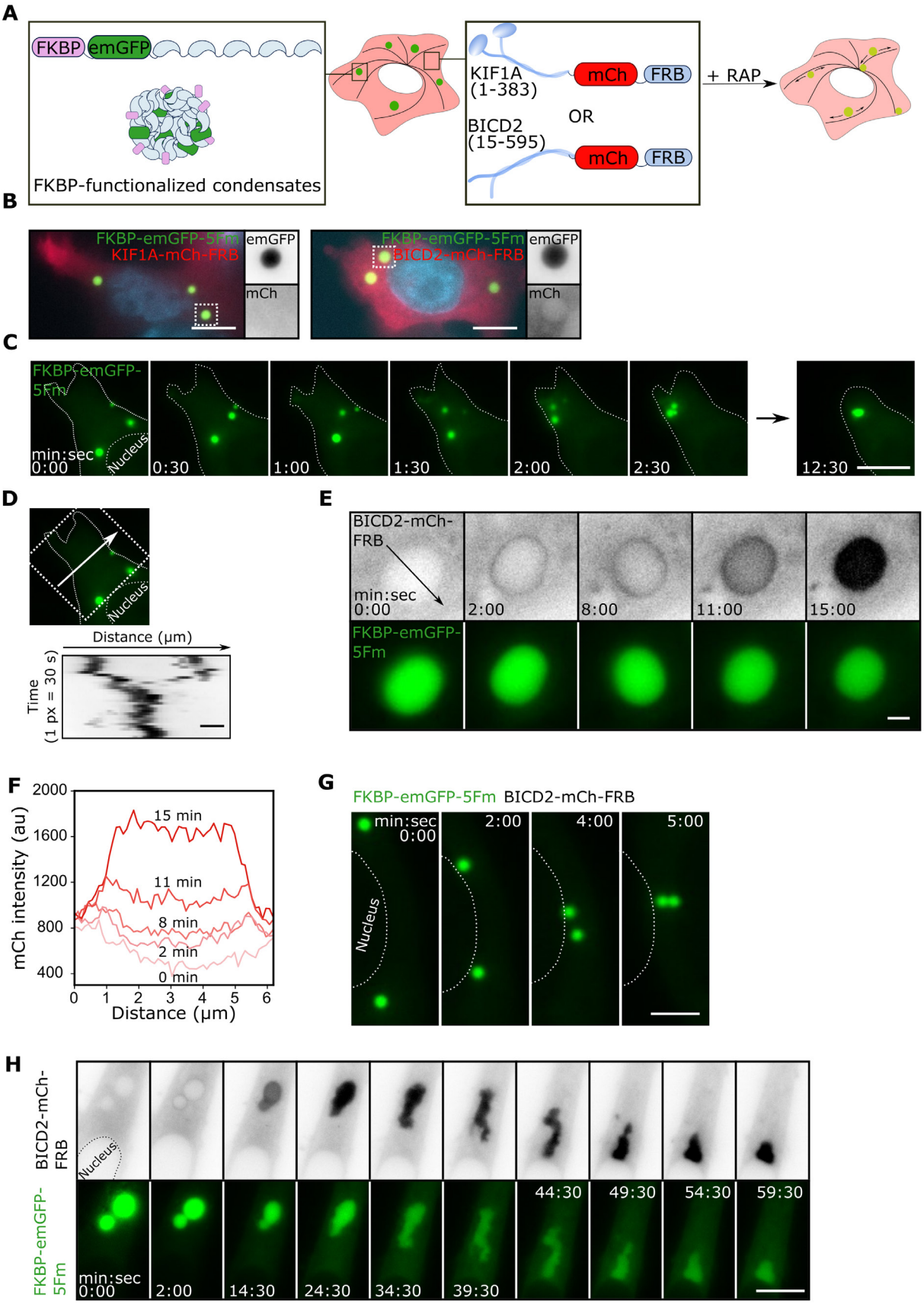

Figure 4: Chemically-induced binding of non-functionalized condensates to molecular motors led to their repositioning in cells. A. Schematic of the expected transport of FKBP condensates upon induction of their interaction with plus-end (KIF1A) or minus-end motors (dynein through BICD2) using Rapamycin (RAP) in HeLa cells. **B.** Representative epifluorescence imaging of cells expressing the FKBP-emGFP-5Fm LLPS scaffold and KIF1A-mCh-FRB (left) or BICD2-

mCh-FRB (right) in the absence of rapamycin. Nuclei were stained with DAPI (blue). Grayscale inserts correspond to the green (emGFP) and red (mCh) channels of the region delineated by dashed squares. Scale bar, 10 µm. **C.** Time-lapse epifluorescence imaging of FKBP-emGFP-5Fm condensates undergoing transport towards the cell periphery and coalescence after addition of rapamycin at time 0. Scale bar, 10 µm. **D.** For the cell shown in (C), kymograph analysis along the 200 px-wide strip delineated by the arrows (~ 21.7 µm), showing the coalescence of condensates over time. Scale bar, 2 µm. **E.** Epifluorescence imaging of the recruitment of BICD2-mCh-FRB (top) around a FKBP condensate (bottom), followed by progressive mixing of the two components. The black arrow corresponds to where the profile plots in (F) were plotted. Scale bar, 2 µm. **F.** Evolution of the mCherry intensity along the black arrow in **E** over time. **G.** Epifluorescence imaging of the transport of two FKBP condensates in a cell expressing BICD2-mCh-FRB after addition of rapamycin. Scale bar, 5 µm. **H.** Epifluorescence imaging of the recruitment and incorporation of BICD2-mCh-FRB (top) in a FKBP condensate (bottom) after addition of rapamycin, followed by transport towards the nuclear envelope with a liquid-like behavior. Scale bar, 10 µm.

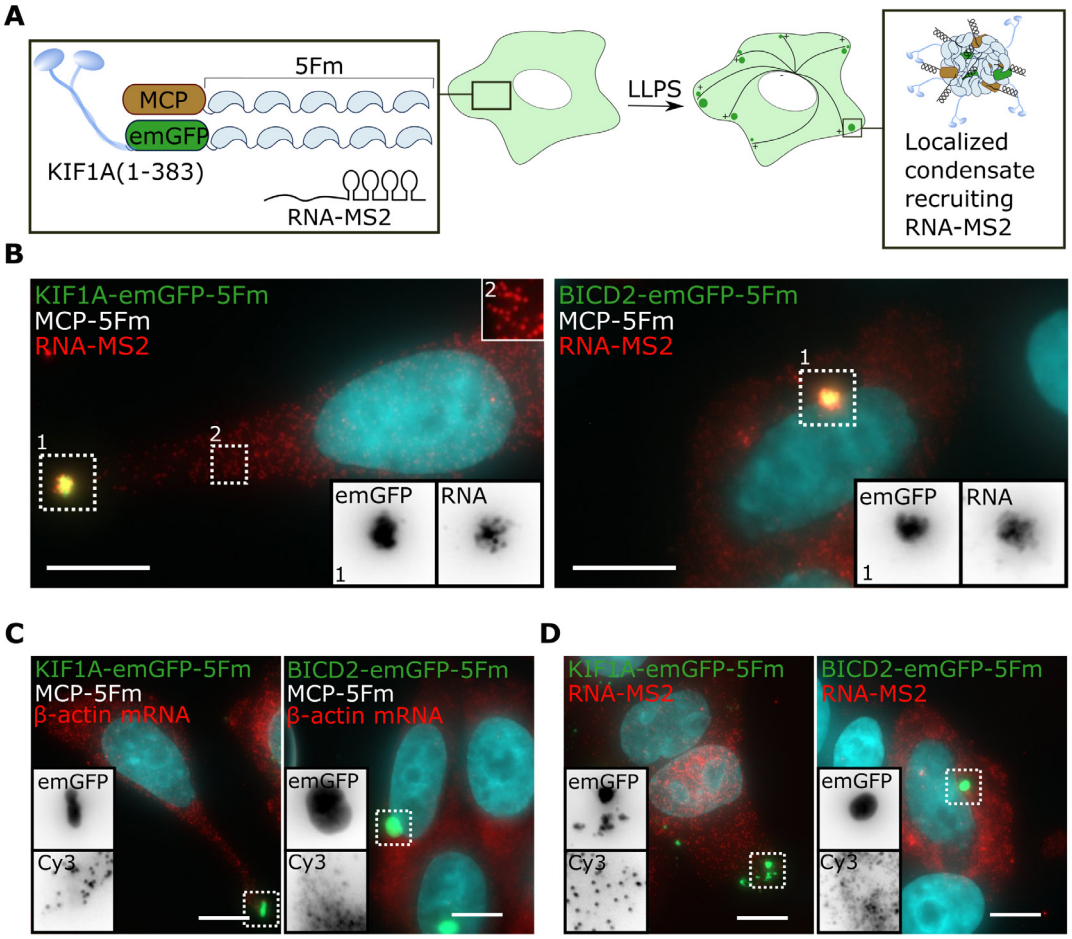

Figure 5: Motor/MCP condensates recruit RNA-MS2 and are efficiently positioned at the cell periphery or at the centrosome. A. Schematic of the formation of KIF1A/MCP condensates able to recruit the heterologous RNA-MS2. **B.** Representative epifluorescence imaging of cells containing KIF1A/MCP or BICD2/MCP condensates (green, left and right panels, respectively) following RNA-MS2 analysis by smiFISH (Cy3 probe, red). Nuclei were stained with DAPI (blue). The red channel setup allows for the visualization of dispersed RNA molecules while saturating the signal in the condensate. Grayscale inserts (1) correspond to the non-saturated green (emGFP) and red (Cy3) channels of the regions delineated by dashed squares. Insert 2 shows isolated RNA-MS2 molecules. Scale bar, 10 µm. **C.** Epifluorescence imaging of cells containing MCP condensates (green) following β-actin mRNA analysis by smiFISH (Cy3 probe, red). Scale bar, 10 µm. **D.** Epifluorescence imaging of cells containing condensates lacking MCP (green) following RNA-MS2 analysis by smiFISH (Cy3 probe, red). Scale bar, 10 µm.

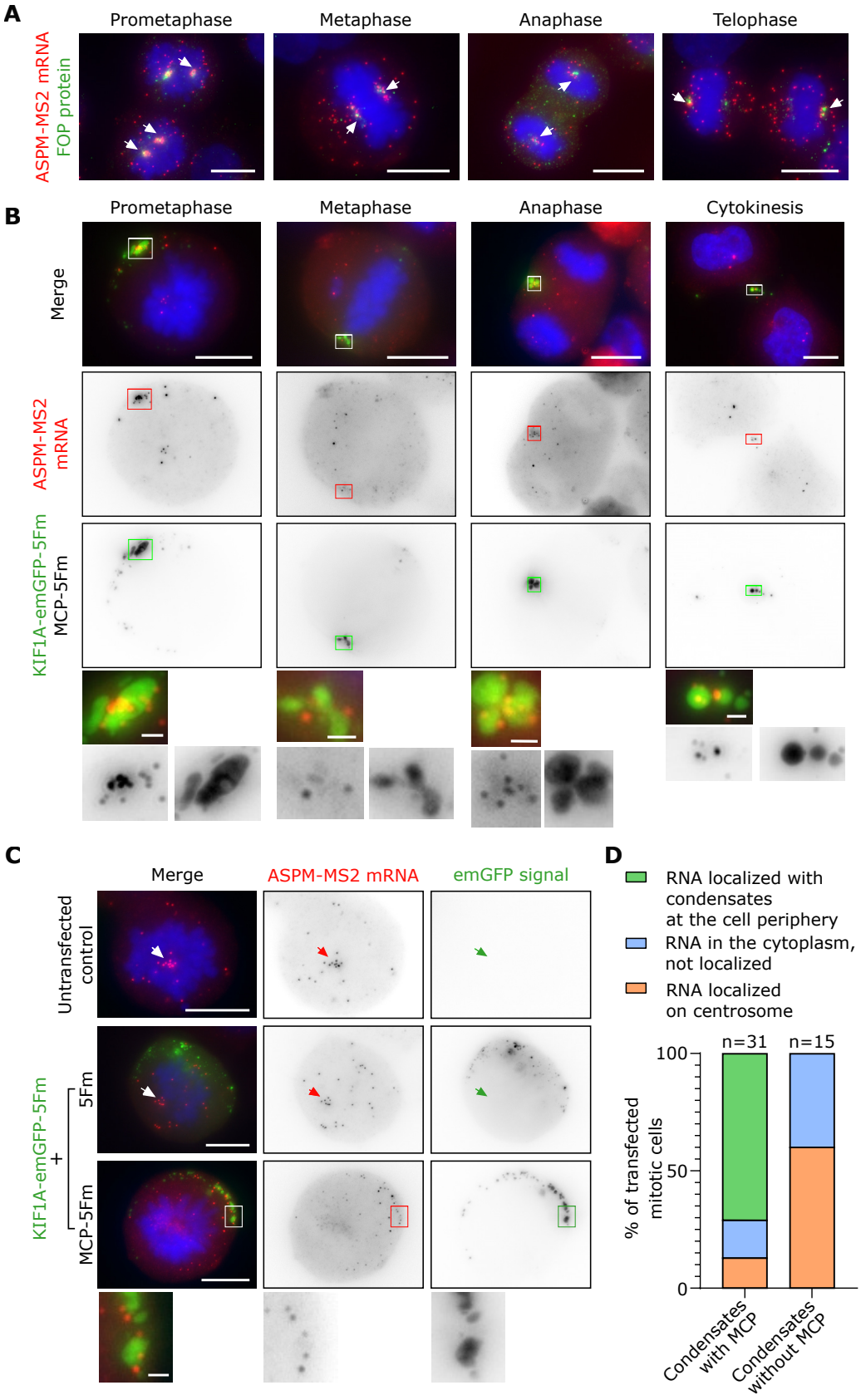

Figure 6: KIF1A condensates can efficiently delocalize ASPM-MS2 RNA towards the cell membrane during mitosis. **A.** Epifluorescence imaging of HeLa/ASPM-MS2 cells at different stages of mitosis after immunostaining of FOP (green) as a centrosome marker. The RNA was revealed by smFISH using a MS2 probe (red). DNA was stained with DAPI (blue). Scale bar, 10 µm. White arrows point to centrosomal mRNA accumulation. **B.** Epifluorescence imaging of HeLa/ASPM-

MS2 containing KIF1A/MCP condensates at different stages of mitosis. Middle and bottom panels show the ASPM-MS2 mRNA revealed by smFISH (red channel) and the GFP condensates (green channel), respectively. Upper panels show the merged channels with DAPI-stained DNA in blue. Scale bar, 10 μm. Squares depicting areas near the cell membrane where granules and RNA co-localize are enlarged below. **C.** Epifluorescence imaging of prometaphase cells untransfected or expressing KIF1A condensates, with or without MCP. Left panels show the merged channels with DAPI-stained DNA in blue. Middle and right panels show the ASPM-MS2 mRNA revealed by smFISH (red channel) and the GFP condensates (green channel), respectively. Scale bar, 10 μm. Arrows point to centrosomal mRNA accumulation. Scale bar, 10 μm. The boxed area where the RNA and granules co-localize at the cell membrane, is enlarged below. Scale bar, 1 μm. **D.** For the two conditions shown in (C), bar graph representing the % of mitotic cells with ASPM-MS2 mRNA localized at the cell periphery, dispersed in the cytoplasm, or localized on centrosome (N= 31 and 15 cells, as indicated, each from two independent experiments).

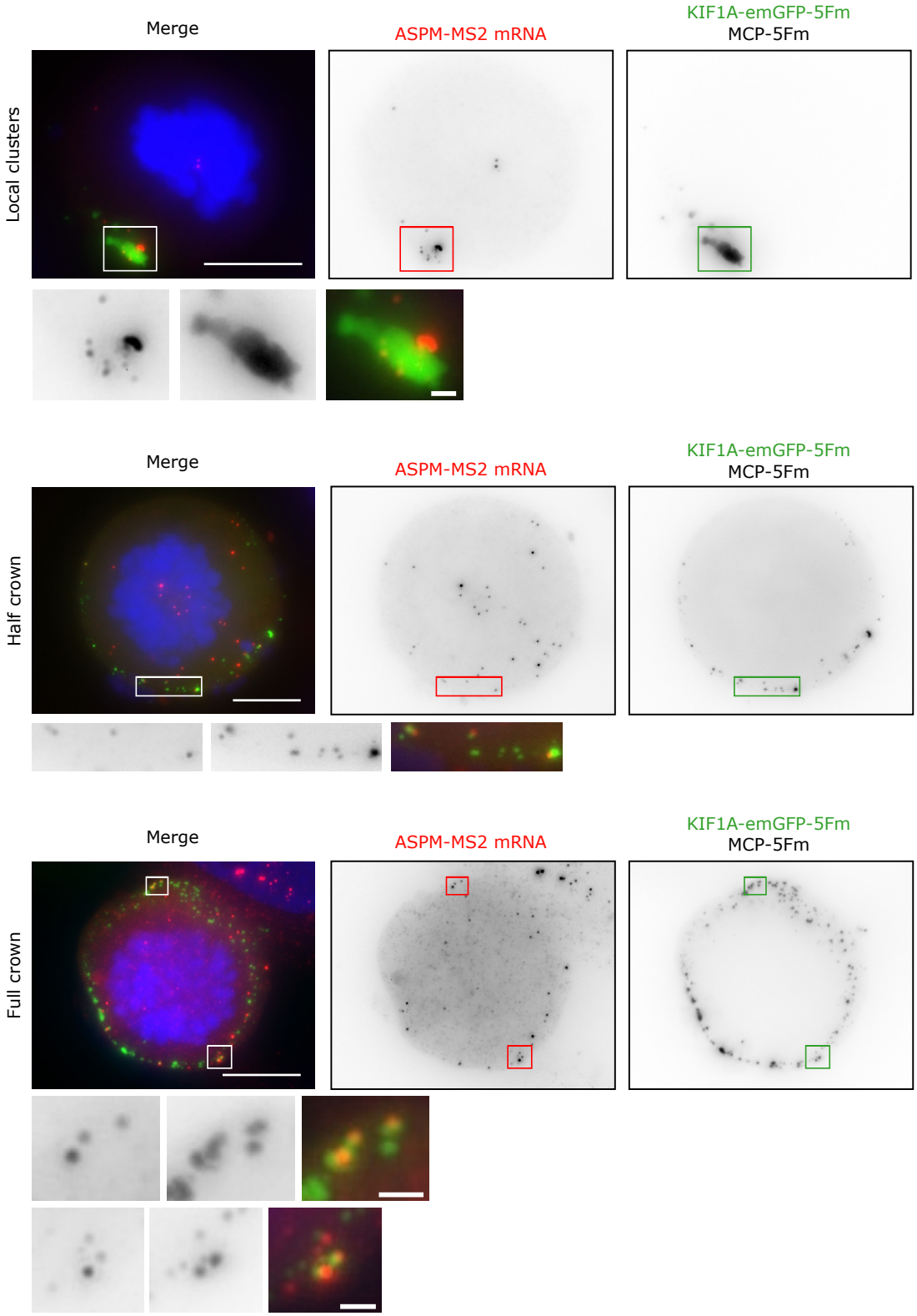

Figure S3: KIF1A/MCP condensates delocalized ASPM-MS2 mRNAs away from centrosomes and display three patterns in mitotic cells. Epifluorescence imaging of prometaphasic HeLa/ASPM-MS2 cells containing KIF1A/MCP condensates. Left panels show the merged channels with DAPI-stained DNA in blue. Left and middle panels show the ASPM-MS2 mRNA revealed by smFISH (red channel) and the GFP condensates (green channel), respectively. Scale bar, 10 µm. Squares depicting areas near the cell membrane where granules and RNA co-localize are enlarged below. Scale bar, 1 µm.

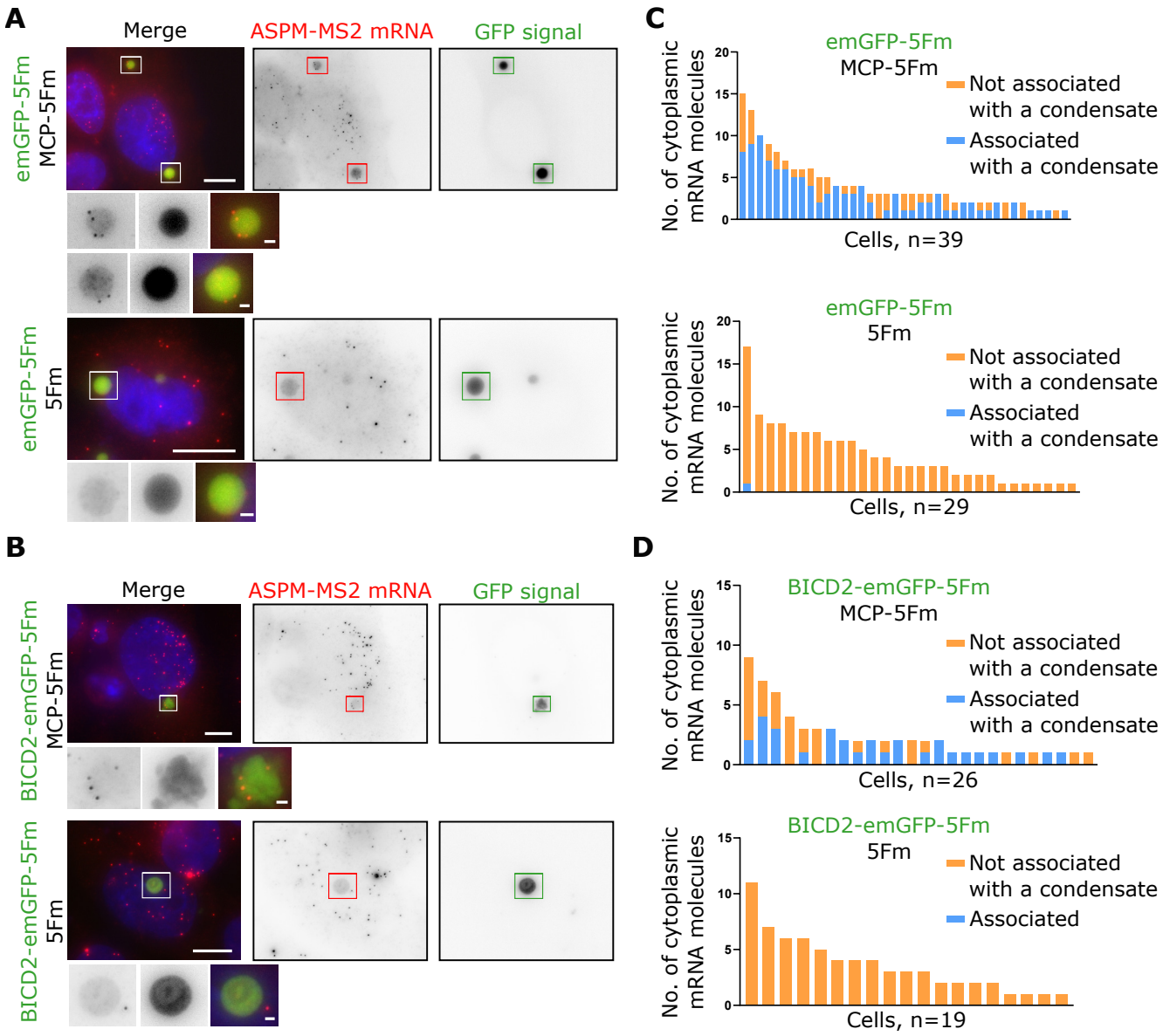

Figure S4: Motor-free BICD2 condensates can recruit ASPM-MS2 RNA in interphase. A. Epifluorescence imaging of interphasic HeLa/ASPM-MS2 cells containing motor-free condensates. Left and middle panels show the ASPM-MS2 mRNA revealed by smFISH (red channel) and the GFP condensates (green channel), respectively, either with (upper panels) or without (lower panels) MCP. Right panels show the merged channels with DAPI-stained nuclei in blue. Scale bar, 10 µm. Squares containing condensates that may (upper panels) or may not (lower panels) contain RNA are enlarged below. Scale bar, 1 µm. **B.** For the two conditions shown in (A), the bar graph shows the number of ASPM-MS2 RNAs per cell co-localizing or not with a condensate (N=39 and 29 cells, as indicated, each from two independent experiments). **C, D.** Same as in (A, B) for condensates containing the BICD2 motor adaptor.

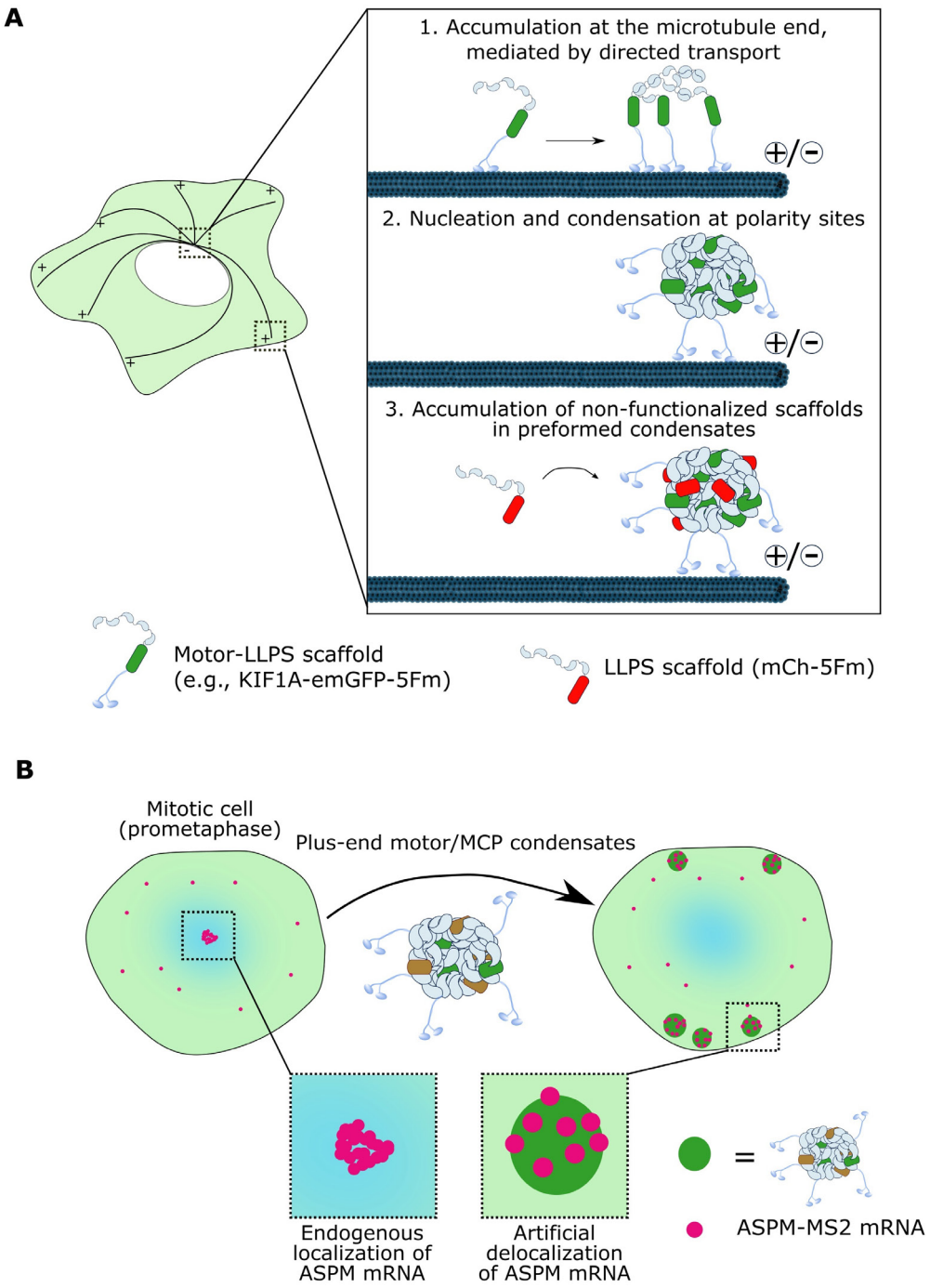

Figure 7: Model of localized nucleation and growth of condensates allowing for delocalization of ASPM-MS2 mRNA. **A.** Schematic model of the spatial localization of motor-functionalized condensates based on a stepwise mechanism: (1) active transport of the condensate scaffolds leading to their localization at microtubules extremities; (2) nucleation of motor condensates through a mechanism possibly mediated by prewetting or cooperative binding; (3) non-functionalized LLPS scaffolds accumulate in the preformed condensates. **B.** Artificial condensates drive the delocalization of individual ASPM-MS2 mRNAs at the cell periphery, suggesting that they outperform endogenous mRNA localization mechanisms by rewiring the transport machinery.

CONCLUSION

Bioengineering phase-separated condensates in cells, by allowing the same compositional control as *in vitro* experiments, circumvents the complexity of native biomolecular condensates while providing the ability to work in the cellular context. Such approaches can undoubtedly be powerful to examine the mechanisms underlying the formation of condensates and regulating their biophysical properties (size, number, material properties…).

My Ph.D. work consisted in building new tools falling within these lines. It aimed first at investigating how RNA, a ubiquitous component of cytosolic condensates, could impact their formation. Here, I took advantage of the ArtiGranule system, developed before the beginning of my Ph.D. by Zoher Gueroui's lab. Transfection of the ArtiGranule modules results in the spontaneous formation of artificial condensates in cells by liquid-liquid phase separation. For a quantitative insight on the role of RNA in the formation of condensates, we added in the scaffold of ArtiGranules the MCP RBP which is orthogonal to the cell and specifically binds to a single heterelogously-expressed RNA species, RNA-MS2. As revealed by the labelling of the target RNA-MS2 molecules via smFISH, the recruited molecules were localized at the surface of ArtiGranules condensates. We showed that this surface recruitment induced a hardening of the condensates. Moreover, our ability to detect individual RNA-MS2 molecules allowed us for the first time to quantify the effect of surface RNA on condensates size and number. We found that the higher the RNA surface density was, the smaller and more numerous the condensates were. High RNA surface density moreover also correlates with clusters of condensates reminiscent of hindered coalescence events. Our findings can be explained by physical constraints limiting condensates growth by sub-unit addition and coalescence. These new insights on the impact of surface RNA on condensate biophysical properties may be relevant for endogenous condensates, whose interface is emerging as distinct from the cores of the condensates or the surrounding cellular environment, with its own composition and organization. These results are the subject of a paper published in Biophysical Journal (Cochard et al., Biophysical Journal, 2022).

In the second part of my Ph.D., we looked into the interplay between proteins able to phase separate and microtubules. To do so, we first developed a variant of the ArtiGranule system, based on a linear fusion of five repeats of the Fm protein that can homodimerize. This linear system, called 5Fm, benefits from the possibility to fuse proteins of interest of both sides of the repeats. Fusion of kinesin motor or dynein adaptor domains to the repeats led to bioengineered condensates that were robustly positioned at the periphery of cells or near the centrosome, depending on the direction of processivity of motors. Interestingly, time-lapse imaging uncovered a pathway for the spatial positioning of biomolecular condensates whereby nucleation of motor-functionalized condensates is favored at polarity sites. Adding the MCP RBP in the scaffold of the 5Fm system already functionalized with

motor domains allowed us to manipulate the localization of target mRNAs in cells, both heterelogously-expressed or endogenous. These proof-of-concept experiments showed that our system may be a powerful tool to examine the importance of mRNA subcellular localization. These results are online on BioRxiv (Cochard et al., BioRxiv, 2022).

Altogether, the two projects of my Ph.D. showed the high potential of our bioengineering approach to address broad questions still elusive about biomolecular condensates. The ArtiGranule and 5Fm systems display interesting advantages. First, both are easy to implement. Secondly, the formation and dissolution of the condensates in both systems can be temporally controlled, which brings flexibility. Finally, the systems are highly modular. The multivalence of the interacting proteins underlying phase separation and formation of the condensates can be readily modified, which would lead to condensates with different material properties (more or less liquid-like). Adding different proteins of interest could moreover allow to look into different aspects of condensate biology, in particular related to the evolution from healthy to pathological condensates involved in neurodegenerative diseases and cancer.

REFERENCES

1. Banani, S. F., Lee, H. O., Hyman, A. A. & Rosen, M. K. Biomolecular condensates: organizers of cellular biochemistry. *Nature Reviews Molecular Cell Biology* **18**, 285–298 (2017).

2. Cohan, M. C. & Pappu, R. v. Making the Case for Disordered Proteins and Biomolecular Condensates in Bacteria. *Trends in Biochemical Sciences* **45**, 668–680 (2020).

3. Azaldegui, C. A., Vecchiarelli, A. G. & Biteen, J. S. The emergence of phase separation as an organizing principle in bacteria. *Biophysical Journal* **120**, 1123–1138 (2021).

4. Pederson, T. The Nucleolus. *Cold Spring Harbor Perspectives in Biology* (2011) doi:10.1101/cshperspect.a000638.

5. Staněk, D. Cajal bodies and snRNPs-friends with benefits. *RNA Biology* **14**, 671–679 (2017).

6. Lallemand-Breitenbach, V. & de Thé, H. PML nuclear bodies. *Cold Spring Harbor perspectives in biology* vol. 2 Preprint at https://doi.org/10.1101/cshperspect.a000661 (2010).

7. Spector, D. L. & Lamond, A. I. Nuclear speckles. *Cold Spring Harbor Perspectives in Biology* **3**, 1–12 (2011).

8. Schmidt, H. B. & Görlich, D. Transport Selectivity of Nuclear Pores, Phase Separation, and Membraneless Organelles. *Trends in Biochemical Sciences* **41**, (2016).

9. Standart, N. & Weil, D. P-Bodies: Cytosolic Droplets for Coordinated mRNA Storage. *Trends in Genetics* **34**, (2018).

10. Ivanov, P., Kedersha, N. & Anderson, P. Stress Granules and Processing Bodies in Translational Control. *Cold Spring Harb Perspect Biol* **11**, (2019).

11. Dalla Costa, I. *et al.* The functional organization of axonal mRNA transport and translation. *Nature Reviews Neuroscience 2020 22:2* **22**, 77–91 (2020).

12. Brangwynne, C. P. *et al.* Germline P Granules Are Liquid Droplets That Localize by Controlled Dissolution/Condensation. *Science (1979)* **324**, 1729–1732 (2009).

13. Boisvert, F. M., Hendzel, M. J. & Bazett-Jones, D. P. Promyelocytic leukemia (PML) nuclear bodies are protein structures that do not accumulate RNA. *Journal of Cell Biology* **148**, 283–292 (2000).

14. Ahmad, Y., Boisvert, F. M., Gregor, P., Cobley, A. & Lamond, A. I. NOPdb: Nucleolar proteome database - 2008 Update. *Nucleic Acids Research* **37**, (2009).

15. Jain, S. *et al.* ATPase-Modulated Stress Granules Contain a Diverse Proteome and Substructure. *Cell* **164**, 487–498 (2016).

16. Khong, A. *et al.* The Stress Granule Transcriptome Reveals Principles of mRNA Accumulation in Stress Granules. *Molecular Cell* **68**, 808-820.e5 (2017).

17. Hubstenberger, A. *et al.* P-Body Purification Reveals the Condensation of Repressed mRNA Regulons. *Mol Cell* **68**, 144-157.e5 (2017).

18. Moon, S. L. *et al.* Multicolour single-molecule tracking of mRNA interactions with RNP granules. *Nature Cell Biology* vol. 21 162–168 Preprint at https://doi.org/10.1038/s41556-018-0263-4 (2019).

19. van Damme, E., Laukens, K., Dang, T. H. & van Ostade, X. A manually curated network of the PML nuclear body interactome reveals an important role for PML-NBs in SUMOylation dynamics. *International Journal of Biological Sciences* **6**, 51 (2010).

20. Ishov, A. M. *et al.* PML Is Critical for ND10 Formation and Recruits the PML-interacting Protein Daxx to this Nuclear Structure When Modified by SUMO-1. *The Journal of Cell Biology* **147**, 221–233 (1999).

21. Banani, S. F. *et al.* Compositional Control of Phase-Separated Cellular Bodies. *Cell* **166**, 651–663 (2016).

22. Hamill, D. R., Severson, A. F., Carter, J. C. & Bowerman, B. Centrosome maturation and mitotic spindle assembly in C. elegans require SPD-5, a protein with multiple coiled-coil domains. *Developmental Cell* **3**, 673–684 (2002).

23. Yamazaki, T. *et al.* Functional Domains of NEAT1 Architectural lncRNA Induce Paraspeckle Assembly through Phase Separation. *Molecular Cell* **70**, 1038–1053 (2018).

24. Decker, C. J. & Parker, R. P-Bodies and Stress Granules: Possible Roles in the Control of Translation and mRNA Degradation. doi:10.1101/cshperspect.a012286.

25. Platani, M., Goldberg, I., Swedlow, J. R. & Lamond, A. I. In Vivo Analysis of Cajal Body Movement, Separation, and Joining in Live Human Cells 7. *The Journal of Cell Biology* **151**, 1561–1574 (2000).

26. Chen, Y. C. M., Kappel, C., Beaudouin, J., Eils, R. & Spector, D. L. Live cell dynamics of promyelocytic leukemia nuclear bodies upon entry into and exit from mitosis. *Molecular Biology of the Cell* **19**, 3147–3162 (2008).

27. Brangwynne, C. P., Mitchison, T. J. & Hyman, A. A. Active liquid-like behavior of nucleoli determines their size and shape in Xenopus laevis oocytes. *Proc Natl Acad Sci U S A* **108**, 4334–9 (2011).

28. Phair, R. D. & Misteli, T. High mobility of proteins in the mammalian cell nucleus. *Nature 2000 404:6778* **404**, 604–609 (2000).

29. Dundr, M. *et al.* In vivo kinetics of Cajal body components. *The Journal of Cell Biology JCB Article The Journal of Cell Biology* **164**, 831–842 (2004).

30. Weidtkamp-Peters, S. *et al.* Dynamics of component exchange at PML nuclear bodies. *Journal of Cell Science* **121**, 2731–2743 (2008).

31. Patel, A. *et al.* A Liquid-to-Solid Phase Transition of the ALS Protein FUS Accelerated by Disease Mutation. *Cell* **162**, 1066–1077 (2015).

32. Hyman, A. A., Weber, C. A. & Ulicher, F. J. ¨. Liquid-Liquid Phase Separation in Biology. *Annu. Rev. Cell Dev. Biol* **30**, 39–58 (2014).

33. Shin, Y. *et al.* Spatiotemporal Control of Intracellular Phase Transitions Using Light-Activated optoDroplets. *Cell* **168**, 159-171.e14 (2017).

34. Wang, J. *et al.* A Molecular Grammar Governing the Driving Forces for Phase Separation of Prion-like RNA Binding Proteins. *Cell* **174**, 688-699.e16 (2018).

35. Riback, J. A. *et al.* Composition-dependent thermodynamics of intracellular phase separation. *Nature* 1–6 (2020) doi:10.1038/s41586-020-2256-2.

36. Heidenreich, M. *et al.* Designer protein assemblies with tunable phase diagrams in living cells. *Nature Chemical Biology* **16**, 939–945 (2020).

37. Li, P. *et al.* Phase transitions in the assembly of multivalent signalling proteins. *Nature* **483**, 336–340 (2012).

38. Berry, J., Brangwynne, C. P. & Haataja, M. Physical principles of intracellular organization via active and passive phase transitions. *Reports on Progress in Physics* vol. 81 046601 Preprint at https://doi.org/10.1088/1361-6633/aaa61e (2018).

39. Banjade, S. & Rosen, M. K. Phase transitions of multivalent proteins can promote clustering of membrane receptors. *Elife* **3**, (2014).

40. Uversky, V. N., Kuznetsova, I. M., Turoverov, K. K. & Zaslavsky, B. Intrinsically disordered proteins as crucial constituents of cellular aqueous two phase systems and coacervates. *FEBS Letters* **589**, 15–22 (2015).

41. Nott, T. J. *et al.* Phase Transition of a Disordered Nuage Protein Generates Environmentally Responsive Membraneless Organelles. *Molecular Cell* **57**, 936–947 (2015).

42. Elbaum-Garfinkle, S. *et al.* The disordered P granule protein LAF-1 drives phase separation into droplets with tunable viscosity and dynamics. *Proceedings of the National Academy of Sciences* **112**, 7189–7194 (2015).

43. Feric, M. *et al.* Coexisting Liquid Phases Underlie Nucleolar Subcompartments. *Cell* **165**, 1686–1697 (2016).

44. Molliex, A. *et al.* Phase Separation by Low Complexity Domains Promotes Stress Granule Assembly and Drives Pathological Fibrillization. *Cell* **163**, 123–133 (2015).

45. Mitrea, D. M. *et al.* Nucleophosmin integrates within the nucleolus via multi-modal interactions with proteins displaying R-rich linear motifs and rRNA. *Elife* **5**, (2016).

46. Yang, P. *et al.* G3BP1 Is a Tunable Switch that Triggers Phase Separation to Assemble Stress Granules. *Cell* **181**, 325-345.e28 (2020).

47. Peng, A. & Weber, S. C. Evidence for and against Liquid-Liquid Phase Separation in the Nucleus. *Non-Coding RNA 2019, Vol. 5, Page 50* **5**, 50 (2019).

48. Hirose, T. *et al.* NEAT1 long noncoding RNA regulates transcription via protein sequestration within subnuclear bodies. *Molecular Biology of the Cell* **25**, 169–183 (2014).

49. Chujo, T., Yamazaki, T. & Hirose, T. Architectural RNAs (arcRNAs): A class of long noncoding RNAs that function as the scaffold of nuclear bodies ☆. (2015) doi: 10.1016/j.bbagrm.2015.05.007.

50. Berry, J. *et al.* RNA transcription modulates phase transition-driven nuclear body assembly. *Proc Natl Acad Sci U S A* **112**, E5237–E5245 (2015).

51. Yamazaki, T. *et al.* Paraspeckles are constructed as block copolymer micelles. *The EMBO Journal* **40**, e107270 (2021).

52. Erdel, F. & Rippe, K. Formation of Chromatin Subcompartments by Phase Separation. *Biophysical Journal* **114**, 2262 (2018).

53. Miné-Hattab, J. *et al.* Single molecule microscopy reveals key physical features of repair foci in living cells. *Elife* **10**, 1–56 (2021).

54. Raff, J. W. Phase Separation and the Centrosome: A Fait Accompli? (2019) doi:10.1016/j.tcb.2019.04.001.

55. Hondele, M., Heinrich, S., de Los Rios, P. & Weis, K. Membraneless organelles: phasing out of equilibrium. *Emerging Topics in Life Sciences* **4**, 331–342 (2020).

56. Wang, Z., Lou, J. & Zhang, H. Essence determines phenomenon: Assaying the material properties of biological condensates. *Journal of Biological Chemistry* **298**, 101782 (2022).

57. Zhu, L. *et al.* Controlling the material properties and rRNA processing function of the nucleolus using light. *Proceedings of the National Academy of Sciences* **116**, (2019).

58. Lyon, A. S., Peeples, W. B. & Rosen, M. K. A framework for understanding the functions of biomolecular condensates across scales. *Nature Reviews Molecular Cell Biology 2020 22:3* **22**, 215–235 (2020).

59. Zhao, E. M. *et al.* Light-based control of metabolic flux through assembly of synthetic organelles. *Nature Chemical Biology* **15**, 589–597 (2019).

60. Dzuricky, M., Rogers, B. A., Shahid, A., Cremer, P. S. & Chilkoti, A. De novo engineering of intracellular condensates using artificial disordered proteins. *Nature Chemistry* **12**, 814–825 (2020).

61. Feric, M. *et al.* Structure-function relationships in mitochondrial transcriptional condensates. *bioRxiv* (2022) doi:10.1101/2021.12.30.474545.

62. Wei, M. T. *et al.* Nucleated transcriptional condensates amplify gene expression. *Nature Cell Biology* **22**, 1187–1196 (2020).

63. Trojanowski, J. *et al.* Transcription activation is enhanced by multivalent interactions independent of phase separation. *Molecular Cell* **82**, 1878-1893.e10 (2022).

64. Leidescher, S. *et al.* Spatial organization of transcribed eukaryotic genes. *Nature Cell Biology 2022 24:3* **24**, 327–339 (2022).

65. Lu, T. & Spruijt, E. Multiphase Complex Coacervate Droplets. *J Am Chem Soc* **142**, 2905–2914 (2020).

66. Fromm, S. A. *et al.* In Vitro Reconstitution of a Cellular Phase-Transition Process that Involves the mRNA Decapping Machinery. *Angewandte Chemie International Edition* **53**, 7354–7359 (2014).

67. Schuster, B. S. *et al.* Controllable protein phase separation and modular recruitment to form responsive membraneless organelles. *Nature Communications 2018 9:1* **9**, 1–12 (2018).

68. Pak, C. W. *et al.* Sequence Determinants of Intracellular Phase Separation by Complex Coacervation of a Disordered Protein. *Molecular Cell* **63**, 72–85 (2016).

69. Qamar, S. *et al.* FUS Phase Separation Is Modulated by a Molecular Chaperone and Methylation of Arginine Cation-π Interactions. *Cell* **173**, 720-734.e15 (2018).

70. Brady, J. P. *et al.* Structural and hydrodynamic properties of an intrinsically disordered region of a germ cell-specific protein on phase separation. *Proceedings of the National Academy of Sciences* **114**, E8194–E8203 (2017).

71. Yoshizawa, T. *et al.* Nuclear Import Receptor Inhibits Phase Separation of FUS through Binding to Multiple Sites. *Cell* **173**, 693-705.e22 (2018).

72. Reed, E. H., Schuster, B. S., Good, M. C. & Hammer, D. A. SPLIT: Stable Protein Coacervation Using a Light Induced Transition. *ACS Synthetic Biology* **9**, 500–507 (2020).

73. Lasker, K. *et al.* A modular platform for engineering function of natural and synthetic biomolecular condensates. *bioRxiv* 2021.02.03.429226 (2021) doi:10.1101/2021.02.03.429226.

74. Nakamura, H., Derose, R. & Inoue, T. Harnessing biomolecular condensates in living cells. *The Journal of biochemistry* **166**, 13–27 (2019).

75. Garcia-Jove Navarro, M. *et al.* RNA is a critical element for the sizing and the composition of phase-separated RNA–protein condensates. *Nature Communications* **10**, 3230 (2019).

76. Watanabe, T. *et al.* Genetic visualization of protein interactions harnessing liquid phase transitions. *Scientific Reports* **7**, 1–13 (2017).

77. Yoshikawa, M., Yoshii, T., Ikuta, M. & Tsukiji, S. Synthetic Protein Condensates That Inducibly Recruit and Release Protein Activity in Living Cells. *J Am Chem Soc* **143**, 6434–6446 (2021).

78. Bracha, D. *et al.* Mapping Local and Global Liquid Phase Behavior in Living Cells Using Photo-Oligomerizable Seeds. *Cell* **175**, 1467–1480 (2018).

79. Shimobayashi, S. F., Ronceray, P., Sanders, D. W., Haataja, M. P. & Brangwynne, C. P. Nucleation landscape of biomolecular condensates. *Nature* 1–4 (2021) doi:10.1038/s41586-021-03905-5.

80. Shin, Y. *et al.* Liquid Nuclear Condensates Mechanically Sense and Restructure the Genome. *Cell* **175**, 1481-1491.e13 (2018).

81. Dine, E., Gil, A. A., Uribe, G., Brangwynne, C. P. & Toettcher, J. E. Protein Phase Separation Provides Long-Term Memory of Transient Spatial Stimuli. *Cell Systems* **6**, 655-663.e5 (2018).

82. Lee, S. *et al.* Reversible protein inactivation by optogenetic trapping in cells. *Nature Methods* **11**, 633 (2014).

83. Kim, N. Y. *et al.* Optogenetic control of mRNA localization and translation in live cells. *Nature Cell Biology* 1–12 (2020) doi:10.1038/s41556-020-0468-1.

84. Nakamura, H. *et al.* Intracellular production of hydrogels and synthetic RNA granules by multivalent molecular interactions. *Nature Materials* **17**, 79–88 (2018).

85. van Treeck, B. & Parker, R. Emerging Roles for Intermolecular RNA-RNA Interactions in RNP Assemblies. *Cell* vol. 174 791–802 Preprint at https://doi.org/10.1016/j.cell.2018.07.023 (2018).

86. Boeynaems, S. *et al.* Spontaneous driving forces give rise to protein−RNA condensates with coexisting phases and complex material properties. *PNAS* **116**, (2019).

87. Mann, J. R. *et al.* RNA Binding Antagonizes Neurotoxic Phase Transitions of TDP-43. *Neuron* **102**, 321-338.e8 (2019).

88. Langdon, E. M. *et al.* mRNA structure determines specificity of a polyQ-driven phase separation. *Science (1979)* **360**, 922–927 (2018).

89. Asamitsu, S. Potential roles of G-quadruplex structures in RNA granules for physiological and pathological phase separation. *Journal of Biochemistry* (2021) doi:10.1093/jb/mvab018.

90. Drino, A. & Schaefer, M. R. RNAs, Phase Separation, and Membrane-Less Organelles: Are Post-Transcriptional Modifications Modulating Organelle Dynamics? *BioEssays* **40**, 1800085 (2018).

91. Ries, R. J. *et al.* m6A enhances the phase separation potential of mRNA. *Nature* **571**, 424–428 (2019).

92. Khong, A., Matheny, T., Huynh, T. N., Babl, V. & Parker, R. Limited effects of m6A modification on mRNA partitioning into stress granules. *bioRxiv* 2021.03.19.436090 (2021) doi:10.1101/2021.03.19.436090.

93. Guillén-Boixet, J. *et al.* RNA-Induced Conformational Switching and Clustering of G3BP Drive Stress Granule Assembly by Condensation. *Cell* **181**, 346-361.e17 (2020).

94. Brangwynne, C. P. Phase transitions and size scaling of membrane-less organelles. *Journal of Cell Biology* **203**, 875–881 (2013).

95. Decker, M. *et al.* Limiting amounts of centrosome material set centrosome size in C. elegans embryos. *Current Biology* **21**, 1259–1267 (2011).

96. Zwicker, D., Hyman, A. A. & Jülicher, F. Suppression of Ostwald ripening in active emulsions. *PHYSICAL REVIEW E* **92**, 12317 (2015).

97. David Wurtz, J. & Lee, C. F. Chemical-Reaction-Controlled Phase Separated Drops: Formation, Size Selection, and Coarsening. *Physical Review Letters* **120**, (2018).

98. Weber, C. A., Zwicker, D., Jülicher, F. & Lee, C. F. Physics of active emulsions. *Reports on Progress in Physics* **82**, 064601 (2019).

99. Bressloff, P. C. Active suppression of Ostwald ripening: Beyond mean-field theory. *Physical Review E* **101**, 42804 (2020).

100. Zwicker, D., Decker, M., Jaensch, S., Hyman, A. A. & Jülicher, F. Centrosomes are autocatalytic droplets of pericentriolar material organized by centrioles. *Proc Natl Acad Sci U S A* **111**, E2636–E2645 (2014).

101. Ranganathan, S. & Shakhnovich, E. I. Dynamic metastable long-living droplets formed by sticker-spacer proteins. *Elife* **9**, 1–25 (2020).

102. Dar, F. & Pappu, R. Restricting the sizes of condensates. *eLife* vol. 9 1–3 Preprint at https://doi.org/10.7554/eLife.59663 (2020).

103. Feric, M., Brangwynne, C. P., Cell, N. & Author, B. A nuclear F-actin scaffold stabilizes RNP droplets against gravity in large cells. *Nat Cell Biol* **15**, 1253–1259 (2013).

104. Snead, W. T., Gerbich, T. M., Seim, I., Hu, Z. & Gladfelter, A. S. Membrane surfaces regulate assembly of a ribonucleoprotein condensate. *bioRxiv* 2021.04.24.441251 (2021) doi:10.1101/2021.04.24.441251.

105. Farag, M. *et al.* Condensates of disordered proteins have small-world network structures and interfaces defined by expanded conformations. *bioRxiv* 2022.05.21.492916 (2022) doi:10.1101/2022.05.21.492916.

106. Linsenmeier, M. *et al.* The interface of condensates of the hnRNPA1 low complexity domain promotes formation of amyloid fibrils. *bioRxiv* 2022.05.23.493075 (2022) doi:10.1101/2022.05.23.493075.

107. Welsh, T. J. *et al.* Surface Electrostatics Govern the Emulsion Stability of Biomolecular Condensates. *Nano Letters* **22**, 612–621 (2022).

108. Cuylen, S. *et al.* Ki-67 acts as a biological surfactant to disperse mitotic chromosomes. *Nature* **535**, 308–312 (2016).

109. Kelley, F. M., Favetta, B., Regy, R. M., Mittal, J. & Schuster, B. S. Amphiphilic proteins coassemble into multiphasic condensates and act as biomolecular surfactants. *bioRxiv* 2021.05.28.446223 (2021) doi:10.1101/2021.05.28.446223.

110. Sanchez-Burgos, I., Joseph, J. A., Collepardo-Guevara, R. & Espinosa, J. R. Size conservation emerges spontaneously in biomolecular condensates formed by scaffolds and surfactant clients. *Scientific Reports 2021 11:1* **11**, 1–10 (2021).

111. Folkmann, A. W., Putnam, A., Lee, C. F. & Seydoux, G. Regulation of biomolecular condensates by interfacial protein clusters. *Science (1979)* **373**, (2021).

112. Gallego, L. D. *et al.* Phase separation directs ubiquitination of gene-body nucleosomes. *Nature 2020 579:7800* **579**, 592–597 (2020).

113. Fletcher, D. A. & Mullins, R. D. Cell mechanics and the cytoskeleton. *Nature 2010 463:7280* **463**, 485–492 (2010).

114. Vale, R. D. The molecular motor toolbox for intracellular transport. *Cell* **112**, 467–480 (2003).

115. Koppers, M., Özkan, N. & Farías, G. G. Complex Interactions Between Membrane-Bound Organelles, Biomolecular Condensates and the Cytoskeleton. *Frontiers in Cell and Developmental Biology* **8**, 1661 (2020).

116. Wiegand, T. & Hyman, A. A. Drops and fibers — how biomolecular condensates and cytoskeletal filaments influence each other. *Emerging Topics in Life Sciences* **4**, 247 (2020).

117. Bornens, M. The centrosome in cells and organisms. *Science (1979)* **335**, 422–426 (2012).

118. Hernández-Vega, A. *et al.* Local Nucleation of Microtubule Bundles through Tubulin Concentration into a Condensed Tau Phase. *Cell Reports* **20**, 2304–2312 (2017).

119. Perez-Pepe, M., Fernández-Alvarez, A. J. & Boccaccio, G. L. Life and Work of Stress Granules and Processing Bodies: New Insights into Their Formation and Function. *Biochemistry* **57**, 2488–2498 (2018).

120. Chernov, K. G. *et al.* Role of microtubules in stress granule assembly: Microtubule dynamical instability favors the formation of micrometric stress granules in cells. *Journal of Biological Chemistry* **284**, 36569–36580 (2009).

121. Tsai, N.-P., Tsui, Y.-C. & Wei, L.-N. DYNEIN MOTOR CONTRIBUTES TO STRESS GRANULE DYNAMICS IN PRIMARY NEURONS. *NSC* **159**, 647–656 (2009).

122. Aizer, A. & Shav-Tal, Y. Intracellular trafficking and dynamics of P bodies. *Prion* **2**, 131 (2008).

123. Loschi, M., Leishman, C. C., Berardone, N. & Boccaccio, G. L. Dynein and kinesin regulate stress-granule and P-body dynamics. *Journal of Cell Science* **122**, 3973–3982 (2009).

124. Nadezhdina, E. S., Lomakin, A. J., Shpilman, A. A., Chudinova, E. M. & Ivanov, P. A. Microtubules govern stress granule mobility and dynamics. *Biochimica et Biophysica Acta (BBA) - Molecular Cell Research* **1803**, 361–371 (2010).

125. Martin, K. C. & Ephrussi, A. mRNA Localization: Gene Expression in the Spatial Dimension. *Cell* **136**, 719–730 (2009).

126. Eliscovich, C. & Singer, R. H. RNP transport in cell biology: the long and winding road. *Current Opinion in Cell Biology* **45**, 38–46 (2017).

127. Jansen, R. P. mRNA localization: message on the move. *Nature Reviews Molecular Cell Biology 2001 2:4* **2**, 247–256 (2001).

128. Zimyanin, V. L. *et al.* In Vivo Imaging of oskar mRNA Transport Reveals the Mechanism of Posterior Localization. *Cell* **134**, 843 (2008).

129. Jambor, H., Mueller, S., Bullock, S. L. & Ephrussi, A. A stem-loop structure directs oskar mRNA to microtubule minus ends. *RNA* (2014) doi:10.1261/rna.041566.113.

130. Driever, W. & Nüsslein-Volhard, C. The bicoid protein determines position in the Drosophila embryo in a concentration-dependent manner. *Cell* **54**, 95–104 (1988).

131. Ephrussi, A., Dickinson, L. K. & Lehmann, R. oskar organizes the germ plasm and directs localization of the posterior determinant nanos. *Cell* **66**, 37–50 (1991).

132. Herbert, S. P. & Costa, G. Sending messages in moving cells: mRNA localization and the regulation of cell migration. *Essays Biochem* (2019) doi:10.1042/EBC20190009.

133. Holt, C. E., Martin, K. C. & Schuman, E. M. Local translation in neurons: visualization and function. *Nature Structural & Molecular Biology 2019 26:7* **26**, 557–566 (2019).

134. Wheeler, J. R., Matheny, T., Jain, S., Abrisch, R. & Parker, R. Distinct stages in stress granule assembly and disassembly. *Elife* **5**, (2016).

135. Pitchiaya, S. *et al.* Dynamic Recruitment of Single RNAs to Processing Bodies Depends on RNA Functionality. *Molecular Cell* **74**, 521-533.e6 (2019).

136. Mateju, D. *et al.* Single-Molecule Imaging Reveals Translation of mRNAs Localized to Stress Granules. *Cell* (2020) doi:10.1016/j.cell.2020.11.010.

137. Wilbertz, J. H. *et al.* Single-Molecule Imaging of mRNA Localization and Regulation during the Integrated Stress Response. *Molecular Cell* **73**, 946-958.e7 (2019).

138. Falahati, H., Pelham-Webb, B., Blythe, S. & Wieschaus, E. Nucleation by rRNA Dictates the Precision of Nucleolus Assembly. *Current Biology* **26**, 277–285 (2016).

139. Ma, W., Zheng, G., Xie, W. & Mayr, C. In vivo reconstitution finds multivalent RNA–RNA interactions as drivers of mesh-like condensates. *Elife* **10**, (2021).

140. Sanders, D. W. *et al.* Competing Protein-RNA Interaction Networks Control Multiphase Intracellular Organization. *Cell* **181**, 306-324.e28 (2020).

141. Yang, Y. C. T. *et al.* CLIPdb: A CLIP-seq database for protein-RNA interactions. *BMC Genomics* **16**, 1–8 (2015).

142. Rollins, C. T. *et al.* A ligand-reversible dimerization system for controlling protein-protein interactions. *Proc Natl Acad Sci U S A* **97**, 7096–101 (2000).

143. Coller, J. M., Gray, N. K. & Wickens, M. P. mRNA stabilization by poly(A) binding protein is independent of poly(A) and requires translation. *Genes & Development* **12**, 3226–3235 (1998).

144. Imbert, A. *et al.* FISH-quant v2: a scalable and modular tool for smFISH image analysis. *RNA* **28**, 786–795 (2022).

145. Femino, A. M., Fay, F. S., Fogarty, K. & Singer, R. H. Visualization of single RNA transcripts in situ. *Science (1979)* **280**, 585–590 (1998).

146. Tsanov, N. *et al.* smiFISH and FISH-quant – a flexible single RNA detection approach with super-resolution capability. *Nucleic Acids Research* **44**, e165–e165 (2016).

147. Mueller, F. *et al.* FISH-quant: automatic counting of transcripts in 3D FISH images. **10**, 277–278 (2013).

148. van Bergeijk, P., Hoogenraad, C. C. & Kapitein, L. C. Right Time, Right Place: Probing the Functions of Organelle Positioning. *Trends in Cell Biology* **26**, 121–134 (2016).

149. Passmore, J. B., Nijenhuis, W. & Kapitein, L. C. From observing to controlling: Inducible control of organelle dynamics and interactions. *Current Opinion in Cell Biology* **71**, 69–76 (2021).

150. Korolchuk, V. I. *et al.* Lysosomal positioning coordinates cellular nutrient responses. *Nature Cell Biology* **13**, 453–462 (2011).

151. Cole, N. B., Sciaky, N., Marotta, A., Song, J. & Lippincott-Schwartz, J. Golgi dispersal during microtubule disruption: regeneration of Golgi stacks at peripheral endoplasmic reticulum exit sites. *Molecular Biology of the Cell* **7**, 631–650 (1996).

152. Hoogenraad, C. C. *et al.* Bicaudal D induces selective dynein-mediated microtubule minus end-directed transport. *EMBO Journal* **22**, 6004–6015 (2003).

153. Rawson, R. L. *et al.* Axons Degenerate in the Absence of Mitochondria in C. elegans. *Current Biology* **24**, 760–765 (2014).

154. Rivera, V. M. *et al.* A humanized system for pharmacologic control of gene expression. *Nature Medicine 1996 2:9* **2**, 1028–1032 (1996).

155. Kapitein, L. C. *et al.* Probing intracellular motor protein activity using an inducible cargo trafficking assay. *Biophysical Journal* **99**, 2143–2152 (2010).

156. Esteves da Silva, M. *et al.* Positioning of AMPA Receptor-Containing Endosomes Regulates Synapse Architecture. *Cell Reports* **13**, 933–943 (2015).

157. Willett, R. *et al.* TFEB regulates lysosomal positioning by modulating TMEM55B expression and JIP4 recruitment to lysosomes. *Nature Communications 2017 8:1* **8**, 1–17 (2017).

158. Ritt, M. & Sivaramakrishnan, S. Engaging myosin VI tunes motility, morphology and identity in endocytosis. *Traffic* **19**, 710–722 (2018).

159. Schimert, K. I., Budaitis, B. G., Reinemann, D. N., Lang, M. J. & Verhey, K. J. Intracellular cargo transport by single-headed kinesin motors. *Proc Natl Acad Sci U S A* **116**, 6152–6161 (2019).

160. Kapitein, L. C. *et al.* Myosin-V opposes microtubule-based cargo transport and drives directional motility on cortical actin. *Current Biology* **23**, 828–834 (2013).

161. Miyamoto, T. *et al.* Insufficiency of ciliary cholesterol in hereditary Zellweger syndrome. *The EMBO Journal* **39**, e103499 (2020).

162. Popovic, D., Nijenhuis, W., Kapitein, L. C. & Pelkmans, L. Co-translational targeting of transcripts to endosomes. *bioRxiv* 2020.07.17.208652 (2020) doi:10.1101/2020.07.17.208652.

163. Nijenhuis, W., van Grinsven, M. M. P. & Kapitein, L. C. An optimized toolbox for the optogenetic control of intracellular transport. *Journal of Cell Biology* **219**, (2020).

164. Miyamoto, T. *et al.* Rapid and orthogonal logic gating with a gibberellin-induced dimerization system. *Nature Chemical Biology* **8**, 465–470 (2012).

165. Janssen, A. F. J. *et al.* Myosin-V induces cargo immobilization and clustering at the axon initial segment. *Frontiers in Cellular Neuroscience* **11**, 260 (2017).

166. Wu, H. D. *et al.* Rational design and implementation of a chemically inducible heterotrimerization system. *Nature Methods 2020 17:9* **17**, 928–936 (2020).

167. Strickland, D. *et al.* TULIPs: tunable, light-controlled interacting protein tags for cell biology. *Nature Methods* **9**, 384 (2012).

168. van Bergeijk, P., #1, M. A., Hoogenraad, C. C. & Kapitein, L. C. Optogenetic control of organelle transport and positioning. *Nature* **518**, 111–114 (2015).

169. Harterink, M. *et al.* Light-controlled intracellular transport in Caenorhabditis elegans. *Current Biology* **26**, R153–R154 (2016).

170. Guntas, G. *et al.* Engineering an improved light-induced dimer (iLID) for controlling the localization and activity of signaling proteins. *Proc Natl Acad Sci U S A* **112**, 112–117 (2015).

171. Lu, M. *et al.* The structure and global distribution of the endoplasmic reticulum network are actively regulated by lysosomes. *Science Advances* **6**, (2020).

172. Adrian, M., Nijenhuis, W., Hoogstraaten, R. I., Willems, J. & Kapitein, L. C. A Phytochrome-Derived Photoswitch for Intracellular Transport. *ACS Synthetic Biology* **6**, 1248–1256 (2017).

173. Gutnick, A., Banghart, M. R., West, E. R. & Schwarz, T. L. The light-sensitive dimerizer zapalog reveals distinct modes of immobilization for axonal mitochondria. *Nat Cell Biol* **21**, 768–777 (2019).

174. Engelke, M. F. *et al.* Engineered kinesin motor proteins amenable to small-molecule inhibition. *Nature Communications* (2016) doi:10.1038/ncomms11159.

175. Das, S., Vera, M., Gandin, V., Singer, R. H. & Tutucci, E. Intracellular mRNA transport and localized translation. *Nature Reviews Molecular Cell Biology* 1–22 (2021) doi:10.1038/s41580-021-00356-8.

176. Buxbaum, A. R. In the right place at the right time: visualizing and understanding mRNA localization. *Nature Reviews Molecular Cell Biology* **16**, 95–109 (2015).

177. Engel, K. L., Arora, A., Goering, R., Lo, H. Y. G. & Taliaferro, J. M. Mechanisms and consequences of subcellular RNA localization across diverse cell types. *Traffic* **21**, 404–418 (2020).

178. Edelmann, F. T. *et al.* Molecular architecture and dynamics of ASH1 mRNA recognition by its mRNA-transport complex. *Nature Structural & Molecular Biology* **24**, 152–161 (2017).

179. Turner-Bridger, B. *et al.* Single-molecule analysis of endogenous β-actin mRNA trafficking reveals a mechanism for compartmentalized mRNA localization in axons. *Proc Natl Acad Sci U S A* **115**, E9697–E9706 (2018).

180. Liao, Y. C. *et al.* RNA Granules Hitchhike on Lysosomes for Long-Distance Transport, Using Annexin A11 as a Molecular Tether. *Cell* **179**, 147-164.e20 (2019).

181. Pohlmann, T., Baumann, S., Haag, C., Albrecht, M. & Feldbrügge, M. A FYVE zinc finger domain protein specifically links mRNA transport to endosome trafficking. *Elife* **4**, (2015).

182. Trovisco, V. *et al.* bicoid mRNA localises to the Drosophila oocyte anterior by random Dynein-mediated transport and anchoring. *Elife* **5**, (2016).

183. Forrest, K. M. & Gavis, E. R. Live Imaging of Endogenous RNA Reveals a Diffusion and Entrapment Mechanism for nanos mRNA Localization in Drosophila. *Current Biology* **13**, 1159–1168 (2003).

184. Mofatteh, M. & Bullock, S. L. SnapShot: Subcellular mRNA Localization Cell type Example RNAs Pattern Function RNA binding adaptor Other adaptors Motor(s) Cytoskeletal filament. *Cell* **169**, (2017).

185. Tutucci, E. *et al.* Cyclin CLB2 mRNA localization determines efficient protein synthesis to orchestrate bud growth and cell cycle progression. *bioRxiv* 2022.03.01.481833 (2022) doi:10.1101/2022.03.01.481833.

186. Meer, E. J. *et al.* Identification of a cis-acting element that localizes mRNA to synapses. *Proc Natl Acad Sci U S A* **109**, 4639–4644 (2012).

187. Abil, Z., Gumy, L. F., Zhao, H. & Hoogenraad, C. C. Inducible Control of mRNA Transport Using Reprogrammable RNA-Binding Proteins. *ACS Synthetic Biology* **6**, 950–956 (2017).

188. Banaszynski, L. A., Liu, C. W. & Wandless, T. J. Characterization of the FKBP-rapamycin-FRB ternary complex. *J Am Chem Soc* **127**, 4715–4721 (2005).

189. Safieddine, A. *et al.* A choreography of centrosomal mRNAs reveals a conserved localization mechanism involving active polysome transport. *Nature Communications 2021 12:1* **12**, 1–21 (2021).

RÉSUMÉ

Les condensats biomoléculaires, comme les nucléoles, les corps PML, les granules de stress et les P-bodies, sont essentiels à l'organisation cellulaire. Un modèle commun de formation par séparation de phase liquide-liquide a récemment émergé. La composition biochimique et les fonctions des condensats commencent à être décrites, mais la façon dont les cellules contrôlent leurs propriétés biophysiques (taille, nombre, morphologie…) reste incertaine. Des études de reconstitution ont été développées pour contourner la composition complexe des condensats endogènes, mais la plupart de ces études ont été menées *in vitro* en raison du manque d'outil pour travailler dans le contexte cellulaire. Ici, nous avons développé une méthode pour construire en cellules des condensats artificiels, combinant le contrôle des études de reconstitution *in vitro* et le contexte cellulaire. Leur formation est basée sur la dimérisation de protéines multivalentes qui se séparent en deux phases au-dessus d'une concentration seuil. Nous avons montré la possibilité de prévenir la formation des condensats ou de les dissoudre par addition d'un compétiteur chimique de l'homodimérisation. En outre, les condensats peuvent être enrichis en une protéine de liaison à l'ARN qui recrute un unique ARN synthétique exogène. L'imagerie des molécules d'ARN a montré qu'elles étaient principalement recrutées à la surface des condensats. La quantification du recrutement nous a permis d'établir une corrélation entre la densité d'ARN à la surface et la taille et la morphologie des condensats.
Dans un second temps, le projet doctoral s'est intéressé à la localisation intracellulaire des condensats quand ils sont transportés par des moteurs moléculaires, ce qui peut entre autres permettre la traduction localisée des ARNs des condensats. Pour examiner l'effet des moteurs sur les condensats, nous avons développé une méthode de fonctionnalisation des condensats artificiels en cellules avec des moteurs. Nous avons montré que les condensats étaient localisés dès la nucléation aux extrémités des microtubules. Ensuite, nous avons utilisé cette méthode pour localiser un ARN cible, soit exogène soit endogène. Ces résultats ouvrent de nouvelles possibilités pour étudier l'importance de la localisation intracellulaire des ARN.

MOTS-CLEFS

Condensats biomoléculaires – Séparation de phase liquide-liquide – Moteurs moléculaires – Granules ARN – Localisation de l'ARN

ABSTRACT

Biomolecular condensates, like nucleoli, PML bodies, stress granules, and P-bodies, are key elements of the subcellular organization, with liquid-liquid phase separation (LLPS) as a common model of formation. The biochemical composition and functions of the condensates begin to be deciphered, but how cells regulate their biophysical properties (size, number, morphology…) remains unclear. Reconstitution studies have been developed to circumvent the compositional complexity of endogenous condensates, but most of them are carried out *in vitro* because of a lack of tool to work in a cellular context. Here, we developed a method to build artificial condensates in living cells, combining both the control of *in vitro* reconstitution studies and the cellular environment. Their formation is based on multivalent proteins that dimerize and spontaneously phase separate over a threshold concentration. We showed that we were able to both prevent the formation of the condensates and dissolve them by adding a small chemical competitor. Moreover, the condensates can be enriched in a specific RNA-binding protein that recruits a unique synthetic exogenous RNA. By imaging the RNA molecules, we found that they were mainly recruited on the surface of condensates. Quantifying the recruitment allowed us to highlight a correlation between RNA surface density and the size and morphology of the condensates.
A second part of the doctoral project concerned the subcellular localization of condensates when they undergo transport via interactions with motor proteins, a process that can notably localize the translation of mRNA contained in the condensates. To investigate the effect of molecular motors on phase-separated condensates, we developed a method to reconstitute in cells motor-functionalized condensates. We showed that the condensates displayed as from nucleation robust localization at the microtubules ends. Next, we successfully used this method to localize a target RNA species, heterelogously-expressed or endogenous. These proof-of-concept experiments open new possibilities for the investigation of the importance of mRNA subcellular localization.

KEYWORDS

Biomolecular condensates – liquid-liquid phase separation – Molecular motor – RNA granules – RNA localization